Crustal-Scale Fluid flow and Hydrothermal Ore Deposits

Dissertation

der Mathematisch-Naturwissenschaftlichen Fakultät

der Eberhard-Karls Universität Tübingen

zur Erlangung des Grades eines

Doktors der Naturwissenschaften

(Dr. rer. nat.)

vorgelegt von

Isaac Naaman

aus Sekondi-Takoradi/Ghana

Tübingen

2025

Gedruckt mit Genehmigung der Mathematisch-Naturwissenschaftlichen Fakultät der Eberhard Karls Universität Tübingen.

Tag der mündlichen Qualifikation:	15.09.2025
Dekan:	Prof. Dr. Thilo Stehle
1. Berichterstatter:	Prof. Dr. Paul D. Bons
2. Berichterstatter:	Prof. Dr. M. Peter Süss

Erklärung

Ich erkläre hiermit, dass ich die zur Promotion eingereichte Arbeit selbständig verfasst, nur die angegebenen Quellen und Hilfsmittel benutzt und wörtlich oder inhaltlich übernommene Stellen als solche gekennzeichnet habe. Ich erkläre, dass die Richtlinien zur Sicherung guter wissenschaftlicher Praxis der Universität Tübingen (Beschluss des Senats vom 25.5.2000) beachtet wurden. Ich versichere an Eides statt, dass diese Angaben wahr sind und dass ich nichts verschwiegen habe. Mir ist bekannt, dass die falsche Abgabe einer Versicherung an Eides statt mit Freiheitsstrafe bis zu drei Jahren oder mit Geldstrafe bestraft wird.

Tübingen, 20th July, 2025

PhD Project Supervisor(s)

Prof. Dr. Paul D. Bons

Dr. Enrique Gomez-Rivas

ABSTRACT

Fluids ($H_2O \pm CO_2$) that flow through the earth's crust are major transporters of dissolved elements, such as Mg, Na, Ca, Fe, Ba, as well as more precious elements, such as Pb, Zn, Cu, Co, Ag and Au. Fluids in the crust can also carry significant amounts of heat. Hydrothermal fluids are, by definition, fluids that are hotter than the surrounding rocks and are associated with many ore deposits, for example the huge Olympic Dam U-bearing iron oxide-copper-gold (IOCG) deposit in South Australia and the abundant small deposits in the German Schwarzwald. When such fluids are associated with the formation of breccias, they are referred to as hydrothermal breccia. Hydrothermal fluids are often involved in the process of dolomitization. When crustal fluids (hydrothermal) cause fractures, they may cause significant dilation to create breccia.

Breccias can form in various ways, such as through sedimentation, igneous activity, meteorite impact, tectonic diminution, collapse, or fluid. These can be grouped into three broad categories: (i) igneous, (ii) sedimentary, (iii) tectonic. To classify them prefixes are commonly used, such as volcanic, igneous, hydrothermal, chert, fault, impact and seismic breccias. Hydrothermal breccias may thus share similarities with tectonic, dissolution, as well as collapse breccias. A distinguishing feature of a hydrothermal breccia is that the fracturing processes is dominated by a high fluid pressure and not primarily by elevated differential stresses as is the case for fault and impact breccias.

Apart from their significance for fundamental research, breccias are very important host rocks for ore deposits, and can also be zones of high permeability and thus serve as potential aquifers and reservoirs. One major setback on their study, the sub-classes, is that it’s often difficult to determine based solely on their origin, especially in terms of the genetic and/or textural classification under a major type. Improved definition of the diagnostic signature of the individual breccia types requires improved knowledge on their brecciation mechanisms, as well as their genetic associations and geological setting. This has resulted in hydrothermal breccia receiving a considerable attention in structural geology.

This research discusses the flow regime, fracture initiation and growth in rocks and place emphasis on fluid-assisted fracturing which extensively result in total disintegration (brecciation) of rock and potential fluid mixing and suggest ways in estimating the amount of fluid (pressure/energy) needed to cause or initiate a hydrofracture and fluid-assisted fracture dynamics and estimate sources of fluid (hydrothermal) that is released at depth by for example

dehydration reactions, exhumation or changes in the tectonic stress field. The study also analysed the clast size distribution of some hydrothermal breccias samples and discuss the conversion between different expressions of the size distributions. The new clast-size analyses of hydrothermal breccias from Pozolagua in NW Spain and the SW-German Black Forest is then present. Finally, this research presents model to explain why the power-law exponent is smaller in hydrothermal, fluid-pressure induced, breccias.

Method used is a numerical modelling of fluid flow in a rigid matrix to simulate hydrothermal fluid transport and fracture growth and dynamics, which constrains the minimum amount of pressure/energy the ascending fluids must provide. For the breccia clasts, a statistical analysis of various breccia samples to gauge size distribution using the clast area (2-D) dimension.

Fractures begin to form (rock failure) at some stage when there is continued increasing fluid overpressure. Unstable states that could lead to brecciation at much shallower levels are only reached at high fluid escape through large hydrofractures. Fractures and fluid (hydrothermal) transport dynamics may explain the abundance of deep sourced fluid inclusions and hydrofractures in much shallow levels in the subsurface. results further show that fracture growth varies significantly with proportionately constant fluid overpressure and that deep sourced fluid mixing is possible with well-connected fractures. Finally, as the formation of hydrofractures can dictate local effective permeability, intensive fracturing can lead to brecciation and mineral precipitation at much shallower levels as hydrofractures aid in upwelling deep sourced fluid to the near surface. It appears that clast sizes in all cases tend to follow a power-law (mean *n*-value of ~1.68) distribution, but power-law exponents can vary significantly, even within a single setting. Like the clast size distribution, fractures from the simulation also follows a power law, except those large ones that reached the surface. It appears that a rapidly ascending hydrofractures will tap fluids from all levels of the infiltrated rock column, and as well mix these fluids during ascent.

Zusammenfassung

Fluide ($H_2O \pm CO_2$), die durch die Erdkruste fließen, sind wichtige Transporteure von gelösten Elementen wie Mg, Na, Ca, Fe, Ba sowie von wertvolleren Elementen wie Pb, Zn, Cu, Co, Ag und Au. Die Fluide in der Kruste können auch erhebliche Wärmemengen transportieren. Hydrothermale Fluide sind per Definition Fluide, die heißer sind als das umgebende Gestein und mit vielen Erzlagerstätten in Verbindung gebracht werden, z. B. mit der riesigen U-haltigen Eisenoxid-Kupfer-Gold-Lagerstätte Olympic Dam in Südaustralien und den zahlreichen kleinen Lagerstätten im deutschen Schwarzwald. Wenn solche Fluide mit der Bildung von Brekzien verbunden sind, werden sie als hydrothermale Brekzien bezeichnet. Hydrothermale Fluide sind häufig am Prozess der Dolomitisierung beteiligt. Wenn Krustenflüssigkeiten (hydrothermale Flüssigkeiten) Brüche verursachen, können sie zu einer erheblichen Dilatation führen und Brekzien entstehen lassen.

Brekzien können auf verschiedene Weise entstehen, z. B. durch Sedimentation, Eruption, Meteoriteneinschlag, tektonische Abtragung, Kollaps oder Flüssigkeit. Sie können in drei große Kategorien eingeteilt werden: (i) magmatisch, (ii) sedimentär, (iii) tektonisch. Zur Klassifizierung werden häufig Präfixe verwendet, wie z. B. vulkanische, magmatische, hydrothermale, Hornstein-, Bruch-, Impakt- und seismische Brekzien. Hydrothermale Brekzien können daher Ähnlichkeiten mit tektonischen, Auflösungs- und Einsturzbrekzien aufweisen. Hydrothermale Brekzien zeichnen sich dadurch aus, dass die Bruchvorgänge durch einen hohen Flüssigkeitsdruck dominiert werden und nicht in erster Linie durch erhöhte Differenzspannungen, wie dies bei Bruch- und Impaktbrekzien der Fall ist.

Abgesehen von ihrer Bedeutung für die Grundlagenforschung sind Brekzien sehr wichtige Wirtsgesteine für Erzlagerstätten und können auch Zonen mit hoher Durchlässigkeit sein und somit als potenzielle Grundwasserleiter und Reservoirs dienen. Ein großer Nachteil bei der Erforschung der Unterklassen ist, dass es oft schwierig ist, sie allein aufgrund ihrer Herkunft zu bestimmen, insbesondere was die genetische und/oder texturelle Zuordnung zu einem Haupttyp betrifft. Eine bessere Definition der diagnostischen Signatur der einzelnen Brekzientypen erfordert bessere Kenntnisse über ihre Brekziationsmechanismen sowie über ihre genetischen Zusammenhänge und geologischen Gegebenheiten. Dies hat dazu geführt, dass hydrothermalen Brekzien in der Strukturgeologie große Aufmerksamkeit zuteil wird.

In dieser Studie werden das Fließregime, die Entstehung und das Wachstum von Brüchen in Gesteinen erörtert, wobei der Schwerpunkt auf der fluidunterstützten Bruchbildung liegt, die

weitgehend zu einer vollständigen Auflösung (Brekziation) des Gesteins und einer potenziellen Fluidvermischung führt, und es werden Möglichkeiten zur Abschätzung der Fluidmenge (Druck/Energie) vorgeschlagen, die erforderlich ist, um einen Hydrobruch und die fluidunterstützte Bruchdynamik zu verursachen oder zu initiieren, sowie zur Abschätzung der Fluidquellen (hydrothermal), die in der Tiefe beispielsweise durch Dehydratationsreaktionen, Exhumierung oder Veränderungen im tektonischen Spannungsfeld freigesetzt werden. Im Rahmen der Studie wurde auch die Klastengrößenverteilung einiger hydrothermaler Brekzienproben analysiert und die Umrechnung zwischen verschiedenen Ausprägungen der Größenverteilungen diskutiert. Anschließend werden die neuen Analysen der Klastengrößen von hydrothermalen Brekzien aus Pozalagua in Nordwestspanien und dem südwestdeutschen Schwarzwald vorgestellt. Schließlich wird ein Modell vorgestellt, das erklären soll, warum der Potenzgesetz-Exponent in hydrothermalen, fluiddruckinduzierten Brekzien kleiner ist.

Bei der verwendeten Methode handelt es sich um eine numerische Modellierung der Flüssigkeitsströmung in einer starren Matrix, um den hydrothermalen Flüssigkeitstransport sowie das Wachstum und die Dynamik von Brüchen zu simulieren, was die Mindestmenge an Druck/Energie, die die aufsteigenden Flüssigkeiten liefern müssen, einschränkt. Für die Brekzienklasten wird eine statistische Analyse verschiedener Brekzienproben durchgeführt, um die Größenverteilung anhand der (2-D-)Dimension der Klastenfläche zu ermitteln.

Die Bildung von Brüchen (Gesteinsversagen) setzt zu bestimmten Zeitpunkten ein, wenn der Flüssigkeitsdruck weiter steigt. Instabile Zustände, die zu Brekziation in viel flacheren Schichten führen könnten, werden nur bei hohem Flüssigkeitsaustritt durch große Hydrofrakturen erreicht. Die Ergebnisse zeigen außerdem, dass das Bruchwachstum bei proportional konstantem Flüssigkeitsüberdruck erheblich variiert und dass eine Vermischung von Flüssigkeiten aus der Tiefe mit gut vernetzten Brüchen möglich ist. Da die Bildung von Hydrofrakturen die lokale effektive Durchlässigkeit bestimmen kann, kann intensives Brechen zu Brekziation und Mineralausfällung in viel flacheren Schichten führen, da Hydrofrakturen den Auftrieb von tiefem Fluid zur nahen Oberfläche unterstützen. Es hat den Anschein, dass die Klastengrößen in allen Fällen tendenziell einer Potenzgesetz-Verteilung (mittlerer n-Wert von ~1,68) folgen, aber die Exponenten der Potenzgesetze können erheblich variieren, sogar innerhalb einer einzigen Umgebung. Wie die Schottergrößenverteilung folgt auch die Verteilung der Brüche aus der Simulation einem Potenzgesetz, mit Ausnahme der großen Brüche, die die Oberfläche erreicht haben. Es scheint, dass eine schnell aufsteigende Hydrofraktur Fluide aus allen Ebenen der infiltrierten Gesteinssäule anzapft und diese Fluide während des Aufstiegs auch vermischt.

Acknowledgements

My PhD research over the past years would not have been possible without the support, guidance, and encouragement of many individuals. First and foremost, I would like to express my deepest gratitude to my supervisor, Prof. Dr. Paul D. Bons for his guidance, patience, unwavering support and insightful feedback throughout this journey. I have indeed benefited from his immense scientific knowledge, experience and expertise in my chosen career field. He, simply, was understanding and accommodating. I say thank you Prof. I would like to extend my sincere thanks to my Assistant supervisor, Dr. Enrique Gomez-Rivas for his support during my research days and during my field trips in Spain.

Special thanks, is due DAAD for funding and supporting this research, Research Grants ST32, 2020/21 (57507871) Personal ref no. 91731924. Their resources and opportunities greatly contributed to my academic development.

Many thanks to my colleagues in structural geology workgroup of Prof. Bons in Tübingen and all my friends for the stimulating discussions, shared moments, and the field trips we made together that made the research environment both productive and enjoyable. In particular, I would like to thank Dr. Till Sachau, Tamara de Riese, Yuanbang Hu, Dongsheng Cao, Yu Zhang and Oliver Vonderschmidt for their support and friendship over the years.

To my family, I owe my deepest appreciation. I sincerely acknowledge the support from my parents, Moses Naaman and Joana Odai, thank you for your unconditional love, sacrifices, and belief in me. I show my sincere appreciation to my Gueandaline Naaman. I am much grateful to you all.

Table of Contents

Chapter 1

Introduction

1.0 Introduction

Fluids are common within the crust and their flow is the dominant process associated with mass and energy transport in the crust (Ingebritsen and Manning, 2010; Ingebritsen et al., 2006; Ague, 2003; Cathles, 1981; Fyfe et al., 1978). Such fluids ($H_2O \pm CO_2$) that flow through the Earth's crust are major transporters of dissolved elements, such as Mg, Na, Ca, Fe, Ba, including more precious elements e.g. Pb, Zn, Cu, Co, Ag and Au. They (fluids) can also carry significant amounts of heat (Sharma & Srivastava, 2014, Heinrich & Candela, 2014). When such fluids exist at relatively high temperatures and pressures within the crust, predominantly aqueous and contain such various dissolved substances (Morishita, & Hammond, 2024; Pirajno, 2013; Skinner, 1979) it's known as hydrothermal fluid. Thus, by definition, hydrothermal fluids are fluids that carry heat and are hotter than the surrounding rocks (Norton, 1984; Ague, 2014). Such fluids acquire their heat through known geological processes, mostly by igneous activities and including the heating of groundwater by hot rocks (Pirajno, 2009; Hanson, 1995). When fluids, such as seawater or meteoric water (infiltrating surface water into the crust), come into contact with hot rock near a magma chamber, they are rapidly heated. Again, when fluids percolate deeper into the earth's crust along fractures, faults, or permeable rock layers, they encounter hotter conditions, heating up as they descend (geothermal heating). This is a prevalent, passive mechanism of heating. Metamorphism and convective circulation also serve as sources of heat, as fluids repeatedly exposed to high temperatures when they circulate within the crust (Pirajno, 2009; Ranalli & Rybach, 2005; Hanson, 1995; Fournier, 1989).

Some importance attached to these fluids are the many ore deposits which formed through their flow within the crust, from the huge Olympic Dam U-bearing iron oxide-copper-gold (IOCG) deposit in South Australia to abundant small deposits in the German Black forest (Staude et al. 2009; Pollard, 2006). Again, Hydrothermal fluids are often involved in the process of dolomitization, where calcite in limestones is converted to dolomite (Qaisar et al., 2023; Sibley and Gregg, 1987). Furthermore, a major contribution of geofluids (hydro) within the subsurface

is in the creation of 'mobile' hydrofractures (Spence and Turcotte, 1985; Dahm, 2000; Bons, 2001; Bons et al., 2022). This happens when the elevated fluid pressure equals or exceeds the overburden pressure, $P_{lith} = \rho_{rock} \cdot g \cdot z - P_f$, (i.e. strength of the rock) causing fractures to form and propagate (Bons et al., 2014; Sibson, 1981; Hubbert and Willis 1957). Such fractures are termed hydrofractures (see de Riese et al., 2020; Bons et al., 2022 and the references therein). In the absence of tectonic forces that initiate and grow fractures, (significant) fluid overpressure seems to be the only means to cause and grow fractures within the crust. Such fractures usually start on a micro scale level and develop with significant dilation to propagate at the tips (Pollard and Aydin, 1988; Anderson and Anderson, 1995). When fractures grow large enough and connect with each other extensively, breccias may form Fig.1. They are termed hydrothermal because fluids of such nature have initiated and/or caused their formation (Shukla and Sharma, 2018, Weisheit et al., 2013, Jébrak, 1997).

Despite advances made in the knowledge of fluid flow and hydrofracture dynamics within the crust, the following questions remain: (i) how do large hydrofractures sprout from the base all through to the surface with circulating fluid within the fractured rock column?, (ii) what is the mechanism in fracture dynamics, transport and mixing of deep sourced hydrothermal and meteoric fluids at much shallower levels?, (iii) What induces extensive fracturing to cause brecciation in hydrothermal deposits which suggest a transition in flow and fracture dynamics? (Marshall & Oliver 2006), and (iv) how do permeability and fluid pressure variations affect the development, distribution, and linking of hydrofractures? De Riese et al. (2020) us a modified sandpile model to explore the effect of the relative contributions of Darcian porous flow and flow through hydrofractures on crustal-scale fluid flow. They proposed that this is achieved through varying the fluid pressure diffusivity, as a function of permeability, with a constant fluid flux and assume fluid transport through the crust as a bimodal transport system. In the case of the hydrothermal breccia, the study sorts to address uncertainties that bothers the comparison between different studies on size distribution and hence present a model to explain why the power-law exponent is smaller in hydrothermal, fluid-pressure induced, breccias than in fault breccias.

This study uses simulations analogous to the sandpile model (Bak et al., 1988) - a build-up on that of de Riese et al. (2020), to simulate and discuss the flow regime, fracture initiation and growth path in rocks. It also sorts to analyse the clast size distribution of some hydrothermal breccias: breccias associated with dolomitising fluids and ore-related breccias and provide ways to estimate the total amount of fluid pressure/energy necessary to cause or initiate a

hydrofracture and fracture dynamics. Finally, as the formation of hydrofractures can dictate local effective permeability, this study presents a model that shows that excessive fracturing can lead to brecciation, fluid mixing at much shallower levels within the crust regardless of the level and distribution of the fluid source. The last chapter of this study throws more light on two main approaches to assess the effect on failure of an elevated fluid pressure and the products of hydrofracturing.

Figure 1. Field photographs of a fluid altered breccia outcrop. Evidence of breccia in a well fractured zone with a conduit/column of hydrothermal breccia.

2.0 Crustal fluid source

Existence of crustal fluids is evident in the hydrothermal reservoirs and ore deposits (Ague and Rudnick, 2003). The main three sources or reservoirs of fluid in deeper levels of the crust are (i) pore fluid, (2) fluid released by devolatilization reactions, and (3) fluid released by igneous activity. Fluid-filled porosity of 0.5-1% may exist down to almost 10 km depth, even in metamorphic/metaigneous rocks, as was observed in the Continental Deep Drilling project (KTB, Emmermann & Lauterjung, 1997). Although the amount of pore fluid in a low-porosity rock volume is limited, fluid circulation may greatly enhance the total flux of fluid passing through rocks (Ague, 2014; Yardley and Bodnar 2014; Ague and Rudnick, 2003; Oliver, 1996). As opposed to this, fluids released by devolatilization of H_2O-bearing minerals or crystalizing magma provide 'single pass' fluid flow events, which significantly reduces the total fluid budget.

Much work has been devoted to determining fluid sources and their (relative) reservoir volumes by considering the "budgets" of major/trace elements, isotopes, halogens, etc. (Yardley and Bodnar, 2014, Ague, 2014, and the references therein). For instance, Staude et al. (2009) estimate the required volume of fluid to produce the Jurassic deposits in the Black Forest (Black forest) at ca ~12 km^3, while modelled calculations showed that ~ 6-12 km^3 could have been released due to decompression. In the Hidden Valley, similarly, Weisheit et al. (2013) suggest that at least ~20 km^3 of fluid is required in the Hidden Valley mega-brecciation in South Australia and discussed the various fluid sources that may have contributed to this volume, such as ~ 8-21 km^3 from biotite dehydration and/or ~ 5-10 km^3 by decompression.

2.1 Crustal fluid composition and alteration in rocks

Hydrothermal fluid, a form of crustal fluids exists at relatively high temperatures and pressures deep within the Earth's crust. They are usually aqueous in solution that contain various dissolved substances, including minerals and gases, predominantly rich in metals and other elements (Pirajno, 2013; Morishita, & Hammond, 2024; Skinner, 1979). Fluids within the crust are of many forms of which aqueous (H_2O) and gas (water vapour) phases are dominant. Regardless of their numerous possible sources in the crust, fluids in sedimentary, magmatic and/or metamorphic environments are known to exhibit predominantly a system of H_2O and gas and normally reflect on equilibrium with rocks and melts at the relevant pressure-temperature conditions (see Yardley & Bodnar, 2014 and the references therein; Pirajno, 2013). The gas component in many geological environments is dominated by CO_2, CH_4, as well as various sulphur and nitrogen-rich gases. But how much inclusions in any crustal fluid, the temperature and pressure directly dictate the concentrations of such fluid compositions. For example, the concentrations of NaCl (halite), CaSO4 (anhydrite) and SiO_2 (quartz) minerals are dependants on the contrasting P-T of the fluid. Sulphate minerals such as anhydrite as well as carbonate minerals, become less soluble with increasing fluid temperature (Rimstidt, 1997, Leach et al., 2005, Bodnar et al., 2014). Works on some hydrothermal deposits for instance, the Mississippi Valley-Type deposits that form in sedimentary basins indicate that fluids are predominantly high in salinity (Na, Ca) brines that have significant metal-carrying capacity (Weisheit et al., 2013a, Bodnar et al., 2014).

2.2 Hydrothermal fluids

Now let consider how hydrothermal fluids are realized within the crust and their flow in the crustal column. Fluids that are elevated in temperature and are hotter (at least 5ºC) than the surrounding rocks (Davies and Smith, 2006) are known as hydrothermal fluids. Before they become heated and termed hydrothermal in nature, fluids within the crust must get their heat from either of these two main mechanisms, (i) fluids driven by primarily magma activities when it is heated by underlying magma - igneous activities and other hot geological formations e.g. metamorphic reactions within settings with significant tectonic activity where crustal heat flow is elevated and (ii) percolating fluids which are heated by geothermal gradient whilst infiltrating (Bons et al., 2012; Ingebritsen and Appold, 2012; Cox, 2010; Cathles, 1981, 1997). In a crustal setting, fluid flow through fractures and faults are required to flow fast enough to maintain an elevated temperature compared to that of the host rock (Bons et al., 2012 and the references therein). At a much shallower depth, ca. ~2 km fluid mixing is prominent. According to Bons et al., (2012) hydrothermal fluid temperatures may thus converge to ~374 °C if they were originally hotter. After being elevated in temperature, hydrothermal fluids must be able to carry heat to colder sections/regions within the crust. For example, fluid inclusions in the Schwarzwald and Taunus hydrothermal deposits indicate temperatures of up to around 300°C, although the ambient temperatures at the shallow level of their formation were probably less than ~125°C. But for a fluid to maintain its thermal energy it carries; the fluid must therefore flow rapid/fast enough to stay hot.

2.3 Fluid Flow within the crust

Fluids flow down hydraulic head gradients. When fluids are sourced at depth, they mainly flow upwards. Fluids (hydrothermal) that ascend from the source cool and decompress during ascent, which may lead to precipitation of minerals. Flow is often controlled by the column's permeability structure and the presence of open pathways. Hydrothermal fluid flow typically is of two forms: (i) Fracture or focused flow - fluid move through well-defined fractures, or faults in the crust, where permeability is much higher. Here, flow is typically fast and localized (Fyfe et al, 1978; Cathles, 1990; Ingebritsen & Manning, 2010), and (ii) diffuse flow – advective fluid flow down gradient in hydraulic head controlled by the permeability of the rock according to Darcy's law. That is, flow rate is proportional to the pressure gradient and the permeability of the material. Darcian flow can be termed 'diffusive', not because the fluid diffuses, but because the change in fluid overpressure can be described as diffusive. For diffusive or pervasive flow,

fluids move slowly through the interconnected pore spaces of rocks. It is driven primarily by pressure or thermal gradients.

At depth fluid pressure in the crust increases from hydrostatic to close to lithostatic as the permeability decreases with depth (Ingebritsen & Gleeson, 2015; Ingebritsen & Manning, 2010; Ingebritsen et al., 2006).

3.0 Natural hydrofractures

Fractures within the crust are cracks with no movement resulting from either weathering, stress (exceeding the rock's strength) or movements of the crust. Fractures, a term used for all types of generic discontinuities and generally, initiate and propagate. They are sometimes termed as joint, shear or tensile depending on the size and how the fracture occurs (Bons et al., 2022; Gudmundsson, 2011; Jaeger et al., 2009; Pollard & Aydin, 1988). A fracture thus, is a mechanical break involving discontinuities in displacement in rocks across surfaces or narrow zones. These fractures, when associated or initiated by crustal fluid in their growth and propagations, are called hydrofracture. They typically form below c. 2–3 km depth within the crust (Bons et al., 2022). Hydrofractures therefore, denote fractures whose formation is induced or triggered by an elevated fluid pressure, contrary to other fractures in the crust formed by differential stresses, primarily due to tectonic stresses, for example at depths greater than ca. 10 km, extensional fractures formed under metamorphic conditions are hydrofractures as they can only occur when there is high fluid overpressure. For extensional fractures which form at shallow crustal levels however, could have resulted from tectonic stresses without a reduction of the effective stresses due to an elevated fluid pressure and so may not entirely be hydrofractures (see chapter 4, the review paper on hydrofractures from Bons et al., 2022 for a detailed clarification).

The initial formation of hydrofractures may not be initiated by fluid overpressure but may be taken over later on as in the case of igneous dykes. Therefore, a fracture may occur due to a naturally elevated fluid pressure, or artificial induced increase of the fluid pressure, elevated tectonic stresses (a tectonic fracture), or possible combination of these which is usually the case. This means that once such fractures are formed, a complex stress field may develop, particularly at these fracture tips (Engelder, 1999) and tends to propagate them.

Once fractures form, they may either increase permeability and or leak the overpressured fluids. The fracture pattern may then evolve dynamically if the pressure is not dissipated. A simulation

of injection of fluid associated fracturing (Ghani et al. 2013; Koehn et al. 2020) illustrate this further with seal in the structural column see (Chapter 4, Fig.5, Bons et al., 2022). They explained how the initial fractures follow Terzaghi's principle and showed why they are vertical and parallel to the largest principal stress. Chapter 4, of this study, presents in details, a review of hydrofractures and the associated products through their process of formation and growth.

3.1 Breccias – hydrothermal breccia

When a fracture does not only propagate at its tip, but branches out in many directions to connect and reconnect to other fractures, breccias are formed. In other words, when rocks are disintegrated into many fragments or clasts, they are termed breccia Fig.1/3 (Shukla and Sharma, 2018; Jébrak, 1997; Weisheit et al. 2013 and the references therein). This comes as the onset of brecciation significant dilation. For any alteration or deformation in rocks, the initial resistance of the rock strength must be overcome through external forces mechanically and or chemical alteration within the rock. Hydrothermal ore deposits and alteration zones typically show brecciation Fig. 3 (Weisheit et al. 2013a,).

Breccias typically found in hydrothermal deposits (e.g. Black forest and the Hidden-Valley), suggests that the hydrothermal fluids were able to disintegrate the rock (see Staude et al., 2007; Weisheit et al. 2013,). Breccias are termed hydrothermal when they are formed by hydrothermal fluid processes and are notable primarily from other breccias based on their mode of formation and genetic characteristics. Such breccias can be classified as a tectonic breccia (Shukla and Sharma, 2018; Phillips, 1972; Jèbrak 1997; Scholz, 1990; Hubbert and Willis, 1957) but is treated as a separate class (Jébrak, 1997) for purpose this research. A distinguishing feature of a hydrothermal breccia is that the fracturing processes is dominated by a high fluid pressure and not primarily by elevated differential stresses as is the case for fault and impact breccias. In chapter 2, breccia types are briefly discussed. Regardless of mode of formation of any breccia type, usually a combination of both chemical and physical processes (Middleton, 1961; Stanton, 1966; Friedman, 1997; Kolodny et al., 2005) follow their emplacement within their geological setting. Later on, hydrothermal alterations occur in some emplaced breccia bodies resulting in clast size modification. These fluidised alterations and modifications are subject to, most of the time, the mineral block of the rock rather than their physical properties especially in fault breccias where porosity is enhanced, and in dolomitic rocks Fig.3.

3.2 Clast-size distribution and clast shape

To create a breccia, a volume of coherent rock must basically be divided into multiple sub-volumes, the fragments or clasts, that remain internally coherent, but have lost coherence with other clasts. Coherence can, of course, be restored subsequently through cementation (Jackson, 1997). The cause for loss of coherence between clasts under consideration here is fracturing, thus excluding other processes, such as, for example, dissolution. A power-law distribution of clast sizes means that the breccia is self-similar in this respect. This means that the ratio of number of clasts of size *s* and *s*/10 is the same, irrespective of the value of *s*. This again implies that there is no characteristic length scale in the brecciation process. The Mohr-Coulomb-Griffith theory for brittle failure has no characteristic length scale, as the parameters are stresses, fluid pressure and the material properties tensional strength, cohesion, and internal angle of friction (Bons et al. 2022; Royer, 2014; Terzaghi, 1943; Hubbert, 1951; and Secor, 1965). The theory has proven to be successful in predicting when a fracture will form and in which orientation, but not where it will form or what size the fracture has. Considering this, a power-law clast-size distribution is to be expected, at least within a certain range.

To distinguish hydrothermal breccias from other known types, the clast size morphology and distribution can be used, in particular their fractal dimension, which is related to the disintegration processes of the rock mass (Jébrak, 1997). A number of studies therefore measured the clast-size distribution in breccias (Lorilleux et al. 2002; Barnett, 2004; Keulen et al. 2007; Weisheit et al. 2013a). These studies concurred with Jébrak et al. (1997) that breccia clast sizes typically show a power-law distribution with small clasts more frequent than bigger clasts. This distribution is often given in the cumulative form:

$$N_{(\geq s_i)} = k_i \cdot (s_i)^{-n_i}, \tag{1}$$

with $N_{(s)}$ the number of clasts larger or equal to size *s*, and *n* power-law exponent that is smaller for hydrothermal breccias than for fault breccias (Jébrak, 1997). *k* is the number of clasts larger or equal to the unit size. The subscript *i* refers to the dimension in which the size is expressed, with *i*=3 for volume, *i*=2 for cross-sectional area, and *i*=1 for diameter.

Instead of the cumulative size distribution (Eq. 1), one can also use the frequency (*f*) distribution, given by:

$$f_{(s)} = -\frac{dN_{\geq s}}{dV} = nk \cdot s^{-n-1} \tag{2}$$

The advantage of using a frequency distribution is that it is not sensitive to sampling errors at the upper end of the size range or potential variations in the exponent with size. A disadvantage is that the frequency distribution is sensitive to the choice of bins.

Although clasts are 3-dimensional objects, clast sizes are usually reported in the literature as either diameter or area and not as volume. This hampers comparison between different studies. The conversion between different expressions of the size distributions is thus, discussed below. A new clast-size analyses of hydrothermal breccias from Pozalagua in NW Spain (Swennen et al., 2012; Aranburu et al. 2002) and the SW-German Black Forest (Geyer and Gwinner, 1986; Kalt et al., 2000; Staude et al., 2009) is presented. Finally, a model is presented to explain why the power-law exponent is smaller in hydrothermal, fluid-pressure induced, breccias than in fault breccias. The lower end of the power-law range is typically the grain size. The uppermost end of the range is controlled by the size of the breccia, as the largest clast must simply be smaller than the whole breccia. The power-law range can thus be large for clasts from <1 mm^2 to about 1 km^2 in area in the 10 km^2 (Weisheit et al. 2013)

4.0 Relationship between power-law exponent and dimension

Rocks are 3-dimensional and therefore we can start the analysis of the relationship between the power-law exponent and the dimension in which clast sizes are measured with the three-dimensional case (n_3) as a reference. A low value of n_3 means that the second largest clast is much smaller than the largest clast compared to a high value of n_3 (Fig. 2). This means that for a small n_3 value a relatively large proportion of the breccia volume is occupied by the largest clasts. For a large n_3 value the largest clasts only occupy a relatively small fraction of the total breccia volume.

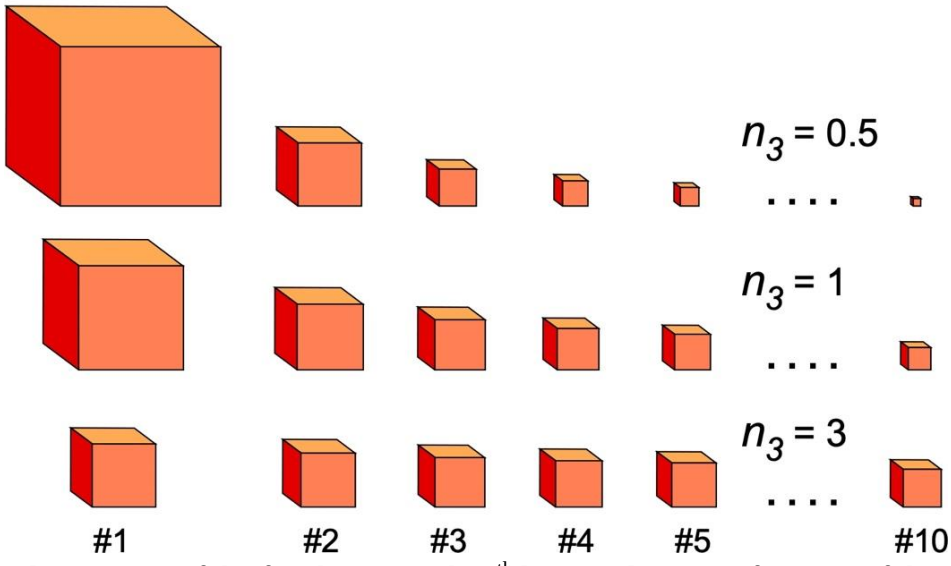

Figure 2. Relative sizes of the five largest and 10th largest clasts as a function of the power-law exponent n_3, for n_3 = 0.5, 1, and 3.

A problem with the practical measurement of clast sizes and their distribution is that we normally do not have a 3-dimensional view of the clasts, but instead typically a 2-dimensional outcrop surface that intersects the breccia and its clasts. The area of the intersection of a clast and an arbitrary erosion surface depends on its shape and where it is intersected. Using a shape factor α, we can approximate the average intersection area s_2 as a function of clast volume s_3. Equations for the computed size dimensions are presented in chapter 2.

Table 1 summarises the conversion equations for different power-law exponents derived in one or two dimensions to the volumetric n_3 for the cumulative clast-volume distribution. Jébrak (1997) used the power-law exponent (n_1) of the cumulative particle diameter (s_1) as an indicator of the amount of energy that was introduced into the system. He found that a low n_1 (~2) for fluid-assisted brecciation and values of $n_1 \geq 3$ for wear abrasion and shear. These values correspond to the cumulative volumetric n_3 (Eq. 1) of ~1 and 1.33, respectively. Weisheit et al. (2013) obtained an exponent of $n_2 \approx 1$ for the cumulative distribution of clast areas in the hydrothermal Hidden Valley breccia. From this we derive a volumetric $n_3 \approx 1$ for the Hidden Valley breccia.

Table 1**:** Conversion of the power-law exponent for clast area and diameter distributions to the volumetric exponent n_3, including examples from the literature and this study.

Measurement	**Distribution**	**Volumetric n_3**	**Reference**	**Derived volumetric n_3**
Cumulative				
True area	$N_{\geq s_2} \propto (s_2)^{-\left(\frac{3}{2}n_3\right)}$	$n_3 = \frac{2}{3}n_2$		
Area in section	$N'_{\geq s_2} \propto (s_2)^{-\left(\frac{3}{2}n_3-\frac{1}{2}\right)}$	$n_3 = \frac{2}{3}\left(n_2+\frac{1}{2}\right)$	Weisheit et al. (2013)	$n_2 \approx 1 \rightarrow n_3 \approx 1$
Diameter in section	$N'_{\geq s_1} \propto (s_2)^{-(3n_3-1)}$	$n_3 = \frac{n_1+1}{3}$	Jébrak (1997)	fluid assisted: $n_1 \approx 2 \rightarrow n_3 \approx 1$ wear abrasion, shear: $n_1 \geq 3 \rightarrow n_3 \geq \frac{4}{3}$
Frequency				
True area	$f_{\geq s_2} \propto (s_2)^{-\left(\frac{3}{2}n_3+1\right)}$	$n_3 = \frac{2}{3}(n_2-1)$		
Area in section	$f'_{\geq s_2} \propto (s_2)^{-\left(\frac{3}{2}n_3+\frac{1}{2}\right)}$	$n_3 = \frac{2}{3}\left(n_2-\frac{1}{2}\right)$	This study, Pozalagua Teufelsgrund	$1 < n_2 \leq 2 \rightarrow \frac{1}{3} < n_3 < 1$ $n_2 \approx 1.5 \rightarrow n_3 \approx \frac{2}{3}$
Diameter in section	$f'_{\geq s_1} \propto (s_2)^{-(3n_3-1)}$	$n_3 = \frac{1}{3}(n_1+1)$		

5.0 Scope of the project

The whole research project addresses the topics of hydrothermal breccias and crustal fluids flow and hydrofracture dynamics. It sorts to explain what hydrothermal breccias are and the underlying mechanical and morphological characteristics in terms of their formation, associations and size distributions. Based on an existing model (sandpile model) from previous works, this study generally simulates crustal fluid flow and associated fracture dynamics. A field survey to supports the knowledge about hydrothermal breccia outcrops. The aim is to establish hydrothermal fluid involvement during and/or after brecciation. The crustal fluid flow and hydrofracture dynamics provide key insights into the formation and evolution of breccias – fluid induced fracturing and their size distribution, highlighting fluid processes within the subsurface environments. Thus, this project is centred on the following sections:

(i) the morphological characteristics of hydrothermal breccias – dolomitic breccias from the Pozalagua, Northern Spain and from the Black forest, Germany. From where new clast-size analyses are presented. It discusses the conversion between different expressions of the size distributions and present new clast-size analyses of hydrothermal breccias from Pozolagua in NW Spain and the SW-German Black Forest. The study also extends to present a model to explain why the power-law exponent is smaller in hydrothermal, fluid-pressure induced,

breccias than in fault breccias. To address and analyse distribution relating to the clast size evolution, a general model for the breccia statistics is also presented.

(ii) A numerical simulation on the fluid flow and hydrofractures. For the hydrofractures, various publications presented dealt with the contrasting features and dynamics, depending on the geological processes. For fluids and hydrofracture dynamics, chapter 4, addresses and gives a comprehensive review on natural hydrofractures and explains when a fracture could be classified as a hydrofracture. The numerical simulation which is the main research study method is run to ascertain fluid flow and associated fracture dynamics. This gives the background to address the question as why the fluids ascend and how breccias and ore deposits formed.

This project thus, focusses and build on some fundamental research works to interpret the dynamic evolution and alterations of hydrothermal processes within the crust - crustal fluid flow, fractures and associated ore deposits.

6.0 Methodology

This research employs a numerical modelling for the flow and fracture dynamics within the crust and a statistical analysis to evaluate the hydrothermal breccias that results from hydrothermal processes allowing for both simulation-based prediction and data-driven interpretation. The first section (6.1) deals with the model simulation for the flow and fracture dynamics and the second part (section 6.2) for the hydrothermal breccia statistics.

6.1 Model simulation

The same model as de Riese et al. (2020) was used in this research, but with some modifications. The model simulates a 2-dimensional, vertical section through the crust. The model is divided up in a rectangular grid of 200 x 200 elements of linear size $\lambda \sim 100$m (Chapter 3, Fig. 1). Each element represents a volume of rocks with a porosity (ϕ) and a rigid matrix. Adding fluid to the pores then increases the fluid pressure, depending on the fluid compressibility (α). Contrary to de Riese at al. (2020), this model does not introduce fluid at the base of the model, but in a fluid-production zone (FPZ), typically all elements in the bottom half of the model. Each time step fluid is added to all elements one by one in the FPZ by raising the fluid pressure. It is then checked if any hydrofractures form because the fluid pressure exceeds the lithostatic pressure. If this is the case in an element it is set to have a hydrofracture, which can then lead to a cascade

of hydrofracture propagation (see below). The propagation continues until either a fracture system reaches the surface, draining all fluid) or when the fluid pressure in all fractured elements is below the lithostatic pressure. Next, the fluid pressure field is adapted by diffusion to simulate Darcy-type fluid flow. Fluid pressure at the Earth's surface, i.e., in the top row of elements is always set to zero after each round of fracture and porous flow, meaning that fluid that reaches the surface is removed from the system.

Chapter 3, Fig.1, presents a simplified model diagram of the numerical simulation and the resultant lithostatic pressure and fluid pressure illustrating, the level at which fracture are likely to form and grow, i.e. the level where P_{lith} equals or less the P_f. To some extent, this simulation cannot entirely depict the geofluids flow processes within the crust in the sense that, it oversimplifies subsurface processes. It does not consider a-3D scaling dimensions in a real-world situation but here presented in 2D. Specific boundary conditions are often unrealistic for real world as boundaries in the subsurface are influenced by geological structures, seals, aquifers, or reservoirs, as well as explicit modelling of fluid properties.

6.1.1 Model Scaling

Time step

All fluid that enters the model escapes through to top boundary. The total time-averaged flux above the fluid-production zone (FPZ) is thus equal to the fluid production in that zone. This total time-averaged fluid flux is set at $J_f = 10^{-11}$ m/s after Ingebritsen and Manning (1999). Each time step fluid is entered into the system by increasing the pressure P of cells in the FPZ by a random increment ΔP between 0 and 0.002 model pressure units, i.e., on average $\Delta P = 0.001$. the model uses a simple constant rock and fluid density of 2800 kg/m^3 and 1000 kg/m^3, respectively. The difference of the lithostatic overpressure and the hydrostatic fluid pressure at the lower boundary of the model at 20 km depth is thus 360 MPa, equivalent to 200 model pressure units. The average ΔP is thus $0.001 \cdot 200/360 = 5.5 \cdot 10^{-4}$ MPa.

The fluid overpressure (P) is thus, tracked and recorded for each element or cell with:

$$P = P_f - P_h \tag{3}$$

Where, P, is defined as the difference between the actual fluid pressure (P_f) and the hydrostatic fluid pressure (P_h). The hydrostatic pressure is set to zero at the top row of the elements and increases with depth z. The model assumes a fluid viscosity $\eta = 0.001$ Pa·s, although the viscosity of water varies depending on pressure and temperature (Abramson, 2007). The fluid

compressibility was set to $\alpha = 2$ GPa (similar to Staude et al., 2009). Porosity ϕ, can vary widely from <1% to around 30% at shallow depth (Liebscher, 2010). As the main focus is on rocks at >10 km depth, and set the porosity at $\phi = 0.01$. In the model, the coefficient of D for the model setup (D_{mod}) is set for the different values for all the simulation. The input model (D_{mod}) values for D (0 – 0.0002) are presented in Table 2.

Using the pore volume of one element ($\phi \cdot \lambda^2$) as reference volume we have:

$$\Delta P = \alpha \frac{\Delta V}{\phi \lambda^2}, \quad \text{or} \qquad \Delta V = \frac{\phi \lambda^2 \Delta P}{\alpha} = \frac{10^{-2} \cdot 10^4 \cdot 5.5 \cdot 10^{-4}}{2000} = 2.75 \cdot 10^{-5}\ \text{m}^3 \tag{4}$$

If the height of the FPZ is 100 elements, and each element is 100 m wide, the total time-averaged flux emanating from the FPZ is $2.75 \cdot 10^{-5}$ m^3 per m^2 and per model time step. it follows that the model time step is $2.75 \cdot 10^{-5}$ / 10^{-11} = $2.75 \cdot 10^6$ s, which is about a month. In complementary simulations with different FPZ-heights, ΔP is adjusted to maintain the same time-averaged fluid flux at the top of the model, and hence the same time step.

Diffusion

In one dimension the fluid flux is described with Darcy's law:

$$J = -\frac{\kappa}{\eta} \frac{\partial P}{\partial z} \tag{5}$$

The flux J in m/s is the velocity of the fluid, or the volume ΔV of fluid travelling through a one m^2 window. It depends on the permeability (κ in m^2) of the rock and the viscosity (η in Pa·s) of the fluid. Assuming a constant κ and η, that the rate of change in fluid volume is:

$$\frac{\partial V}{\partial t} = -\frac{\kappa}{\eta} \frac{\partial^2 P}{\partial z^2}, \quad \text{and with Eq. (4):} \qquad \frac{\partial P}{\partial t} = \frac{\kappa \alpha}{\eta \phi} \frac{\partial^2 P}{\partial z^2} = D \frac{\partial^2 P}{\partial z^2} \tag{6}$$

Equation (6) is equivalent to Ficks's second law for diffusion, with D (in m^2/s) the diffusion coefficient for fluid overpressure diffusion. The unit of the diffusion coefficient is (length unit)^2/time unit. For the real-world diffusion coefficient D, we get:

$$D_{mod} = \frac{100 \cdot 100}{2.75 \cdot 10^6} D, \text{ giving} \qquad D = 275 \cdot D_{mod} \tag{7}$$

From Eq. (6) we can now derive the permeability κ in m^2:

$$\frac{\kappa \alpha}{\eta \phi} = D = 275 \cdot D_{mod}, \text{ giving} \qquad \kappa = \frac{275 \eta \phi}{\alpha} D_{mod} \tag{8}$$

With the settings of the simulations, $\kappa = 1.38 \cdot 10^{-12}$ m^2 for D_{mod}=1.

In case of a change in diffusion coefficient between two elements, the effective diffusion coefficient D_{eff} is considered.

6.1.2 The model hydrofractures

The model depicts the sandpile model and simulates flow in a form of diffusional flow and fracture flow. Using the pressure diffusion equation (6), fluid flow is implicitly modelled by tracking the evolution of *P*. The simulation runs for a duration (endtime = 500000) for all coefficients of *D*, updating the grid at each timestep. The model set the system to have a variability of flux within the medium and assume that fluid is set in bottom half-way of the model. An avalanche (fracture) initiate and propagate when a failure criterion is reached. It is assumed that flow through a fracture is fast enough so that pressures within it are equalised effectively instantaneously. The main loop consists of adding fluid randomly and letting the pressures diffuse over time. Fluid diffuses between neighbouring elements. When *P* exceeds a critical threshold, the system then evolves towards a state where an avalanche (fracture) occurs - the time and size (number of broken elements) of the cluster is recorded. Fluid then flows rapidly (avalanche-like behaviour).

The basic loop in the simulation follows that: An element/cell is randomly selected in bottom row and model pressure in that element is increased by ΔP_{mod} =0.001(on average). If *P* in an element increases ($P > P_{\text{lith}}$ in any element), the system breaks an element and selects random neighbour and break too until *P* equalizes in cluster. The system will drain fluid in the cluster if this cluster reaches the surface ($P_s = 0$) otherwise if $P > P_{\text{lith}}$ anywhere in the cluster, an element is broken in this sense. If the failure threshold ($P - P_{\text{lith}} > 0$) in that element is reached, the system selects randomly a direct neighbour element. This subloop is repeated until either: (i) none of the elements in the cluster reaches the failure criterion, (i.e. no avalanche) or (ii) the cluster reaches the surface. In an event where the cluster reaches the surface, the pressure in all elements within the cluster is set to zero as any excess fluid is released at the surface. When the cluster does not expand any more, all 'broken' elements are reset to 'not broken' to simulate closure or sealing of the fracture.

6.1.3 Simulations

The main set of simulations varied the model diffusion coefficient from 0 to 0.2, keeping all other parameters constant. Fluid input was in the bottom half of the model. Four more simulations were carried out to show the effect of changing the fluid-producing region or zone,

which was set to (i) input at the bottom (equivalent to the simulations of de Riese et al. (2020)), and (ii) fluid input throughout the model. For the case of fluid input in the bottom half of the model, the effect of a higher permeability (D_{mod}) in the top half than in the bottom half, and vice versa is also show. All model settings are listed in Table 2.

Table 2. Summary of the modelled Simulations with different D values used in the model. D_{real} and the permeability κ (m²) are the real in nature. All other parameters were unchanged

Model Dimension	Model D (D_{mod})	D_{real} (m^2s^{-1})	Permeability κ (m²)	Number of fracture event	Timestep (Δt) in s
$\lambda^2=10^4$	$2.0\cdot10^{-1}$	55	$2.75 \cdot 10^{-14}$	0	$2.75\cdot10^6$
$\lambda^2=10^4$	$2.0\cdot10^{-2}$	5.5	$2.75 \cdot 10^{-15}$	46	$2.75\cdot10^6$
$\lambda^2=10^4$	$2.0\cdot10^{-3}$	$5.5 \cdot 10^{-1}$	$2.75 \cdot 10^{-16}$	16	$2.75\cdot10^6$
$\lambda^2=10^4$	$2.0\cdot10^{-4}$	$5.5 \cdot 10^{-2}$	$2.75 \cdot 10^{-17}$	840	$2.75\cdot10^6$
$\lambda^2=10^4$	0	–	–	741	$2.75\cdot10^6$
	Diff source region				
	Source at bottom				
$\lambda^2=10^4$	$2.0\cdot10^{-3}$	$5.5 \cdot 10^{-1}$	$2.75 \cdot 10^{-16}$	87300	$2.75\cdot10^6$
	Whole model sourced				
$\lambda^2=10^4$	$2.0\cdot10^{-3}$	$5.5 \cdot 10^{-1}$	$2.75 \cdot 10^{-16}$	411	$2.75\cdot10^6$
	Variable D (D_{mod})				
$\lambda^2=10^4$	top = $2.0\cdot10^{-1}$ bottom = $2.0\cdot10^{-3}$	55 $5.5 \cdot 10^{-1}$	$2.75 \cdot 10^{-14}$ $2.75 \cdot 10^{-16}$	39	$2.75\cdot10^6$
$\lambda^2=10^4$	top = $2.0\cdot10^{-3}$ bottom = $2.0\cdot10^{-1}$	$5.5 \cdot 10^{-1}$ 55	$2.75 \cdot 10^{-16}$ $2.75 \cdot 10^{-14}$	33359	$2.75\cdot10^6$

6.2 Breccia statistics

This section presents the method used in the breccia clasts statistics. The clast size distribution of the hydrothermal breccia at Pozalagua and from the Black forest were analysed. These breccias samples from Pozalagua quarry are dolomitic and resulted from the dolomitization of the host limestone. Photographs of flat or approximately flat breccia surfaces on outcrops were used for the clast size (area) analyses. Clasts outlines were drawn manually, making sure that

the outlines do not intersect. This is to avoid two adjacent clasts being considered as one single clast. Clasts outline that were not completely drawn were excluded from the analysis. The "Analyse particles" option of ImageJ (Rasband, 1997-2021) was then used to determine the area of each clast in the images. Without any further processing, clast areas can be plotted as reverse cumulative plots of number of clasts equal or greater in area than a certain clast area ($N_{\geq s2}$) against that area (s_2). Measured clast areas ranged from < ~ 1mm^2 to ~ 2000 cm^2 but for sample *E* (Teufelsgrund) the unit measure is in pixel. In the sampled analysed, the parameter used were the cross-sectional surface (2-D). The sample image *B* unlike *A*, *C* and *D* shows altered dolomite breccia. Clasts look elongated and less angular with respect to the other samples and are seen entirely surrounded by fine matrix erasing all evidence of dislodging from larger lasts as appears in e.g. *A*, *C* and *D*.

The problem with cumulative plots is that deviations from a power-law distribution at the large end of the clast-size range propagate through the whole data set. It is therefore preferred to use frequency plots (Fig. 4). This, however, raises the problem of binning. A MATLAB script that uses dynamic binning is used to ensure that each bin has at least 10 clast areas and is not smaller than 0.005 cm^2. A second problem is that the smallest clast sizes are inevitably underrepresented as you are at the limit of image resolution. At the other end of the spectrum, large clasts may also be underrepresented due to bias in taking images (you do not want an image with only one clast) or clasts that are not fully within the image. Therefore, frequency data at both the very least and high end of the size spectrum is excluded.

A power-fit for clast size (area) distribution results when the number of clasts N'_{s2} (frequency), is plotted against the area *a* in a log–log plot (clast size distributions of all samples were fitted by equation 2 (Marone and Scholz 1989; Perfect 1997, Weisheit et al., 2013). It must be noted however that the extreme ends of the power-law fit made of the smallest (grain) and largest clast sizes tend to influence the curve significantly i.e. extreme upper end (small clasts) flattens the curve where larger clast sizes increase the slope. The output data on clast dimensions measured include diameter, area, circularity, and sphericity (ellipticity) of clasts for each sample but here, a clast area for our analysis is used. All clast size distribution data is presented in (Table 3).

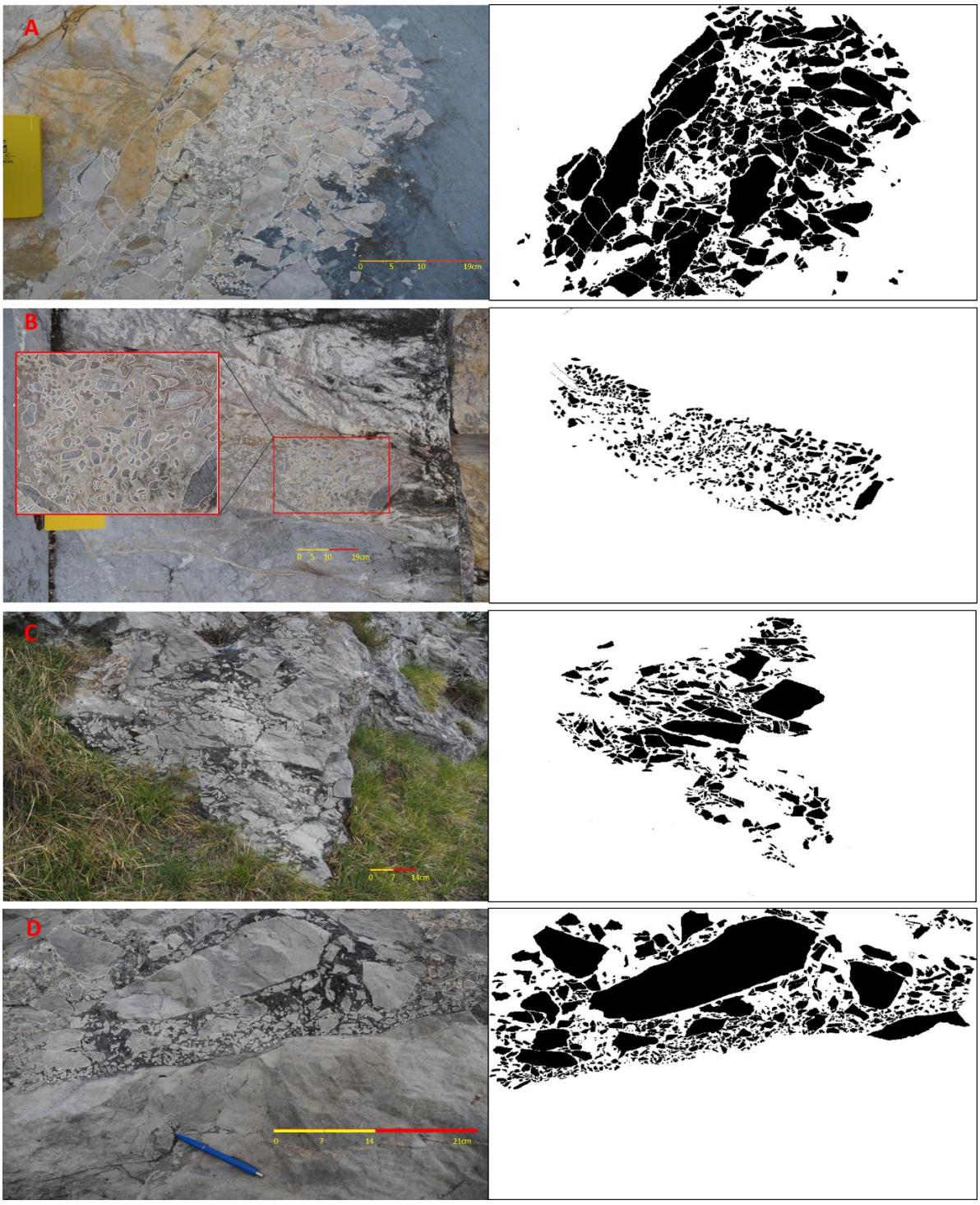

Figure 3. Field images of a hydrothermal breccia from the Pozalagua area analysed in this study. The 2nd column is the delineated breccia clasts from the field image samples *A*, *B*, *C*, and *D*, respectively. The delineated clasts show a graphical representation of clast shape, distribution and orientation of a typical hydrothermally brecciated rocks in situ. *B* however shows altered clasts size by fluid

Table 3. Summary of the data sets for the clast size (area) distribution.

File_name	No. of clasts	Minimum clast area (cm^2)	Maximum clast area (cm^2) Sample E (in px)	n_2 -value	Range (n_2-*value*)
A	682	0.001	84.2765	1.45	-1.50 / -1.32
B	644	0.0011	46.7475	2.01	-2.18 / -1.81
C	615	0.0023	469.0781	1.58	-1.68 / -1.38
D	804	0.0005	148.8318	1.67	-1.83 / -1.68
E (Teufelsgrund)	1678	1	1746616	1.54	-1.57 / -1.51

7.0 Results

The result for the breccia clast size distribution and the model simulation for the hydrothermal fracturing and flow dynamics is presented in sections 7.1 and 7.2 respectively.

7.1 Breccia clast size distribution

The study presents the result of the clast size distribution of the breccia samples used. Figure 3 (2^{nd} column), shows the delineated clast size (area) dimension from the breccia clasts samples respectively. The result for the frequency plots ($f'_{(s2)}$) for the 2-D data set is presented in Fig. 4. The total number of clasts for each sample for the n_2 used to compute for the n_3 values (Table 3) is with a set range at 95% minimum and maximum of all the data set. Exclusion of the extreme data set are omitted for the plots. These are the very small and the largest clasts sets, making up 5% is excluded in determining the *n*-values (exponents). The cumulative frequency plots of the breccia clasts conform to power-law which connotes the form in equation (1). The slope of the straight line in the log-log plots (Fig.4) represents the power-law exponents, herein denoting *n* (e.g. Sammis et al, 1987, Otsuki, 1998). The values for the power-law exponents (the *n*-values) for the analysed samples in *n*-values are, ~1.45, ~2.00, ~1.58, ~1.67 and ~1.54 for *A*, *B*, *C*, *D* and *E* (TG) respectively. For the corresponding volumetric n_2 values used to determine the n_3, the average of the values is used for simplicity. When the individual samples

are considered, sample *B* has relatively a higher power exponent ($n \approx 2.00$) even though their clasts range is comparable smaller. In summary, the n_2 values for the exponents do not go beyond the threshold of ~2 for the fluid assisted brecciation in conjunction with what Jébrak, (1997) proposed. In all, data value for n_2 for the power-law exponents is averaging around ~1.68 excluding that of sample *E* (Teufelsgrund) is used in arriving at $1<n_2\leq 2$. For the breccias at Teufelsgrund, sample *E*, an n_2 value of 1.54 resulted which is as well close to that of the dolomitic hydrothermal breccias in Pozalagua.

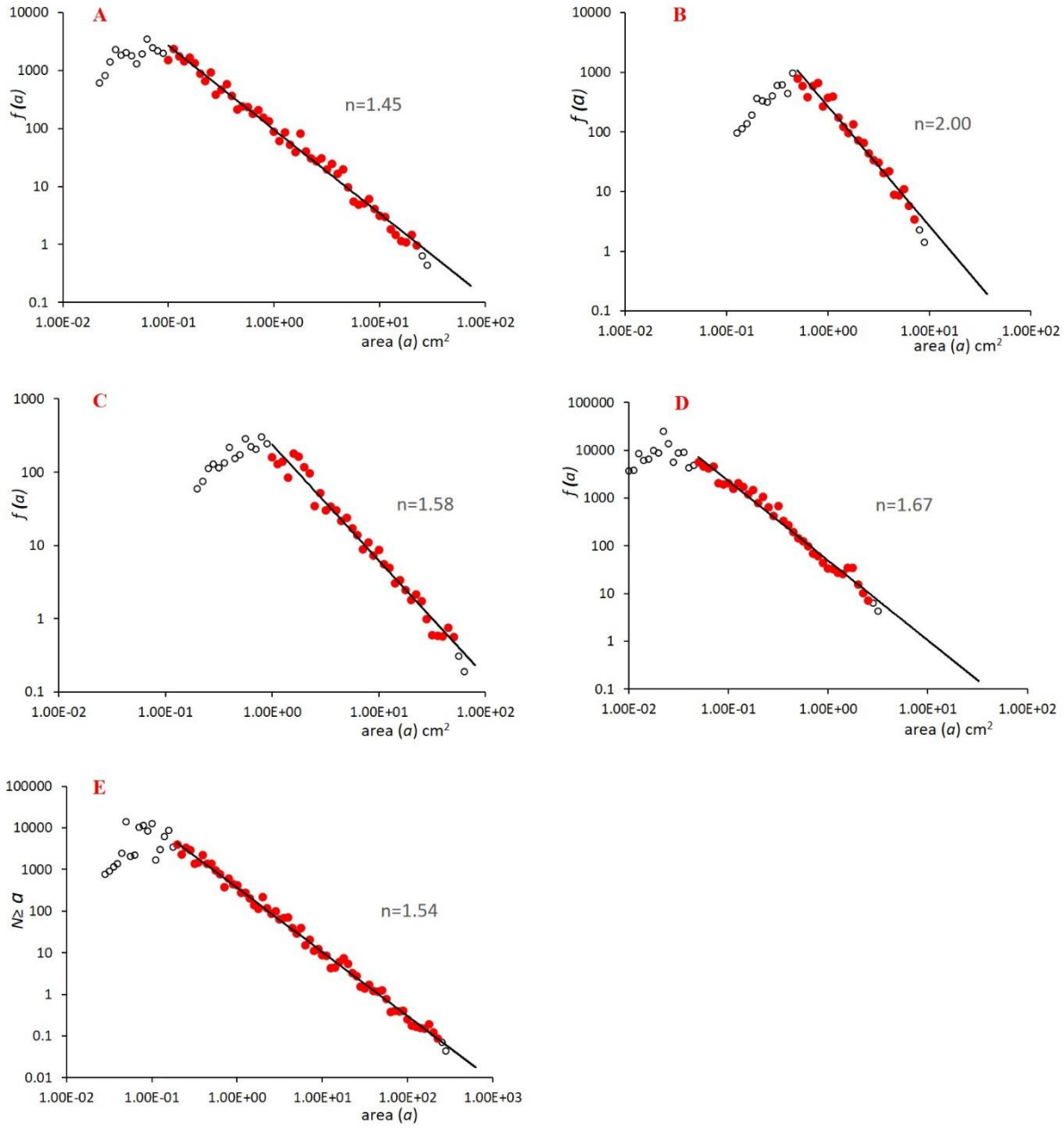

Figure 4. Results of clasts size analyses of the field sampled breccias presented in a log-log plot. Number of breccia clast (*f*) is plotted against area (*a*), the size of the breccia distribution. Slope of the straight sections in these logarithmic plots is the fractal dimension. The *n-dimension* indicates the degree of roundness or angularity of the breccia clasts. All analyses combined give a fractal dimension averaging as n~1.5 for the hydrothermal breccias a, b, c, d and e.

To compute for the n_3, let refer to the output data for the n_2 (area dimension) values. The n_3 for the volumetric size analysis is surmised in Table 1. Computed n_3 values from n_2 equate to ~0.63, ~1.01, ~0.72, ~0.78 and ~0.69 from A to E respectively). This show that averagely, the 3-D volume for the clast sizes is less than 1 (n_3<1). This shows that proportionate change in volume (n_3) -from largest clast to the next largest, is about same with respect to volume change.

To know when does the fit no longer represent power-law, this study considers a situation of dissolution or reduction of all clast sizes proportionately. A dissolution breccia commonly associated with carbonate rocks, are formed when the clasts are subjected to erosion as dissolution of rock surface by fluids. This results in the collapse and potential infilling, leading to a breccia rock structure often found in carbonate and hydrothermal settings (intrusive settings). Here, clasts are reduced from its original sizes due to the peripheral erosion. When such happens, the effect on the power-law exponent is that, the power-fit is significantly shifted to the left (reduced *n-value*) even with small amount of clasts volume change (see Chapter 2, Fig. 4).

The result will be a decreased slop that may not fit as power-law with the distribution. In Chapter 2, Fig. 4 for example, when a 0.5-unit volume reduction of all data points (1000 in this regard) is considered. It appears that the value *n* decreases, which results in a decreased slope and does not inherently follow a power-law fit. Now, when we consider Fig. 3B, there is a clear indication of clast alterations which may not necessarily be termed a dissolution because the power-law exponent appropriately. It appears to be larger than the other samples resulting in steeper fit (slope) when we consider the volumetric n_2 value of ~2.00. Thus, sample B cannot be concluded as a dissolution breccia even when the face looks more like a dissolution breccia. The dolomitic breccia clasts however, seem reworked by fluid which may have contributed to the eroding of the clasts to its current clasts size, there is no statistical evidence to buttress it. This process has resulted in a mixture of these 'quasi angular' clasts cemented together in fine-grained matrix. Variations in the slope, thus, is a function of a proportional change in the clast sizes.

7.2 Simulation result

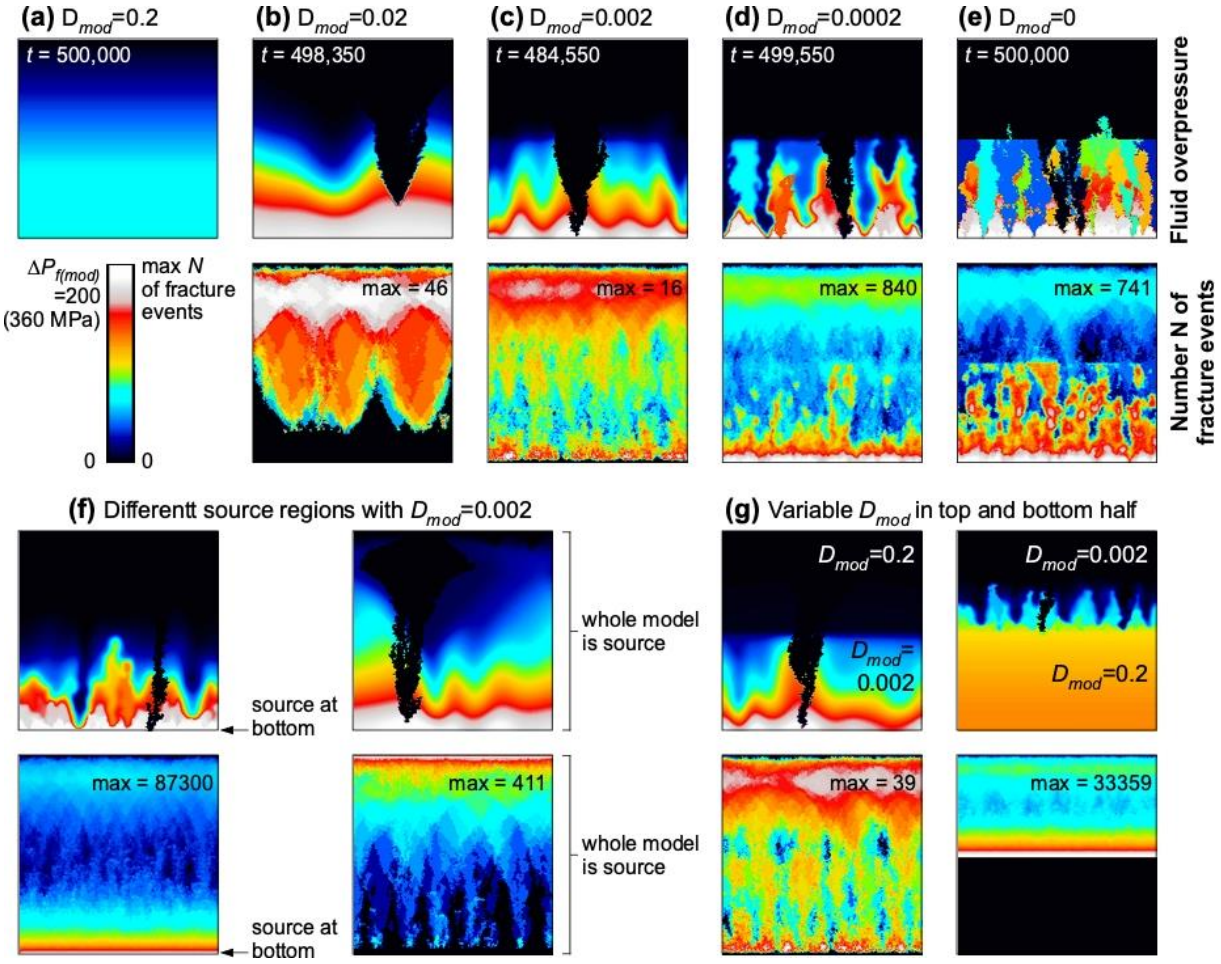

Figure 5. Maps of fluid pressure (P_{mod}) and number of times an element was fractured (from timestep 100,000 to 500,000). The top row shows the fluid overpressure maps for the different simulations and their bottom rows the fracture maps with number of fractured events. Note that the maximum number of fracture events varies greatly.

The result for the model simulation is presented in snapshots and graphical figures and Table for all D_{mod} values (0 – 0.2) and also for varying D_{mod} in the top and bottom halves of the medium. Figure 5 shows snapshots of the result of the modelled pressure distribution depicting fracture growth and distribution (see video Appendix 2B). The pressure graphs and table for the real D and κ and number of fractured events are also presented. The average pressure in the model shows a saw-tooth pattern indicating that pressure builds up and drops when a fracture reaches the surface and drains its contained fluid. Here, fluctuation is at minimum when D is high. When D_{mod}=0.2, Darcy flow is sufficient to drain the fluid without P_f ever reaching the failure criterion which differ in the case of different D_{mod} (Fig. 5a). At the initially stage, mean overpressure (P_{mod}) rises to ca ~ 90 (model scale) in the system and consistently builds up and

gets to a level where it drops abruptly to ca~ <40 but not to zero, recording the system's first avalanche. This shows the initial transient phase before the system settles to a dynamic steady state. With time, the mean over pressure also shows that (i) the frequency of the average pressure drops decreases as D_{mod} decreases and (ii) their magnitude increases with increasing D_{mod}. Overall, the time-averaged P_f increases with increasing D_{mod}. This means we have fewer, but larger fractures that reach the surface to drain fluid with increasing D_{mod} (Chapter 3 Fig 2).

Results from the simulation show that, P_f is highest at the base. Without fracturing (Fig.5a, when D_{mod}=0.2) P_f increases linearly with depth. At lower D_{mod}, fractures occur. Within the model set-up the top half of the model is set close to zero P_f. At high D_{mod} (0.02 in Fig.5b) P_f gradients are smooth, except where a fracture that reached the surface has just occurred, draining all its fluid and thus setting P_f =0. With lower D_{mod}, Darcy flow is not sufficient to quickly erase sharp gradients in the fluid pressure. Variations in pressure gradient also happen when D is varied in the upper and bottom sections of the medium. For different sourced (fluids) regions and varied coefficient of D_{mod} result in either increase or decrease in fluid overpressure depending on the section where high or low D is introduced, see Chapter 3 Fig.4.

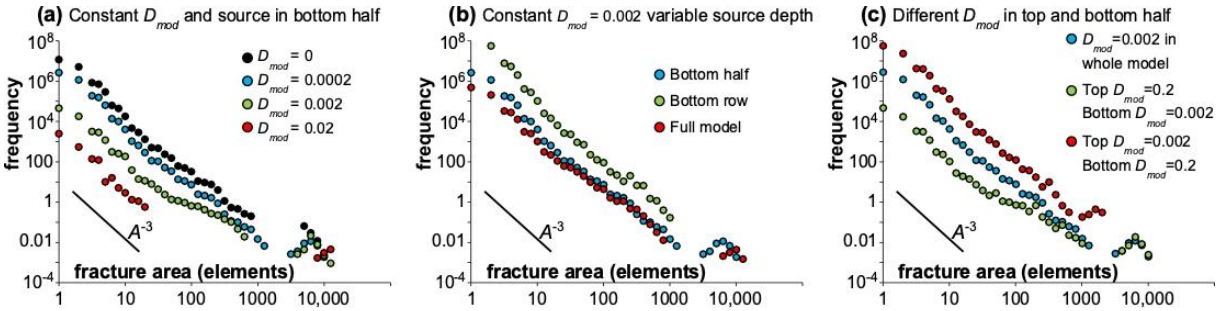

Figure 6**.** Frequencies of fractures as a function of their area in elements. Only fractures formed between timestep 50,000 and 500,000 are shown here to exclude the initial transient phase before the system settles to a dynamic steady state. Plots shows that section of the size (area) distribution follows a power law.

The average P_f as a function of depth and the effective time-average diffusion coefficient shows that from zero (black sections of the snapshots), P_f increases to ca ~180 MPa at depth ~10 km and continue to increase with depth. Assuming model constant parameters are realised in real world, it would appear that depth controls pressure as average P_f increase steadily to ca ~ 360 MPa at ~20 km, Fig.4 in Chapter 3. At the FPZ average P_f increases suggesting an elevated average fluid pressure. Again, the effective diffusion-depth curve is smoother with high D_{mod}

and fluctuate with decreasing D_{mod}. Trend also changes when the fluid source and D_{mod} is varied within the system – top and bottom half. The results for the average P_f also indicate that the linear pressure profile will decrease in the case of diffusional transport. Therefore, with high D, pressure peaks become minimal and would not make hydrofractures. D_{mod}=0.2 in this case shows no abrupt change in pressure gradient at the level of the FPZ though continues to increase steadily. Apart from the highest D_{mod} =0.2, other D_{mod} respond differently in gradient at the level of the FPZ. Different D_{mod} at the top and bottom halves (D_{mod} =0.002 and 0.2). With a different D in the top and bottom, pressure gradient increases with depth, however at decreasing rate with high D at the bottom half and increases at an increasing rate with high D at the top respectively. The opposite happens when top section has higher D_{mod} and low D_{mod} at the bottom half (Chapter 3, Fig.4c).

For the fracture frequency of size distribution, result presented in Fig. 6, with fractured events with the corresponding D_{mod} showing in Fig.5. The simulation shows that fractures mostly form at the bottom and propagate upward from the level of the sourced fluid. The number of fractures varies with different D_{mod} (Fig.5). With an increasing D, the hydrofracture frequency decreases (Fig. 5/6), this includes both large hydrofractures that reach the surface and those small fractures that do not. This is also the case with size of fractures that reach the surface. At $D_{mod}=2.0\cdot10^{-4}$ (except when D is varied in the system, Fig.5g) the model creates more fractures that are mostly (small fractures) confined to the bottom of the crustal column. That is, fluid move through well-defined fractures. Thus, large bursts of fluid are eminent and may reach all the way to the top half of the model. Fractures are created predominantly within the fluid production zone. These fractures w.r.t our simulations begin at about ~10 km depth. Fractures that do not reach the surface follows a power-law distribution with an average power-law exponent of ~3. These fractures that do not reach the surface are confined to the bottom half of the model. The few large fractures that get through to the top half of the medium tends to drain the fluid.

8.0 Discussion

Before a rock deforms, it first must be preceded by weakening the rock whether by stress or fluid overpressure (Bons et al., 2022; Mohr, 1882). Fractures will begin to form only when the shear strength of the rock is less or equal to that of the external force acting on it (Jaeger et al., 2007; Scholz, 2002; Goodman, 1991; Atkinson 1984). Within the crust, an increase in fluid overpressure may results from injection of fluid so that the high fluid pressure within the

column may initiate or propagate an existing fracture (Bons et al., 2022). This overpressure is set to fall when the permeability increases due to fractures. It is suggested from the simulation that, with time, after when these fractures (hydro) form, the P_f falls. From the onset, these hydrofractures may not necessarily be large but may coalesce over time and that they may later appear as one large fracture from a burst, (see Fig.5).

From the simulation(s), the initial mean overpressure rises in the system until a fracture (probably large) is realised and then the pressure significantly falls but not to zero. The first events of break may be considered 'ballistic' such that fracturing becomes abrupt considering the geological time scale. This may be due to the system's gradual build-up of pressure until high enough to fracture. After the fracturing events, the system reorganises (self-organised) at some stage when there is continued increase fluid injection which eventually raises the pressure again. With time, the whole system gets to critical state and the process is reactivated. This means that most of these hydrofractures have resulted at much earlier stage during the whole dynamic process. Again, burst events in the system are sporadic considering how these fractures network develop over time. High incidence of fluctuations therefore, result from low diffusion coefficient, i.e., low permeability with less fractures however few large fractures that could drain the fluids.

With time, the average fluid overpressure in the system falls when fractures form. With increasing diffusion coefficient, D, the hydrofracture frequency will also decrease (Fig. 5; Table 2). Therefore, for hydrofractures to continue to form, the system must not be too permeable to hinder the build-up of the fluid overpressure to be high enough to cause fractures. A raised κ, lessens the fluctuation intensity. Therefore, at a steady state, an elevated or constant fluid pressure within the medium only makes 'one more' fracture with time.

Considering how these fractures are induced hydraulically to extensively link, at a high D (D_{mod}=0.2), the P_f is not high enough to cause fracture, this translate that the medium is permeable and flow is diffusional. Before a fracture event at lower D_{mod}, the average pressure increases linearly (Fig. 5a) from the base to the top of the model until an avalanche occur. Irrespective of where the fluid is introduced in the crustal column, fracture growth always is to be from bottom to the top (considering a simple 2D medium). Thus, fluid released from different levels within the crust get transported upwards when fractures link up, creating ever bigger fractures (Bons and van Milligen, 2001). When hydrofractures begin to form, continued fluid overpressure may sustain the growing hydrofractures, connect and link them. These fractures may transport overpressured fluids from the source that are capable of inducing more

fracture propagation and even hydraulic brecciation. This means that for a hydrothermal fluid working on rock to break down, a desirable critical fluid pressure in terms of the energy required to carry out the fracturing is paramount (Ague, 2014 and references therein). The resultant propagation of these fractures once formed reveal that fractures that are filled with a pressurized fluid becomes strong enough to carry on with the propagation.

When fracture form, permeability increases and subsequently, the pressure falls significantly Fig.5, so that flow would be driven only by fractures. How fast these fluids (hydrothermal) flow within the crust is directly linked to the rate of fracture growth and propagation i.e. these fractures merge and get connected extensively to transport the pressure driven fluids from source to sink (for example, Hickey et al. 2014). Large fractures predominately drain the system and thus reduce P_f in the system. Hypothetically, after the formation of hydrofractures, flow of fluid may occur in batches and move upward very rapidly. As mentioned earlier, hydrofractures that reach the surface are consistently large and greatly controls flow and mixing of fluids at different levels of the medium. At much shallower levels, mixing of high-temperature fluid with meteoric or ambient fluid is possible as porosity is higher at this level. This means that almost all carried elements are precipitated in this region. For example, brecciation at much shallow depth is possible, and as well traps fluids which may then initially be hotter than the ambient temperature and can precipitate dissolved minerals upon cooling of the hot fluid (see Bons et al. 2014).

With focused flow, a hydrothermal fluid may ascent so fast that the fluids will not have enough time to cool to ambient temperatures during ascent – suggesting that (i) precipitation (of dissolved minerals) is largely controlled by the frequency and size of the large hydrofractures that carry mineralized fluids to the surface from below (ii) this controls how fluids interact (rummage) with the country rocks and or dissolving minerals to be carried along. Bons (2001), suggests that at ca. 0.1 m s^{-1}, a batch of fluid can ascend 10 km in about a day. In a real geological setting, a possible formation of these hydrothermal deposits, will result from a rapid transport of large volumes of fluids which are under pressure from deep to shallow crustal levels. However, upon reaching such shallower levels within the crust, their pressure is expected to fall to close to hydrostatic. Considering relation in mixing of fluids in hydrothermal ore deposits e.g. that of Hidden Valley hydrothermal breccias and the Black forest district, evidence-based inclusions suggest that flow from deep sources have carried significant minerals to that level where mixing with meteoric water aided their precipitation. These are made

possible by focused flow (in batches) when such fractures connect all the way from a km scale to few metres at much shallower levels.

At depth, an existing seal or an impermeable layer for example, can control the fluid overpressure due to increase in fluids or thermal expansion in fluids in the adjacent rock strata and subsequently cause a failure/fracture, (see Chapter 4, Fig 5). Where the fluid pressure is not released, fractures grow extensively and the pattern may evolve dynamically resulting in a complete brecciation – hydrothermal breccia.

The development of a breccia (hydrothermal) is significantly connected to the energy needed to do the disintegration (e.g. Weisheit et al., 2013) as they significantly estimate how much energy in terms of hydrothermal fluid, required to result in e.g. the Hidden Valley breccias. In fluid-assisted (hydrothermal) brecciation, fragments are angular and brecciation is typically believed to follow newly created or pre-existing fractures after the resistance of the rock strength is overcome. These breccia formations may result from stages known to have started as (i) veins/micro fractures, (ii) nucleation and growth of fractures and (iii) dilation of these fractures resulting in well-connected joints. Therefore, fluid assisted dilation consequently results in hydrothermal breccia.

For the clast size distribution, the most considerable and easy parameter to measure on irregular clast size is the area (2-D) and the diameter (1-D) when there is an assumption of a projected clast circularity (Brittain, 2001). Exception to this is in the dissolution breccias where the initial process of breaking and clast size has been erased by the dissolution process, e.g. chemical dissolution in dolomites.

When hydrofracturing result in breccias, there is thus a large range in clasts sizes resulting in the largest clasts occupying a relatively large fraction of the total volume see Fig. 3D. This is in consistent with the observation that it is difficult to define the largest clast in a breccia (hydrothermal) as they typically do not have clearly defined boundaries. Large clasts in outcrops may be due to a shorter duration of the hydrofracturing process. Once a clast is fully surrounded by fluid, it would not further disintegrate. This is independent of their size, so large clasts may be incorporated in the breccia and remain large. At Pozalagua like those in Hidden Valley (Weisheit et al., 2013a) there is no evidence of re-brecciation but possible reduction of clasts sizes at some sections. Clasts fully surrounded by fluid may rotate and mingle. Thus, to further allow the volume expansion that the overpressure causes, the fracturing front would expand resulting in more breccia formation.

9.0 Conclusion of the thesis

The entire project focuses on the crustal scale fluid flow and fracture growth and tends to model the flow and statistically analyse the resulting hydrothermal breccias which results through extensive fracturing and propagation. Fracturing (and/or hydrothermal brecciation) in rocks provides a better understanding of fluid–rock interactions, time-scale of stress evolution and crustal scale fluid flux. The dynamic feedbacks between fluid flow, permeability and rock failure, however, more complex to explain with a single phenomenon and remain challenging tasks to resolve. Hydrothermal breccias, basically found in many geological settings and are associated with fluid circulations e.g. from Black forest and Pozalagua in Northern Spain. For clarification, the nature of the breccia types is known from a number of factors by which they are classified and categorized as proposed by some authors. Major mechanisms of physical brecciation that are distinct to the hydrothermal vein-type deposits: tectonic comminution, fluid-assisted brecciation (hydraulic and critical), wear abrasion, dissolution (volume reduction), impact, and collapse are commonly used.

A controlled simulation is used to investigate fluid flow, fracture growth with pressure interplay within the crust using a model that is analogous to the sandpile model which simulate flow in a grid to monitor and record increments in fluid pressure, momentary discharge through the cells to represent the fracturing and fluid escape. To make fracture and subsequently brecciate rocks hydrothermally, the fluid must achieve the level of fluid overpressure to at least equate the lithostatic pressure within the crustal column. The higher the permeability, the lower the fracture intensity as fluid overpressure will never build up to be high enough to cause more rock failure. That is, where permeability within the column becomes high enough to dissipate pressure build-up, hydrofractures get truncated. Hydrofractures begin to appear at the level of fluid insertion and develops instantaneously linking-up to the top. Fractures and fluid (hydrothermal) transport dynamics may thus explain the abundance of deep sourced fluid inclusions and hydrofractures in much shallow levels in subsurface and that a rapidly ascending hydrofracture will tap fluids from all levels of the infiltrated rock column and as well mix these fluids during ascent. Evidence of such processes are printed in the resulting ore deposits. It appears that regardless of where fluid is introduced within the medium, fractures always appears to grow from bottom (below) to top (surface), welling much deeper fluids to the surface. Large fractures stemming from below with ‘interlocking cone shaped’ roof near the surface could explain why; (i) hydrothermal breccias with/without ore deposits are found at such levels within the crust (ii) high permeability at such crustal levels where fracturing is truncated. With no

effect of external forces e.g. tectonic activities, the extent and length of these hydrofractures depend on factors such as the fluid flux, permeability, and the rock's mechanical properties within the crust.

For hydrothermal breccias, their development comes as a response to extensive fracture growth and propagation process, (Scholz, 1990) and is considered as one of the most common mechanisms of brecciation observed at all scales. It appears that even though hydrothermal breccias have many striking similarities with most forms of non-sedimentary origin breccias especially fault and collapse breccias, they are distinct in many forms. Clast size dimension follow a power-law distribution with a mean *n*-value of ~1.68, but power-law exponents can vary significantly, even within a single setting. The low *n*-values are consistent with a hydrothermal origin of the studied breccias. It happened that a decreased slope/fit may not necessarily conform to a power-law fit when the breccia is dissoluional. That is when the original clast size is eroded by fluid introduced later in the breccia outcrop. At some sections of the hydrothermal breccia, the irregular sub-rounded shape in a well cemented breccia slabs suggest that sections of the emplaced breccia formed at the Pozalagua quarry resulted from injection or recirculation of fluid after the initial breccias were formed.

10.0 Future perspectives

The study provides knowledge on bimodal flow of crustal fluid within the crust and shows how fluid transport within the system controls fracture dynamics. It suggests how large burst of fluids within the crust are controlled mainly by few large hydrofractures and proposes that regardless of where fluid is introduced within the crustal column, fractures always appear to grow from bottom (below) to the surface, bringing deep fluids to the surface. It appears that fracture size and breccia clasts size distribution follow a power-law fit and the limit to the end members may be ‘scale-dependent’.

However, some questions still remain unanswered. Like many other numerical models, this simulation is geared towards exploring fluid flow fracture dynamics in a real-world geological system. The following are suggested for further investigation and upgrade:

1. To some extent, this simulation does not entirely depict geofluids flow processes within the crust in the sense that it oversimplifies subsurface flow processes and treat flow as discrete. Thus, it suggests that an upscale simulation which would employ a 3D

simulation be made to simulate flow in a 3-D, it is only natural that flow of fluid (hydro) must be continuous and not in grid as discrete.

2. Again, it does not consider the scaling dimensions from a 2D to a 3D simulation of the subsurface in a real-world. A conversion with an up-scaled realistic boundary conditions is recommended. Specific boundary conditions are often unrealistic for real world, as boundaries in the subsurface are influenced by geological structures, seals, aquifers, or reservoirs, as well as explicit modelling of fluid properties.
3. The energy budget components (heat and potential energy due to compression). This study does not consider the energy budget of the subsurface and proposes that future study must include and model flow depicting the real energy flow within the crustal column.

This study thus, suggests that a more upgrade be made in the future investigation building on the above stated parameters and suggestions. Once all main fluid and rock properties and operating processes are implemented in a 3-dimension, a more robust model will better represent the real-world events.

Reference:

- Ague, J. J. (2014). Fluid Flow in the Deep Crust. In Treatise on Geochemistry (pp. 203–247). Elsevier. https://doi.org/10.1016/B978-0-08-095975-7.00306-5
- Ague, J. J., & Rudnick, R. L. (2003). Fluid flow in the deep crust. The crust, 3, 195-228.
- Altherr R., Holl A., Hegner E., Langer C. & Kreuzer, H. (2000). High-potassium, calc-alkaline I-type plutonism in the European Variscides: northern Vosges (France) and northern Schwarzwald (Germany). Lithos 50:51–73
- Anderson, T. L., & Anderson, T. L. (2005). Fracture Mechanics: Fundamentals and Applications, Third Edition (3rd ed.). CRC Press. https://doi.org/10.1201/9781420058215
- Aranburu, A., Fernández-Mendiola, P. A., López-Horgue, M. & García Mondéjar, J. (2002). Syntectonic hydrothermal calcite in a faulted carbonate platform margin (Albian of Jorrios, northern Spain). Sedimentology, 49, 875–890.
- Atkinson, B. K. (1984). Subcritical crack growth in geological materials. Journal of Geophysical Research: Solid Earth, 89(B6), 4077–4114. https://doi.org/10.1029/JB089iB06p04077
- Baatartsogt, B., Schwinn, G., Wagner, T., Taubald, H., Beitter, T. & Markl, G. (2007). Contrasting paleofluid systems in the continental basement: a fluid inclusion and stable isotope study of hydrothermal vein mineralization, Schwarzwald district, Germany. Geofluids, 7, 123-147.
- Bak, P., Tang, C., & Wiesenfeld, K. (1988). "Self-organized criticality," Physical Review A, vol. 38, no. 1, pp. 364–374,
- Bakker R. J., & Elburg, M. A. (2006). A magmatic-hydrothermal transition in Arkaroola (Northern Flinders Ranges, South Australia): from diopside-titanite pegmatites to hematite-quartz growth. Contrib Mineral Petrol 152:541–569
- Barnett, W. (2004). Subsidence breccias in kimberlite pipes: an application of fractal analysis. Lithos 76, 299–316.
- Bear, J. (2013). Dynamics of fluids in porous media. Courier Corporation.
- Bliedtner, M. & Martin, M. (1986). Erz- und Minerallagerstätten des Mittleren Schwarzwaldes. LGRB, Freiburg, Germany.
- Bodnar, R. J., Lecumberri-Sanchez, P., Moncada, D., & Steele-MacInnis, M. (2014). Fluid Inclusions in Hydrothermal Ore Deposits. In Treatise on Geochemistry: Second Edition (Vol. 13, pp. 119–142). https://doi.org/10.1016/B978-0-08-095975-7.01105-0
- Bons, P. D., Cao, D., De Riese, T., González-Esvertit, E., Koehn, D., Naaman, I., Sachau, T., Tian, H., & Gomez-Rivas, E. (2022). A review of natural hydrofractures in rocks. Geological Magazine, 159(11–12), 1952–1977. https://doi.org/10.1017/S0016756822001042

- Bons, P.D., Fusswinkel, T., Gomez-Rivas, E., Markl, G., Wagner, T., & Walter, B. (2014). Fluid mixing from below in unconformity-related hydrothermal ore deposits. Geology 42, 1035-1038, https://doi.org/10.1130/G35708.1

- Bons, P. D., Elburg, M. A., & Gomez-Rivas, E. (2012). A review of the formation of tectonic veins and their microstructures. Journal of Structural Geology, 43, 33–62. https://doi.org/10.1016/j.jsg.2012.07.005

- Bons, P.D. (2001). The formation of large quartz veins by rapid ascent of fluids in mobile hydrofractures. Tectonophys. 336, 1-17.

- Bons, P. D., & Van Milligen, B.P. (2001). A new experiment to model self-organized critical transport and accumulation of melt and hydrocarbons from their source rocks. Geology 29, 919-922.

- Brittain, H. G. (2001). Particle-size distribution part 1, representation of particle shape, size, and distribution. Pharmaceutical Technology 25, 38–45.

- Cámara, P. (1997). The Basque Cantabrian Basin's Mesozoic tectono-sedimentary evolution. Mém. Soc. Geol. France, 171, 187–192.

- Cathles, L. M. (1997). Thermal aspects of ore formation. In: Barnes, H. L. (ed.) Geochemistry of Hydrothermal Ore Deposits. 3rd ed., 191-227

- Cathles, L. M. (1990). Scales and effects of fluid flow in the upper crust. Science, 248(4953), 323-329. http://doi.org/10.1126/science.248.4953.323

- Cathles, L. M., Erendi, A. H. J., & Barrie, T. (1997). How long can a hydrothermal system be sustained by a single intrusive event? Economic Geology, 92(7–8), 766–771. https://doi.org/10.2113/gsecongeo.92.7-8.766

- Cathles, L. M. (1981). Fluid Flow and Genesis of Hydrothermal Ore Deposits. In B. J. Skinner (Ed.), Seventy-Fifth Anniversary Volume (p. 0). Economic Geology Publishing Company. https://doi.org/10.5382/AV75.13

- Cobbold, P. R., & Rodrigues, N. (2007). Seepage forces, important factors in the formation of horizontal hydraulic fractures and bedding-parallel fibrous veins ("beef" and "cone-in-cone"). Geofluids 7, 313–22.

- Cox, S. F. (2010). The application of failure mode diagrams for exploring the roles of fluid pressure and stress states in controlling styles of fracture-controlled permeability enhancement in faults and shear zones. Geofluids, 10, 217-233.

- Curnelle, R. (1983). Evolution structuro-sédimentaire du Trias et de l'Infra-Lias d'Aquitaine. Bull. Centres Rech. Explor. Prod. Elf-Aquit., 7, 69–99.

- Dahm, T. (2000). On the shape and velocity of fluid-filled fractures in the Earth. Geophysical Journal International 142, 181–92.

- Davies, G. R. & Smith, L. B., Jr. (2006). Structurally controlled hydrothermal dolomite reservoir facies: an overview. AAPG Bull., 90, 1641–1690

- de Riese, T., Bons P. D., Gomez-Rivas E., & Sachau, T. (2020). Interaction between crustal-scale Darcy and hydrofracture fluid transport: a numerical study. Geofluids 2020, 1–14.

- Emmermann, R., & Lauterjung, J. (1997). The German Continental Deep Drilling Program KTB — Overview and Major Results. Journal of Geophysical Research, 102, 18179–18201. https://doi.org/10.1029/96JB03945

- Engelder, T. (1999). Transitional–tensile fracture propagation: A status report. Journal of Structural Geology, 21(8), 1049–1055. https://doi.org/10.1016/S0191-8141(99)00023-1

- Fournier, R. O. (1989). Geochemistry and dynamics of the Yellowstone National Park hydrothermal system. Annual Review of Earth and Planetary Sciences, 17(1), 13-53.

- Friedman, G. M. (1997). Dissolution-collapse breccias and paleokarst resulting from dissolution of evaporite rocks, especially sulphates. Carbonates and Evaporites, *12*(1), 53–63. https://doi.org/10.1007/BF03175802

- Fyfe, W.S., Price, N. J., & Thompson, A.B. (1978). Fluids in the Earth's Crust: Their Significance in Metamorphic, Tectonic and Chemical Transport, Elsevier, 383 pp.

- García-Mondéjar, J., Agirrezabala, L. M., Aranburu, A., Fernández, P. A., Gómez-Pérez, I., López-Horgue, M. & Rosales, I. (1996). Aptian-Albian Tectonic pattern of the Basque-Cantabrian Basin (northern Spain). Geol. J., 3, 13– 45.

- Geyer, O. F. & Gwinner, M. P. (2011). Geologie von Baden-Württemberg. – 5., völlig neu bearbeitete Auflage. Schweizerbartsche Verlagsbuchhandlung (Nägele u. Obermüller), Stuttgart, p. 627

- Geyer, O. F. & Gwinner, M. P. (1986). Geologie von Baden-Württemberg. Schweizerbart, Stuttgart, Germany.

- Ghani, I., Koehn, D., Toussaint, R. & Passchier, C. W. (2013). Dynamic development of hydrofracture. Pure and Applied Geophysics 170, 1685–703.

- Goodman, R. E. (1991). Introduction to Rock Mechanics. John Wiley & Sons.

- Gudmundsson, A. (2011). Rock Fractures in Geological Processes. Cambridge: Cambridge University Press, 592 pp.

- Hann, H. P., Chen, F., Zedler, H., Frisch, W. & Loeschke J. (2003). The Rand Granite in the southern Schwarzwald and its geodynamic significance in the Variscan belt of SW Germany. Intern J Earth Sci 92: 821–842

- Hanson, R. B. (1995). The hydrodynamics of contact metamorphism. Geological Society of America Bulletin, 107, 595–611.

- Heinrich, C. A., & Candela, P. A. (2014). Fluids and Ore Formation in the Earth's Crust. In Treatise on Geochemistry (pp. 1–28). Elsevier. https://doi.org/10.1016/B978-0-08-095975-7.01101-3

- Hickey, K. A., Barker, S. L. L., Dipple, G. M., Arehart, G. B., & Donelick, R. A. (2014). The Brevity of Hydrothermal Fluid Flow Revealed by Thermal Halos around Giant Gold Deposits: Implications for Carlin-Type Gold Systems. Economic Geology, 109(5), 1461–1487. https://doi.org/10.2113/econgeo.109.5.1461

- Hubbert, M. K., & Willis, D. G. (1957). Mechanics of hydraulic fracturing. Transactions of the American Institute of Mining, Metallurgical and Petroleum Engineers, 210, 153–168.

- Hubbert, M. K. (1951). Mechanical basis for certain familiar geologic structures. Geological Society of America Bulletin 62, 355–72.

- Immenhauser, A., Schlager, W., Burns, S. J., Scott, R.W., Geel, T., Lehmann, J., Van Der Gaast, S. & Bolder- Schrijver, L. J. A. (1999). Late Aptian to Late Albian sea-level fluctuations constrained by geochemical and biological evidence (Nahr Umr Fm, Oman). J. Sed. Res., 69, 434–446.

- Ingebritsen, S. E., & Gleeson, T. (2015). Crustal permeability: Introduction to the special issue. Geofluids, 15(1–2), 1–10. https://doi.org/10.1111/gfl.12118

- Ingebritsen, S. E., & Appold, M. S. (2012). The Physical Hydrogeology of Ore Deposits. Economic Geology, 107(4), 559–584. https://doi.org/10.2113/econgeo.107.4.559

- Ingebritsen, S. E., & Manning, C. E. (2010). Permeability of the continental crust: Dynamic variations inferred from seismicity and metamorphism. Geofluids, 10(1–2), 193–205. https://doi.org/10.1111/j.1468-8123.2010.00278.x

- Ingebritsen, S. E., Sanford, W. E., & Neuzil, C. E. (2006). Groundwater in Geologic Processes. Cambridge University Press.

- Ingebritsen, S. E., & Manning, C. E. (1999). Geological implications of a permeability-depth curve for the continental crust. Geology, 27(12), 1107. https://doi.org/10.1130/0091-7613(1999)027<1107:GIOAPD>2.3.CO;2

- Jackson, J. A. (1997). Glossary of geology, 4th ed.: American Geological Institute, Alexandria, Virginia, 769 p.

- Jaeger, J. C., Cook, N. G. W. & Zimmerman, R. (2007). Fundamentals of Rock Mechanics. Chichester: Wiley.

- Jébrak, M. (1997). Hydrothermal breccias in vein-type ore deposits: A review of mechanisms, morphology and size distribution. Elsevier Science B.V.

- Jaeger, J. C., Cook, N. G. W., & Zimmerman, R. (2009). "Fundamentals of Rock Mechanics." Wiley. This text provides an in-depth look into rock deformation, including mechanisms that lead to tensile and shear fractures.

- Kalt, A., Altherr, R. & Hanel, M. (2000). The Variscan basement of the Schwarzwald. Eur. J. Mineral. Bh. 12, 1–43.

- Keulen, N., Heilbronner, R., Stünitz, H., Boullier, A-M. & Ito, H. (2007). Grain size distribution of fault rocks: a comparison between experimentally and naturally deformed granitoids. J Struct Geol 29:1282–1300

- Koehn, D., Piazolo, S., Sachau, T. & Toussaint, R. (2020). Fracturing and porosity channeling in fluid overpressure zones in the shallow earth's crust. Geofluids 2020,1–17.

- Kolodny, Y., Chaussidon, M. & Katz, A. (2005). Geochemistry of a chert breccia. Geochem. Cosmochim. Acta 69 (2), 427-439.

- Leach, D. L, Sangster, D. F, & Kelley K. D. (2005). Sediment-hosted lead-zinc deposits; a global perspective. In: Sangster DF (ed.) Carbonate Hosted Lead-Zinc Deposits. Society of Economic Geologists Special Publication 4, pp. 144–170. Littleton, CO: Society of Economic Geologists.

- Loges, A., Wagner, T., Kirnbauer, T., Göb, S., Bau, M., Berner, Z., & Markl, G. (2012). Source and origin of active and fossil thermal spring systems, northern Upper Rhine Graben, Germany. Applied Geochemistry, 27(6), 1153–1169. https://doi.org/10.1016/j.apgeochem.2012.02.024

- Lorilleux, G., Jébrak M., Cuney, M. & Baudemont, D. (2002). Polyphase hydrothermal breccias associated with unconformity-related uranium mineralization (Canada): from fractal analysis to structural significance. J Struct Geol 24:323–338

- Markl, G., von Blanckenburg, F. & Wagner, T. (2006). Iron isotope fractionation during hydrothermal ore deposition and alteration. Geochimica et Cosmochimica Acta, 70, 3011-3030.

- Marone, C. & Scholz, C. H. (1989). Particle-size distribution and microstructures within simulated fault gouge. J Struct Geol 11:799814

- McKibbin, R. (2005). Modelling heat and mass transport processes in geothermal systems. Porous media, 545.

- Metz, R., Richter, M. & Schürenberg, H. (1957). Die Blei-Zink-Erzgänge des Schwarzwaldes. Geologisches Jahrbuch, Bh. 29, 277 pp.

- Middleton, G. V. (1961). Evaporite solution breccias from the Mississippian of southwest Montana. J. Sediment. Petrol. 31, 189-195.

- Morishita, Y., & Hammond, N. Q. (2024). Geochemistry and genesis of hydrothermal ore deposits. Minerals. MDPI.

- Mohr O (1882) Über die Darstellung des Spannungzustandes eines Korpelementes. Zivil Ingenieure 28, 113.

- National Academies of Sciences, Engineering, and Medicine. (1996). Rock Fractures and Fluid Flow: Contemporary Understanding and Applications. Washington, DC: The National Academies Press. https://doi.org/10.17226/2309.

- Norton, D. L. (1984). Theory of hydrothermal systems. Annual Review of Earth and Planetary Sciences, Vol. 12, p. 155, 12, 155.

- Nunn, J. A. (1994). Free thermal convection beneath intracratonic basins: thermal and subsidence effects. Basin Research, *6*(2-3), 115-130.

- Oliver, N. H. S., Rubenach, M. J., Fu, B., Baker, T., Blenkinsop, T. G., Cleverley, J. S., Marshall, L. J., & Ridd, P. J. (2006). Granite-related overpressure and volatile release in the mid crust: Fluidized breccias from the Cloncurry District, Australia. Geofluids, 6(4), 346–358. https://doi.org/10.1111/j.1468-8123.2006.00155.x

- Oliver, N. H. S. (1996). Review and classification of structural controls on fluid flow during regional metamorphism. Journal of Metamorphic Geology, 14(4), 477–492. https://doi.org/10.1046/j.1525-1314.1996.00347.x

- Otsuki, K. (1998). An empirical evolution law of fractal size frequency of fault population and its similarity law. Geophysical Research Letters, *25*(5), 671–674. https://doi.org/10.1029/98GL00380

- Perfect, E. (1997). Fractal models for the fragmentation of rocks and soils: a review. Eng Geol 48:185–198

- Pfaff, K., Romer, R. L. & Markl, G. (2009a). U-Pb ages of ferberite, chalcedony, agate, U-mica and pitchblende: constraints on the mineralization history of the Schwarzwald ore district. European Journal o Mineralogy, 21, 817-836.

- Pirajno, F. (2013). "Hydrothermal Mineral Deposits." In Encyclopaedia of Earth Science (pp. 23-41)

- Pirajno, F. (2009). Hydrothermal processes and wall rock alteration. In Hydrothermal Processes and Mineral Systems (ed. F Pirajno), pp. 73–164. Dordrecht: Springer.

- Pirajno, F. (2008). Hydrothermal Processes and Mineral Systems. Springer Science & Business Media.

- Phillips, W. J. (1972). Hydraulic fracturing and mineralization. J. Geol. Soc. London, 128, 337–359.

- Pollard, P. J. (2006). An intrusion-related origin for Cu–Au mineralization in iron oxide - copper -gold (IOCG) provinces. Mineralium Deposita, 41(2), 179–187. https://doi.org/10.1007/s00126-006-0054-x

- Pollard, D. D., & Aydin, A. (1988). Progress in understanding jointing over the past century. Geological Society of America Bulletin 100, 1181–204.

- Qaisar, S., Zhao, X., Khan, S., Khan, I. U., Alam, A., Ul Haq, J., Ahmad, S., & Zhao, X. (2023). Hydrothermal dolomitization in the Devonian Khyber Limestone Peshawar Basin, Pakistan: Evidence from outcrop analogue, petrography, and geochemistry. Carbonates and Evaporites, 38(4), 79. https://doi.org/10.1007/s13146-023-00901-w

- Ranalli, G., & Rybach, L. (2005). Heat flow, heat transfer and lithosphere rheology in geothermal areas: Features and examples. Journal of Volcanology and Geothermal Research, 148(1–2), 3–19. https://doi.org/10.1016/j.jvolgeores.2005.04.010

- Rasband, W. S. (1997-2021). ImageJ. U.S. National Institutes of Health, Bethesda, Maryland, USA. https://imagej.nih.gov/ij/.

- Rat, P. (1988). The Basque - Cantabrian Basin between the Iberian and European plates: some facts but still many problems. Rev. Soc. Geol. Esp., 1, 327–348.

- Rimstidt JD (1997) Quartz solubility at low temperatures. Geochimica et Cosmochimica Acta, 61, 2553–8.

- Royer, J. J. (2014). Hydraulic Fracturing in Transverse Isotropic Media - A Theoretical Framework. ECMOR XIV - 14th European Conference on the Mathematics of Oil Recovery, Catania, Sicily, Italy. https://doi.org/10.3997/2214-4609.20141885

- Rupf, I. & Nitsch, E. (2008). Das Geologische Landesmodell von Baden-Württemberg: Datengrundlagen, technische Umsetzung und erste geologische Ergebnisse. Landesamt für Geologie, Rohstoffe und Bergbau Baden-Württemberg. LGRB-Information 21:1–82

- Sammis, C. G. & Biegel, R. L. (1986). A self-similar model for the kinematics of gouge deformation. AGU fall meeting. Eos Trans.67 (44), 1187.

- Sandiford, M., Hand, M. & McLaren, S. (1998). High geothermal gradient metamorphism during thermal subsidence. Earth Planet Sci Lett 163:149–165

- Scholz, C. H. (2002). The Mechanics of Earthquakes and Faulting, second ed. Cambridge University Press, Cambridge.

- Scholz, C. H. (1990). The Mechanics of Earthquakes and Faulting. Cambridge Univ. Press, p. 439.

- Schwinn, G., Wagner, T., Baatartsogt, B., & Markl, G. (2006). Quantification of mixing processes in ore-forming hydrothermal systems by combination of stable isotope and fluid inclusion analyses: Geochimica et Cosmochimica Acta, v. 70, p. 965–982.

- Schwinn, G. & Markl, G. (2005). REE systematics in hydrothermal fluorite. Chemical Geology, 216, 225_248.

- Secor, D. T. (1965). Role of fluid pressure in jointing. American Journal of Science. 263, 633–46

- Sharma, R., & Srivastava, P. K. (2014). Hydrothermal fluids of magmatic origin. Modelling of magmatic and allied processes, 181-208.

- Shukla, M. K., & Sharma, A. (2018). A brief review on breccia: It's contrasting origin and diagnostic signatures. Solid Earth Sciences, *3*(2), 50–59. https://doi.org/10.1016/j.sesci.2018.03.001

- Sibley, D. F., & Gregg, J. (1987). Classification of dolomite rock textures. SEPM J Sediment Res. https://doi.org/10.1306/212f8cba-2b24-11d7-8648000102c1865d

- Sibson, R. H. (2000a). Fluid involvement in normal faulting. Journal of Geodynamics 29, 469–99.

- Sibson, R. H. (1981). Fluid flow accompanying faulting: Field evidence and models. Pure and Applied Geophysics, 124(1–2), 159–175. https://doi.org/10.1007/BF00875720

- Sibuet, J. C., Srivastava, S. P., & Spakman, W. (2004). Pyrenean orogeny and plate kinematics. Journal of Geophysical Research 109, B08104.

- Skinner, B. J. (1979). The many origins of hydrothermal mineral deposits. In: Barnes H L (ed) Geochemistry of hydrothermal ore deposits, 2nd edn. John Wiley & Sons, New York, pp 3–21

- Spence, D. A., & Turcotte, D. L. (1985). Magma-driven propagation of cracks. Journal of Geophysical Research: Solid Earth 90, 575–80.

- Stanton, R. J. (1966). The solution brecciation process: Geological Society of America Bulletin, v, 77, p. 843-848.

- Staude, S., Mordhorst, T., Nau, S., Pfaff, K., Brügmann, G., Jacob, D.E., & Markl, G. (2012). Hydrothermal carbonates of the Schwarzwald ore district, southwestern Germany: Carbon source and conditions of formation using d18O, d13C, $^{87}Sr/^{86}Sr$, and fluid inclusions: Canadian Mineralogist, v. 50, p. 1401–1434, doi: 10.3749/canmin.50.5.1401

- Staude, S., Bons, P. D., & Markl, G. (2009). Hydrothermal vein formation by extension-driven dewatering of the middle crust: An example from SW Germany. Earth Planet. Sci. Letts 286, 387-395.

- Swennen, R., Dewit, J., Fierens, E., Muchez, P., Shah, M., Nader, F., & Hunt, D. (2012). Multiple dolomitization events along the Pozalagua Fault (Pozalagua Quarry, Basque–Cantabrian Basin, Northern Spain), Journal of Int. Ass. of Sed. Sedimentology (2012) 59, 1345–1374.

- Terzaghi, K. (1943). Theoretical Soil Mechanics. New York and London: John Wiley and Sons, 510 pp

- Todt, W. (1976). Zirkon U/Pb-Alter des Malsburg-Granits vom Südschwarzwald. N Jb Mineral Monatsh 12:532–544

- Von Damm, K. L. (2019). Chemistry of Hydrothermal Vent Fluids. In Encyclopaedia of Ocean Sciences (pp. 282–290). Elsevier. https://doi.org/10.1016/B978-0-12-409548-9.10859-0

- Walter, B. F., Burisch, M., & Markl, G. (2016). The long-term chemical evolution of continental basement brines - a field study from the Schwarzwald, SW Germany. Geofluids 16:604–623

- Weertman, J. (1971). Velocity at which liquid-filled cracks move in the Earth's crust or in glaciers: Journal of Geophysical Research, v. 76, p. 8544–8553

- Weisheit, A., Bons, P. D., Danišík, M. & Elburg, M. A. (2013b). Crustal-scale folding: palaeozoic deformation of the Mt Painter Inlier, South Australia. In Deformation Structure and

Processes within the Continental Crust (eds S Llana-Funez, A Marcos and F Bastida), pp. 53–77. Geological Society of London, Special Publication no. 394.

- Weisheit, A., Bons, P. D., & Elburg, M. A. (2013a). Long-lived crustal-scale fluid flow: The hydrothermal mega-breccia of Hidden Valley, Mt. Painter Inlier, South Australia. International Journal of Earth Sciences, 102(5), 1219–1236. https://doi.org/10.1007/s00531-013-0875-7

- Yardley, B. W. D., & Bodnar, R. J. (2014). Fluids in the Continental Crust. Geochemical Perspectives, 3(1), 1–127. https://doi.org/10.7185/geochempersp.3.1

- Yardley, B. W. D. (2009). The role of water in the evolution of the continental crust. Journal of the Geological Society, 166(4), 585–600. https://doi.org/10.1144/0016-76492008-101

Scientific contributions

Chapter 2

Naaman, I., Bons, P., Gomez-Rivas, E.: **Morphological Characteristics and properties of Hydrothermal Breccia**.

This manuscript/paper highlights the relationship between brecciation mechanisms, as well as their genetic associations and geological setting. The paper analysed the clast size distribution of some hydrothermal breccias: breccias associated with dolomitising fluids at Pozalagua (North Spain) and ore-related breccias from the Black Forest (Southwest Germany) based on field data and provide ways to estimate the total energy (fluid) required for the brecciation.

Scientific ideas	**Data generation**	**Analysis and interpretation**	**Paper writing**
20%	**100%**	**80%**	**80%**
Initial scientific idea of the hydrothermal breccia and brecciation mechanism by supervisor P. Bons.	Breccia clasts data presented in the paper by IN. Field images of the samples by P. Bons.	All data analysis and interpretations by IN and supervisor P. Bons	Paper writing by IN. Comments, insertions and proof-reading by supervisor P. Bons

Chapter 3

Naaman, I., Bons, P.: **A numerical simulation of source fluids, flow and fracture dynamics within the crust**

This paper is fully based on numerical modelling of fluid flow in a rigid matrix to simulate hydrothermal fluid transport and fracture growth, which constrains the minimum amount of pressure/energy an ascending fluid must provide.

Scientific ideas	Data generation	Analysis and interpretation	Paper writing
10%	**80%**	**60%**	**70%**
Initial scientific idea of flow mechanisms by supervisor P. Bons and IN. Initial idea of the fluid flow model by previous PhD candidate TD	Generation of the numerical simulation data presented in this paper including programme code by supervisor P. Bons and IN	All analysis and interpretation IN and PDB	Paper writing by IN. Comments, insertions and proof-reading by supervisor P. Bons

Chapter 4

Paul D Bons1; Dongsheng Cao; Tamara de Riese; Eloi González-Esvertit; Daniel Koehn; **Isaac Naaman**; Till Sachau; He Tian; and Enrique Gomez-Rivas: **A review of natural hydrofractures in rocks**.

This paper focus on the formation and evolution of non-igneous hydrofractures. It reviews the basic theory of the role of fluid pressure in rock failure and discusses the propagation of hydrofractures after initial failure, where networks of hydrofractures may form or ascend through the crust as mobile hydrofractures.

Scientific ideas	Data generation	Analysis and interpretation	Paper writing
10%	N/A	10%	**10%**
Initial scientific idea by P. Bons, D. Koehn, EGR	This paper is generally a review paper	Analysis related to various theories and models by PB, DK, TD, EGR	Most paper writing and editing by PDB major contributions Comments, insertions and proof-reading by co-authors

Chapter 2

Morphological Characteristics and properties of Hydrothermal Breccia

Naaman Isaac*[1] Bons Paul D.[1] & Gomez-Rivas Enrique[2]

[1]Department of Geosciences, Eberhard-Karls University Tübingen, Schnarrenbergstr. 94-96, 72076 Tübingen, Germany
[2]Departament de Mineralogia, Petrologia i Geologia Aplicada, Facultat de Ciències de la Terra, Universitat de Barcelona. C/Martí i Franquès s/n, Barcelona, 08028, Spain

**Corresponding email:* isaac.naaman@uni-tuebingen.de

Abstract

Keywords: Hydrothermal, breccia, tectonic, dissolution

Breccias are rocks composed of fragments or clasts of broken rock in a matrix of finer clasts and/or cement of precipitated minerals. They form either by sedimentary, tectonic, igneous and fluid-flow processes, or a combination of them. Apart from their significance for fundamental research, breccias are very important host rocks for ore deposits, and can also be zones of high permeability and thus serve as potential aquifers. One problem is that it may be difficult to determine what the origin of breccia actually is, especially in terms of the genetic and/or textural classification of tectonic, hydrothermal and dissolution breccias. Improved definition of the diagnostic signature of the individual breccia types requires better knowledge of the relationship between brecciation mechanisms, as well as their genetic associations and geological setting.

Here we analysed the clast size distribution of a number of some hydrothermal breccias: breccias associated with dolomitising fluids at Pozalagua (North Spain), ore-related breccias from the Black Forest (Southwest Germany) and provide ways to estimate the total amount of fluid required for the brecciation. Clast sizes in all cases tend to follow a power-law distribution, but power-law exponents can vary significantly, even within a single setting. We suggest that this may be due to the progressive disintegration of the rock, from just dislodging clasts towards floating and rotated clasts, which requires significant dilation and/or dissolution.

Introduction

Hydrothermal fluids are, by definition, fluids that are hotter than the surrounding/country rocks (Davies and Smith, 2006). Their circulation within the crust is important for their associations with many ore deposits and rock alteration in the crust that are related to these fluids that can transport dissolved elements towards these deposits (Fyfe et al. 1978; McKibben, 2005). The giant Olympic Dam U-bearing iron oxide-copper-gold deposit in South Australia to abundant small deposits in the German Black Forest (Schwarzwald) are prominent examples (Courtney-Davies et al., 2020; Bons et al., 2014; Staude et al., 2012). In a crustal setting, rapid fluid transport is required to maintain an elevated temperature compared to the host rock, which can be achieved by fluid flow through fractures and faults (McKibben, 2005; Bons et al., 2022 and references therein).

At depths below a few kilometres the creation of fractures is achieved by hydrofracturing by which fluid overpressure is the dominant factor in fracture creation, opening and propagation (Fyfe et at., 1978; Sachau et all, 2015; Cobbold & Rodrigues, 2007; Bons et al. 2022; Cox, 2005). Hydrofractures can rapidly propagate and merge with other fractures to efficiently move fluids upwards (Weertman, 1971; Bons and van Milligen, 2001; Bons, 2001). When a fracture does not only propagate at its tip, but branches out in many directions, breccias are formed by disintegration of the rock into many fragments or clasts. (Jébrak, 1997; Weisheit et al. 2013 and the references therein). Hydrothermal ore deposits and alteration zones typically show brecciation Fig.2 (Weisheit et al. 2013, Jébrak, 1997).

Breccias can form in various ways, such as through sedimentation, igneous activity, meteorite impact, tectonic diminution, collapse, or fluid overpressure (Shukla and Sharma, 2018; Jébrak, 1997; Weisheit et al. 2013; Bons et al 2014). These can be grouped into three broad categories: (i) igneous, (ii) sedimentary, (iii) tectonic (Shukla and Sharma, 2018). Prefixes are commonly used, such as volcanic, igneous, hydrothermal, chert, fault, impact and seismic breccias. Igneous breccias are typically formed through volcanic processes and are composed primarily of angular volcanic fragments in a fine-grained matrix (Reynolds, 1928; Fisher, 1958; 1960; Wright and Bowes, 1963). Sedimentary breccias, as the name implies, are formed by various sedimentary processes (Jackson, 1997). Tectonic breccias, the third category, are made of angular fragmented clasts that are typically formed as a result of brittle rock fracturing and disintegration as a result of tectonic stresses, such as caused by fault movement (Fault breccias; Wise et al., 1984; Sibson, 1986; Reimold et al., 2012). Impact breccias can be included in this category, although the cause of elevated stress here is meteorite impact instead of tectonic

processes. Dissolutional breccias are formed in the subsurface by fragmentation due to downward movement of sedimentary strata into voids that are created by the dissolution of underlying strata. This type of process is usually a combination of both chemical and physical processes (Middleton, 1961; Stanton, 1966; Friedman, 1997; Kolodny et al., 2005). Hydrothermal breccias can be classified as a tectonic breccia (Shukla and Sharma, 2018; Phillips, 1972; Jèbrak 1997; Scholz, 1990; Hubbert and Willis, 1957) but is here treated as a separate class (Jébrak, 1997). A distinguishing feature of a hydrothermal breccia is that the fracturing processes is dominated by a high fluid pressure and not primarily by elevated differential stresses as is the case for fault and impact breccias. Hydrothermal breccias are often associated with dissolution or alteration (e.g. dolomitization) of clasts as the arrival of hot fluids creates a chemically active system (Davies and Smith 2006). Fluids may cause dilation upon entering the breccia zone, but also subsequent collapse when they leave the zone again, as was envisaged by Weisheit et al. (2013a) to cause mixing of clasts. Hydrothermal breccias may thus share similarities with tectonic, dissolution, as well as collapse breccias.

To distinguish hydrothermal breccias from other known types, the clast size morphology and distribution can be used, in particular their fractal dimension, which is related to the disintegration processes of the rock mass (Jébrak, 1997). A number of studies therefore measured the clast-size distribution in breccias (Lorilleux et al. 2002; Barnett, 2004; Keulen et al. 2007; Weisheit et al. 2013a). These studies concurred with Jébrak et al. (1997) that breccia clast sizes typically show a power-law distribution with small clasts more frequent than bigger clasts. This distribution is often given in the cumulative form:

$$N_{(\geq s_i)} = k_i \cdot (s_i)^{-n_i}, \quad (1)$$

with $N_{(s)}$ the number of clasts larger or equal to size *s*, and *n* power-law exponent that is smaller for hydrothermal breccias than for fault breccias (Jébrak, 1997). *k* is the number of clasts larger or equal to the unit size. The subscript *i* refers to the dimension in which the size is expressed, with *i*=3 for volume, *i*=2 for cross-sectional area, and *i*=1 for diameter.

Instead of the cumulative size distribution (Eq. 1), one can also use the frequency (*f*) distribution, given by:

$$f_{(s)} = -\frac{dN_{\geq s}}{dV} = nk \cdot s^{-n-1} \quad (2)$$

The advantage of using a frequency distribution is that it is not sensitive to sampling errors at the upper end of the size range or potential variations in the exponent with size. A disadvantage is that the frequency distribution is sensitive to the choice of bins.

Although clasts are 3-dimensional objects, clast sizes are usually reported in the literature as either diameter or area, not as volume. This hampers comparison between different studies. We therefore discuss the conversion between different expressions of the size distributions. We then present new clast-size analyses of hydrothermal breccias from Pozolagua in NW Spain (Swennen et al., 2012; Aranburu et al. 2002) and the SW-German Black Forest (Geyer and Gwinner, 1986; Kalt et al., 2000; Staude et al., 2009). Finally, we present a model to explain why the power-law exponent is smaller in hydrothermal, fluid-pressure induced, breccias than in fault breccias.

Breccia clast-size distribution and clast shape

To create a breccia, a volume of coherent rock must basically be divided into multiple sub-volumes, the fragments or clasts, that remain internally coherent, but have lost coherence with other clasts. Coherence may be restored subsequently through cementation (Jackson, 1997). The cause for loss of coherence between clasts under consideration here is fracturing, thus excluding other processes, such as dissolution. A power-law distribution of clast sizes means that the breccia is self-similar in this respect such that the ratio of number of clasts of size s and $s/10$ is the same, irrespective of the value of s. This again implies that there is no characteristic length scale in the brecciation process. The Mohr-Coulomb-Griffith theory for brittle failure has no characteristic length scale, as the parameters are stresses, fluid pressure and the material properties tensional strength, cohesion, and internal angle of friction (Bons et al. 2022; Royer, 2014; Terzaghi, 1943; Hubbert, 1951; and Secor, 1965). The theory has proven to be successful in predicting when a fracture will form and in which orientation, but not where it will form or what size the fracture has. Considering this, a power-law clast-size distribution is to be expected, at least within a certain range.

The lower end of the power-law range is typically the grain size. It is at this length scale where brittle-failure properties change from those of a rock to that of the individual minerals that constitute the grains. The uppermost end of the range is controlled by the size of the breccia, as the largest clast must simply be smaller than the whole breccia. The power-law range can thus be large, as was shown by Weisheit et al. (2013) who showed a continuous power-law range for clasts from <1 mm^2 to about 1 km^2 in area in the 10 km^2 Hidden Valley Breccia in South Australia.

Relationship between power-law exponent and dimension

Rocks are 3-dimensional and we therefore start the analysis of the relationship between the power-law exponent and the dimension in which clast sizes are measured with the three-dimensional case (n_3) as a reference. A low value of n_3 means that the second largest clast is much smaller than the largest clast compared to a high value of n_3 (Fig. 1). This means that for a small n_3 value a relatively large proportion of the breccia volume is occupied by the largest clasts. For a large n_3 value the largest clasts only occupy a relatively small fraction of the total breccia volume.

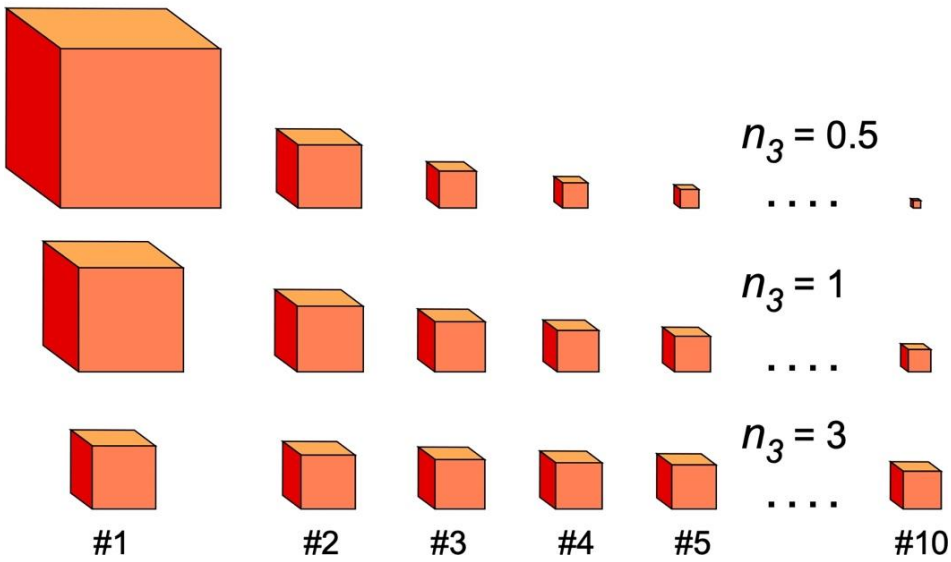

Figure 1. Relative sizes of the five largest and 10th largest clasts as a function of the power-law exponent n_3, for n_3 = 0.5, 1, and 3.

A problem with the practical measurement of clast sizes and their distribution is that we normally do not have a 3-dimensional view of the clasts, but instead typically a 2-dimensional outcrop surface that intersects the breccia and its clasts. The area of the intersection of a clast and an arbitrary erosion surface depends on its shape and where it is intersected. Using a shape factor α, we can approximate the average intersection area s_2 as a function of clast volume s_3 with:

$$s_2 = (\alpha s_3)^{2/3} \tag{3}$$

The frequency of cross-sectional areas is:

$$f_{s_2} = -\frac{d\left(k\alpha^{n_3}\left({s_2}^{3/2}\right)^{n_3}\right)}{ds_2} \propto (s_s)^{\frac{-3}{2}n_3-1} \tag{4}$$

Proportionality is used here, as we are only concerned with the power-law exponent. This way the poorly constrained constants, such as shape factors drop out. We must also consider that a small clast has a smaller chance to intersect the erosion surface than a large clast. The chance P is proportional to the mean diameter s_1 of a clast, which in turn depends on the shape of the clasts that can again be approximated with a shape factor. The frequency of exposed clasts (f'_{s2}) with area s_2 is now:

$$f'_{s_2} \propto (s_2)^{-n_2} \propto P \cdot f_{s_2} \propto (s_2)^{1/2} \cdot (s_2)^{\frac{-3}{2}n_3-1} \propto (s_2)^{\frac{-3}{2}n_3-\frac{1}{2}} \quad (5)$$

From this we can integrate to obtain the number N'_{s2} of clasts with an area larger than s_2 that are exposed in an outcrop:

$$N'_{s_2} \propto (s_2)^{\frac{-3}{2}n_3+\frac{1}{2}} \quad (6)$$

Jébrak (1997), used the diameter (s_1) of clasts as the measure of their size. We can use the same procedure and assumptions as above to derive the one-dimensional frequency(f'_{s1}) and cumulative frequency (N'_{s1}) distribution in outcrop surface.

$$f'_{s_1} \propto (s_1)^{-n_1} \propto P \cdot f_{s_1} \propto s_1 \cdot (s_1)^{-3n_3-1} \propto (s_1)^{-3n_3} \quad (7)$$

and $$N'_{s_1} \propto (s_1)^{-3n_3+1} \quad (6)$$

Table 1 summarises the conversion equations for different power-law exponents derived in one or two dimensions to the volumetric n_3 for the cumulative clast-volume distribution. Jébrak (1997) used the power-law exponent (n_1) of the cumulative particle diameter (s_1) as an indicator of the amount of energy that was introduced into the system. He found that a low n_1 (~2) for fluid-assisted brecciation and values of $n_1 \geq 3$ for wear abrasion and shear. These values correspond to the cumulative volumetric n_3 (Eq. 1) of ~1 and 1.33, respectively. Weisheit et al. (2013) obtained an exponent of $n_2 \approx 1$ for the cumulative distribution of clast areas in the hydrothermal Hidden Valley breccia. From this we derive a volumetric $n_3 \approx 1$ for the Hidden Valley breccia.

Table 1: Conversion of the power-law exponent for clast area and diameter distributions to the volumetric exponent n_3, including examples from the literature and this study.

Measurement	Distribution	Volumetric n_3	Reference	Derived volumetric n_3
Cumulative				
True area	$N_{\geq s_2} \propto (s_2)^{-\left(\frac{3}{2}n_3\right)}$	$n_3 = \frac{2}{3}n_2$		
Area in section	$N'_{\geq s_2} \propto (s_2)^{-\left(\frac{3}{2}n_3-\frac{1}{2}\right)}$	$n_3 = \frac{2}{3}\left(n_2+\frac{1}{2}\right)$	Weisheit et al. (2013)	$n_2 \approx 1 \rightarrow n_3 \approx 1$
Diameter in section	$N'_{\geq s_1} \propto (s_2)^{-(3n_3-1)}$	$n_3 = \frac{n_1+1}{3}$	Jébrak (1997)	fluid assisted: $n_1 \approx 2 \rightarrow n_3 \approx 1$ wear abrasion, shear: $n_1 \geq 3 \rightarrow n_3 \geq \frac{4}{3}$
Frequency				
True area	$f_{\geq s_2} \propto (s_2)^{-\left(\frac{3}{2}n_3+1\right)}$	$n_3 = \frac{2}{3}(n_2-1)$		
Area in section	$f'_{\geq s_2} \propto (s_2)^{-\left(\frac{3}{2}n_3+\frac{1}{2}\right)}$	$n_3 = \frac{2}{3}\left(n_2-\frac{1}{2}\right)$	This study, Pozalagua Teufelsgrund	$1 < n_2 \leq 2 \rightarrow \frac{1}{3} < n_3 < 1$ $n_2 \approx 1.5 \rightarrow n_3 \approx \frac{2}{3}$
Diameter in section	$f'_{\geq s_1} \propto (s_2)^{-(3n_3-1)}$	$n_3 = \frac{1}{3}(n_1+1)$		

Geological Setting

This study, focuses on two areas of known hydrothermal breccia bodies on which clast size statistics were measured.

Pozalagua – Northern Spain

The Pozalagua area is located in the northern part of Castilla-Leon, west of Bilbao, in northern Spain and comprises the landward part of the Cantabrian Ranges. The locality is characterised by intra-continental rift basins that formed from transtensional movements along predominantly north-west to south-east faults superimposed on Hercynian structural trends (Rat, 1988; García-Mondéjar et al., 1996) and have been filled with terrigeneous and evaporitic sedimentary sequences (Curnelle, 1983). A thick prism of sediments, up to 7 km, accumulated during the Aptian–Albian within the basinal settings (Immenhauser et al., 1999; Cámara, 1997).

The South-eastward Iberia drift along NW–SE faults with strike-slip motion (e.g. Sibuet et al., 2004) caused Basque Cantabrian Basin (BCB) partitioning into highs and lows with shallow marine carbonate and deeper marine terrigenous sedimentation, respectively. At a later period, (Lower Oligocene), the continuing convergence of Iberia with Europe resulted in a westward propagation of the Pyrenean deformation front into the Cantabrian region. The Pozalagua Quarry area predominantly showcase dolomitic (dark-grey) limestone of recrystallized bioclastic to intraclastic wackestones to mudstones. Dolomitization in the basin, likely begun

during the Jurassic period, and was associated with extensional tectonics and the circulation of magnesium-rich fluids. Later events of dolomitization occurred during the Cretaceous and Cenozoic times, linked to both continued extensional tectonics and later compressional phases of the Pyrenean orogeny (Swennen et al., 2012). Karst cavities within the localised setting and probably the development of the Pozalagua Fault system may have aided the subsequent development of the hydrothermal karst, i.e. a series of fracturing, dissolution, corrosion and cementation events observed in the area. This sequence of events also characterizes the emplacement of the dolomites embedded in limestone (Swennen et al., 2012; Aranburu et al. 2002). The carbonates in the Pozalagua quarry show the products of various fluid pulses expelled along the Pozalagua Fault system (Swennen et al. 2012; Immenhauser et al., 1999; Cámara, 1997).

Black forest - Germany

The Black forest in South-West Germany forms part of the European Variscan basement (Kalt et al., 2000), and consists of mostly granites and gneisses unconformably overlain by a 1.5-km-thick succession of Permian–Triassic to Jurassic clastic sediments and carbonates (Geyer and Gwinner, 1986; Staude et al., 2009). The metamorphic rocks which form about ~ 50% of the exposed Schwarzwald basement were intruded between ca. 335 and 315 Ma by post collisional granites (Todt 1976; Altherr et al. 2000; Hann et al. 2003) and is covered by these partly eroded Palaeozoic and Mesozoic sedimentary sequence (Geyer and Gwinner, 2011 and references therein). Middle Triassic to Jurassic carbonates and evaporites were preceded by the sedimentary successions with Permian and Lower Triassic red beds (Geyer and Gwinner, 1986). The Black Forest area is marked by periods of hydrothermal vein formation within the basement and its overlying strata that produced over 400 known hydrothermal ore deposits (Metz et al., 1957; Bliedtner and Martin, 1986; Schwinn and Markl, 2005; Markl et al., 2006; Schwinn et al., 2006; Baatartsogt et al., 2007; Staude et al., 2007). These hydrothermal veins were formed over a time period from ca. ~300 Ma to the presence (Pfaff et al., 2009a) and have been classified into late-Variscan quartz veins, post-Variscan Jurassic and Paleogene Upper Rhinegraben (URG) rift-related barite–fluorite-dominated deposits. Five of such major hydrothermal deposits have been described extensively by Walter et al. (2016). Exhumation of the area since the late Cretaceous was strongly asymmetric (Rupf and Nitsch 2008; Geyer and Gwinner 2011). Later, the tectonic (partial) subsidence during the Paleogene caused the whole succession to be exposed from the Jurassic in the east down to about 2 km below the

unconformity in the southwest (Staude et al. 2009). Propagation of hydrothermal fluids was triggered during these times of high sedimentation rates which is said to have been driven by the subsidence of the basin (Staude et al. 2009). Typically, deposits at the Black Forest exhibit fracture-hosted veins with breccias that indicate a recurring fracturing processes and mineralization with no known significant tectonic and or fault activity at the time of ore formation, as the deposits lack evidence of any tectonic movements along the fractures (Staude et al., 2012 and references therein).

Materials and Method

We analysed the clast size distribution of the hydrothermal breccia at Pozalagua (North Spain), and breccias from the Black forest (Schwarzwald), Southwest Germany. These breccias samples from Pozalagua quarry are dolomitic and resulted from the dolomitization of the host limestone. Photographs of flat or approximately flat breccia surfaces on outcrops were used as the base for the clast area analyses. Clasts outlines were drawn manually, making sure that the outlines do not intersect. This is to avoid that two adjacent clasts are considered one single clast. Clasts that were truncated by the edge of the image were excluded from the analysis. The "Analyse particles" option of ImageJ (Rasband, 1997-2021) was then used to determine the area of each clast in the images. The sample image *B* unlike *A*, *C* and *D* shows altered dolomite breccia. Clasts look elongated and less angular with respect to the other samples and are seen entirely surrounded by fine matrix erasing all evidence of dislodging from larger lasts as appears in e.g. *A*, *C* and *D*. The original clasts are altered by circulation fluid that probably were not the original fluid that disintegrated the rock.

Without any further processing, clast areas can be visualized as reverse cumulative plots of number of clasts equal or greater in area than a certain clast area ($N_{\geq s2}$) against that area (s_2). Measured clast areas ranged from < ~ 1mm^2 to ~ 2000 cm^2 but for sample *E* (Teufelsgrund) the unit measure is in pixel. In the sampled analysed, the parameter used were the cross-sectional surface (2-D). Raw data are shown as frequency plots (Eq. 2) in Fig. 5. The problem with cumulative plots is that deviations from a power-law distribution at the large end of the clast-size range propagate through the whole data set. It is therefore preferred to use frequency plots (Fig. 5). This, however, raises the problem of binning. We use a MATLAB script that uses dynamic binning to ensure that each bin has at least 10 clast areas and is not smaller than 0.005 cm^2.

A second problem is that the smallest clast sizes are inevitably underrepresented as clasts are at the limit of image resolution. At the other end of the spectrum, large clasts may also be underrepresented due to bias in taking images (you do not want an image with only one clast) or clasts that are not fully within the image. Therefore, frequency data at both the very least and high end of the size spectrum is excluded.

A power-fit for clast size (area) distribution results when the number of clasts N'_{s2} (frequency), is plotted against the area a in a log–log plot (clast size distributions of all samples were fitted by equation 2 (Marone and Scholz 1989; Perfect 1997, Weisheit et al., 2013). It must be noted however that the extreme ends of the power-law fit made of the smallest (grain) and largest clast sizes tend to influence the curve significantly i.e. extreme upper end (small clasts) flattens the curve where larger clast sizes increase the slope. The output data on clast dimensions measured include diameter, area, circularity, and sphericity (ellipticity) of clasts for each sample but here, we used clast area for our analysis. All clast size distribution data is presented in (Table 2).

Table 2. Summary of the data sets for the clast area distribution.

File name	No. of clasts	Minimum clast area (cm^2)	Maximum clast area (cm^2) Sample E (in px)	n_2 -value	Range (n_2-*value*)
A	682	0.001	84.2765	1.45	-1.50 / -1.32
B	644	0.0011	46.7475	2.01	-2.18 / -1.81
C	615	0.0023	469.0781	1.58	-1.68 / -1.38
D	804	0.0005	148.8318	1.67	-1.83 / -1.68
E (Teufelsgrund)	1678	1	1746616	1.54	-1.57 / -1.51

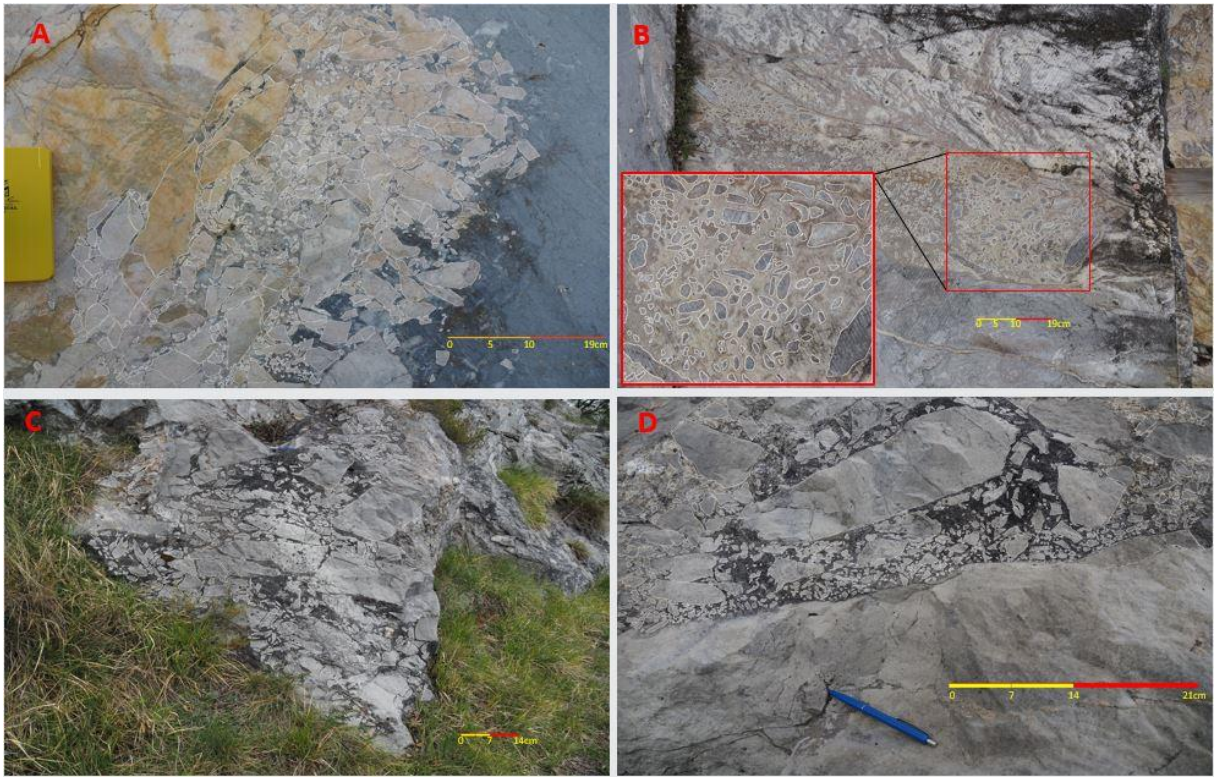

Figure 2. Field photographs of a hydrothermal breccia from the Pozalagua area analysed in this study. Image A, B, and D, are typical evidence of known hydrothermal breccia with no evidence of alteration and B being recognised as dissolution breccia i.e. the emplaced body has been altered due to erosion by circulating fluids after the original emplacement.

Result and Discussion

Figure 3, shows the apparent clast size (area) dimension delineated from the breccia clasts samples from Fig. 2 respectively. The result for the frequency plots ($f'_{(s2)}$) and the cumulative frequency plot for the 2D data set is presented in Fig. 5. The total data points for each sample for the n_2 which we used to compute for the n_3 values (see Appendix 1) is with a set range at 95% minimum and maximum of all the data set. From the binned data points, the extreme -the very small and the largest clasts, making up 5% is excluded in determining the *n*-values (exponents). The cumulative frequency plots of the breccia clasts conform to power-law which connotes the form in equation (1). The slope of the straight line in the log-log plots (Fig. 5) represents the power-law exponents, *n* (e.g. Sammis et al, 1987, Otsuki, 1998). The power-law exponents (the *n*-values) for the analysed samples resulted apparently in *n*-values, ~1.45, ~2.01, ~1.58, ~1.67 and ~1.54 for *A*, *B*, *C*, *D* and *E* (TG) respectively. The corresponding volumetric n_2 values used to determine the n_3 is the average for simplicity. When we consider the individual samples, we realize that *B* has relatively higher power exponent ($n \approx 2.01$) even though their

clasts range is comparable smaller. In general, the n_2 values for the exponents do not go beyond the threshold of ~2 for fluid assisted brecciation when we consider what Jébrak, (1997) proposed. In summary, data value for n_2 for the power-law exponents is averaging around ~1.68 excluding that of *E* (Teufelsgrund) is used in arriving at $1<n_2\leq 2$. For the breccias at Teufelsgrund, sample *E*, we obtained an n_2 value of 1.54 which is as well close to that of the dolomitic hydrothermal breccias in Pozalagua.

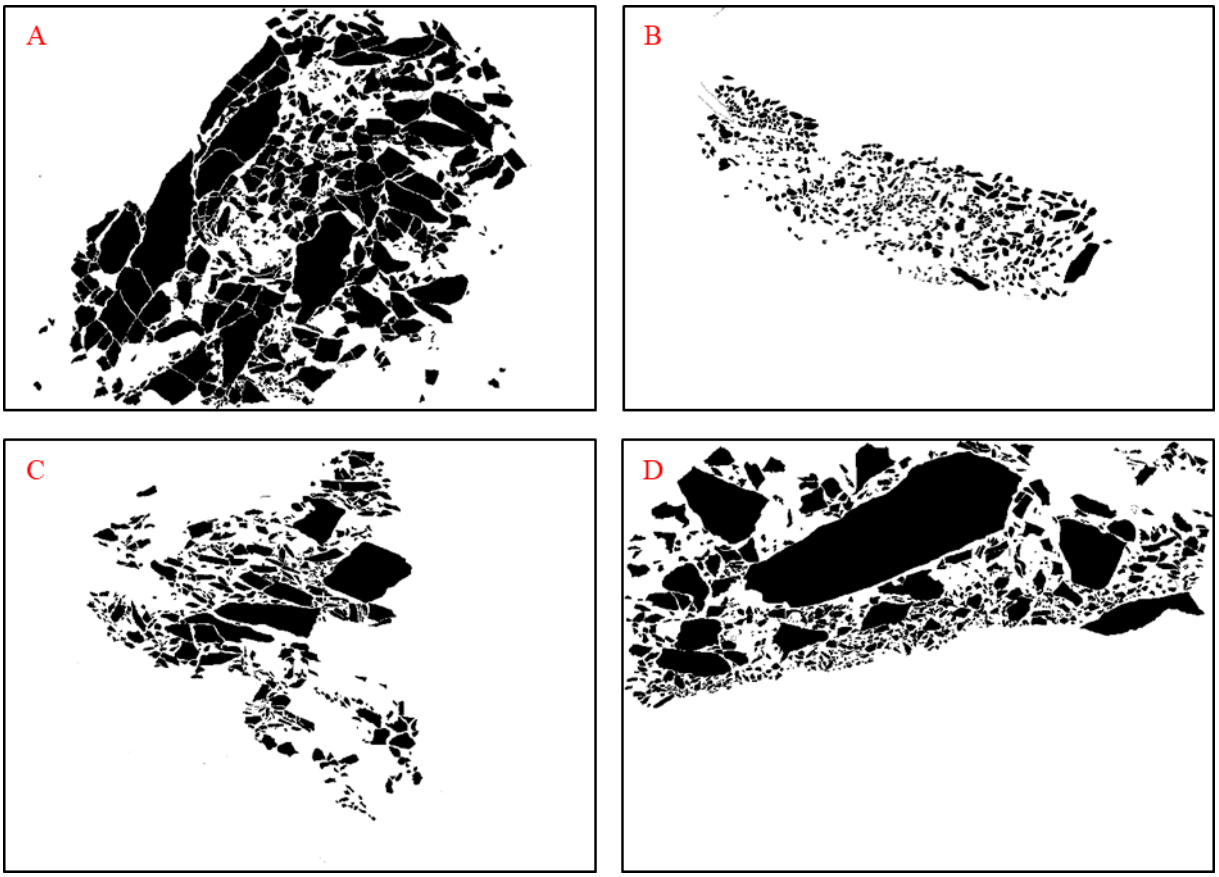

Figure 3. Analysed breccia clasts from the field image samples A, B, C, and D, with ac and d showing a typical hydrothermally brecciated rocks and little or no alteration in situ. Sample b however shows altered and re-worked (rounded) clasts by fluid after emplacement.

Now, let consider the individual *n*-values for the n_2 of each sample to the n_3 for the volumetric size analysis surmised in Table 1. Computed n_3 values from n_2 equate to ~0.63, ~1.01, ~0.72, ~0.78 and ~0.69 from *A* to *E* respectively. This show that averagely, the 3-D volume for the clast sizes is less than 1 ($n_3<1$) (Fig.1). This shows that proportionate change in volume (n_3) - from largest clast to the next largest, is about same with respect to volume change (see Figure 1). For sample B, the $n_2 \rightarrow n_3$ of ~1.01 lies in-between $n_3 \approx 0.5$ and 3 in Fig.1. Here the volume change (n_3) is not as large as in the case of lower n_3 values. That at a lower exponent, (low n_3-

value), there is proportionately large volume change from the largest clasts to the second largest clasts (Fig.1) and that the smaller clasts occupy a small section of the whole breccia with the largest clast about as large as the whole breccia. In consonance with Jébrak (2007) and Weisheit et al. (2013), our low n_2 values respectively correspond to their volumetric change and confirms these breccias in Pozalagua have resulted from fluid-assisted brecciation.

In Fig. 2A, a continued dislodged clast from the main block shows a 'mosaic pattern' and a continued brecciation process is evident such that these breccia clasts further result in complete fluidized fracture network e.g. fig. 2C and 2D. In an occasion where there may be a repeating process from the onset of brecciation to the truncation or cessation of the whole process, there could be what is termed as re-brecciation in some outcrops which is absent here in our case. From the breccia samples, trend in breaking shows that, dislodged clast from the main block are prominent e.g. in A, giving a clue of movement (showing pattern) from the immediate clast they are separated from.

One major diagnostic signatures of such hydrothermal breccia units are the presence of angular fragments predominantly larger than 0.005 cm^2 in area (Shukla and Sharma, 2018) over the entire area. In Fig.3B however, these underlying typical hydrothermal breccia characteristics is not clearly seen but poses much similarity in clast distribution for dissolution breccia (Stanton,1966) erasing every evidence of a fluid assisted process as such breccias – hydrothermal, develop early through vein formation as the process of fracture growth is triggered (Shukla and Sharma, 2018, Jèbrak, 1997, Scholz, 1990).

Dissolution breccia are commonly associated with carbonate rocks, formed when the clasts are subjected to erosion as dissolution of rock surface by fluids, result in the collapse and potential infilling, leading to a breccia rock structure often found in carbonate and hydrothermal settings (intrusive settings). Here, clasts are reduced from its original sizes due to the peripheral erosion. The effect on the power-law exponent is that, the power-fit is significantly shifted to the left (reduced *n-value*) even with small amount of clasts volume change, Fig. 4.

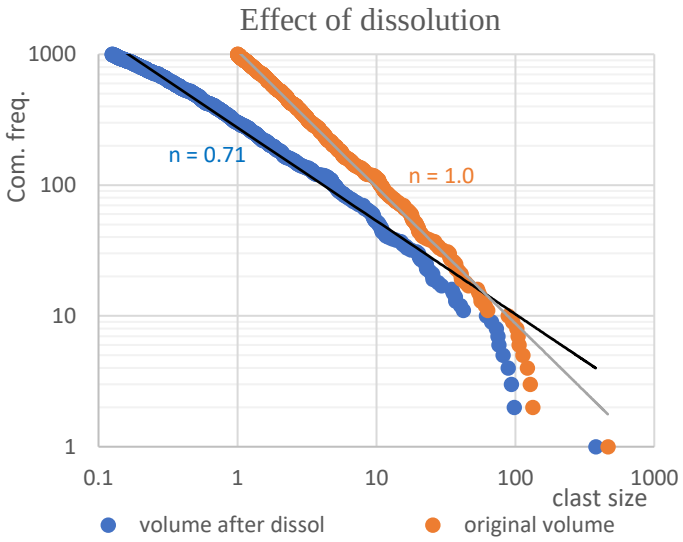

Figure 4. Effect of dissolution on the cumulative volume distribution. Orange is for 1000 clasts with volumes between 1 and 1000 and an exponent n_3=1. Assuming a cubic shape, when 0.5 is removed from the size of each clast ($S=V^{1/3}$) and then calculated the new volume after dissolution: $V' = (S-0.5)^3$. You see that the distribution is not exactly power-law anymore and the slope decreases.

This may result in a decreased slope that may not be a power-law fit with the distribution after all. In Fig.4 for example, when we consider a 0.5-unit volume reduction of all data points (1000 in this regard), it showed that the *n*-value decreases, resulting in a decreased slope which does not inherently follow a power-law fit. Now, when we consider our sample/fig. 2B, there is indication of clast alterations which may not necessarily be termed a dissolution because the power-law exponent appears to be even larger than the other samples resulting in steeper fit (slope) when we consider the volumetric n_2 value of 2.01. Sample B from our analysis cannot be concluded as a dissolution breccia base on only physical appearance. However, we may not be wrong other than statistical analysis proving otherwise where the evidence is handy for sample B. For instance, the dolomitic breccia clasts seem reworked by fluid which may have contributed to the dissolution of the clast to its current clasts size. This process has resulted in a mixture of these 'quasi angular' clasts cemented together in fine-grained matrix. Variations in the slope, thus, is a function of a proportional change in the clast sizes.

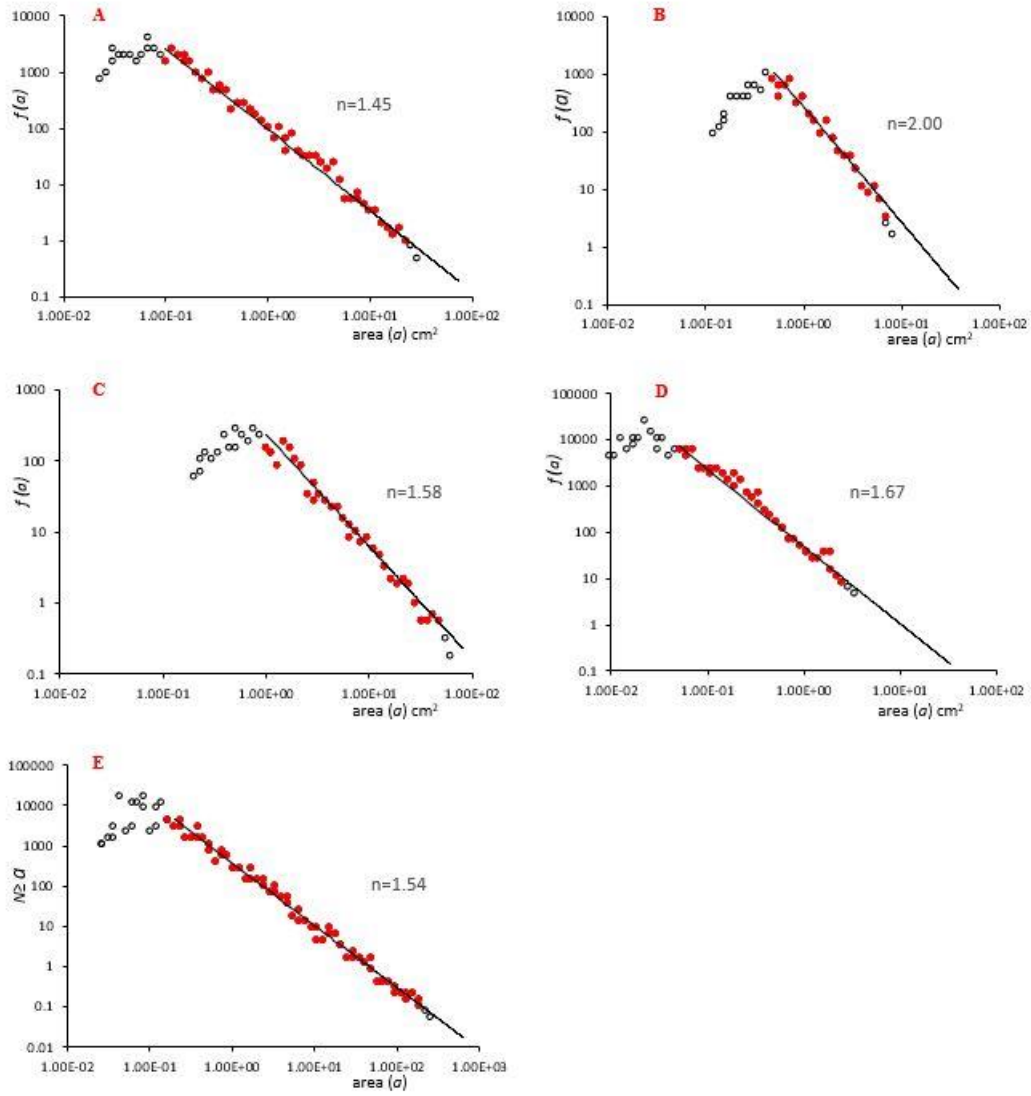

Figure 5. Results of clasts size analyses of the field sampled breccias presented in a log-log plot. Number of breccia clast (*f*) is plotted against area (*a*), the size of the breccia distribution. Slope of the straight sections in these logarithmic plots is the fractal dimension. The *n-dimension* indicates the degree of roundness or angularity of the breccia clasts. All analyses combined give a fractal dimension averaging as n~1.5 for the hydrothermal breccias A, B, C, D and E.

Again, development of a breccia (hydrothermal) is significantly connected to the total fluid volume needed to drive the disintegration (e.g. Weisheit et al., 2013,) as they significantly estimated how much in terms of hydrothermal fluid, required to result in the Hidden Valley breccias. In fluid-assisted (hydrothermal) brecciation e.g. Fig.2, fragments are angular and brecciation is typically believed to follow newly created or pre-existing fractures after the resistance (of the rock) strength is overcome. These breccia formations may result from stages known to have started as (i) veins/micro fractures, (ii) nucleation and growth of fractures and

(iii) dilation of these fractures resulting in well-connected joints. Fluid assisted dilation (mobile hydrofractures) consequently results in hydrothermal breccia.

For the analysis of the clast size distribution, the most considerable and easy parameter to measure on irregular clast size is the area (2-D) and the diameter (1-D) when there is an assumption of a projected clast circularity (Brittain, 2001). Exception to this is in the dissolution breccias where the initial process of breaking and clast size has been erased by the dissolution process, e.g. chemical dissolution in dolomites.

There is thus a large range in clasts sizes resulting in the largest clasts occupying a relatively large fraction of the total volume see fig. 2D/3D. This is in consistent with the observation that it is difficult to define the largest clast in a breccia (hydrothermal) as they typically do not have clearly defined boundaries. Large clasts in outcrops may be due to a shorter duration of the brecciation process. If a hydrothermal breccia forms by a pulse of fluid (pressure energy) input, brecciation would start from a point or plane and gradually extends its fractures outwards. Once a clast is fully surrounded by fluid, it would not further disintegrate. This is independent of their size, so large clasts may be incorporated in the breccia and remain large. At Pozalagua like those in Hidden Valley (Weisheit et al., 2013a) we see no re-brecciation but dissolutions at some sections. Clasts fully surrounded by fluid may rotate and mingle. Thus, to further allow the volume expansion that the overpressure causes, the fracturing front would expand resulting in more breccia formation.

Other than the matrix composition, texture, mineralization and geological settings, breccia produced by tectonic processes is also distinguishable from fluid assisted breccia with *n*-value varying significantly (larger than fluid assisted brecciation) compared to hydrothermally brecciated rocks (see Jébrak, 1997).

Conclusion

Development of hydrothermal breccia comes as a response to extensive fracture growth and propagation, a process considered as one of the most common mechanisms of brecciation that is observed at all scales. Analysed clast distributions of breccias that we know are hydrothermal and their distribution follows a power-law fit. We find that they have n_2-values in the range of ~1 to ~2, translating to n_3 between ~1/3 and ~1. In Jébrak's (1997) classification, the boundary in his fractal dimension is between 2 and 3, which translates to $1 \leq n_3 \leq 4/3$. The findings in this study confirm this, as all breccias have $n_3<1$. Dissolution breccias may not be power-law, so

the apparent *n*-value may be larger than for dissolution-free hydrothermal breccias. We established that a decreased slope may not necessarily conform to a power-law fit when the breccia is dissolutional. That is when the original clast size is eroded by fluid introduced later in the outcrop.

Acknowledgements

This work is supported by the DAAD: German Academic Exchange Service (DAAD), Section ST32, 2020/21(57507871) Personal ref. no. 91731924.

References

Altherr R., Holl A., Hegner E., Langer C. & Kreuzer, H. (2000). High-potassium, calc-alkaline I-type plutonism in the European Variscides: northern Vosges (France) and northern Schwarzwald (Germany). Lithos 50:51–73

Aranburu, A., Fernández-Mendiola, P. A., López-Horgue, M. & García Mondéjar, J. (2002). Syntectonic hydrothermal calcite in a faulted carbonate platform margin (Albian of Jorrios, northern Spain). Sedimentology, 49, 875–890.

Baatartsogt, B., Schwinn, G., Wagner, T., Taubald, H., Beitter, T. & Markl, G. (2007). Contrasting paleofluid systems in the continental basement: a fluid inclusion and stable isotope study of hydrothermal vein mineralization, Schwarzwald district, Germany. Geofluids, 7, 123-147.

Barnett, W. (2004). Subsidence breccias in kimberlite pipes: an application of fractal analysis. Lithos 76, 299–316.

Bliedtner, M. & Martin, M. (1986). Erz- und Minerallagerstätten des Mittleren Schwarzwaldes. LGRB, Freiburg, Germany.

Bons, P. D., Cao, D., De Riese, T., González-Esvertit, E., Koehn, D., Naaman, I., Sachau, T., Tian, H., & Gomez-Rivas, E. (2022). A review of natural hydrofractures in rocks. Geological Magazine, 159(11–12), 1952–1977. https://doi.org/10.1017/S0016756822001042

Bons, P. D. (2001). The formation of large quartz veins by rapid ascent of fluids in mobile hydrofractures. Tectonophys. 336, 1-17.

Bons, P. D., & Van Milligen, B. P. (2001). A new experiment to model self-organized critical transport and accumulation of melt and hydrocarbons from their source rocks. Geology 29, 919-922.

Bons, P. D., Fusswinkel, T., Gomez-Rivas, E., Markl, G., Wagner, T. & Walter, B. (2014). Fluid mixing from below in unconformity-related hydrothermal ore deposits. Geology 42, 1035-1038, doi: 10.1130/G35708.1.

Brittain, H. G. (2001). Particle-size distribution part 1, representation of particle shape, size, and distribution. Pharmaceutical Technology 25, 38–45.

Cámara, P. (1997). The Basque Cantabrian Basin's Mesozoic tectono-sedimentary evolution. Mém. Soc. Geol. France, 171, 187–192.

Cobbold, P. R., & Rodrigues, N. (2007). Seepage forces, important factors in the formation of horizontal hydraulic fractures and bedding-parallel fibrous veins ('beef' and 'cone-in-cone'). *Geofluids*, *7*(3), 313–322. https://doi.org/10.1111/j.1468-8123.2007.00183.x

Courtney-Davies, L., Ciobanu, C. L., Verdugo-Ihl, M. R., Cook, N. J., Ehrig, K. J., Wade, B. P., Zhu, Z.-Y., & Kamenetsky, V. S. (2020). ~1760 Ma magnetite-bearing protoliths in the Olympic Dam deposit, South Australia: Implications for ore genesis and regional

metallogeny. Ore Geology Reviews, 118, 103337. https://doi.org/10.1016/j.oregeorev.2020.103337

Cox, S. F. (2005). Coupling between Deformation, Fluid Pressures, and Fluid Flow in Ore-Producing Hydrothermal Systems at Depth in the Crust. In J. W. Hedenquist, J. F. H. Thompson, R. J. Goldfarb, & J. P. Richards (Eds.), One Hundredth Anniversary Volume (p. 0). Society of Economic Geologists. https://doi.org/10.5382/AV100.04

Curnelle, R. (1983). Evolution structuro-sédimentaire du Trias et de l'Infra-Lias d'Aquitaine. Bull. Centres Rech. Explor. Prod. Elf-Aquit., 7, 69–99.

Davies, G. R. & Smith, L. B., Jr. (2006). Structurally controlled hydrothermal dolomite reservoir facies: an overview. AAPG Bull., 90, 1641–1690

Fisher, R.V. (1958). Definition of volcanic breccia. Geol. Soc. Am. Bull. 69, 1071-1073.

Fisher, R.V. (1960). Classification of volcanic breccias. Bull. Geol. Soc. Am. 71, 973-982.

Friedman, G. M. (1997). Dissolution-collapse breccias and paleokarst resulting from dissolution of evaporite rocks, especially sulphates. Carbonates and Evaporites, *12*(1), 53–63. https://doi.org/10.1007/BF03175802

Fyfe, W. S., Price, N. J. & Thompson, A. B. (1978). Fluids in the Earth's Crust. (Developments in Geo- chemistry, 1) Elsevier, Amsterdam, 383 pp.

García-Mondéjar, J., Agirrezabala, L. M., Aranburu, A., Fernández, P. A., Gómez-Pérez, I., López-Horgue, M. & Rosales, I. (1996). Aptian-Albian Tectonic pattern of the Basque-Cantabrian Basin (northern Spain). Geol. J., 3, 13– 45.

García-Mondéjar, J., López-Horgue, M.A., Aranburu, A. & Fernández-Mendiola, P. A. (2005). Pulsating subsidence during a rift episode: stratigraphic and tectonic consequences (Aptian–Albian, northern Spain). Terra Nova, 17, 517–525.

Geyer, O. F. & Gwinner, M. P. (2011). Geologie von Baden-Württemberg. – 5., völlig neu bearbeitete Auflage. Schweizerbartsche Verlagsbuchhandlung (Nägele u. Obermüller), Stuttgart, p. 627

Geyer, O. F. & Gwinner, M. P. (1986). Geologie von Baden-Württemberg. Schweizerbart, Stuttgart, Germany.

Hann, H. P., Chen, F., Zedler, H., Frisch, W. & Loeschke J. (2003). The Rand Granite in the southern Schwarzwald and its geodynamic significance in the Variscan belt of SW Germany. Intern J Earth Sci 92: 821–842

Hubbert, M. K. & Willis, D. G. (1957). Mechanics of Hydraulic Fracturing. Transactions of Society of Petroleum Engineers of AIME, 210, 153-163.

Hubbert, M. K. (1951). Mechanical basis for certain familiar geologic structures. Geological Society of America Bulletin 62, 355–72.

Immenhauser, A., Schlager, W., Burns, S. J., Scott, R.W., Geel, T., Lehmann, J., Van Der Gaast, S. & Bolder- Schrijver, L. J. A. (1999). Late Aptian to Late Albian sea-level fluctuations constrained by geochemical and biological evidence (Nahr Umr Fm, Oman). J. Sed. Res., 69, 434–446.

Jackson, J. A. (1997). Glossary of geology, 4th ed.: American Geological Institute, Alexandria, Virginia, 769 p.

Jébrak, M. (1997). Hydrothermal breccias in vein-type ore deposits: A review of mechanisms, morphology and size distribution. Elsevier Science B.V.

Kalt, A., Altherr, R. & Hanel, M. (2000). The Variscan basement of the Schwarzwald. Eur. J. Mineral. Bh. 12, 1–43.

Keulen, N., Heilbronner, R., Stünitz, H., Boullier, A-M. & Ito, H. (2007). Grain size distribution of fault rocks: a comparison between experimentally and naturally deformed granitoids. J Struct Geol 29:1282–1300

Kolodny, Y., Chaussidon, M. & Katz, A. (2005). Geochemistry of a chert breccia. Geochem. Cosmochim. Acta 69 (2), 427-439.

Laznicka, P. (1988). Breccias and Coarse Fragmentites: Petrology, Environments, Associations, Ores. Elsevier Science Ltd.

López-Horgue, M. A., Iriarte, E., Schroder, S., Fernandez-Mendiola, P. A., Caline, B., Corneyllie, H., Frémont, J., Sudrie, M. & Zerti, S. (2010). Structurally controlled hydrothermal dolomites in Albian carbonates of the Aséon valley, Basque Cantabrian Basin, Northern Spain. Mar. Petrol. Geol., 27, 1069–1092

Lorilleux, G., Jébrak M., Cuney, M. & Baudemont, D. (2002). Polyphase hydrothermal breccias associated with unconformity-related uranium mineralization (Canada): from fractal analysis to structural significance. J Struct Geol 24:323–338

Markl, G., von Blanckenburg, F. & Wagner, T. (2006). Iron isotope fractionation during hydrothermal ore deposition and alteration. Geochimica et Cosmochimica Acta, 70, 3011-3030.

Marone, C. & Scholz, C. H. (1989). Particle-size distribution and microstructures within simulated fault gouge. J Struct Geol 11:799814

Marshall, L. J., & Oliver, N. H. S. (2006). Monitoring fluid chemistry in iron oxide–copper–gold-related metasomatic processes, eastern Mt Isa Block, Australia. Geofluids, 6, 45–66.

Martín-Chivelet, J., Berastegui, X., Rosales, I., Vilas, L., Vera, J. A., Caus, E., Gráfe, K., Mas, R., Puig, C., Segura, M., Robles, S., Floquet, M., Quesada, S., Ruiz-Ortiz, P. A., Fregenal Martinez, M. A., Salas, R., Arias, C., Garcia, A., Martin-Algarra, A., Melendez, M. N., Chacon, B., Molina, J. M., Sanz., J. L., Castro, J. M., Garcia-Hernandez, M., Careneas, B., Garcia Hidalgo, J., Gil, J. & Ortega, F. (2002). Cretaceous. In: The Geology of Spain (Eds W. Gibbons and M.T. Moreno), pp. 255–292. Geological Society of London, London.

McKibbin, R. (2005). Modelling heat and mass transport processes in geothermal systems. Porous media, 545.

Metz, R., Richter, M. & Schürenberg, H. (1957). Die Blei-Zink-Erzgänge des Schwarzwaldes. Geologisches Jahrbuch, Bh. 29, 277 pp.

Middleton, G. V. (1961). Evaporite solution breccias from the Mississippian of southwest Montana. J. Sediment. Petrol. 31, 189-195.

Mitcham, T. W. (1974). "Origin of breccia pipes". American Journal of Science. **69** (3): 412–413.

Otsuki, K. (1998). An empirical evolution law of fractal size frequency of fault population and its similarity law. Geophysical Research Letters, *25*(5), 671–674. https://doi.org/10.1029/98GL00380

Perfect, E. (1997). Fractal models for the fragmentation of rocks and soils: a review. Eng Geol 48:185–198

Pfaff, K., Romer, R. L. & Markl, G. (2009a). U-Pb ages of ferberite, chalcedony, agate, U-mica and pitchblende: constraints on the mineralization history of the Schwarzwald ore district. European Journal o Mineralogy, 21, 817-836.

Phillips, W. J. (1972). Hydraulic fracturing and mineralization. J. Geol. Soc. London, 128, 337–359.

Rasband, W. S. (1997-2021). ImageJ. U.S. National Institutes of Health, Bethesda, Maryland, USA. https://imagej.nih.gov/ij/.

Rat, P. (1988). The Basque - Cantabrian Basin between the Iberian and European plates: some facts but still many problems. Rev. Soc. Geol. Esp., 1, 327–348.

Reimold, W. U., Hansen, B. K., Jacob, J., Artemieva, N. A., Wünnemann, K. & Meyer, C. (2012). Petrography of the impact breccias of the Enkingen (SUBO 18) drill core, southern Ries crater, Germany: new estimate of impact melt volume. Geol. Soc. Am. Bull. 124 (1-2), 104-132.

Reimold, W. U. (1998). Exogenic and endogenic breccias: a discussion of major problematic. Earth Sci. Rev. 43, 25-47.

Reynolds, S. H. (1928). Breccias. Geological Magazine, 65(3), 97–107. https://doi.org/10.1017/S0016756800037614

Royer, J. J. (2014). Hydraulic Fracturing in Transverse Isotropic Media - A Theoretical Framework. ECMOR XIV - 14th European Conference on the Mathematics of Oil Recovery, Catania, Sicily, Italy. https://doi.org/10.3997/2214-4609.20141885

Rupf, I. & Nitsch, E. (2008). Das Geologische Landesmodell von Baden-Württemberg: Datengrundlagen, technische Umsetzung und erste geologische Ergebnisse. Landesamt für Geologie, Rohstoffe und Bergbau Baden-Württemberg. LGRB-Information 21:1–82

Sachau, T., Bons, P. D. & Gomez-Rivas, E. (2015). Transport efficiency and dynamics of hydraulic fracture networks. Frontiers in Physics, section Interdisciplinary Physics, special issue on "Flow and Transformations in Porous Media". doi:10.3389/fphy.2015.00063.

Sammis, C. G. & Biegel, R. L. (1986). A self-similar model for the kinematics of gouge deformation. AGU fall meeting. Eos Trans.67 (44), 1187.

Scholz, C. H. (1990). The Mechanics of Earthquakes and Faulting. Cambridge Univ. Press, p. 439.

Schwinn, G. & Markl, G. (2005). REE systematics in hydrothermal fluorite. Chemical Geology, 216, 225_248.

Schwinn, G., Wagner, T., Baatartsogt, B., & Markl, G. (2006). Quantification of mixing processes in ore-forming hydrothermal systems by combination of stable isotope and fluid inclusion analyses: Geochimica et Cosmochimica Acta, v. 70, p. 965–982.

Secor, D. T. (1965). Role of fluid pressure in jointing. American Journal of Science. 263, 633–46

Secor, D. T., & Pollard, D. D. (1975). On the stability of open hydraulic fractures in the Earth's crust. Geophysical Research Letters 2, 510 – 5013

Shukla, M. K., & Sharma, A. (2018). A brief review on breccia: It's contrasting origin and diagnostic signatures. Solid Earth Sciences, *3*(2), 50–59. https://doi.org/10.1016/j.sesci.2018.03.001

Sibuet, J. C., Srivastava, S. P., & Spakman, W. (2004). Pyrenean orogeny and plate kinematics. Journal of Geophysical Research 109, B08104.

Stanton, R. J. (1966). The solution brecciation process: Geological Society of America Bulletin, v, 77, p. 843-848.

Staude, S., Bons, P. D. & Markl, G. (2009). Hydrothermal vein formation by extension-driven dewatering of the middle crust: An example from SW Germany. Earth Planet. Sci. Letts 286, 387-395.

Staude, S., Mordhorst, T., Nau, S., Pfaff, K., Brügmann, G., Jacob, D.E., & Markl, G. (2012). Hydrothermal carbonates of the Schwarzwald ore district, southwestern Germany: Carbon source and conditions of formation using $\delta^{18}O$, $\delta^{13}C$, $^{87}Sr/^{86}Sr$, and fluid inclusions: Canadian Mineralogist, v. 50, p. 1401–1434, doi: 10.3749/canmin.50.5.1401.

Staude, S., Wagner, T. & Markl, G. (2007). Mineralogy, mineral compositions and fluid evolution at the Wenzel hydrothermal deposit, Southern Germany: Implications for the formation of Kongsberg-type silver deposits. The Canadian Mineralogist, 45, 1147-1176.

Swennen, R., Dewit, J., Fierens, E., Muchez, P., Shah, M., Nader, F., & Hunt, D. (2012). Multiple dolomitization events along the Pozalagua Fault (Pozalagua Quarry, Basque–Cantabrian Basin, Northern Spain), Journal of Int. Ass. of Sed. Sedimentology (2012) 59, 1345–1374.

Taylor, R. G. & Pollard, P. J. (1993). Mineralized Breccia Systems: Methods of Recognition and Interpretation. Economic Geology Res. Unit, Key Centre in Economic Geology, James Cook University of North Queensland, Townsville. Contrib. 46, 3l pp.

Terzaghi, K. (1943). Theoretical Soil Mechanics. New York and London: John Wiley and Sons, 510 pp

Todt, W. (1976). Zirkon U/Pb-Alter des Malsburg-Granits vom Südschwarzwald. N Jb Mineral Monatsh 12:532–544

Walter, B. F., Burisch, M., & Markl, G. (2016). The long-term chemical evolution of continental basement brines - a field study from the Schwarzwald, SW Germany. Geofluids 16:604–623

Weertman, J. (1971). Velocity at which liquid-filled cracks move in the Earth's crust or in glaciers: Journal of Geophysical Research, v. 76, p. 8544–8553, doi:10.1029/JB076i035p08544.

Weisheit, A., Bons, P. D., & Elburg, M. A. (2013a). Long-lived crustal-scale fluid flow: the hydrothermal mega-breccia of Hidden Valley, Mt. Painter Inlier, South Australia. Int J Earth Sci (Geol Rundsch) (2013) 102:1219–1236

Wetzel, A., Allenbach, R. & Allia, V. (2003). Reactivated basement structures affecting the sedimentary facies in a tectonic 'quiescent' epicontinental basin: an example from the NW Switzerland. Sedimentary Geology, 157, 153-172.

Wright, A. E. & Bowes, D. R. (1963). Classification of volcanic breccias: A discussion. *GSA Bulletin*, *74*(1), 79–86. https://doi.org/10.1130/00167606(1963)74[79:COVBAD]2.0.CO;2

Yilmaz, P. O., Norton, I. O., Leary, D. & Chuchla, R. J. (1996). Tectonic evolution and paleogeography of Europe. In: Peri-Tethys Memoir 2: Structure and Prospects of Alpine Basins and Forelands (Me´m. Natn. Hist. Nat., 170, 47–60).

Ziegler, P. A. (1990). Geological Atlas of Western and Central Europe. Shell International Petroleum, Maatschappij B.V., Den Haag.

Chapter 3

A numerical simulation of sourced fluids, flow and fracture dynamics within the crust

Naaman Isaac[1*], Bons Paul D.[1]

[1]Department of Geosciences, Eberhard-Karls University Tübingen, Schnarrenbergstr. 94-96, 72076 Tübingen, Germany

*Corresponding email: isaac.naaman@uni-tuebingen.de

Abstract

Fluids ($H_2O \pm CO_2$) that flow through the Earth's crust are major transporters of dissolved elements, such as Mg, Na, Ca, Fe, Ba, as well as more precious elements, such as Pb, Zn, Cu, Co, Ag and Au. Fluids can also carry significant amounts of heat. Hydrothermal fluids are, by definition, fluids that are hotter than the surrounding rocks and are associated with many ore deposits, for example the huge Olympic Dam U-bearing iron oxide-copper-gold (IOCG) deposit in South Australia and the abundant small deposits in the German Schwarzwald. Hydrothermal fluids are furthermore often involved in the process of dolomitization. Hydrothermal dolomites are often associated with Mississippi Valley-type hydrothermal Pb-Zn deposits.

This research discusses the flow regime, fracture initiation and growth in rocks and place emphasis on fluid-assisted fracturing and suggest ways in estimating the amount of fluid (pressure/energy) needed to cause or initiate a hydrofracture and fluid-assisted fracture dynamics and estimate sources of fluid (hydrothermal) that is released at depth by for example dehydration reactions, exhumation or changes in the tectonic stress field. We further show that fracture growth varies significantly and that deep sourced fluid mixing is possible with well-connected fractures. Finally, as the formation of hydrofractures can dictate local effective permeability, intensive fracturing can lead to brecciation and mineral precipitation at much shallower levels as possible hydrofractures aid in transporting deep sourced fluid to the near surface.

We use numerical modelling of hydrothermal fluid flow in a rigid matrix to simulate hydrothermal fluid transport and fracture growth, which constrains the minimum amount of pressure/energy the ascending fluids must provide. Fractures begin to form (rock failure) at some stage when there is continued increasing fluid pressure. Unstable states that could lead to brecciation at much shallower levels are only reached at high fluid escape rates through large hydrofractures. Fractures and (hydrothermal) fluid transport dynamics may explain the abundance of deep sourced fluid inclusions and hydrofractures in much shallow levels in the subsurface.

1.0 Introduction

Fluids ($H_2O \pm CO_2$) that flow through the Earth's crust are major transporters of dissolved elements, such as Mg, Na, Ca, Fe, Ba, as well as more precious elements, such as Pb, Zn, Cu, Co, Ag and Au. Such fluids can also carry significant amounts of heat (Sharma & Srivastava, 2014, Heinrich & Candela, 2014). When such fluids have a relatively high temperature compared to the surrounding rock, are predominantly aqueous and contain such various dissolved substances (Pirajno, 2013; Morishita, & Hammond, 2024; Skinner, 1979) they are known as hydrothermal fluids. By definition, hydrothermal fluids are fluids that carry heat and are hotter than the surrounding rocks (Norton, 1984; Ague, 2014). Such fluids acquire their heat through known geological processes, mostly by igneous activities and including the heating of groundwater by hot rocks (Pirajno, 2009; Hanson, 1995). When fluids, such as seawater or meteoric water (infiltrating surface water into the crust), come into contact with hot rock near a magma chamber, they are rapidly heated. Again, when fluids percolate deeper into the earth's crust along fractures, faults, or permeable rock layers, they encounter hotter conditions, heating up as they descend (geothermal heating). This is a prevalent, passive mechanism of heating. Metamorphism and convective circulation also serve as sources of heat, as fluids are repeatedly exposed to high temperatures when they circulate within the crust (Pirajno, 2009; Ranalli & Rybach, 2005; Hanson, 1995; Fournier, 1989, Lybach, 1981).

Some importance attached to these hydrothermal fluids are the many ore deposits which formed through fluid flow within the crust, from the huge Olympic Dam U-bearing iron oxide-copper-gold (IOCG) deposit in South Australia to abundant small deposits in the German Black forest (Staude et al. 2009; Pollard, 2006). Hydrothermal fluids are often involved in the process of dolomitization, where calcite in limestones is converted to dolomite (Qaisar et al., 2023; Sibley and Gregg, 1987). Furthermore, a major contribution of geofluids within the subsurface is in the creation of extensional hydrofractures (Spence and Turcotte, 1985; Dahm, 2000; Bons, 2001; Bons et al., 2022). This happens when the elevated fluid pressure (P_f) equals or exceeds the overburden pressure, $P_f \geq \rho_{rock} \cdot g \cdot z$ (i.e. tensional strength of the rock, with ρ_{rock} the average density of the rocks in the column, g the gravitational acceleration, and z the depth), causing fractures to form and propagate (Hubbert and Willis 1957; Sibson, 1981; Bons et al., 2014). Such fractures are termed hydrofractures (see Bons et al., 2022 and the references therein). In the absence of tectonic forces that initiate and grow fractures, (significant) fluid overpressure seems to be the only means to cause and grow fractures within the crust. Such fractures usually start on the micro-scale level and develop with significant dilation by

propagation at the tips (Pollard and Aydin, 1988; Anderson and Anderson, 1995). When fractures grow large enough and connect with each other extensively, breccias may form. They are termed hydrothermal breccias because fluids of such nature have initiated and/or caused their formation (Shukla and Sharma, 2018, Weisheit et al., 2013, Jébrak, 1997).

Over the years, a number of researchers modelled crustal fluid flow and associated dynamics in fracture formation (de Riese et al. 2020, Cao et al., 2018, Kraaijeveld et al., 2013, Vychytil & Horii, 1998). Though flow within the crust is a complex phenomenon even within different geological setting, a simple flow model e.g. sandpile model (Bak et al. 1988), has been used to simulate how flow and fractures occur within a porous media. Given the vast number of different geological environments in which fluids evolve in space, time and physicochemical properties, such a model review is necessary and thus, have seen some adaptation and modification to simulate fluid flow and fracture dynamics within the crust (see de Riese et al. 2020; Bons & van Milligen 2001 and Miller & Nur 2000).

Despite advances made in the knowledge of fluid flow and hydrofracture dynamics within the crust, questions remain: (i) how do large hydrofractures sprout from the base all through to the surface with circulating fluid within the fractured rock column?, (ii) what is the mechanism in fracture dynamics, transport and mixing of deep sourced hydrothermal and meteoric fluids at much shallower levels?, (iii) What induces extensive fracturing to cause brecciation in hydrothermal deposits which suggest a transition in flow and fracture dynamics? (Marshall & Oliver 2006), and (iv) how do permeability and fluid pressure variations affect the development, distribution, and linking of hydrofractures? De Riese et al. (2020) us a modified sandpile model to explore the effect of the relative contributions of Darcian porous flow and flow through hydrofractures on crustal-scale fluid flow. They proposed that this is achieved through varying the fluid pressure diffusivity, as a function of permeability, with a constant fluid flux and assume fluid transport through the crust as a bimodal transport system.

We use simulations analogous to the sandpile model (Bak et al., 1988) to simulate and discuss the flow regime, fracture initiation and growth path in rocks. This model is a build-up on that of de Riese et al. (2020). However, this model set the system to have a variability of flux within the medium contrary to that of de Riese et al. (2020).

This paper highlights fluid-assisted fractures and suggests ways in estimating the amount of fluid pressure/energy necessary to cause or initiate a hydrofracture and fracture dynamics. We further show that fracture growth varies significantly and deep sourced fluid mixing is possible regardless of the level and distribution of the fluid source as hydrofractures aid in transporting

deep sourced fluid to the near surface. Finally, as the formation of hydrofractures can dictate local effective permeability, we present a model that shows that excessive fracturing can lead to brecciation and mineral precipitation at much shallower levels within the crust.

2.0 Crustal fluid Source

Fluids are common within the crust (Ingebritsen and Manning, 2010; Ingebritsen et al., 2006; Ague, 2003; Cathles, 1981; Fyfe et al., 1978). Their presence is evident, for example from hydrothermal reservoirs and ore deposits (Ague and Rudnick, 2003). The main three sources or reservoirs of fluid in deeper levels of the crust are (i) pore fluid, (2) fluid released by devolatilization reactions, and (3) fluid released by igneous activity. Fluid-filled porosity of 0.5-1% may exist down to almost 10 km depth, even in metamorphic/metaigneous rocks, as was observed in the Continental Deep Drilling project (KTB, Emmermann & Lauterjung, 1997). Although the amount of pore fluid in a low-porosity rock volume is limited, fluid circulation may greatly enhance the total flux of fluid passing through rocks (Ague, 2014; Yardley and Bodnar 2014; Ague and Rudnick, 2003; Oliver, 1996). As opposed to this, fluids released by devolatilization of H_2O-bearing minerals or crystalizing magma provide 'single pass' fluid flow events, which significantly reduces the total fluid budget.

Much work has been devoted to determining fluid sources and their (relative) reservoir volumes by considering the "budgets" of major/trace elements, isotopes, halogens, etc. (Yardley and Bodnar, 2014, Ague, 2014, and the references therein). For instance, Staude et al. (2009) estimate the required volume of fluid to produce the Jurassic deposits in the Black Forest (Black forest) at ca ~12 km^3, while modelled calculations showed that ~ 6-12 km^3 could have been released due to decompression. In the Hidden Valley, similarly, Weisheit et al. (2013) suggest that at least ~20 km^3 of fluid is required in the Hidden Valley mega-brecciation in South Australia and discussed the various fluid sources that may have contributed to this volume, such as ~ 8-21 km^3 from biotite dehydration and/or ~ 5-10 km^3 by decompression.

2.1 Fluid Flow within the crust

Fluids flow down hydraulic head gradients. When fluids are sourced at depth, they mainly flow upwards. Fluids that ascend from the source cool and decompress during ascent, which may lead to precipitation of minerals. Flow is often controlled by the column's permeability structure and the presence of open pathways, i.e., fractures. There are two basic types of fluid flow:

(i) Fracture or focused flow - fluid move through well-defined fractures, or faults in the crust, where permeability is much higher. Here, flow is typically fast and localized (Fyfe et al, 1978; Cathles, 1990; Ingebritsen & Manning, 2010),

(ii) diffuse flow – advective fluid flow down gradients in hydraulic head controlled by the permeability of the rock according to Darcy's law. That is, flow rate is proportional to the gradients in hydraulic head and the permeability of the material. Darcian flow can be termed 'diffusive', not because the fluid diffuses, but because the evolution of the fluid-pressure field can be described as diffusive. For diffusive or pervasive flow, fluids move slowly through the interconnected pore spaces of rocks.

At depth fluid pressure in the crust increases from hydrostatic to close to lithostatic as the permeability decreases with depth (Ingebritsen & Gleeson, 2015; Ingebritsen & Manning, 2010; Ingebritsen et al., 2006).

2.2 Crustal fluid and hydrofractures

Fluid pressure reduces the effective stresses in rocks (Terzaghi, 1923; Bons et al. 2022) and may therefore enable fractures to form at low or zero differential stress. To create a hydrofracture by fluid pressure only, the fluid pressure must exceed the minimum principal stress and the tensile strength of the rock. But in the absence of fluid pressure, the effective normal stress and the shear stress acting on a plane in the rock must reach the failure criterion to cause a fracture (Hobbs & Ord, 2022; Bons et al, 2022). These fractures begin initially as microcracks that link up or coalesce, creating fractures in a stepwise fashion to facilitate fluid flow (Bons and van Milligen, 2001). Only at shallow depths (up to a few km at the most) can extensional fractures form mainly due to tectonic stresses (Gudmundsson, 2011; Bons et el. 2022). This means that extensional fractures below a few kilometres depth are almost always the result of elevated fluid pressure, i.e., hydrofractures (Cobbold & Rodrigues, 2007; Sibson, 2000a; Gudmundsson, 2011; Bons et el. 2022 and the references therein).

2.2 The interaction between porous flow and hydrofractures

A crucial difference between porosity and fractures as fluid pathways is that open fractures are not permanent structures. Instead, they only form when fluid pressure is sufficiently high and they may close again, either by mechanical closure or by clogging the fracture space with new grown minerals, forming veins (Ramsay 1980; Bons et al., 2012). Opening a fracture suddenly

creates a very high, but local and temporary, permeability. This allows for the transport of a 'batch' of fluid. Bons and van Milligen (2001) invoked the analogy with the sandpile model of Bak et al. (1988) where an avalanche of sand from the pile (a punctual transport event) would be analogous to a fluid transport event through newly opened hydrofractures. Once these hydrofractures have transported the fluid that induced the high fluid pressure, they close. Bons and van Milligen (2001) presented a one-dimensional numerical model and showed that it produced the same rich dynamics as the sandpile model, indicating that the system reaches a self-organised critical (SOC) state. De Riese et al. (2020) extended the model to two dimensions and investigated the transition from pure porous flow towards flows mostly through hydrofractures. This system is analogous to the modified sandpile model of Sánchez et al. (2001). In this sandpile model the local height of the sandpile is modified by diffusion (analogous to porous flow) and avalanches are induced when the local slope reaches a threshold (hydrofracture flow). De Riese et al. (2020) achieved this in a model where fluid was entering at the base of the model at a constant rate (with noise). The resulting fluid pressure would diffuse upwards with a diffusion rate directly related to the permeability of the system. The smaller the permeability, and hence the pressure-diffusion coefficient, the steeper the fluid pressure gradient must be to dissipate the imposed fluid flux. Hydrofractures were induced in the model when the fluid pressure reached the lithostatic pressure, allowing for sudden and rapid transport of fluid. De Riese et al. (2020) explored the full range from porous flow only to hydrofracture flow only by varying the diffusion coefficient, while keeping the imposed fluid flux constant. They found that, at low diffusion coefficient, fractures form ad that their size distribution follows a power law, typical of SOC. These fractures form at the base of the model. Only occasionally would these hydrofractures join up to propagate all the way up through the model, causing a main fluid drainage event. Increasing the diffusion coefficient leads to fewer hydrofractures to form, but bigger drainage events that become regularly spaced or cyclical in time.

The model of de Riese at al. (2020) may not be realistic, as it has a fluid influx from the bottom of the model. In case of fluid release due to devolatization mineral reactions, one may expect fluid to be produced in a certain depth region instead. The effect of fluid input in a depth region is the main topic of the new numerical simulations presented here. We also briefly address the effect of having different diffusion coefficients inside and above the fluid-producing region.

Table 1. List of symbols

Symbol	Unit	Description
A	element	Fracture area
n	-	Exponent in power-law distribution
J_f	$s^{-1}\ m^{-1}$	Fluid Flux
ϕ		porosity
P_{lith}	Pa	Pressure
D	$m^2\ s^{-1}$	Diffusion coefficient for fluid overpressure
P_f	Pa	Fluid Pressure
P_h	Pa	Hydrostatic Pressure
λ		Model dimension/element size
α	Pa^{-1}	Compressibility
t	s	Time
V	m^3	Volume
g	ms^{-1}	Gravitational acceleration
η	Pa·s	Fluid viscosity
κ	m^2	Permeability
ρ_{lith}	Kg/m^3	Rock density
z	m	Depth below the surface
mod (subscript)		Model parameter description
ρ_f	Kg/m^3	Fluid Density
P_{real}	Pa	Real Pressure
J_P	Pa	Pressure flux

3.0 Method

We used the same model as de Riese et al. (2020), but with some modifications. The model simulates a 2-dimensional, vertical section through the crust. The model is divided up in a rectangular grid of 200 x 200 elements of linear size $\lambda \sim 100$m (fig. 1). Each element represents a volume of rocks with a porosity (ϕ) and a rigid matrix. Adding fluid to the pores then increases the fluid pressure, depending on the fluid compressibility (α). Contrary to de Riese at al. (2020), we do not introduce fluid at the base of the model only, but in a fluid-production zone (FPZ), typically all elements in the bottom half of the model. Each time step fluid is added to all elements one by one in the FPZ by raising the fluid pressure. It is then checked if any hydrofractures form because the fluid pressure exceeds the lithostatic pressure. If this is the

case in an element it is set to have a hydrofracture, which can then lead to a cascade of hydrofracture propagation (see below). The propagation continues until either a fracture system reaches the surface (draining all fluid) or when the fluid pressure in all fractured elements is below the lithostatic pressure. Next, the fluid pressure field is adapted by diffusion to simulate Darcy-type fluid flow. Fluid pressure at the Earth's surface, i.e., in the top row of elements is always set to zero after each round of fracture and porous flow, meaning that fluid that reaches the surface is removed from the system.

We present below, a model diagram which shows the derived lithostatic Pressure and fluid pressure to show the level at which fracture are likely to form and grow (failure level within the rock column). That is the level where P_{lith} equals or less the P_f.

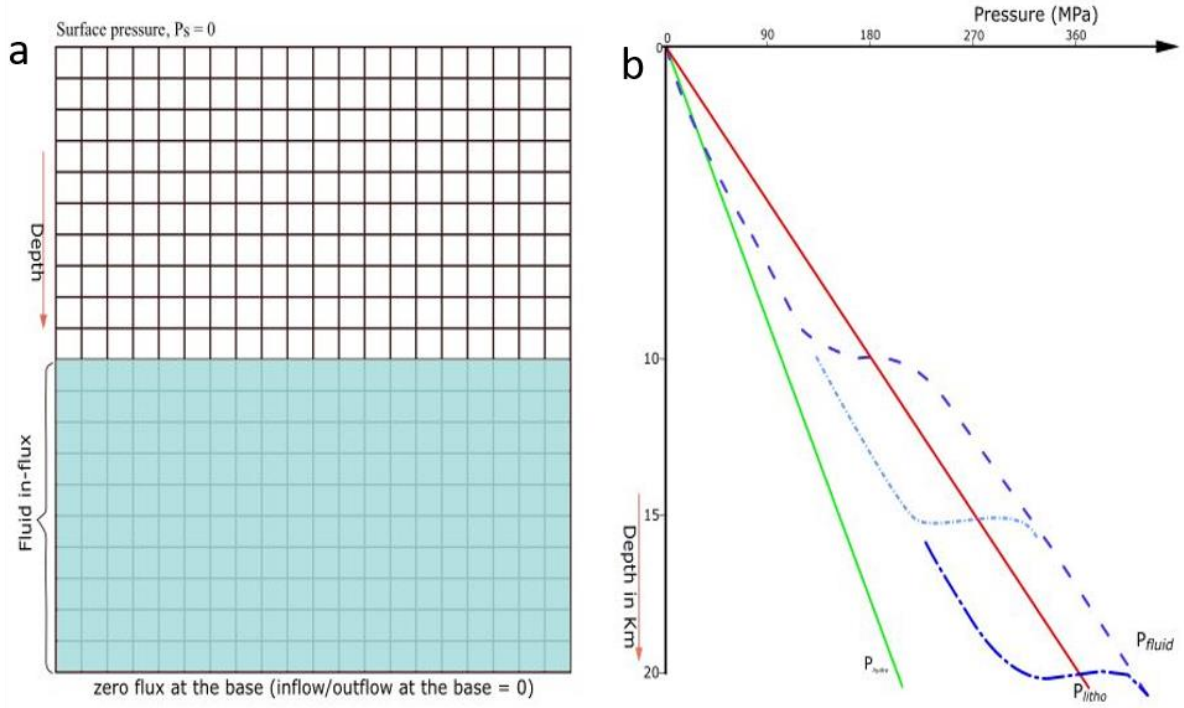

Figure 1. A simplified model diagram of the numerical simulation. The model depicts a grid mesh of *200 × 200* elements in which localized fluid pressure above the hydrostatic fluid pressure is recorded. Fluid influx is set at the mid (half-way) of the model and is simulated by incrementally increasing the pressure in the cells row of the model setup. The top row of the grid is set for the fluid escape i.e. $P_s = 0$. A well detailed flow simulation of the model is presented in de Riese et al (2020). (b) depicts the pressure gradient with increasing depth. Increase in the fluid pressure at the level where $P_f \sim\geq P_{lith}$ results from the level of fluid influx.

3.1 Model setup and scaling

Time step

All fluid that enters the model escapes through to top boundary. The total time-averaged flux above the fluid-production zone (FPZ) is thus equal to the fluid production in that zone. We set this total time-averaged fluid flux at $J_f = 10^{-11}$ m/s after Ingebritsen and Manning (1999). Each time step fluid is entered into the system by increasing the pressure P of cells in the FPZ by a random increment ΔP between 0 and 0.002 model pressure units, i.e., on average $\Delta P = 0.001$. We use a simple constant rock and fluid density of 2800 kg/m^3 and 1000 kg/m^3, respectively. The difference of the lithostatic overpressure and the hydrostatic fluid pressure at the lower boundary of the model at 20 km depth is thus 360 MPa, equivalent to 200 model pressure units. The average ΔP is thus $0.001 \cdot 200/360 = 5.5 \cdot 10^{-4}$ MPa.

The fluid overpressure (P) is thus, tracked and recorded for each element or cell with:

$$P = P_f - P_h \tag{1}$$

Where, P, is defined as the difference between the actual fluid pressure (P_f) and the hydrostatic fluid pressure (P_h). The hydrostatic pressure is set to zero at the top row of the elements and increases with depth z. We assume a fluid viscosity $\eta = 0.001$ Pa·s, although the viscosity of water varies depending on pressure and temperature (Abramson, 2007). The fluid compressibility was set to $\alpha = 2$ GPa (similar to Staude et al., 2009). Porosity ϕ, can vary widely from <1% to around 30% at shallow depth (Liebscher, 2010). As the main focus is on rocks at >10 km depth, we set the porosity at $\phi = 0.01$. In our model, the coefficient of D for the model setup (D_{mod}) is set for the different values for all the simulation. The input model (D_{mod}) values for D (0 – 0.0002) are presented in Table 2.

Adding fluid to rigid pore space increases the fluid density (ρ) as well as the pore pressure according to:

$$\frac{\partial \rho}{\rho \partial P} = -\alpha \tag{2}$$

From this we obtain, using the pore volume of one element ($\phi \cdot \lambda^2$) as reference volume:

$$\Delta P = \alpha \frac{\Delta V}{\phi \lambda^2}, \quad \text{or} \quad \Delta V = \frac{\phi \lambda^2 \Delta P}{\alpha} = \frac{10^{-2} \cdot 10^4 \cdot 5.5 \cdot 10^{-4}}{2000} = 2.75 \cdot 10^{-5}\ \mathrm{m}^3 \tag{3}$$

If the height of the FPZ is 100 elements, and each element is 100 m wide, the total time-averaged flux emanating from the FPZ is $2.75 \cdot 10^{-5}$ m^3 per m^2 and per model time step. it follows

that the model time step is $2.75 \cdot 10^{-5}$ / 10^{-11} = $2.75 \cdot 10^{6}$ s, which is about a month. In complementary simulations with different FPZ-heights, ΔP is adjusted to maintain the same time-averaged fluid flux at the top of the model, and hence the same time step.

Diffusion

In one dimension the fluid flux is described with Darcy's law:

$$J = -\frac{\kappa}{\eta}\frac{\partial P}{\partial z} \tag{4}$$

The flux J in m/s is the velocity of the fluid, or the volume ΔV of fluid travelling through a one m^2 window. It depends on the permeability (κ in m^2) of the rock and the viscosity (η in Pa·s) of the fluid. From Eq. (1) it follows, assuming a constant κ and η, that the rate of change in fluid volume is:

$$\frac{\partial V}{\partial t} = -\frac{\kappa}{\eta}\frac{\partial^2 P}{\partial z^2}, \quad \text{and with Eq. (3):} \qquad \frac{\partial P}{\partial t} = \frac{\kappa\alpha}{\eta\phi}\frac{\partial^2 P}{\partial z^2} = D\frac{\partial^2 P}{\partial z^2} \tag{5}$$

Equation (5) is equivalent to Ficks's second law for diffusion, with D (in m^2/s) the diffusion coefficient for fluid overpressure diffusion. Fluid flow is therefore simulated by diffusing the fluid overpressure with the explicit forward finite-difference method:

$$\left(\frac{\Delta P_{mod}}{\Delta t_{mod}}\right)_{(x,z)} = D_{mod}\left\{4P_{mod(x,z)} - P_{mod(x+1,z)} - P_{mod(x-1,z)} - P_{mod(x,z+1)} - P_{mod(x,z-1)}\right\} \tag{6}$$

The indices x and z refer to the horizontal and vertical direction, respectively, and the subscript 'mod' to model parameters. Equation (6) holds for the case that D_{mod} is constant. The unit of the diffusion coefficient is (length unit)^2/time unit. For the real-world diffusion coefficient D we get:

$$D_{mod} = \frac{100 \cdot 100}{2.75 \cdot 10^{6}} D, \text{ giving} \qquad D = 275 \cdot D_{mod} \tag{7}$$

From Eq. (5) we can now derive the permeability κ in m^2:

$$\frac{\kappa\alpha}{\eta\phi} = D = 275 \cdot D_{mod}, \text{ giving} \qquad \kappa = \frac{275\eta\phi}{\alpha} D_{mod} \tag{8}$$

With the settings of the simulations, $\kappa = 1.38 \cdot 10^{-12}$ m^2 for D_{mod}=1.

In case of a change in diffusion coefficient between two elements, we need to use an effective diffusion coefficient D_{eff}. We consider two adjacent elements with positions x and x+1,

respectively. We assume that D_x applies from x-1/2 to x+1/2, and D_{x+1} from x+1/2 to x+3/2. From Fick's first law, and that the flux J is constant between positions x and x+1, it follows that:

$$P_{x+1} = P_x - \frac{J}{D_{eff}} = C_x - \frac{J}{2D_x} - \frac{J}{2D_{x+1}} \rightarrow \frac{1}{D_{eff}} = \frac{1}{2D_x} + \frac{1}{2D_{x+1}} \Leftrightarrow D_{eff} = 2\left(\frac{1}{D_x} + \frac{1}{D_{x+1}}\right)^{-1} \quad (9)$$

To calculate the change in pressure for one time step, we now add the fluxes into and out of the central elements with the effective diffusion coefficients.

3.2 Hydrofractures

As stated earlier, the model simulates flow in a form of diffusional flow and fracture flow. Using the pressure diffusion equation (5), fluid flow is implicitly modelled by tracking the evolution of *P*. The simulation runs for a duration (endtime = 500000) for all coefficients of *D*, updating the grid at each timestep. The model set the system to have a variability of flux within the medium and assume that fluid is set in bottom half-way of the model. An avalanche (fracture) initiate and propagate when a failure criterion is reached. It is assumed that flow through a fracture is fast enough so that pressures within it are equalised effectively instantaneously. The main loop consists of adding fluid randomly and letting the pressures diffuse over time. Fluid diffuses between neighbouring elements. When *P* exceeds a critical threshold, the system then evolves towards a state where an avalanche (fracture) occurs - the time and size (number of broken elements) of the cluster is recorded. Fluid the flows rapidly (avalanche-like behaviour).

The basic loop in the simulation follows that: An element/cell is randomly selected in bottom half and model pressure in that element is increased by ΔP_{mod} =0.001(on average). If *P* in an element increases ($P > P_{lith}$ in any element), the system breaks that element and selects one random direct neighbour and breaks that one too. Next the *P* in the cluster of the broken elements is equalized, keeping the total amount of fluid inside the cluster constant. This is repeated until no element has a *P* exceeding P_{lith} or one element is in the top row of the model and thus reach the surface. The system will drain the fluid in the cluster if this cluster reaches the surface by setting $P = 0$. This subloop is repeated until either: (i) none of the elements in the cluster reaches the failure criterion, (i.e. no avalanche) or (ii) the cluster reaches the surface. In an event where the cluster reaches the surface, the pressure in all elements within the cluster is set to zero as any excess fluid is released at the surface. When the cluster does not expand any more, all 'broken' elements are reset to 'not broken' to simulate closure or sealing of the fracture.

3.3 Post-processing

The output data resulting from the simulation are processed using the freeware ImageJ or a spreadsheet. There are five output datasets:

1. Every user-defined interval, the excess fluid pressure field is saved as a 200x200 pixel 8-bit bitmap with grey scales ranging from 0 at the top to a maximum of 200 at the base.
2. A second bitmap records how often an element experiences a hydrofracture event. Every time this happens, the grey value for that element is raised by one. Grey values are reset to zero after the bitmap is saved at the end of the user-defined interval.
3. A list with the mean excess fluid pressure in the model, the total amount of fluid (as excess fluid pressure) added over the time interval, as well as the fluid pressures of elements at 0.2, 0.4, 0.6, 0.7 and 1.0 times the depth along a vertical column through the middle of the model.
4. A list of each hydrofracture event recording the model time step and the element where it started, its depth, the total number of elements involved and the total average fluid pressure in the cluster of elements that constituted one hydrofracture event.
5. The time averaged excess fluid pressure (P_{mod}) for each row of elements in the model, which is used to calculate the effective vertical diffusion coefficient.

Simulations were typically run for 500,000 steps (ca. 44,000 yrs) with save intervals of 25 steps (ca. 2.2 years).

3.4 Simulations

In the main set of simulations, we varied the model diffusion coefficient from 0 to 0.2, keeping all other parameters constant. Fluid input was in the bottom half of the model. Four more simulations were carried out to show the effect of changing the fluid-producing region, which was set to (i) input at the bottom (equivalent to the simulations of de Riese et al. (2020)), and (ii) fluid input throughout the model. For the case of fluid input in the bottom half of the model, we also show the effect of a higher permeability (D_{mod}) in the top half than in the bottom half, and vice versa. All model settings are listed in Table 2.

Table 2. Summary of the modelled Simulations with different D values used in the model. D_{real} and the permeability κ (m^2) are the real in nature. All other parameters were unchanged

Model Dimension	Model D (D_{mod})	D_{real} (m^2s^{-1})	Permeability κ (m^2)	Number of fracture event	Timestep (Δt) in s
$\lambda^2=10^4$	$2.0\cdot10^{-1}$	55	$2.75\cdot10^{-14}$	0	$2.75\cdot10^6$
$\lambda^2=10^4$	$2.0\cdot10^{-2}$	5.5	$2.75\cdot10^{-15}$	46	$2.75\cdot10^6$
$\lambda^2=10^4$	$2.0\cdot10^{-3}$	$5.5\cdot10^{-1}$	$2.75\cdot10^{-16}$	16	$2.75\cdot10^6$
$\lambda^2=10^4$	$2.0\cdot10^{-4}$	$5.5\cdot10^{-2}$	$2.75\cdot10^{-17}$	840	$2.75\cdot10^6$
$\lambda^2=10^4$	0	–	–	741	$2.75\cdot10^6$
	Diff source region				
	Source at bottom				
$\lambda^2=10^4$	$2.0\cdot10^{-3}$	$5.5\cdot10^{-1}$	$2.75\cdot10^{-16}$	87300	$2.75\cdot10^6$
	Whole model sourced				
$\lambda^2=10^4$	$2.0\cdot10^{-3}$	$5.5\cdot10^{-1}$	$2.75\cdot10^{-16}$	411	$2.75\cdot10^6$
	Variable D (D_{mod})				
$\lambda^2=10^4$	top = $2.0\cdot10^{-1}$ bottom = $2.0\cdot10^{-3}$	55 $5.5\cdot10^{-1}$	$2.75\cdot10^{-14}$ $2.75\cdot10^{-16}$	39	$2.75\cdot10^6$
$\lambda^2=10^4$	top = $2.0\cdot10^{-3}$ bottom = $2.0\cdot10^{-1}$	$5.5\cdot10^{-1}$ 55	$2.75\cdot10^{-16}$ $2.75\cdot10^{-14}$	33359	$2.75\cdot10^6$

4.0 Result

The result of the simulations is presented in snapshots, graphs and in table for the modelled pressure and fracture distribution– for all D_{mod} values (0 – 0.2) and also for varying D_{mod} in the top and bottom halves of the medium. The pressure graphs and table for the real D and κ and number of fractured events are also presented. The average pressure in the model shows a saw-tooth pattern (Fig.2a) that shows that pressure builds up and drops when a fracture reaches the surface and drains its contained fluid. Here, fluctuation is at minimum when D is high. This happens in all simulations, except when D_{mod}=0.2, in which case Darcy flow is sufficient to drain the fluid without P_f ever reaching the failure criterion (Fig. 3a). At the initially stage, see Fig. 2a, mean overpressure (P_{mod}) rises to ca ~ 90 (model scale) in the system and consistently builds up and gets to a level where it drops abruptly to ca~ <40 but not to zero, recording the system's first avalanche. This shows the initial transient phase before the system settles to a dynamic steady state. Figure 2a, also shows that (i) the frequency of the average pressure drops

decreases as D_{mod} decreases and (ii) their magnitude increases with increasing D_{mod}. Overall, the time-averaged P_f increases with increasing D_{mod}. This means we have fewer, but larger fractures that reach the surface to drain fluid with increasing D_{mod} (the graph Fig.2a only indicates those fractures that reach the surface to drain fluid. Fractures that do not do so are not visible, because they only redistribute fluid, so do not affect the average P_f).

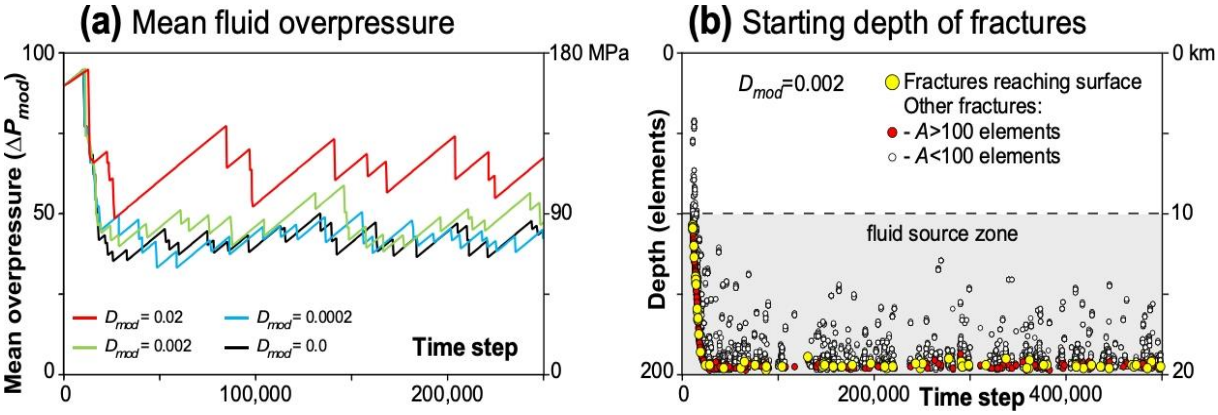

Figure 2. Mean over pressure-time plot as a function of *D*mod. Higher diffusion coefficients result in high pressure build-up with less sporadic pressure fluctuations.

From the simulation, P_f is highest at the base. Without fracturing (Fig.3a. when D_{mod}=0.2) P_f increases linearly with depth. At lower D_{mod}, fractures occur. Within the model set-up the top half of the model is set close to zero P_f. At high D_{mod} (0.02 in Fig.3b) P_f gradients are smooth, except where a fracture that reached the surface has just occurred, draining all its fluid and thus setting P_f =0. With lower D_{mod}, Darcy flow is not sufficient to quickly erase sharp gradients in the fluid pressure. Variations in pressure gradient also happen when D is varied in the upper and bottom sections of the medium. For different sourced (fluids) regions and varied coefficient of D_{mod} result in either increase or decrease in fluid overpressure depending on the section where high or low D is introduced Fig.4.

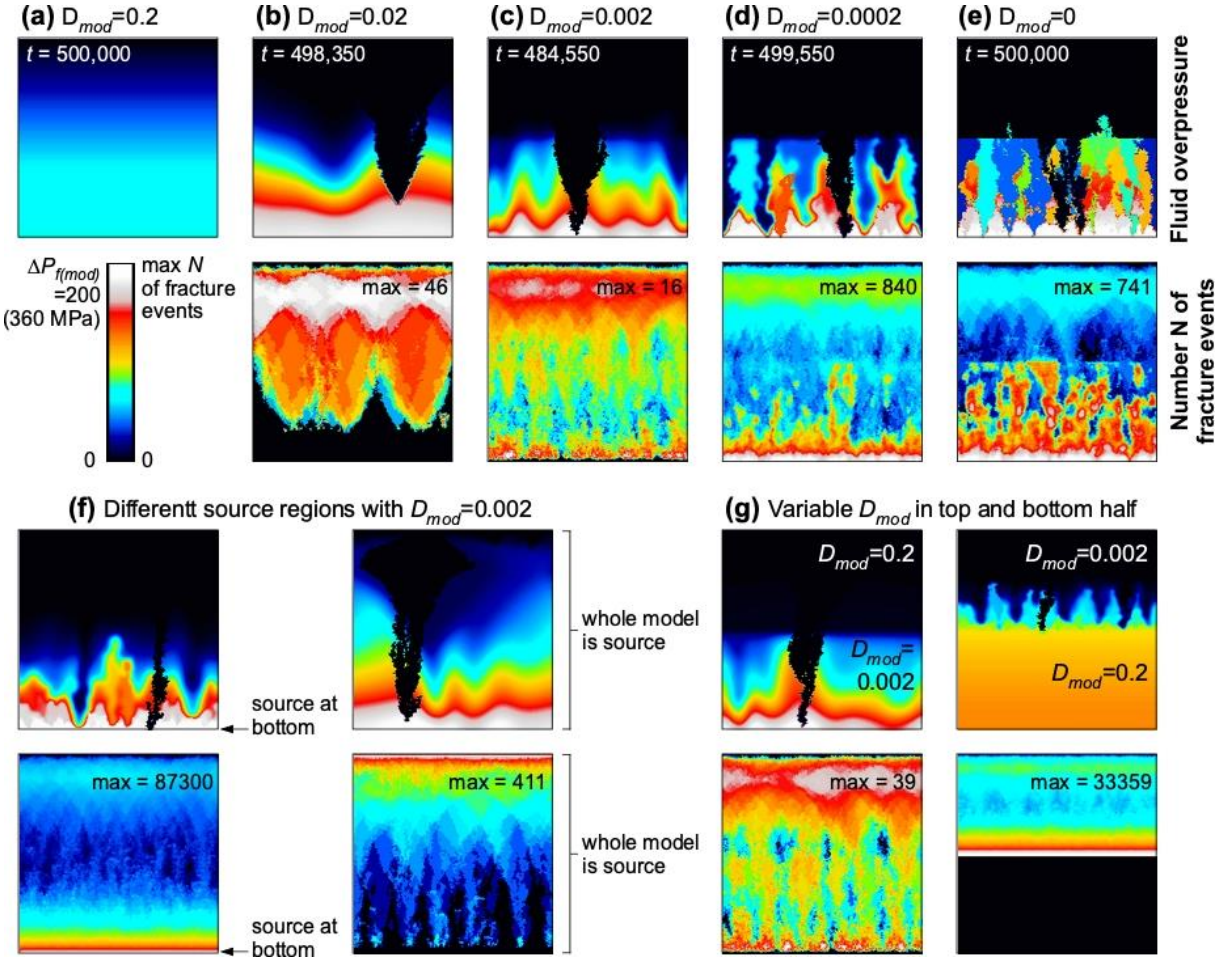

Figure 3. Maps of fluid pressure (P_{mod}) and number of times an element was fractured (from timestep 100,000 to 500,000). The top row shows the fluid overpressure maps for the different simulations and their bottom rows the fracture maps with number of fractured events. Note that the maximum number of fracture events varies greatly.

In Fig.4, result shows the average P_f as a function of depth and the effective time-average diffusion coefficient. From zero (black sections of the snapshots), P_f increases to ca ~180 MPa at depth ~10 km and continue to increase with depth. Assuming model constant parameters are realised in real world, it would appear that depth controls pressure as average P_f increase steadily to ca ~ 360 MPa at ~20 km Fig.4. At the FPZ average P_f increases suggesting an elevated average fluid pressure.

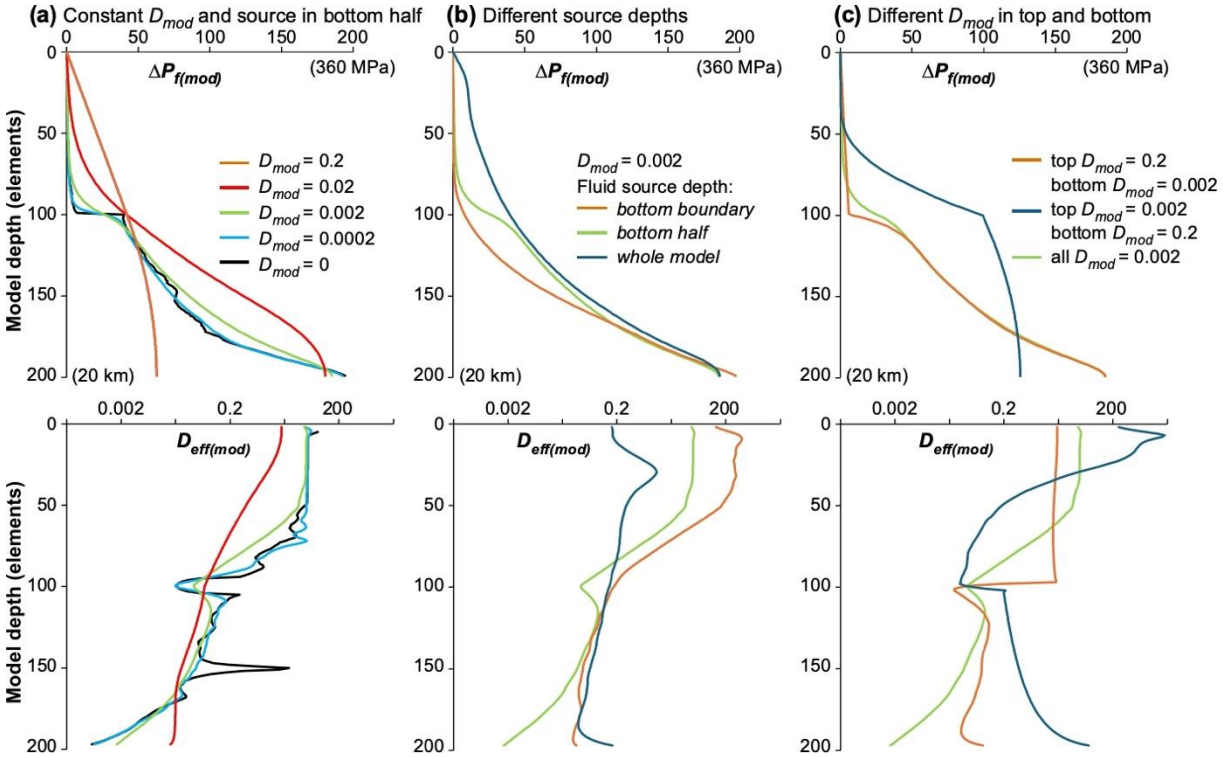

Figure 4. Top row: average fluid overpressure as a function of depth between timestep 50,000 and 500,000. Bottom row: Effective time-averaged diffusion coefficient ($D_{eff(mod)}$).

Again, the effective diffusion-depth curve is smoother (Fig.4a) with high D_{mod} and fluctuate with decreasing D_{mod}. These spikes in effective D may have resulted when fracture events are recorded. However, the trend changes when the fluid source and D_{mod} is varied within the system – top and bottom half (Fig.4b/c). The results indicate that the linear pressure profile will decrease in the case of diffusional transport. Therefore, with high D, pressure peaks become minimal and would not make hydrofractures. D_{mod}=0.2 in (Fig. 4a) shows no abrupt change in pressure gradient at the level of the FPZ though continues to increase steadily. Apart from the highest D_{mod} =0.2, Other D_{mod} respond differently in gradient at the level of the FPZ. Different D_{mod} at the top and bottom halves (D_{mod} =0.002 and 0.2) Fig.4c show an increasing pressure gradient with depth however at decreasing rate with high D at the bottom half and increases at an increasing rate with high D at the top respectively. The opposite happens when top section has higher D_{mod} and low D_{mod} at the bottom half.

Result from the simulation on the fracture frequency of size distribution is presented in Fig. 5, with fractured events with the corresponding D_{mod} showing in Fig.3. The simulation show that fractures mostly form at the bottom and propagate upward from the level of the sourced fluid (Fig. 2b). The number of fractures varies with different D_{mod} (Fig.3). With an increasing D, the

hydrofracture frequency decreases (Fig. 3/5), this includes both large hydrofractures that reach the surface and those small fractures that do not. This also is the case with size of fractures that reach the surface (Fig. 5). At $D_{mod}=2.0\cdot10^{-4}$ (except when D is varied in the system, Fig.3g) the model creates more fractures that are mostly (small fractures) confined to the bottom of the crustal column. That is, fluid move through well-defined fractures. Thus, large bursts of fluid are eminent and may reach all the way to the top half of the model. Fractures are created predominantly within the fluid production zone Fig.2b. These fractures w.r.t our simulations begin at about ~10 km depth Fig.2b. Fractures that do not reach the surface follows a power-law distribution with an average power-law exponent of ~3. These fractures that do not reach the surface are confined to the bottom half of the model. Few large fractures get through to the top half and tends to drain the fluid from the medium.

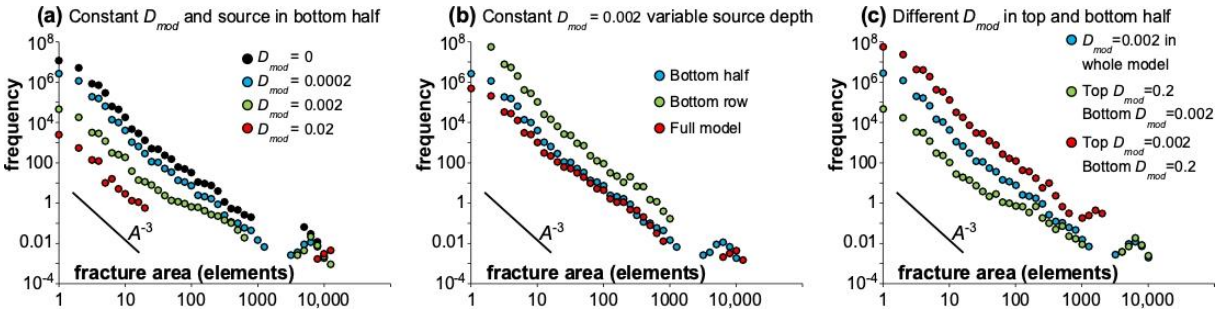

Figure 5. Frequencies of fractures as a function of their area in elements. Only fractures formed between timestep 50,000 and 500,000 are shown here to exclude the initial transient phase before the system settles to a dynamic steady state. Plots shows that section of the size (area) distribution follows a power law.

5.0 Discussion

In a crustal column where there is high P_f, fractures may form and or advance an existing fracture (Bons et al., 2022). This increase in fluid overpressure results from injection of fluid in a crustal column so that the fluid pressure within the column would be higher than its surroundings. This overpressure is set to fall when the permeability increases due to fractures. Our simulation suggests that, with time, after when these fractures (hydro) form, the P_f falls. From the onset, these hydrofractures may not necessarily be large but may coalesce over time and that they may later appear as one large fracture from a burst, (see Fig.3).

From the simulation(s), the initial mean overpressure rises in the system until a fracture (probably large) is realised and then the pressure significantly falls but not to zero (Fig.2a). The

first events of break may be considered 'ballistic' such that fracturing is abrupt considering the geological time scale. This may be due to the system's gradual build-up of pressure until high enough to fracture. After the fracturing events, the system reorganises (self-organised) at some stage when there is continued increase fluid injection which eventually raises the pressure again. With time, the whole system gets to critical state and the process is reactivated. This means that most of these hydrofractures have resulted at much earlier stage during the whole dynamic process. Again, burst events in the system are sporadic considering how these fractures network develop over time. High incidence of fluctuations therefore, result from low diffusion coefficient, i.e., low permeability with less fractures however few large fractures that could drain the fluids.

The average fluid overpressure in the system falls with time when fractures begin to form. With increasing *D*, the hydrofracture frequency will also decrease (Fig. 3; table 2). Therefore, for hydrofractures to continue to form, the system must not be too permeable to hinder the build-up of the fluid overpressure to be high enough to cause fractures. In Fig. 2, for example, when κ is raised, fluctuation intensity lessens. Therefore, at a steady state, an elevated or constant fluid pressure within the medium only makes 'one more' fracture with time.

At a high *D* (D_{mod}=0.2), the P_f is not high enough to cause fracture this translate that the medium is permeable and flow is diffusional. Before a fracture event at lower D_{mod}, the average pressure increases linearly (Fig. 3a) from the base to the top of the model until an avalanche occur. Irrespective of where the fluid is introduced in the crustal column, fracture growth always is to be from bottom to the top (considering a simple 2D medium). Thus, fluid released from different levels within the crust get transported upwards when fractures link up, creating ever bigger fractures (Bons and van Milligen, 2001). When hydrofractures begin to form, continued fluid overpressure may sustain the growing hydrofractures, connect and link them. These fractures may transport overpressured fluids from the source that are capable of inducing more fracture propagation and even hydraulic brecciation.

Fracture distributions show that these hydrofractures that reach the surface do not follow power law and their number relative to those that do not get to the surface is small. These small fractures are basically concentrating within and/or near the fluid-production zone, where *P* is higher, and can be associated with hydrothermal breccias when they extensively link-up. Contrary to those large hydrofractures that reach the surface small fractures follow a power-law distribution. In case where only large fractures are considered, the limit may be 'scale-

dependent'. Thus, where different scaling regimes are used, segments/sections of the distributions may show power-law fit.

Considering a variable *D* within the system see Fig.3g, high *D* at the bottom half and low *D* at the top half results in significantly higher number of fractures. Similarly, more hydrofractures also occur where influx to the medium is set at the bottom (de Reise et al., 2020). High permeability at the base means that high pressured fluid from below would attempt ascent through the less permeability layer above. The extent of upward fluid transport therefore depends on the pressure difference, permeability contrast between the two halves (layers), and the thickness of the overlying low-permeability layer. This may explain the fracture dynamics and frequency in low permeability rock column when a less permeable strata with an overpressured fluid column underneath would grow and advance hydrofractures.

When fracture form, permeability increases and subsequently, the pressure falls significantly Fig.3, so that flow would be driven only by fractures. How fast these fluids (hydrothermal) flow within the crust is directly linked to the rate of fracture growth and propagation i.e. these fractures merge and get connected extensively to transport the pressure driven fluids from source to sink (for example, Hickey et al. 2014). Large fractures predominately drain the system and thus reduce P_f in the system. Hypothetically, after the formation of hydrofractures, flow of fluid may occur in batches and move upward very rapidly. As mentioned earlier, hydrofractures that reach the surface are consistently large and greatly controls flow and mixing of fluids at different levels of the medium. At much shallower levels, mixing of high-temperature fluid with meteoric or ambient fluid is possible as porosity is higher at this level. This means that almost all carried elements are precipitated in this region. For example, brecciation at much shallow depth is possible, and as well traps fluids which may then initially be hotter than the ambient temperature and can precipitate dissolved minerals upon cooling of the hot fluid (see Bons et al. 2014).

If fluid, hydrothermal in nature, ascent is fast enough, as due to focused flow, the fluids will not have enough time to cool to ambient temperatures during ascent – suggesting that (i) precipitation (of dissolved minerals) is largely controlled by the frequency and size of the large hydrofractures that carry mineralized fluids to the surface from below (ii) this controls how fluids interact (rummage) with the country rocks and or dissolving minerals to be carried along. In a real geological setting, a possible formation of these hydrothermal deposits, will result from a rapid transport of large volumes of fluids which are under pressure from deep to shallow crustal levels. However, upon reaching such shallower levels within the crust, their pressure is

expected to fall to close to hydrostatic. Though some deposits show textural evidence for focused or fracture flow, diffusional flow at this level is useful in understanding the key aspects of hydrothermal fluid transport, mixing and mineral precipitation (Bons et al., 2014, Ingebritsen et al., 2006). Considering relation in mixing of fluids in hydrothermal ore deposits e.g. that of Hidden Valley hydrothermal breccias and the Black forest district, evidence-based inclusions suggest that flow from deep sources have carried significant minerals to that level where mixing with meteoric water aided their precipitation. These are made possible by focused flow (in batches) when such fractures connect all the way from a km scale to few metres at much shallower levels.

Like many other numerical models, this simulation is geared towards exploring crustal fluid flow and associated fracture dynamics in a real-world geological system. The model gives a simplified analogue to pressure diffusion and flow in the subsurface, however, the limitations cannot be overemphasised. To some extent, this simulation cannot entirely depict the geofluids flow processes within the crust in the sense that, it oversimplifies subsurface processes. It does not consider the scaling dimensions which is 3D in a real-world situation but here presented in 2D. Specific boundary conditions are often unrealistic for real world as boundaries in the subsurface are influenced by geological structures, seals, aquifers, or reservoirs, as well as explicit modelling of fluid properties. Again, the interplay between diffusion, permeability and hydrofractures is complex and depends on various factors, including rock type, pore structure, and to some extent the incidence of pre-existing fractures.

6.0 Conclusion

We use a numerical model that is analogous to the sandpile model to simulate flow in a grid to monitor and record increments in fluid pressure, momentary discharge through the cells to represent the fracture events and fluid (transport) escape. Diffusion and Fluid Production Zone is varied within the system to explore fracture frequency and dynamics as pressure gradient varies with different diffusion coefficients. A high permeability results in few fracturing events as fluid overpressure may never build-up to be high enough to cause extensional failure. At lower permeability, fluid pressure builds up to cause fracture formation, which can locally and temporarily increase permeability and ensuing fluid pressure reduction. With time, the system self-organizes to a critical state where fractures can release fluid at any moment.

Fracture flow subsequently control the fluid transport within the system and large burst of fluids within the crust are controlled mainly by few large hydrofractures that grows all the way to the

top. It appears that regardless of where fluid is introduced within the medium, fractures always appear to grow from bottom (below) to top (surface), bringing deep fluids to the surface.

Large-scaled fluid ascent may explain possible formation of hydrothermal breccias and associated ore deposit at much shallow depth where fracturing is extensive. With time, deep sourced fluid that get to much shallower depth where they can mix with ambient/meteoric fluids. Formation of many hydrothermal ore systems are created through these processes. It appears that a rapidly ascending hydrofractures will tap fluids from all levels of the infiltrated rock column, and as well mix these fluids during ascent.

Acknowledgement

This work is supported by the DAAD: German Academic Exchange Service (DAAD), Section ST32, 2020/21(57507871) Personal ref. no. 91731924.

Supplementary material/data/movie:

References

Abramson, E. H. (2007). Viscosity of water measured to pressures of 6 GPa and temperatures of 300° C. *Physical Review E, 76*(5), 051203. https://doi.org/10.1103/PhysRevE.76.051203

Ague, J. J. (2014). Fluid Flow in the Deep Crust. In Treatise on Geochemistry (pp. 203–247). Elsevier. https://doi.org/10.1016/B978-0-08-095975-7.00306-5

Ague, J. J., & Rudnick, R. L. (2003). Fluid flow in the deep crust. The crust, 3, 195-228.

Ague, J. J. (1998). Simple models of coupled fluid infiltration and redox reactions in the crust. Contributions to Mineralogy and Petrology 132: 180–197.

Anderson, T. L., & Anderson, T. L. (2005). Fracture Mechanics: Fundamentals and Applications, Third Edition (3rd ed.). CRC Press. https://doi.org/10.1201/9781420058215

Bak, P., Tang, C., & Wiesenfeld, K. (1988). "Self-organized criticality," Physical Review A, vol. 38, no. 1, pp. 364–374,

Bakker R. J., & Elburg, M. A. (2006). A magmatic-hydrothermal transition in Arkaroola (Northern Flinders Ranges, South Australia): from diopside-titanite pegmatites to hematite-quartz growth. Contrib Mineral Petrol 152:541–569

Bear, J. (2013). Dynamics of fluids in porous media. Courier Corporation.

Bons, P. D., Cao, D., De Riese, T., González-Esvertit, E., Koehn, D., Naaman, I., Sachau, T., Tian, H., & Gomez-Rivas, E. (2022). A review of natural hydrofractures in rocks. Geological Magazine, 159(11–12), 1952–1977. https://doi.org/10.1017/S0016756822001042

Bons, P.D., Fusswinkel, T., Gomez-Rivas, E., Markl, G., Wagner, T., & Walter, B. (2014). Fluid mixing from below in unconformity-related hydrothermal ore deposits. Geology 42, 1035-1038, https://doi.org/10.1130/G35708.1

Bons, P.D. (2001). The formation of large quartz veins by rapid ascent of fluids in mobile hydrofractures. Tectonophys. 336, 1-17.

Bons, P. D., & Van Milligen, B. P. (2001). A new experiment to model self-organized critical transport and accumulation of melt and hydrocarbons from their source rocks. Geology 29, 919-922.

Cao, T. D., Hussain, F., & Schrefler, B. A. (2018). Porous media fracturing dynamics: Stepwise crack advancement and fluid pressure oscillations. Journal of the Mechanics and Physics of Solids, 111, 113–133. https://doi.org/10.1016/j.jmps.2017.10.014

Cathles, L. M. (1997). Thermal aspects of ore formation. In: Barnes, H. L. (ed.) Geochemistry of Hydrothermal Ore Deposits. 3rd ed., 191-227

Cathles, L. M. (1990). Scales and effects of fluid flow in the upper crust. Science, 248(4953), 323-329. http://doi.org/10.1126/science.248.4953.323

Cathles, L. M. (1981). Fluid Flow and Genesis of Hydrothermal Ore Deposits. In B. J. Skinner (Ed.), Seventy-Fifth Anniversary Volume (p. 0). Economic Geology Publishing Company. https://doi.org/10.5382/AV75.13

Cobbold, P. R., & Rodrigues, N. (2007). Seepage forces, important factors in the formation of horizontal hydraulic fractures and bedding-parallel fibrous veins ("beef" and "cone-in-cone"). Geofluids 7, 313–22.

Cox, S. F. (2010). The application of failure mode diagrams for exploring the roles of fluid pressure and stress states in controlling styles of fracture-controlled permeability enhancement in faults and shear zones. Geofluids, 10, 217-233.

Dahm, T. (2000). On the shape and velocity of fluid-filled fractures in the Earth. Geophysical Journal International 142, 181–92.

de Riese T, Bons PD, Gomez-Rivas E., & Sachau, T. (2020). Interaction between crustal-scale Darcy and hydrofracture fluid transport: a numerical study. Geofluids 2020, 1–14.

Fournier, R. O. (1989). Geochemistry and dynamics of the Yellowstone National Park hydrothermal system. Annual Review of Earth and Planetary Sciences, 17(1), 13-53.

Fyfe, W.S., Price, N. J., & Thompson, A.B. (1978). Fluids in the Earth's Crust: Their Significance in Metamorphic, Tectonic and Chemical Transport, Elsevier, 383 pp.

Gudmundsson, A. (2022). The propagation paths of fluid-driven fractures in layered and faulted rocks. Geological Magazine, 159(11–12), 1978–2001. https://doi.org/10.1017/S0016756822000826

Gudmundsson, A. (2011). Rock Fractures in Geological Processes. Cambridge: Cambridge University Press, 592 pp.

Hanson, R. B. (1995). The hydrodynamics of contact metamorphism. Geological Society of America Bulletin, 107, 595–611.

Heinrich, C. A., & Candela, P. A. (2014). Fluids and Ore Formation in the Earth's Crust. In Treatise on Geochemistry (pp. 1–28). Elsevier. https://doi.org/10.1016/B978-0-08-095975-7.01101-3

Hickey, K. A., Barker, S. L. L., Dipple, G. M., Arehart, G. B., & Donelick, R. A. (2014). The Brevity of Hydrothermal Fluid Flow Revealed by Thermal Halos around Giant Gold Deposits: Implications for Carlin-Type Gold Systems. Economic Geology, 109(5), 1461–1487. https://doi.org/10.2113/econgeo.109.5.1461

Hobbs, B., & Ord, A. (2022). Failure modes in fluid saturated rocks: Deformation processes and mode-switching. Geological Magazine, 159(11–12), 2002–2019. https://doi.org/10.1017/S0016756822000516

Hubbert, M. K., & Willis, D. G. (1957). Mechanics of hydraulic fracturing. Transactions of the American Institute of Mining, Metallurgical and Petroleum Engineers, 210, 153–168.

Ingebritsen, S. E., & Gleeson, T. (2015). Crustal permeability: Introduction to the special issue. Geofluids, 15(1–2), 1–10. https://doi.org/10.1111/gfl.12118

Ingebritsen, S. E., & Appold, M. S. (2012). The Physical Hydrogeology of Ore Deposits. Economic Geology, 107(4), 559–584. https://doi.org/10.2113/econgeo.107.4.559

Ingebritsen, S. E., & Manning, C. E. (2010). Permeability of the continental crust: Dynamic variations inferred from seismicity and metamorphism. Geofluids, 10(1–2), 193–205. https://doi.org/10.1111/j.1468-8123.2010.00278.x

Ingebritsen, S. E., Sanford, W. E., & Neuzil, C. E. (2006). Groundwater in Geologic Processes. Cambridge University Press.

Ingebritsen, S. E., & Manning, C. E. (1999). Geological implications of a permeability-depth curve for the continental crust. Geology, 27(12), 1107. https://doi.org/10.1130/0091-7613(1999)027<1107:GIOAPD>2.3.CO;2

Jébrak, M. (1997). Hydrothermal breccias in vein-type ore deposits: A review of mechanisms, morphology and size distribution. Elsevier Science B.V.

Kraaijeveld, F., Huyghe, J. M., Remmers, J. J. C., & De Borst, R. (2013). Two-Dimensional Mode I Crack Propagation in Saturated Ionized Porous Media Using Partition of Unity Finite Elements. Journal of Applied Mechanics, 80(2), 020907. https://doi.org/10.1115/1.4007904

Liebscher, A. (2010). Aqueous fluids at elevated pressure and temperature. Geofluids, 10(1–2), 3–19. https://doi.org/10.1111/j.1468-8123.2010.00293.x

Marshall, L. J., & Oliver, N. H. S. (2006). Monitoring fluid chemistry in iron oxide-copper-gold-related metasomatic processes, eastern Mt Isa Block, Australia. Geofluids 6, 45-66.

Miller, S. A., & Nur, A. (2000.). Permeability as a toggle switch in fluid-controlled crustal processes. Earth and Planetary Science Letters.

Morishita, Y., & Hammond, N. Q. (2024). Geochemistry and genesis of hydrothermal ore deposits. Minerals. MDPI.

Norton, D. L. (1984). Theory of hydrothermal systems. Annual Review of Earth and Planetary Sciences, Vol. 12, p. 155, 12, 155.

Nunn, J. A. (1994). Free thermal convection beneath intracratonic basins: thermal and subsidence effects. Basin Research, 6(2-3), 115-130.

Oliver, N. H. S. (1996). Review and classification of structural controls on fluid flow during regional metamorphism. *Journal of Metamorphic Geology*, *14*(4), 477–492. https://doi.org/10.1046/j.1525-1314.1996.00347.x

Pirajno, F. (2013). "Hydrothermal Mineral Deposits." In Encyclopaedia of Earth Science (pp. 23-41)

Pirajno, F. (2008). Hydrothermal Processes and Mineral Systems. Springer Science & Business Media.

Pollard, P. J. (2006). An intrusion-related origin for Cu–Au mineralization in iron oxide - copper -gold (IOCG) provinces. Mineralium Deposita, 41(2), 179–187. https://doi.org/10.1007/s00126-006-0054-x

Pollard, D. D., & Aydin, A. (1988). Progress in understanding jointing over the past century. Geological Society of America Bulletin 100, 1181–204.

Qaisar, S., Zhao, X., Khan, S., Khan, I. U., Alam, A., Ul Haq, J., Ahmad, S., & Zhao, X. (2023). Hydrothermal dolomitization in the Devonian Khyber Limestone Peshawar Basin, Pakistan: Evidence from outcrop analogue, petrography, and geochemistry. Carbonates and Evaporites, 38(4), 79. https://doi.org/10.1007/s13146-023-00901-w

Ramsay, J. G. (1980). Shear zone geometry: A review. *Journal of Structural Geology*, *2*(1), 83–99. https://doi.org/10.1016/0191-8141(80)90038-3

Ranalli, G., & Rybach, L. (2005). Heat flow, heat transfer and lithosphere rheology in geothermal areas: Features and examples. Journal of Volcanology and Geothermal Research, 148(1–2), 3–19. https://doi.org/10.1016/j.jvolgeores.2005.04.010

Rybach, L. (1981). Geothermal Systems, Conductive Heat Flow, Geothermal Anomalies in Geothermal Systems: Principles and Case Histories. Wiley, pp. 3-36.

Sandiford, M., Hand, M., & McLaren, S. (1998). High geothermal gradient metamorphism during thermal subsidence. Earth Planet Sci Lett 163:149–165

Sánchez, R., Newman, D. E., & Carreras, B. A. (2001). Mixed SOC diffusive dynamics as a paradigm for transport in fusion devices. *Nuclear Fusion*, *41*(3), 247. https://doi.org/10.1088/0029-5515/41/3/301

Sharma, R., & Srivastava, P. K. (2014). Hydrothermal fluids of magmatic origin. Modelling of magmatic and allied processes, 181-208.

Shukla, M. K., & Sharma, A. (2018). A brief review on breccia: It's contrasting origin and diagnostic signatures. Solid Earth Sciences, 3(2), 50–59. https://doi.org/10.1016/j.sesci.2018.03.001

Sibley, D. F., & Gregg, J. (1987). Classification of dolomite rock textures. SEPM J Sediment Res. https://doi.org/10.1306/212f8cba-2b24-11d7-8648000102c1865d

Sibson, R. H. (2000a). Fluid involvement in normal faulting. Journal of Geodynamics 29, 469–99.

Sibson, R. H. (1996). "Structural permeability of fluid-driven fault-fracture systems." Journal of Structural Geology, 18(8), 1031-1042. https://doi.org/10.1016/0191-8141(96)00032-6

Sibson, R. H. (1981). Fluid flow accompanying faulting: Field evidence and models. Pure and Applied Geophysics, 124(1–2), 159–175. https://doi.org/10.1007/BF00875720

Skinner, B. J. (1979). The many origins of hydrothermal mineral deposits. In: Barnes H L (ed) Geochemistry of hydrothermal ore deposits, 2nd edn. John Wiley & Sons, New York, pp 3–21

Staude, S., Bons, P. D., & Markl, G. (2009). Hydrothermal vein formation by extension-driven dewatering of the middle crust: An example from SW Germany. Earth Planet. Sci. Letts 286, 387-395.

Spence, D. A., & Turcotte, D. L. (1985). Magma-driven propagation of cracks. Journal of Geophysical Research: Solid Earth 90, 575–80.

Terzaghi, K. (1923). Die Berechnung der Durchlässigkeit des Tones aus dem Verlauf der hydromechanischen Spannungserscheinungen. Sitzungsberichte der Kaiserlichen Akademie der Wissenschaften (Wien), Mathematisch-Naturwissenschaftliche Klasse 132, 125–38.

Von Damm, K. L. (2019). Chemistry of Hydrothermal Vent Fluids. In Encyclopaedia of Ocean Sciences (pp. 282–290). Elsevier. https://doi.org/10.1016/B978-0-12-409548-9.10859-0

Vychytil, J., & Horii, H. (1998). Micromechanics-based continuum model for hydraulic fracturing of jointed rock masses during HDR stimulation. Mechanics of Materials, 28(1–4), 123–135. https://doi.org/10.1016/S0167-6636(97)00061-6

Weertman, J. (1971). Velocity at which liquid-filled cracks move in the Earth's crust or in glaciers: Journal of Geophysical Research, v. 76, p. 8544–8553

Weisheit, A., Bons, P. D., Danišík, M. & Elburg, M. A. (2013b). Crustal-scale folding: palaeozoic deformation of the Mt Painter Inlier, South Australia. In Deformation Structure and Processes within the Continental Crust (eds S Llana-Funez, A Marcos and F Bastida), pp. 53–77. Geological Society of London, Special Publication no. 394.

Weisheit, A., Bons, P. D., & Elburg, M. A. (2013a). Long-lived crustal-scale fluid flow: The hydrothermal mega-breccia of Hidden Valley, Mt. Painter Inlier, South Australia. International Journal of Earth Sciences, 102(5), 1219–1236. https://doi.org/10.1007/s00531-013-0875-7

Wong, L. N. Y., Maruvanchery, V., & Liu, G. (2016). Water effects on rock strength and stiffness degradation. Acta Geotechnica, 11(4), 713–737. https://doi.org/10.1007/s11440-015-0407-7

Yardley, B. W. D., & Bodnar, R. J. (2014). Fluids in the Continental Crust. Geochemical Perspectives, 3(1), 1–127. https://doi.org/10.7185/geochempersp.3.1

Yardley, B. W. D. (2009). The role of water in the evolution of the continental crust. Journal of the Geological Society, 166(4), 585–600. https://doi.org/10.1144/0016-76492008-101

Chapter 4

A review of natural hydrofractures in rocks

Paul D. Bons[1,2,*], Dongsheng Cao[2,3,4], Tamara de Riese[2], Eloi González-Esvertit[5], Daniel Koehn[6], **Isaac Naaman**[2], Till Sachau[2], He Tian[2,3,4], Enrique Gomez-Rivas[5]

[1] School of Earth Science and Resources, China University of Geosciences (Beijing), Beijing 100083, China.

[2] Department of Geosciences, Tübingen University, Schnarrenbergstr. 94-96, 72076 Tübingen, Germany

[3] State Key Laboratory of Petroleum Resource and Prospecting in China University of Petroleum, Beijing 102249, China

[4] College of Geoscience, China University of Petroleum, Beijing 102249, China

[5] Departament de Mineralogia, Petrologia i Geologia Aplicada, Facultat de Ciències de la Terra, Universitat de Barcelona. C/Martí i Franquès s/n, Barcelona, 08028, Spain

[6] GeoZentrum Nordbayern, Friedrich-Alexander University of Erlangen-Nuremberg (FAU), Schlossgarten 5, 91054 Erlangen, Germany

*Corresponding author: *paul.bons@uni-tuebingen.de, e.gomez-rivas@ub.edu, daniel.koehn@fau.de*

Abstract

Hydrofractures, or hydraulic fractures, are fractures where a significantly elevated fluid pressure played a role in their formation. Natural hydrofractures are abundant in rocks and are often preserved as magmatic dykes or sills, and mineral-filled fractures or mineral veins. However, we focus on the formation and evolution of non-igneous hydrofractures. Here we review the basic theory of the role of fluid pressure in rock failure, showing that both Terzaghi's and Biot's theories can be reconciled if the appropriate boundary conditions are considered. We next discuss the propagation of hydrofractures after initial failure, where networks of hydrofractures may form or hydrofractures may ascend through the crust as mobile hydrofractures. As fractures can form as a result of both tectonic stresses and an elevated fluid pressure, we address the question on how to ascertain whether a fracture is a hydrofracture. We argue that extensional or dilational fractures that formed below about 2-3 km depth are, under normal circumstances, hydrofractures, but at shallower depth they can be that, but do not need to be. Since veins and breccias are often the products of hydrofractures that are left in the geological record, we discuss these and critically assess which vein structures can, and which do not necessarily indicate hydrofracturing. Hydrofracturing can suddenly and locally change the permeability in a rock by providing new fluid pathways. This can lead to highly dynamic self-organisation of crustal-scale fluid flow.

Keywords: Hydraulic fracturing, Mineral veins, Rock failure, Terzaghi theory, Biot theory, Effective stress, Fluid flow

1. Introduction

Hydraulic fracturing is typically used to improve the permeability of hydrocarbon or geothermal reservoirs by further opening and propagating existing fractures and by creating new fractures to form connected networks as efficient fluid pathways (Montgomery & Smith, 2010). Reservoir stimulation by induced hydraulic fracturing started as early as the 1860s and became standard practice in industry in the late 1940s when the term 'hydraulic fracturing' came in use (Clark, 1949; Krueger, 1973; Montgomery & Smith, 2010; Gehne & Benson, 2019). The basic theory on how fluid pressure affects fracturing was developed simultaneously using the concept of effective stresses (Terzaghi, 1923, 1943; Biot, 1941; see also review of Guerriero & Mazolli, 2021). It was then soon realised that naturally elevated fluid pressures can also induce the formation of hydraulic fractures (Anderson, 1939; Hubbert, 1951; Hubbert and Rubey, 1959, Sibson et al., 1975; Cox et al., 1986; Engelder & Lacazette, 1990). This appears particularly obvious in the case of igneous dykes, *i.e.*, originally magma-filled fractures. With the frozen magma still preserved as the proverbial smoking gun inside the fractures it is clear that the fluid 'magma' caused or at least played a significant role in the formation, opening, and propagation of the fractures. Theory on the formation and propagation of magma-filled fractures rapidly developed from the 1970s (Weertman, 1971; Spence & Turcotte, 1985; Takada, 1990; Rubin, 1995). It is, however, of interest to note that the pioneering paper by Weertman (1971) derived its theory from water-filled crevasses in ice. It is currently widely accepted that fluid pressure must be considered for brittle deformation in fluid-bearing rocks. Although magma-induced hydrofracturing has made a significant impact on hydrofracture theory, we here focus on non-igneous hydrofracturing, by aqueous fluids. A difference with magmas is that aqueous fluids are rarely sourced from a single large volume, such as magma chambers for igneous hydrofractures, and that aqueous fluids do not freeze like a magma, but may leave traces by mineral precipitates or wall rock alterations (see review by Oliver and Bons, 2001). For reviews

that include igneous hydrofractures, the reader is referred to Gudmundsson (2011) and Rivalta et al. (2015).

It was only around 1960 that the term ‘hydrofracture’ as an alternative for ‘hydraulic fracture’ appeared, first in the literature of the former USSR (e.g. Soloyev & Koboleva, 1960). Since then, the term ‘hydrofracture’ became popular in the literature on natural fluid-pressure induced fractures. In the literature related to oil and gas exploration and production, the term ‘hydraulic fracture’ remains mostly used. ‘Fracking’ is as an alternative term for ‘hydraulic fracturing’ that is already in use for at least 60 years (e.g. Rogatz, 1961), but more recently gained negative connotations.

In this paper we provide a review of natural fluid-induced fractures. We first provide definitions of relevant terms in Section 2. In Section 3 we discuss the theory on hydrofracture formation and subsequent propagation. As hydrofractures are fractures formed by elevated fluid pressure (stricter definition discussed below), recognising such fractures is important to potentially infer elevated palaeo-fluid pressures. In Section 4 we therefore address the question of how to recognise a fossil hydrofracture in the geological record. We consider two aspects: first the geological conditions in which fractures can only form when the fluid pressure is elevated and, second, which types of fractures and mineral veins indicate hydrofracturing by their geometry, internal structures or their network properties. As the formation of hydrofractures can change the local effective permeability dramatically, we finally address fluid flow associated with hydrofracturing in Section 5.

Table 1. List of symbols

Symbol	Unit	Description
a		factor incorporating the effect of poroelasticity in Biot-type equations for effective stress
A	m^2	area of a fracture
c	MPa	cohesion
δ_{ij}	-	Kronecker delta
D	m^2/s	diffusion coefficient for fluid overpressure
E	MPa	Young's modulus
ϕ	-	porosity
g	m^2/s	gravitational acceleration
$f_{u/\sigma}(\theta)$		geometrical factor for the displacement (u) and stress ( ) fields as a function of the angle θ theta relative to the long axis of a crack
G	N	total force causing the growth of an extensional fracture
γ	J/m^2	fracture surface energy
Γ	J	total surface energy of a crack
ψ	°	angle of internal friction
K	MPa	bulk modulus
K_c	MPa	fracture toughness
K_i	-	stress intensity factor
L, L_c	m	length of a fracture, critical length
λ	-	pore fluid factor, *i.e.*, the ratio of pore fluid pressure and vertical stress
m	-	power-law exponent for size distribution of breccia clasts
μ	-	coefficient of friction
ν	-	Poisson's ratio
P_f	MPa	Fluid pressure
ΔP_f	MPa	Fluid overpressure: difference between fluid pressure and hydrostatic pressure
P_{hydro}	MPa	Hydrostatic fluid pressure
P_{rock}	MPa	Mean pressure in a volume of rock
P_{solid}	MPa	Mean pressure in the solid phase of a volume of rock
r	m	radius of curvature of crack tip
ρ_f, ρ_{rock}	kg/m^3	density of fluid and rock
S (S_{ij})	MPa	Absolute stress (tensor)
σ (σ_{ij})	MPa	effective stress (tensor)
T	MPa	tensional strength
τ	MPa	shear stress
$U_{e/p/k}$	J	elastic (e), plastic (p) or kinetic (k) energy
W	J	work
z	m	depth below the surface

2. Definitions

In this paper we use the term ‘hydrofracture’, but the reader should bear in mind that, as far as the rock is concerned, it is the same as ‘hydraulic fracture’ as a rock 'does not know' whether the fluid pressure it experiences is natural or human-induced. A ‘fracture’ is a discrete planar

discontinuity in a solid, such as a rock, along which cohesion or continuity across that surface is lost. The process of losing cohesion, *i.e.*, breaking, is called 'failure'. Please note that here we exclude the so-called ductile fractures, which are interpreted to form by the collapse, linkage and coalescence of microvoids and microcracks during creep deformation, i.e., in a rock that dominantly deforms by ductile flow (e.g. Regenauer-Lieb, 1999; Gomez-Rivas & Griera, 2012). Failure ensues when the stress state in the material reaches conditions that the material cannot sustain. Stress components in a porous rock are (i) the mean stress acting on the solid, which is by definition the pressure the solid experiences (P_{solid}; see Table 1 for a list of symbols), (ii) the deviatoric stress tensor, which is the stress tensor minus the solid pressure, and finally (iii) the pressure of the material inside the pores. Here we denote this material in pores with 'fluid', which can be air, gas, oil, liquid, such as an aqueous fluid, or magma. It is assumed that the viscosity of the fluid is so low compared to that of the solid that the differential stress (difference between maximum and minimum stress) in the fluid can usually be considered effectively zero. For a given porosity ϕ, the stress state of the rock $S_{ij}(rock)$ can thus be described as the weighted average of the stress state of the solid $S_{ij}(solid)$ and of the pore fluid, represented by the fluid pressure P_f:

$$S_{ij}\left(rock\right) = f P_f \delta_{ij} + \left(1 - f\right) S_{ij}\left(solid\right), \qquad \text{e} \quad (eq.\ 1)$$

with δ_{ij} the Kronecker delta. The stresses and pressures are averaged over the volume of rock under consideration. Especially stresses inside the solid may vary strongly, for example at grain contacts or at the tips of microfractures. However, pressure in the fluid may also vary, especially when pores are not all connected well.

The 'hydrostatic fluid pressure' (P_{hydro}) is the fluid pressure in a fluid that is at rest and in contact with the Earth's surface. P_{hydro} is the pressure caused by the weight of the water column. For a fluid with a mean density (brackets denote an average) $<\rho_f>$, P_{hydro} at depth z is

$<\rho_f>\cdot g\cdot z$, with g the gravitational acceleration. In the same way, we can define the lithostatic pressure (P_{lith}), which is simply the pressure caused by the weight of the rock column with mean density $<\rho_{rock}>$. For depth z we get: $P_{lith} = <\rho_{rock}>\cdot g\cdot z$. Fluid pressure can be above hydrostatic and is then often referred to as 'overpressure' (e.g., Osborne & Swarbrick, 1997). This may relate to the state of the absolute fluid pressure, for example when Sibson (2003) writes 'overpressures may approach lithostatic values'. In this paper, we, however, prefer to define fluid overpressure (ΔP_f) as the difference between the actual fluid pressure and the hydrostatic fluid pressure: $\Delta P_f = P_f - P_{hydro}$. It should be noted that Gudmundsson (2011) and Philipp (2012) define overpressure as the total fluid pressure minus the normal stress on the fracture plane, which in the literature on fracture propagation is often called the 'driving stress', 'driving pressure' or the 'net pressure' (Rubin, 1995; Spence and Turcotte, 1985; Olson et al. 2009). While fluid overpressure is a scalar with an absolute value, it may sometimes be advantageous to use the fluid pressure relative to another reference pressure. Hubbert & Rubey (1959) introduced the 'pore fluid factor' (λ), which is the ratio of the pore fluid and the total vertical stress (also see Cox, 2010).

The fact that a reservoir can be stimulated by increasing the fluid pressure shows that the fluid pressure plays a role in fracture formation. Failure is thus not only a function of the absolute stresses, but effective stresses, which are the absolute stresses in relation to the fluid pressure. The simplest definition for 'effective stress' is the absolute stress minus the fluid pressure (Terzaghi, 1923). This definition is widely used in geology and we also use it in this paper, although will discuss below alternative definitions as well.

The term hydrofracture is commonly used as denoting fractures whose formation is induced by an elevated fluid pressure, as opposed to those formed by elevated differential stresses, typically because of tectonic stresses, but also due to e.g. meteorite impacts or igneous activity. For simplicity we group the latter fractures under the term 'tectonic fractures'. While

it may be clear that fractures are hydrofractures when they occur due to an artificially increase of the fluid pressure, it is not as simple to ascertain whether a natural fracture is due to an elevated fluid pressure (a hydrofracture), to elevated tectonic stresses (a tectonic fracture), or a combination of both, as is probably usually the case. For natural fractures we therefore here propose to refine the term 'hydrofracture' to *those fractures that are primarily caused by an elevated fluid pressure*. This definition does not exclude a contribution of tectonic stresses. What remains is to define '*primarily*' as this now defines whether a fracture is a hydrofracture or not. We will address this issue further below.

By definition, cohesion is lost across a fracture surface. Over time, cohesion is usually recovered by healing, often by mineral precipitation in the space created in the fracture, i.e., the formation of a 'vein' (Bons et al., 2012; Laubach et al., 2019). However, space for mineral veins can also be created without fracturing, for example by dissolution. We therefore use the general definition by Bons et al. (2012) of veins as 'mineral aggregates that precipitated from a fluid in dilational space, i.e., in space that was created in the rock'. This can be due to tensional failure, but is not restricted to this process. If the space is filled with a frozen magma, it is called a dyke, inclined igneous sheet, or sill. While it is common that the space for veins is created by a fracture, it is important to note that a vein is not necessarily a former fracture. In particular the controversial equation of fibrous or 'beef' veins with fractures will be discussed in this paper, as it has been used to argue for their origin as hydrofractures. Another example of veins not forming by precipitation of minerals within fracture porosity are replacement veins (e.g. Fletcher & Merino, 2001; Pirajno, 2009).

3. Formation of hydrofractures

We divide the theory on hydrofractures in rocks into two topics: (1) the formation or nucleation of a new hydrofracture and (2) the propagation of an existing hydrofracture (Polllard & Aydin, 1988; Gudmundsson, 2011; Guerriero & Mazzoli, 2021). The difference is that for the first one

we can usually assume a homogeneous stress and fluid-pressure state before the fracture forms. Once the fracture is formed, a complex stress field develops, particularly at the fracture tips (Engelder, 1999). Although the two processes are often treated separately, it is clear they are intimately linked as propagation can commence as soon as failure produces the first embryonic fracture. Nevertheless, here we follow the classical division and first deal with the initial formation of hydrofractures. We restrict ourselves to the basic Mohr-Coulomb-Griffith theory that does not take into account the interaction of chemical dissolution and precipitation reactions that intimately interact with a developing fracture or set of fractures, subcritical crack growth and ductile fractures, for which the reader is referred to Atkinson (1984), Weinberg & Regenauer-Lieb (2010), and the extensive review by Laubach et al. (2019).

3.a. Fluid pressure and initial fracture formation

An intact solid, such as a rock, will break or fail when the stress state reaches the failure criterion. The stress state can be described by the stress tensor (S_{ij}), or alternatively by the three principal stresses (S_1, S_2 and S_3) in descending order of magnitude (with compressive stress taken positive here), and their orientations in space. Stresses vary can vary strongly on the small scale (Pollard & Aydin, 1988). It is generally assumed that, at some scale above that of the homogeneous equivalent medium (HEM), the stress state can be described by a single stress tensor. The HEM-scale is the scale well above smaller-scale heterogeneities, such as grains and pores in a sandstone, or stratigraphic layers in a basin. Whether failure occurs and, if it does, the orientation of the resulting fracture is entirely dependent on the stress state, the rock mechanical properties that are potentially anisotropic, and, if a pore fluid is present, the fluid pressure (P_f).

3.a.1. Mohr-Coulomb-Griffith theory for failure

Failure of rocks is conveniently analysed with the Mohr-diagram for stress (Mohr, 1882) in combination with the Mohr-Coulomb-Griffith failure envelope (Terzaghi, 1943; Hubbert, 1951; Secor, 1965). An intact rock volume can be envisaged to contain an infinite number of potential fracture planes in terms of location and orientation, but the Mohr-Coulomb-Griffith failure theory is only concerned with the orientation of the plane or planes (with respect to that of the principal stresses) that will fail to form a fracture. In this theory, only the maximum and minimum principal stresses (S_1 and S_3) play a role and fractures form in a plane parallel to S_2. The two-dimensional construction is thus for the plane that contains S_1 and S_3, and only considers potential fracture planes in the rock that are parallel to S_2. The shear stress (τ) and normal stress (S_n) that a plane (parallel to S_2) that makes an angle α with the smallest principal stress (σ_3) is given by (Mohr, 1882; Hubbert, 1951) (Fig. 1a):

$$t(\alpha) = (S_1 - S_3) \times \cos(\alpha) \sin(\alpha) = \tfrac{1}{2}(S_1 - S_3) \times \sin(2\alpha) \qquad \textit{(eq. 2)}$$

and $$S_n(\alpha) = S_1 \times \cos^2(\alpha) + S_3 \times \sin^2(\alpha) = \tfrac{1}{2}(S_1 + S_3) + \tfrac{1}{2}(S_1 - S_3)\cos(2\alpha) \qquad \textit{(eq. 3)}$$

Equations (2) and (3) describe a circle in a plot of $\tau(\alpha)$ against $S_n(\alpha)$: the Mohr circle for stress (Fig. 1b). Each point on the circle represents the stress state for a plane with orientation α.

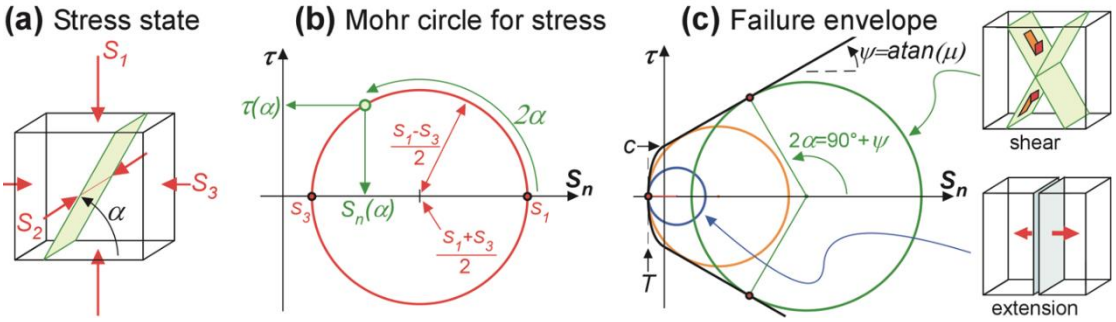

Fig. 1. Construction of the Mohr circle for stress. (a) Definition of the angle α between the minimum principal stress (S_3) and a plane parallel to the intermediate principal stress (S_2). (b) The Mohr circle for stress in a graph of τ versus S_n. The stress state for a plane with orientation α can be found by measuring an angle 2α from the S_1-point on the circle. (c) Mohr diagram with failure envelope, illustrating the two end-member failure types: shear failure and tensional failure. The orange circle is the circle that touches the failure envelope for both tensional and shear failure. Whether this can occur in a rock depends on the shape of the envelope at negative and low normal stress.

Within the τ-S_n space of the Mohr diagram there are τ-S_n conditions that a rock can sustain and those it cannot. This of course depends on the rock properties. The boundary between these two conditions is a line in the Mohr diagram: the failure envelope. A rock will fail as soon as a plane within the rock reaches a τ-S_n combination on the failure envelope. This means that the Mohr circle just touches the failure envelope and, therefore, that the slope of the failure envelope is parallel to the tangent of the circle at the point of contact. As a result, the slope of the failure envelope determines the orientation α of the plane of failure (Fig 1c).

The failure envelope is typically defined by two basic equations. Tensional failure occurs when the minimum stress (S_3) reaches the tensional strength (T). It is common in the literature to report the absolute (positive) value of the tensional strength, although the normal stress on the plane of failure is negative in case of tensional or mode-I failure. To avoid confusion regarding the sign, we here use the real, negative value of T for the tensional strength. The shear-failure criterion is defined by:

$$t = c + m \times S_n, \text{ or } \quad t = c + \tan(y) \times S_n \quad . \qquad \textit{(eq. 4)}$$

Here c is the cohesion, which is the shear stress acting on a fracture plane that experienced zero normal stress when it failed. A planar surface in a rock can typically sustain more shear stress as the normal stress on that surface increases. This is captured by the coefficient of friction (μ) or the slope of the failure envelope, defined by the angle of internal friction (ψ), typically in the order of 30-45°. It follows that $\mu=\tan(\psi)$.

Figure 1c shows the two basic types of failure: the first is shear failure resulting in a shear or mode-II fracture. It occurs when the Mohr circle touches the failure envelope for a plane that experiences a normal stress $S_n \geq 0$. Because of the symmetry of the stress state, the Mohr circle will reach the failure envelope twice in an isotropic rock. A conjugate set of fractures forms with opposite sense of shear. The resulting fractures, parallel to S_2, make an angle of $\alpha=\pm(90°+\psi)/2$ with S_3. As ψ is usually positive, S_1 is in the bisector of the acute angle of $90°-\psi$ between the two fracture orientations (Anderson, 1905). A practical advantage of Anderson's theory of faulting (Anderson, 1905; Anderson, 1951) is that this simple geometrical relationship between the stress field and shear fracture orientations allows revealing both the stress-field orientation and the angle of internal friction by measuring fracture orientations in the field. Gomez-Rivas et al. (2014), for example, used this to track the evolution of the orientation of the stress field in the Jabal Akhdar Dome (Oman) from fault and vein orientations, first as a result of the emplacement and exhumation of the Semail Ophiolite and Hawasina nappes, and subsequently by the movement of the Indian plate relative to the Arabic plate. The second basic type is tensional failure, which occurs when the left-most point on the Mohr circle is the first to reach the failure envelope. This means that failure occurs parallel to the plane normal to S_3. Because this requires a negative normal stress, the resulting fracture is under tension and its two fracture surfaces can diverge: an open extensional or mode-I fracture forms (Fig. 1.c).

Hybrid fractures form in the transition between the end members of extensional and shear fractures. Here the angle of internal friction decreases from 90° down to Ψ for S_n>0. One theoretical model for the failure criterion for hybrid failure was provided by Griffith (1924) for $S_n \leq 0$:

$$\tau^2 = \frac{c^2}{T^2} T(T - S_n), \text{ giving } \mu_{hybrid} = \frac{d\tau}{dS_n} = \frac{c}{2\sqrt{T^2 - S_n T}} \qquad \textit{(eq. 5)}$$

Note that the tensional strength (T) is negative here. The ratio of cohesion and tensional strength is not predefined in our Eq. (5). However, the ratio according to Griffith's theory c/T is -2., therefore, c^2/T^2=4 (Sibson, 2000a; Pollard and Fletcher, 2005; Jaeger et al., 2007; Gudmundsson 2011). Equation (5) implies that the hybrid angle of internal friction depends on the ratio of c and T. A problem is that this may lead to a discontinuity in ψ as S_n increases from negative to positive. With c/T=-2, the angle of internal friction is 45° at σ_n=0 (Eq. 5), although angles of internal friction may vary widely for $\sigma_n \geq 0$ (Gudmundsson 2011). Issues with the transition from hybrid failure to pure shear failure have been discussed by various authors (some examples are Secor, 1965; Phillips, 1972; Engelder, 1999; Ramsey & Chester, 2004; Zhu, 2017), but details of hybrid failure are not the main focus of this paper.

Although the Mohr-Coulomb-Griffith criterion has proven to be a very useful, or at least often employed, tool for the prediction of the onset of failure, as well as the type and orientation of resulting fractures, it cannot predict where a fracture would form, as the actual location where a fracture nucleates is controlled by the presence of flaws that perturb the local stress field (Pollard & Aydin, 1988). The Mohr-Coulomb-Griffith criterion does, however, include the presence of such flaws, as these affect the tensional strength, cohesion and angle of internal friction.

3.a.2. The effect of fluid pressure

So far, we have not considered how a pore fluid affects the stress state at which a rock fails. We have seen that with increasing confining pressure the Mohr circle required to reach failure shifts to the right and increases in size, and hence the required differential stress (S_1-S_3) increases. This is because the confining pressure presses grains together, making it more difficult for them to separate and slide past each other. The basic failure envelope is thus essentially for a dry rock. The presence of a pore fluid with a pressure P_f modifies the stresses at grain contacts and will thus affect the point of failure. Rather than to account for this by adapting the failure envelope, the failure envelopes are kept as they are, and the concept of 'effective stress' is used. The effective stresses are calculated from the actual stresses and the fluid pressure in such a way that the rock with a pressurised pore fluid can be compared with the equivalent dry rock.

The simplest, and in geology most commonly used, way to determine the effective stresses (σ_{ij}) is by subtracting the fluid pressure from the actual stresses (S_{ij}), following the Terzaghi principle (Terzaghi, 1923):

$$\sigma_{ij} = S_{ij} - \delta_{ij} P_f \qquad \textit{(eq. 6)}$$

In the Mohr diagram this has the effect of shifting the Mohr circle to the left by the amount of P_f (Fig. 2.a). When one keeps increasing the fluid pressure the rock will fail at some stage. The rationale is that the pore fluid carries part of the load applied to a rock and thus effectively reduces the stresses within the solid matrix. It should be noted that with the Terzaghi's principle the size of the Mohr circle, and thus the differential stress, does not change as a function of P_f.

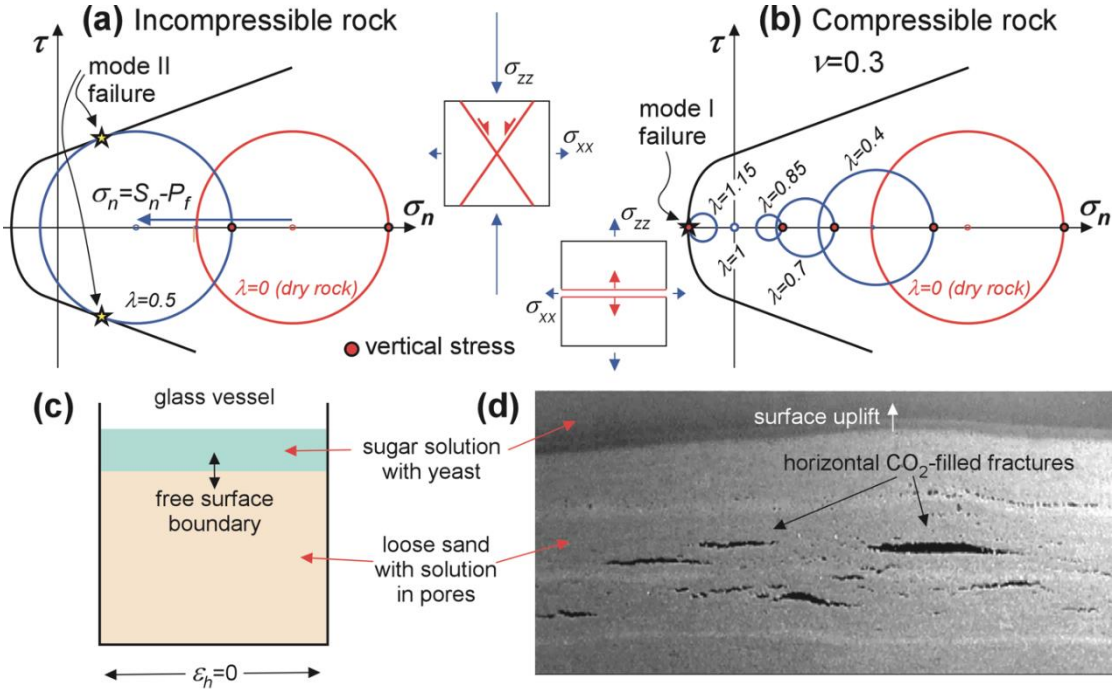

Fig. 2. (a) Terzaghi scenario for an incompressible material with the Mohr circle for the effective stress state moving by an amount of P_f towards the left-hand side without a change in differential stress. In the example with a vertical maximum stress (red dot), increasing the fluid pressure would eventually lead to shear failure. (b) Effect of compressibility in a situation where the vertical total stress is a function of the overburden load, and the horizontal stress is constrained by an imposed zero horizontal strain. Increasing the fluid pressure not only shifts the Mohr circle to the left, but also changes it size. Once fluid pressure exceeds the total vertical stress (λ>1) the effective vertical stress (red dot) becomes the smallest stress and horizontal fractures form in case of failure. (c) Simple experiment illustrating the formation of horizontal extensional or mode-I fractures of Bons & van Milligen (2001). A glass vessel is filled with sand and water with dissolved sugar and yeast. Pressure of the fermentation product CO_2 increases until horizontal fractures form, as shown in (d).

However, Terzaghi's principle is in some cases an oversimplification of the system and may lead to wrong interpretations, as discussed by many authors (e.g. Cleary & Wong, 1985; Meyer, 1986; Gordeyev & Zazovsky, 1992; Tzschichholz et al., 1994; Hillis, 2003; Cobbold & Rodrigues, 2007; Ghani et al., 2013; Koehn et al., 2020). The reason is that the Terzaghi principle essentially ignores that rocks are poroelastic, which means that both the pores and solid matrix, and therefore the bulk rock, change their volume if their pressures are changed. The basic theory for poroelasticity was developed for soils by Biot (1941; 1956) and elaborated on, or modified by, various others (see review by Guerriero & Mazzoli, 2021, and references

therein). Proposed equations for effective stress that take into account poroelasticity are mostly of the form:

$$\sigma_{ij} = S_{ij} - (1 - a)\delta_{ij} P_f \qquad \textit{(eq. 7)}$$

As summarised in de Boer & Ehlers (1988; 1990) and Guerriero & Mazzoli (2021), a number of models for the parameter a have been proposed, such as a equals the porosity (Fillunger, 1936), $a = K_{rock}/K_{solid}$ (for volume change with K the bulk modulus, Skempton, 1960; Nur & Byerlee, 1971), or $a = 1 - \nu/(1 - \nu)$ (with ν the Poisson's ratio; Hillis, 2003) that we discuss below.

Terzaghi's model is a special case with $a = 0$ of the more general Biot model. This is the case when the solid matrix is rigid and load-bearing. Terzaghi's model with $a = 0$ thus applies if the fluid overpressure is building up in a single pore, or in a restricted cell with overpressure in the crust. This is, however, often not even approximately the case, especially in porous sediments that are far from incompressible and therefore have a Poisson ratio of $\nu < 0.5$.

Boundary conditions become important when poroelasticity is relevant. If constant stresses on the boundaries are given, an increase in fluid overpressure will lead to a decrease in the principal effective stresses, but with a constant differential stress as was shown in numerical simulations (Koehn et al., 2020) and experiments (Cobbold & Rodrigues, 2007). This means that the size of the Mohr circle remains unchanged with a change in P_f and the Mohr circle shifts to the left or right according to Eq. (6). If, however, elastic strain is the boundary condition for the volume under consideration, things become more complicated as, for example, Hillis (2003), Cobbold & Rodrigues (2007), and Olson et al. (2009) point out. The reason is that a change in pore pressure requires a change in the applied stresses (S_{ij}) to maintain the given strain.

Hillis (2003) provided an example where a simple application of the Terzaghi principle does not work. The author examined an overpressure zone below a seal in a sedimentary basin and related the lowest effective stress below the seal to the vertical stress (S_v) and fluid pressure.

The example considers a basin at rest so that it is neither extending nor shortening. The horizontal elastic strain is therefore zero (ε_h=0), while the vertical stress (S_v) on the rock is the overburden weight (S_z=<ρ>gz). This is a case of mixed strain and stress boundary conditions.

If fluid pressure would be zero (dry rock equivalent), the horizontal (S_h) and vertical (S_v) stresses are related by (using Hooke's law for linear elasticity and uniaxial strain and stress: S_h=S_x=S_y):

$$Ee_h = S_h - nS_h - nS_z = 0 \Leftrightarrow S_h = \frac{n}{1-n} S_z \qquad \textit{(eq. 9)}$$

In an incompressible rock (ν=0.5) this gives S_h=S_v, that is, zero differential stress. Although this would be correct for an incompressible rock, the resulting zero differential stress cannot simply be applied to a compressible rock. This would mean that the rock would compact equally in all directions and the basin would contract laterally. It is not permissible to use this stress state and simply subtract a non-zero fluid pressure to determine the effective stresses to assess potential failure or compaction. This is because total stresses change with increasing fluid pressure to maintain the boundary conditions. In an Andersonian stress state (Anderson, 1905; 1939) the vertical effective stress, resulting from a vertical stress boundary condition, does follow the straightforward Terzaghi model:

$$\sigma_z = S_z - P_f, \text{ giving } \frac{d\sigma_z}{dP_f} = -1 \qquad \textit{(eq .10)}$$

The horizontal effective stress, however, is a function of the zero horizontal strain boundary condition and the vertical fluid-pressure dependent effective stress, giving (Hillis, 2003; Cobbold & Rodrigues, 2007):

$$\sigma_h = \left(\frac{\nu}{1-\nu}\right)\sigma_z, \text{ giving } \frac{d\sigma_h}{dP_f} = \frac{-\nu}{1-\nu} \qquad \textit{(eq. 11)}$$

This means that with increasing P_f the vertical effective stress is reduced faster than the horizontal effective stress so that both will become zero when S_z=P_f (Fig. 2b). Once the principal stresses reach negative values, the horizontal and vertical stress will become negative,

where now the vertical stress is more negative and a horizontal fracture will develop upon failure (Cobbold & Rodrigues, 2007; Koehn et al., 2020). This can be illustrated with a very simple experiment (Bons & van Milligen, 2001) of a jar filled with loose sand and a pore fluid that initially consists of water, dissolved sugar and yeast (Fig. 2c). The glass walls of the jar provide zero horizontal strain boundary conditions. The top of the wet sand can move vertically, so here we have a stress boundary, with the total vertical stress increasing downwards according to the material density. Fermentation produces CO_2 gas that has a high wetting angle with the sugar solution. Permeability for CO_2 flow is therefore very low, as the gas tends to form bubbles in the pores and is inhibited from flow through the pore throats between the sand grains. The CO_2 pressure (P_f) increases as more and more CO_2 is produced, until finally horizontal mode I extensional fractures form (Fig. 2d). Gas generation in organic-rich shales and coals has been reported to induce natural hydrofractures (e.g. Fall et al., 2015).

The above should not be understood as taking sides in the discussion on whether Biot's or Terzaghi's theory (and derivations thereof) is right or preferred. Both are applicable depending on the rock properties and especially on the imposed boundary conditions. In the above case the vertical effective stress is S_v-P_f (Eq. 9), which is according to Terzaghi's theory, but also Biot's theory with a=0 (Eq. 7). Terzaghi's theory is also applied to calculate the effective horizontal stress as it is applied to Hooke's linear elasticity law (Eq. 8). The difference with the straightforward application of Terzaghi's principle is that, unlike the vertical stress, the total horizontal stress in this case is a function of the fluid pressure itself.

We have now seen that horizontal extensional fractures are expected to form in a basin at rest in which the fluid pressure is increased due to an influx of fluids from below (*e.g.*, due to expulsion of compacting sediments, dehydration reactions, release of hydrocarbons). Typical fluid pressure profiles as a function of depth are shown in figure 3. The presence of a low-permeability seal can locally bring the fluid pressure up to the failure condition (Fig. 3b) or in an overpressured layer, as modelled by Ghani et al. (2013), Ghani et al. (2015) and Koehn et

al. (2020) (Fig. 4a-b). A tacit assumption so far was that there are no lateral gradients in fluid pressure. If these gradients exist, for example in laterally constrained high-pressure cells, the zero horizontal strain condition does not apply anymore and the simulations in Fig. 4c-e show that an increase in fluid pressure leads to fractures in different orientations, and potentially shear fractures as well.

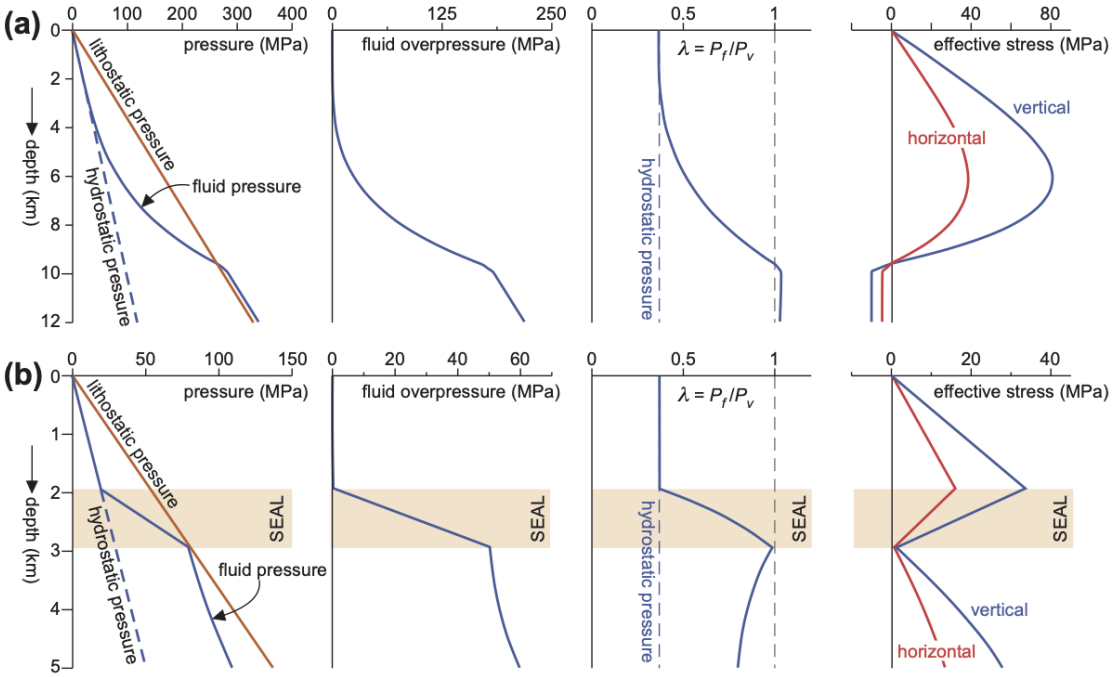

Fig. 3. Depth profiles for a fluid influx of $5 \cdot 10^{-11}$ m/s from below and a permeability that decreases with depth according to Ingebritsen & Manning (1999), (a) without and (b) with a low-permeability seal. From left to right, we show absolute pressures, the fluid overpressure, the pore-fluid factor (λ) and finally the effective stresses for a basin at rest and a Poisson ratio of 0.4.

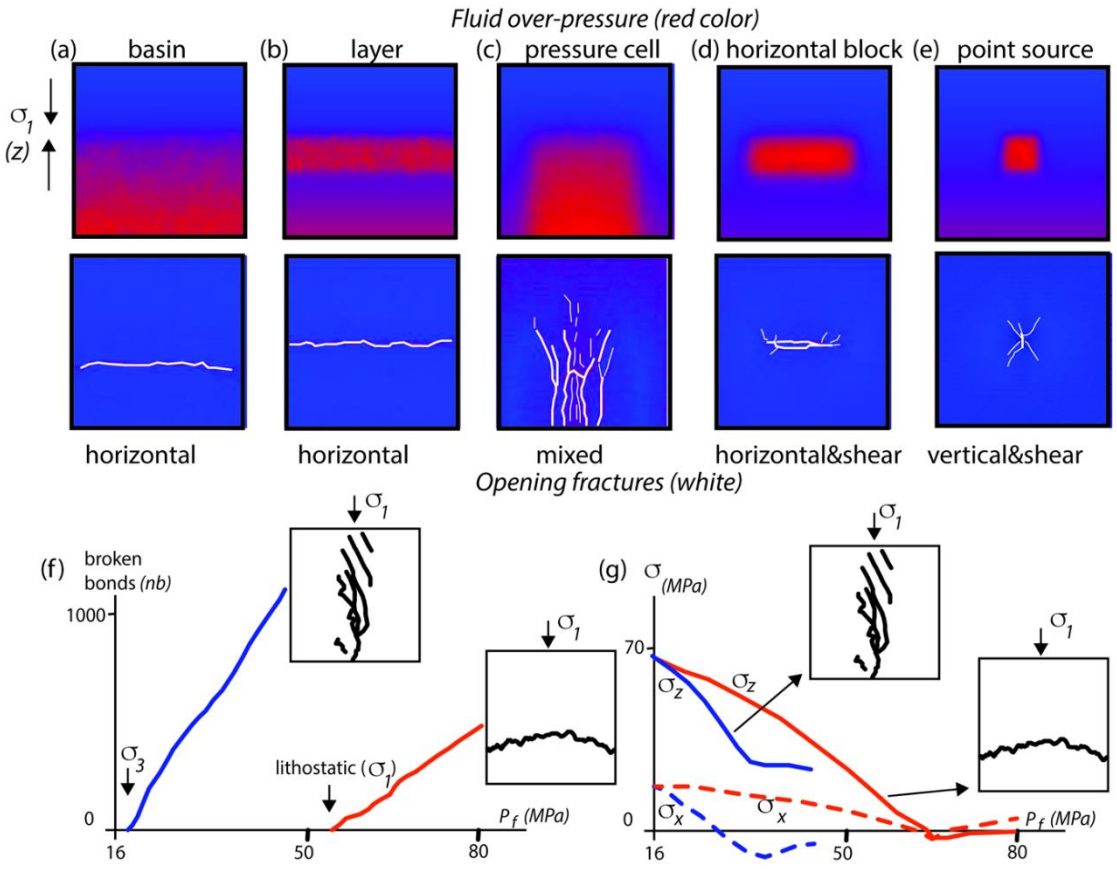

Fig. 4. Variations of the geometry of a high fluid pressure zone in simulations leading to a variety of fracture patterns from horizontal to vertical as well as combinations. (a)-(e) upper pictures show fluid pressure in the model with red high and blue low pressure. (a)-(e) lower pictures show the developing opening fracture patterns for the specific cases in the models in white. (a) and (b) are cases where the boundaries are fixed, and fluid pressure builds up in a sedimentary basin or a horizontal layer and the resulting fracture is horizontal. (c) to (e) show a variation of localised high fluid pressure cells where fracturing can happen in a vertical and horizontal orientation. (f) shows the developing fractures as a function of fluid pressure for two end-member cases representing (a) a sedimentary basin with fixed boundaries in blue, and (c) a fluid pressure cell that represents a horizontal stress boundary in red. The corresponding solid stresses as a function of the fluid pressure are shown in (g) for both cases. Note that fractures develop early in case (c) and the evolving stress field follows Terzaghi's law (blue curves). In case (a), represented by the red curves, differential and mean stress decay and fracturing happens at a much higher fluid pressure.

3.b. Beyond the initial fracture development

3.b.1. Fracture propagation and stress intensity factor

We now look at the propagation of simple cracks using linear elastic fracture mechanics and the idea that crack propagation costs energy because new surface area is created (Griffith, 1920). In order to conserve energy, the work per unit time of an applied load ($\dot{W}$) is equal to

the rates of change in elastic $(\dot{U}_e)$, plastic $(\dot{U}_p)$, and kinetic energy ($\dot{U}_k$), as well as the energy per unit time spent to increase the crack area $(\dot{\Gamma})$ (Griffith, 1920; Richard and Sander 2016):

$$\dot{W} = \dot{U}_E + \dot{U}_P + \dot{U}_k + \dot{\Gamma} \qquad \textit{(eq. 12)}$$

If we assume that the crack propagation is slow, then the kinetic energy can be neglected. With this the rate of change of potential energy of the system as a function of crack surface area change, i.e. crack growth, can be calculated.

For a simple extensional crack in an extensional system that is purely elastic this formulation leads to the Griffith criterion for extensional cracks where *G*, the crack extension force, is proportional to changes in elastic and surface area according to (Griffith, 1920; Richard and Sander 2016):

$$G = \frac{\partial U_E}{\partial A} \qquad \textit{(eq. 13)}$$

Using the stress solutions by Inglis (1913), Griffith (1920) derived a strength criterion that can be used to estimate at what stress (*T*) a material will fail:

$$T = \sqrt{\frac{E\gamma r}{4lL}} \qquad \textit{(eq. 14)}$$

with E the elastic modulus, γ the surface free energy, r the radius of curvature of the crack tip, l the bond length of the material and L the crack length. It is worth noting that the original Griffith formulation was derived for a crack with internal stress on the walls, which is the same as an external extensional load on an infinite plate. Therefore, the simplest hydrofracture is an extensional fracture, where the internal fluid pressure is equivalent to an external negative stress on the medium. Of course, once the fracture propagates and opens, changes in the fluid pressure as well as geometrical changes of the crack have to be taken into account.

For certain scenarios the stress, strain and displacement fields for a crack propagation in an elastic medium can be solved analytically (Westergaard, 1939). This leads to the following expression for the state of stress

$$\sigma_{ij} = \frac{K_i}{\sqrt{2\pi r}} f_{ij}(\theta) \qquad \textit{(eq. 15)}$$

and displacement

$$u_{ij} = \frac{K_i}{2\mu}\sqrt{\frac{r}{2\pi}}\, g(\theta) \qquad \textit{(eq. 16)}$$

with K the stress-intensity factors that contain loading as well as geometrical conditions, r the distance to the crack tip, $f_{ij}(\theta)\ and\ g(\theta)$ functions of the angle θ relative to the long axis of the crack (Sih, 1973; Rooke & Cartwright, 1976). Theoretically these formulations only work away from the actual crack tip, while at the tip (at r=0) stresses form a singularity dominated zone. The stress intensity factor varies for crack types such as extension versus shear as well as boundary conditions and crack geometries. For a simple hydrofracture in terms of the Griffith extensional crack we have:

$$K_i = \sigma\sqrt{\pi L} \qquad \textit{(eq. 17)}$$

A geometrical factor needs to be added for more complex configurations. For constant geometries several known stress intensity factors can be added (Sih, 1973; Rooke & Cartwright, 1976), which essentially leads to the Terzaghi criterion where stresses due to an internal fluid pressure cancel out stresses from an external loading, which leads to the idea of an "effective stress". The superposition of stress intensity factors for variable stress fields known from literature offers advanced approaches extending the Mohr-Coulomb approaches, discussed above, to study hydrofractures that develop under variable boundary conditions in the Earth's crust.

For more complicated fracture propagation problems, stress intensity factors can be determined in continuum simulations to calculate the most probable path of propagation and then re-mesh the model. Another possibility is the use of discrete element models where bonds with a critical breaking threshold break as will be discussed in the following.

3.b.2. Growth of individual fractures and fracture and vein networks

Hydrofractures in general are introduced into the system because there is an overpressure as a result of the difference between the surrounding fluid pressure and a zone where fluid pressure is elevated. The overpressure (ΔP) is a function of the local increase in pressure as a function of time and the advection of the overpressured fluid away from the zone of influx or fluid production. How much the fluid leaks into the system depends on the permeability of the host rock. If the fluid addition is faster than the leaking or if the rock is very impermeable the overpressure builds up until failure occurs. The creation of hydrofractures will now generate a higher permeability. The hydrofractures will grow until they have created enough permeability for the overpressure to dissipate into the rock at a given fluid addition rate. This is shown in a simulation in figure 5 where the fluid overpressure at one point increases until a fracture network develops that drains the incoming fluid (see Supplementary Material for the numerical method). The rock dynamically creates the permeability it needs to be able to drain the injected fluid.

A similar situation to that of the injected fluid case can be envisioned in a scenario at geological time scales. When the system is too permeable the fluid overpressure will never build up to be high enough to cause rock failure. However, if a seal exists or the rock itself is impermeable (Fig. 3b), an increase in fluid overpressure may lead to fracturing. This increase can happen, for example, during exhumation, thermal expansion of fluids, a de-watering reaction, oil maturation or release of fluids from a subducting slab, among other processes. Once fractures form, they may in turn lead to an increase in permeability and leaking of the overpressure. If the pressure is not released the fracture pattern may evolve dynamically. This is illustrated in figure 5 where fractures develop below a seal in a simulation. Here the initial fractures follow Terzaghi's principle and are vertical and parallel to the largest principal stress (in this case vertical because of gravity). However, with increasing fluid pressure the pattern changes and the fluid pressure gradients work upwards and lead to the formation of an increasing number of

horizontal fractures. The developing network is similar to a hydraulic breccia and forms because the seal is not broken. The final fracture network does contain fractures that formed in rather different stress fields. In a natural setting one may not be able to separate the different fractures from each other making it hard to interpret the fracture network.

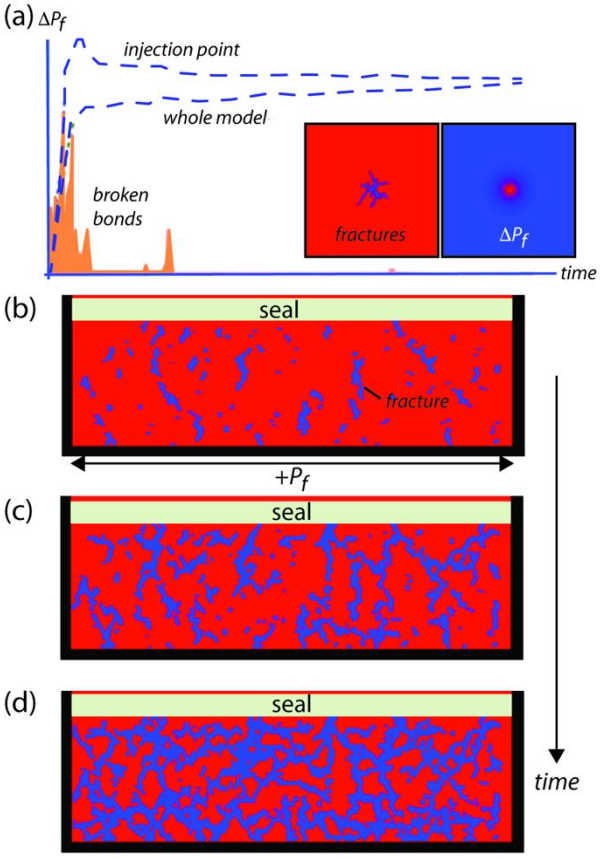

Figure 5. (a) Injection of fluid and associated fracturing in a simulation (Ghani et al., 2013; Koehn et al., 2020). The two dotted curves show the fluid pressure evolution over time, one directly at the centre and one for the whole model. The developing fractures are shown in pink and the inset on the left-hand side shows the fracture pattern in blue and the inset on the right-hand side the fluid pressure (red high, blue low). (b) to (d) Simulations of the development of a fracture network below a seal at the top of the model as a function of an increase in fluid overpressure. The number of fractures, shown in blue, increases with model time and fluid pressure. Vertical stress is highest due to gravity and horizontal stress is a function of the vertical stress. Box walls at the bottom and the right- and left-hand side are fixed.

The system becomes even more complex when the fractures heal and form veins. It is important to note that veins are not equal to fractures meaning that a) the geometry of a vein does not necessarily reflect that of the original fracture, b) not all veins represent fractures (*e.g.*, in the case of replacement veins, veins filling dissolution vugs or fibrous veins, see below), c) not all veins represent fractures that open at the same time (such as in the case of crack-seal veins; Bons et al., 2012; Virgo et al., 2014), d) veins may refracture several times (Ramsay, 1980) and e) veins may change the properties of the system. An example is given in Figure 6 in a simulation following the general setup of Ghani et al. (2013). The fractures develop due to fluid

overpressure build-up below a seal (in blue colour). In these simulations, the fractures can heal following the algorithm of Vass et al. (2014) and once they heal the new bonds can have different properties. New veins either fracture more easily (weak in Figure 6) or are more difficult to fracture (strong in Figure 6) than the host rock. The properties of the veins change the system completely and influence the development of new fractures. The two pictures on the left-hand side in Figure 6 show the open fractures at a given time step and the picture on the right-hand side the vein network. One can see that the vein network and the fracture network are very different and that they vary significantly as a function of the failure properties of the veins. The weak veins have a memory and continue to open leading to a large connected fracture network that breaks the seal. The hard veins produce a system with a large number of veins that do not refracture, while the material hardens and only a small number of open fractures remains. The important message is that we need to be extremely careful to relate vein networks directly to networks of active or open fractures. In the case of Figure 6 a large vein network means very few actually open fractures, because the system clogs itself. The relevance of this issue is illustrated with the discussion on how melt is extracted from partially molten rocks towards dykes that feed plutons and magma chambers. Marchildon & Brown (2003) used outcrops of networks of granitic dykes as evidence for magma transport through hydrofracture networks in support of the 'rivulets-feeding-rivers' model. Bons et al. (2009), however, argued that these networks are the cumulative product of many individual hydrofracture events, whereby new hydrofractures cut already fully solidified dykes. As such, there never was a fully percolating network of hydrofractures that were all filled with liquid magma, which the authors used as an argument against the 'rivulets-feeding-rivers' model.

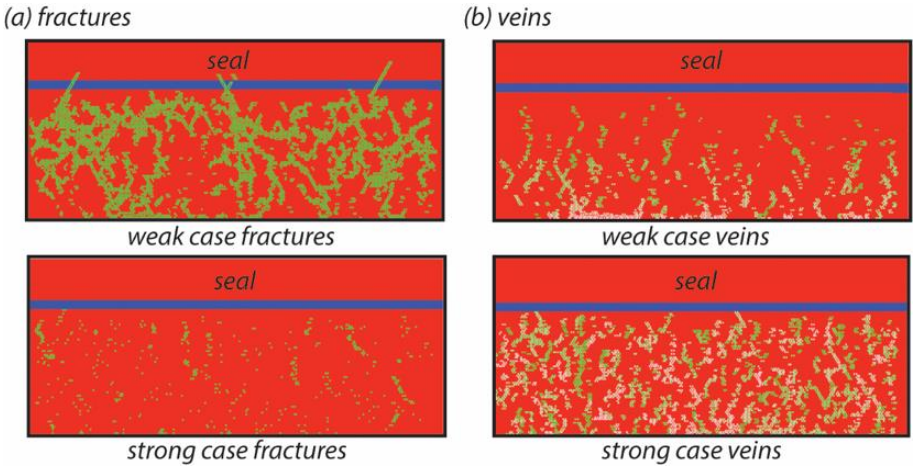

Figure 6. Healing of fractures and the creation of veins with different breaking strength. Fractures in (a) in green colour and veins in (b) in green (early veins) and white (late veins). Weak veins that fracture easier than the host rock are shown in the upper pictures and hard veins that fracture less than the host-rock in the lower pictures (see also Vass et al., 2014). Fluid pressure injected below a seal as in fig. 4 (b) - (d) over the whole width of the model.

3.b.3. Compressible fluids and hydro-mechanical interactions

Although not always considered, fluid compressibility is an important factor (e.g., Engelder & Lacazette, 1990). The compressibility of aqueous fluids typically is one order of magnitude lower than that of the solid (e.g. Gibiansky & Torquato, 1998). In order to understand the interaction between fluid and solid after a hydrofracture network developed, one needs to take the compressibility of both media into account. The resulting structures form fracture-channels of high porosity and compacted areas that dynamically open and close. This can be observed in numerical models (Fig. 7), as well as in experiments with granular media and injecting fluids or air, which in fact is also a fluid (Flekkøy, 2002; Vinningland et al., 2007a, 2007b, 2010, 2012; Johnsen et al., 2006, 2008a, 2008b; Niebling et al., 2010a, 2010b; Goren et al., 2010, 2011; Ghani et al., 2013, 2015; Aleksans et al., 2020; Koehn et al., 2020). In the numerical model the fractures are first created and are then followed by the development of fracture channels that form as connected fractures that can open while the surroundings are compacted and thus closed. This dynamic system can lead to characteristic length-scales in the model

between sets of opening fracture channels that can be observed in experiments and may also be present in real systems.

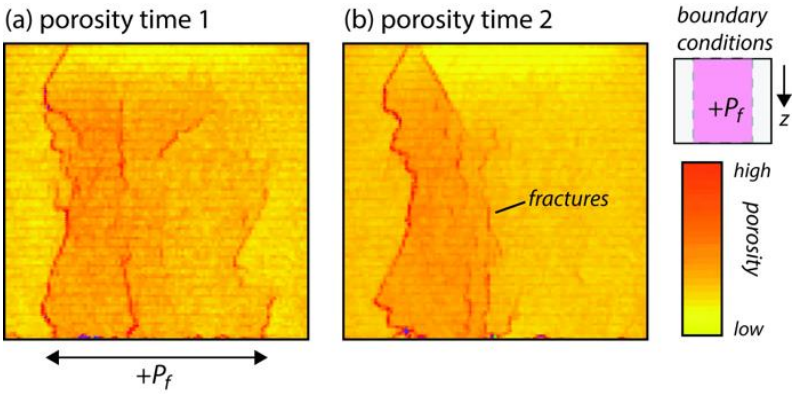

Figure 7. Opening fracture channels that develop in a numerical model with a compressible fluid and full hydro-dynamic interactions (see also Koehn et al., 2020). Colours are porosity with yellow low and red high porosities. Gravity is applied vertically and increase in fluid pressure is concentrated within the centre of the model. Large vertical fracture-channels develop that drain the fluid and open and close dynamically.

Fig. 8. (a) Fluid pressure in a vertical open fracture in relation to lithostatic pressure that acts as a normal stress on the fracture, plotted as a function of depth. (b) Giant quartz vein from Poolamacca Station, far-west New South Wales, Australia, attributed by Bons (2001) to fluid transport by mobile hydrofractures. (c) Similar giant quartz vein northeast of the town of Roses, far-eastern Pyrenees, Spain.

3.b.4. Wholesale propagation of hydrofractures

Fluids in a fracture usually have a lower density than the surrounding wall rock. In case of aqueous fluids this difference can be significant. The resulting buoyancy of the fluid can lead

to unidirectional, upwards propagation at the upper tip of a fluid-filled fracture. Igneous dykes emanating from a magma chamber have a contiguous source volume that can feed the dyke for a prolonged period of time (Secor & Pollard, 1975; Clemens & Mawer, 1992, Rubin, 1995, Gudmundsson, 2011). However, when the fracture is sourced from a partially molten region or is filled with an aqueous fluid a large single feeder volume is usually absent and influx of fluid into the fracture may not keep up with the increasing fracture volume (Bons et al., 2009). In that case the fracture would begin to close at its bottom end (Bons et al., 2001; Rivalta et al., 2015). Weertman (1971) first proposed that if a fracture that is filled with a buoyant fluid is tall enough, it may keep propagating at its upper end, while closing at its bottom end. As a result, the fracture propagates together with its contained fluid. Such hydrofractures have been called 'Weertman (-Nunn) fractures' (Rivalta et al., 2015) or 'mobile hydrofractures' Bons (2001). The basic theory was further developed by e.g. Secor & Pollard (1975), Pollard (1976), Nunn (1996), Dahm (2000) and Dahm et al. (2010) and extensively reviewed by Rivalta et al. (2015). Takada (1990), Dahm (2000), Bons (2001), Bons et al. (2001), and Rivalta et al. (2005) published analogue experiments of the ascent of mobile hydrofractures.

A non-horizontal fracture experiences a normal pressure gradient as the pressure in the wall rock increases faster with depth than inside the fracture that is filled with a lower density fluid (Fig 8). Fluid pressure inside the fracture and elastic strain of the wall rock adapt such that the fluid exceeds the pressure of the wall rock at the upper tip, the amount of which increases with the fracture length L. At a certain length the stress intensity at the upper tip reaches the fracture toughness, K_c, at which point the fracture will start to propagate upwards, while it closes at the base. The critical length, L_c, is given by Dahm (2000):

$$L_c = 2\left(\frac{K_c}{\sqrt{\rho}g\left(\rho_{rock} - \rho_f\right)}\right)^{\frac{2}{3}} \qquad \textit{(eq. 17)}$$

The vertical critical length may be as low as a few metres for a water-filled fracture to kilometres for dykes in the mantle, depending on the density difference between the rock and the fluid, and the poorly constrained fracture toughness, for which estimates range from <1 MPa $m^{1/2}$ to a few GPa $m^{1/2}$ (see discussion in Dahm, 2000). Once a fracture becomes unstable and starts propagating, its velocity is controlled by the viscous drag of the contained fluid that has to flow upwards in the narrow fracture, as well as the fracture toughness at the propagating upper tip. Theoretical estimates for the ascent rate of critical-length mobile hydrofractures range from <m/yr to about >m/s (Spence & Turcotte, 1985; Nunn, 1996; Dahm, 2000). Velocities up to m/s have also been inferred from lifting by the fluid of clasts and mineral fragments in veins and breccias (Oliver et al., 2006b; Okamoto & Tsuchiya, 2009; Weisheit et al., 2013a). The critical length is the length at which instability is reached, and the ascending fracture may get arrested as soon as conditions change. However, channelling along structures, such as faults or pathways of earlier mobile hydrofractures, may lead to the accumulation of multiple fluid batches to create more voluminous and faster mobile hydrofractures that can ascend far up the crust (Maaløe, 1987; Sleep, 1988; Bons, 2001).

A problem with mobile hydrofractures is that, due to their very nature of being mobile, one cannot find these in their mobile state in the fossil record. Indications for active ascent of hydrofractures can be derived from rising microseismicity fronts (Dahm et al., 2010) or pulsed discharge rates of oil in mud volcanoes in the Gulf of Mexico (MacDonald et al., 2000). The fossil record can only provide indirect indications of fluid transport by mobile hydrofractures.

Mobile hydrofractures can theoretically transport batches of fluid upward very rapidly. At 0.1 m/s a batch of fluid can ascend 10 km in about a day. This means that the fluid may not have time to equilibrate with the rapidly changing ambient conditions, except for adiabatic cooling, and can carry its dissolved mineral content up the crust to where the mobile hydrofracture is finally arrested. According to Bons (2001) this transport mechanism may explain the occurrence of huge quartz veins at Poolamacca station in far west New South Wales, Australia

(individual vein volume up to an estimated $5 \cdot 10^5$ m^3) (Fig. 8b), and also found throughout the world, e.g., in the Pyrenees (fig. 8c; González-Esvertit et al., 2022), the Sperrin Mountains of northern Ireland (Rice et al., 2016), the Bavarian Pfahl zone of the Bohemian Massif (Schaarschmidt et al., 2019), the Monte Rosa area in the Western Alps (Pettke & Diamond, 1996), the Bundelkhand craton in the central Indian shield (Pati et al., 2007) or the Alaskan Cordillera (Goldfarb et al., 1993). However, other authors have also invoked different mechanisms for the formation of large quartz veins based on structural and geochemical arguments (e.g., Sharp et al., 2005), and thus the origin and significance of these impressive structures still raises questions.

Although the theory of mobile hydrofractures was originally based on water-filled crevasses in glaciers (Weertman, 1971), it is mostly applied to magma transport in dykes, where it remains controversial. In particular Lister & Kerr, (1990, 1991) and Petford et al. (1993) criticised that it is (i) theoretically impossible to completely close a fracture at the rear end if the contained fluid has a non-zero viscosity and that the fracture would thus lose fluid, and (ii) that a fracture that is just at its critical length L_c would still be so narrow that it would freeze quickly as it ascends into cooler crustal levels. The first point was addressed by Bons et al. (2001), who emphasised that initial critical-length mobile hydrofractures may get stalled and then merge with subsequently arriving hydrofractures, to form mobile hydrofractures that are well beyond the critical length L_c. The second point only applies to igneous fluids that can freeze. However, tall igneous dykes do exist, which is consistent with the fact that such dykes may tap large magma reservoirs that allow continuous feeding of a dyke and avoid pinching off to form isolated ascending magma batches. This is also related to the viscosity of the fluid, which is generally much higher for magmas than for aqueous or hydrocarbon fluids, as is comprehensively discussed in Rivalta et al. (2015).

3.b.5. Dynamics of crustal-scale flow in hydrofractures

Hydraulic breccias (Jébrak, 1997; Weisheit et al., 2013a) and crack-seal veins (Ramsay, 1980) indicate stress states that frequently reach the failure criterion, and in some cases fast and localised fluid flow. In fact, many authors identified episodic pulses of rapid fluid flow (Sibson et al., 1975; Sibson, Robert & Poulsen, 1988; Hunt, 1990; Nakashima, 1993; Cartwright, 1994; Cox, 1995; Eichhubl, 2000; Cox, 2005; Okamoto & Tsuchiya, 2009). It is worth noting that crack-sealing by itself is not necessarily evidence for rapid fluid flow (Becker et al. 2010). However, Darcian flow (e.g., Bear, 1988) is often used in crustal-scale fluid flow models, where fluid is assumed to flow continuously and slowly through pore space, driven by, for example, topography differences (Oliver, 1986; Oliver et al., 2006a; Person et al., 2007) or fluid density gradients associated with thermal instabilities (Matthäi et al., 2004; Zhao et al., 2008). When hydraulic head gradients are low, Darcian porous flow can be described as 'diffusional', because the fluid overpressure evolves in a diffusional way according to a diffusion coefficient related to the permeability. When the rock's permeability is insufficient to drain the fluid, fluid pressure builds up until the failure threshold is reached, thus activating hydrofractures. Open fractures suddenly increase the local permeability, and therefore fluid drainage, or can rapidly propagate together with their contained batch of fluid as mobile hydrofractures (Bons, 2001). These very rapid fluid-flow modes can be termed 'ballistic' (Bons and van Milligen, 2001).

Permeability, as one of the main controls on fluid flux, varies from 10^{-7} m^2 in well-sorted gravels to $<10^{-23}$ m^2 in some crystalline rocks. It generally decreases logarithmically with depth (Manning & Ingebritsen, 1999; Ingebritsen & Manning, 1999; Cox, 2005). In the Earth's crust permeability changes due to a variety of processes, such compaction and decompaction, fluid flow and fluid production (e.g. dehydration reaction, fluid release by crystallising magma), tectonism, and seismicity (e.g., Sibson, Moore & Rankin, 1975; Walder & Nur, 1984; Yardley, 1986; Nor & Walder, 1992; Connolly, 1997; Cox, 2005; Hooker & Fisher, 2021), and has therefore been described as a dynamically self-adjusting property (Townend & Zoback, 2000;

Rojstaczer, Ingebritsen & Hayba, 2008; Weis, 2015; Ghani et al., 2015; Koehn et al., 2020; Fig 5). As permeability can change suddenly over many orders of magnitude, Miller and Nur (2000) described the self-adjustment as a toggle switch that can lead to intermittency and self-organisation (Sibson et al., 1988; Sibson, 2000a; Sibson, 2000b; Cox, 2005; Preisig et al., 2016; Weis, 2015).

Dynamic fluid transport has been numerically modelled with cellular automata in several studies (Miller and Nur, 2000; Bons and van Milligen, 2001; de Riese et al., 2020; Hooker & Fisher, 2021; Wangen, 2022). Miller and Nur (2000) and Bons and van Milligen (2001) both showed that fluid flow self-organizes as soon as a critical state is reached, which activates hydrofracture-controlled fluid flow as a ballistic fluid transport mode, resulting in power-law distributed frequencies of hydrofracture sizes. Wangen (2022) utilised the same approach to model fluid expulsion from compacting sediments. In reality, transport of fluid through the crust is never exclusively diffusive Darcian, nor intermittent hydrofracture flow only, but rather a combination of the two end members (e.g., Shapiro & Dinske, 2009). The interaction between these two end members of fluid flow was investigated in detail in de Riese et al. (2020), and the resulting patterns are shown in figures 9 and 10. A description of the model is given in the Supplementary Material. The model box (Fig.9a,b) illustrates a 10-km tall vertical section through the Earth's crust, with a constant fluid flux entering at the base of the model that is characteristic for crustal metamorphic fluid fluxes at a depth of about 10-15 km (Ingebritsen & Manning, 1999). The model only considers overpressure, which diffuses to simulate porous flow through the rock matrix. The effective pressure diffusion coefficient, D (see Supplementary Material), is varied, which implies a variation in permeability, and allows investigating the interaction of hydrofracture- and Darcian-dominated fluid flow.

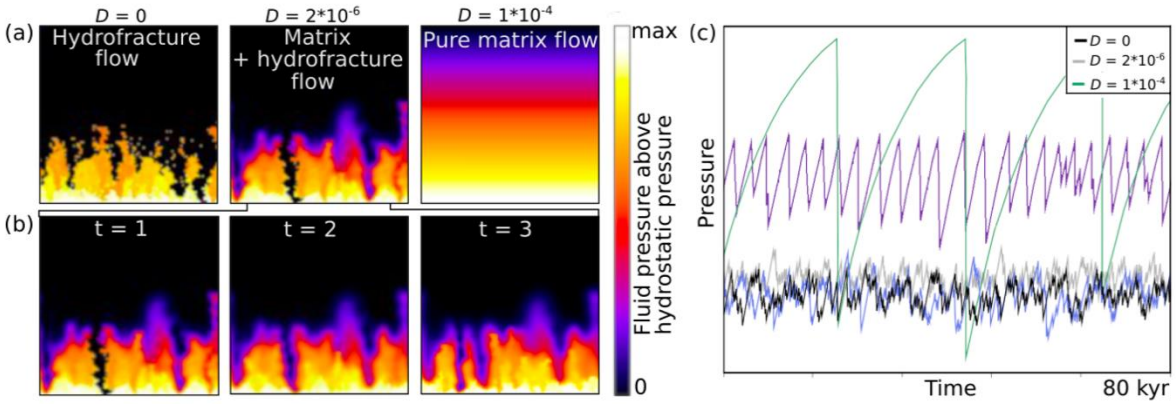

Fig. 9. Modelling results showing behaviour of hydrofracture and Darcian porous flow and the transition between them. (a) and (b) Snapshots of the pressure distribution in the model box with fluid influx from below: (a) for three different fluid-pressure diffusion coefficients D with D = 0 (no diffusion), D = $2 \cdot 10^{-6}$ (slow diffusion) and D = $1 \cdot 10^{-4}$ (fast diffusion), and (b) for three time steps of the simulation with D = $2 \cdot 10^{-6}$, where a hydrofracture reaches the top of the model at time t=1. With time the pressure diffuses into the drained parts of the model and the initially sharp boundary becomes fuzzy. (c) Mean pressure in the model box versus time. A small diffusion coefficient produces irregular and intermittent behaviour. A high diffusion coefficient produces periodical pressure fluctuations. Modified after figures 3 and 4 of de Riese et al. (2020).

Fluid production induces increasing fluid pressures, depending on the fluid overpressure diffusivity *D* (Fig. 9a). As soon as fluid pressure reaches the failure criterion (lithostatic pressure), a hydrofracture develops in the model. It can subsequently propagate depending on the fluid overpresssure in its vicinity. At a very high permeability relative to the fluid flux (D=10^{-4}) almost all fluid overpressure is dissipated by diffusional matrix flow towards the top of the model. In case of zero permeability (D=0) all fluid transport takes place by hydrofracture propagation only. Hydrofractures that reach the top of the model domain drain all the fluid they contain, which effectively means the fluid overpressure is set to zero in that hydrofracture. Figure 9b shows the pressure field evolution with time of a simulation with D=$2 \cdot 10^{-6}$ where both transport modes are active. Drainage of large hydrofractures results in low fluid overpressures in the top half of the model. The pressure field shows how the sharp boundaries of a hydrofracture become fuzzy with time as fluid flows in or out of the fracture after its arrest or drainage out of the top of the model. The mean pressure versus time in the system is shown in figure 9c. In the case of pure hydrofracture flow the fluid pressure fluctuates strongly,

although the input flux is constant. With an increasing *D*, pressure fluctuations start to become periodical, while hydrofracture events become less frequent. When permeability is very high (D=10^{-4}) the mean pressure becomes highly periodical, as fluid pressure can simultaneously build up in the whole model until a single very large hydrofracture discharges all the fluid and the fluid overpressure is reset to a low value throughout.

Sizes of hydrofractures that do not reach the surface have a power-law distribution (Fig. 10). Hydrofractures that can reach the surface have frequency size distributions that do not follow a power law. These hydrofractures are always large and scarce. With an increasing diffusion coefficient *D*, the hydrofracture frequency decreases, especially the frequency of hydrofractures that do not reach the surface (Fig. 10). Meanwhile, the size and fraction of fractures reaching the surface increases. Hydrofractures that are not able to reach the surface are constrained to the bottom part of the model, just above of the fluid source. They spread the fluid within the crust. Their power-law distributions show that large but rare events transport most of the fluid, and indicate self-organised criticality (SOC) in the transport dynamics (Bak et al., 1988; Turcotte, 1999). Self-organisation develops due to the existence of a failure threshold, which leads to the activation of a ballistic transport mode and the discharge of the excess fluid as soon as the failure threshold is locally overcome.

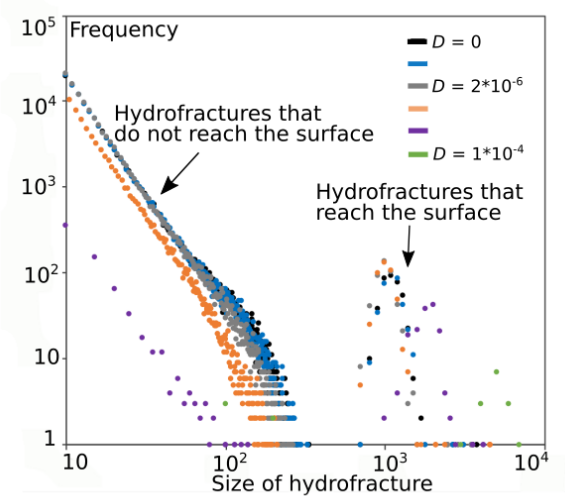

Figure 10. Frequency distributions of hydrofracture sizes (area) for different pressure diffusion coefficients (D). Hydrofractures that do not reach the surface of the model follow a power law distribution as they plot on a straight line in the log-log plot. Modified after de Riese et al. (2020).

Hydrofractures reaching the surface of the model domain transport the entire fluid volume with few but large events (Fig. 10). These large events can be called 'dragon kings' (Sornette, 2009), which are outliers coexisting with power-law distributions, but taking on very high values far beyond those of the power-law distribution. They are usually associated with the development of a tipping point or a bifurcation (Sornette, 2009). They are linked to the small hydrofractures that self-organise the fluid-pressure distribution, trigger avalanches and therefore initiate large fluid-escape events (Bons et al., 2009; de Riese et al., 2020). These large fluid-escape events transport very large fluid volumes with a high velocity from depth to shallow levels in the crust, where they can form hydraulic breccias. If the ascent of fluid is fast enough, as in the case of hydrofracture propagation (Bons, 2001), fluids would not be able to decrease their temperature significantly and, as they may have high concentrations of dissolved elements, these fluids could deposit ores and cause extensive rock alteration. The Black Forest ore province (SW Germany) is characterised by a large number of small ore deposits (Staude et al., 2009), which could have been produced by a large number of small fluid escape events (Bons et al., 2014). It is of interest to note that the volumes of these deposits follow a power law (Fig. 4 in Staude et al., 2009).

4. When is a fracture or vein a hydrofracture?

In this chapter we address the question how to determine whether a fracture or vein found in the geological record was formed as a hydrofracture, and thus could be an indicator of elevated fluid pressure at the time of its formation. Hydrofracturing may appear obvious in the case of igneous dykes, *i.e.*, originally magma-filled fractures. With the frozen magma still preserved inside the fractures it is clear that the fluid 'magma' caused or at least played a significant role in the formation, opening, and propagation of the fractures. In other cases, the question may be more difficult to answer.

4.a. Hydrofractures and depth

Extensional veins are often assumed to have formed from tensional failure (see discussion below), and therefore to indicate elevated fluid pressure or hydrofracturing (*e.g.* Cobbold & Rodrigues, 2007) on Earth, but also on Mars (e.g. Caswell & Milliken, 2017; Kronyak et al., 2019). The rationale is that the Mohr circle for stress must touch the failure envelope in the negative normal stress region to induce extensional (pure mode I or hybrid) fractures. This implies that both the mean stress (midpoint of the Mohr circle) and the differential stress (the diameter of the Mohr circle) are limited in magnitude, because a larger Mohr circle would touch the failure envelope in the non-dilatant shear-fracture regime. Without an elevated fluid pressure, a small mean stress is only found at shallow depths. At greater depths this can only be achieved with an elevated fluid pressure. Etheridge (1983) used this logic to argue that under metamorphic conditions fluids are usually overpressured and differential stresses are limited because extensional veins are common in metamorphic rocks.

Extensional fractures that formed under metamorphic conditions, at depths greater than about 10 km, are hydrofractures as they can only occur when the fluid pressure is raised significantly. However, for extensional fractures formed at shallow depths it is less clear whether they are hydrofractures as they could potentially also be caused by tectonic stresses without a reduction of the effective stresses due to an elevated fluid pressure. We define the critical depth (z_{crit}) as the depth below which extensional fractures can be assumed hydrofractures. Both Sibson (2000a) and Gudmundsson (2011) use $g \cdot \rho_{rock} \cdot z_{crit} = -3T$ that is derived from the Griffith criterion to obtain a maximum depth of 1-2 km for purely tectonic extensional fractures, i.e., those that formed without a contribution of the fluid pressure. Both authors base their outcome on the generally low tensional strengths of bulk rocks, between -3 and -6 MPa according to Gudmundsson (2011). However, Hooker et al. (2015) describe quartz veins that they argue formed as infill of ca 6 km deep tectonic fractures in the absence of an elevated fluid pressure. The authors used C=60 MPa, T=-25 MPa and μ=0.6.

Above we defined hydrofractures as those fractures whose failure was caused primarily by fluid overpressure (P_f). We now define 'primarily' as $P_f \geq (\sigma_1-\sigma_3)/2$, with σ_1 and σ_3 the effective stresses at the point of failure to take into account that the Mohr circle can change in size as fluid pressure changes (Fig. 2). This means that for a hydrofracture the shift of the Mohr circle is larger than the radius of the Mohr circle at the moment of failure.

The Griffith criterion only takes T into account and not the angle of internal friction for $\sigma_n>0$. Here we propose to also use the criteria for shear failure (C and μ or ψ), in addition to T. We neglect hybrid failure, but the poorly constrained hybrid failure criteria allow this simplification. The intention is to find a rough depth below which extensional fractures are most likely hydrofractures. Using these failure criteria, one can find the Mohr circle that touches the failure envelope both at the tensional failure criterion and at that for shear failure (orange circle in figure 1c, and Fig 11a) (Behrmann, 1991). A smaller circle positioned further left will only cause tensional failure, while a larger circle further to the right only shear failure. The principal stresses for a circle that touches the shear failure criterion are given by:

$$\frac{(\sigma_1 - \sigma_3)}{2}\cos\psi = c + \tan\psi\left(\frac{\sigma_1+\sigma_3}{2} - \frac{\sigma_1 - \sigma_3}{2}\sin\psi\right) \qquad \textit{(eq. 18)}$$

The circle reaches the tensional failure criterion at the same time, giving $\sigma_3=T$, giving:

$$\sigma_1 = \frac{\frac{2c}{\tan\psi} + \left(\frac{\cos\psi}{\tan\psi} + 1 + \sin\psi\right)T}{\frac{\cos\psi}{\tan\psi} - 1 + \sin\psi} \qquad \textit{(eq. 19)}$$

In an Andersonian stress configuration the vertical stress at depth z is $\rho_{rock}\cdot g\cdot z$, but the horizontal stress can deviate from this value. A vertical extensional fracture can form if the horizontal effective stress is reduced enough to reach T. We combine the criterion that at the critical depth both tensional and shear failure occur (Eq. 19) and that the fluid pressure is half the diameter of the Mohr circle to obtain:

$$\sigma_1 + P_f = \sigma_1 + \frac{\sigma_1 - T}{2} = \rho g z_{crit} \Leftrightarrow z_{crit} = \frac{3\sigma_1 - T}{2\rho g} \quad \textit{(eq. 20)}$$

Note that we only deal with stress conditions and can thus use Terzaghi's principle without taking into account poro-elastic effects. For these the reader is referred to Olson et al. (2009). Combining Eqs (19) and (20) now gives the critical depth, below which fluid pressure must have contributed at least 50% to tensional failure, as a function of C, T and ψ. We see in Fig. 11 that z_{crit} strongly depends on the assumed failure criteria and can theoretically reach well over 5 km, especially if cohesion is high. However, if the effective tensional strength and cohesion of bulk rocks are indeed rather small, much shallower critical depths are obtained, such as the ~1 km of Gudmundsson (2011) or ~2 km of Sibson (2000a). As our derivation of z_{crit} is not for a dry rock, but for a 50% contribution to failure of fluid pressure, we suggest using a critical depth range of ca 2-3 km below which extensional fractures under most circumstances must have formed with a significantly elevated fluid pressure and can thus be regarded hydrofractures. This maximum depth of tensional failure without high fluid pressure roughly coincides with the calculations of Bourne (2003) for the formation of extensional fractures in multilayer systems that are subjected to remote compression in which alternating beds have contrasting elastic properties. This of course cannot simply be applied to extensional fractures that form part of a fracture network, like extensional jogs in a shear fracture. The above Mohr-Coulomb construction of an isotropic rock does not apply to such more complex systems (Koehn et al. 2005). Based on similar approaches as those presented in this section, other studies proposed shallow depths for the formation of hydrofractures for vein networks, using the elastic crack theory and the vein mean aspect ratio (Philipp, 2012).

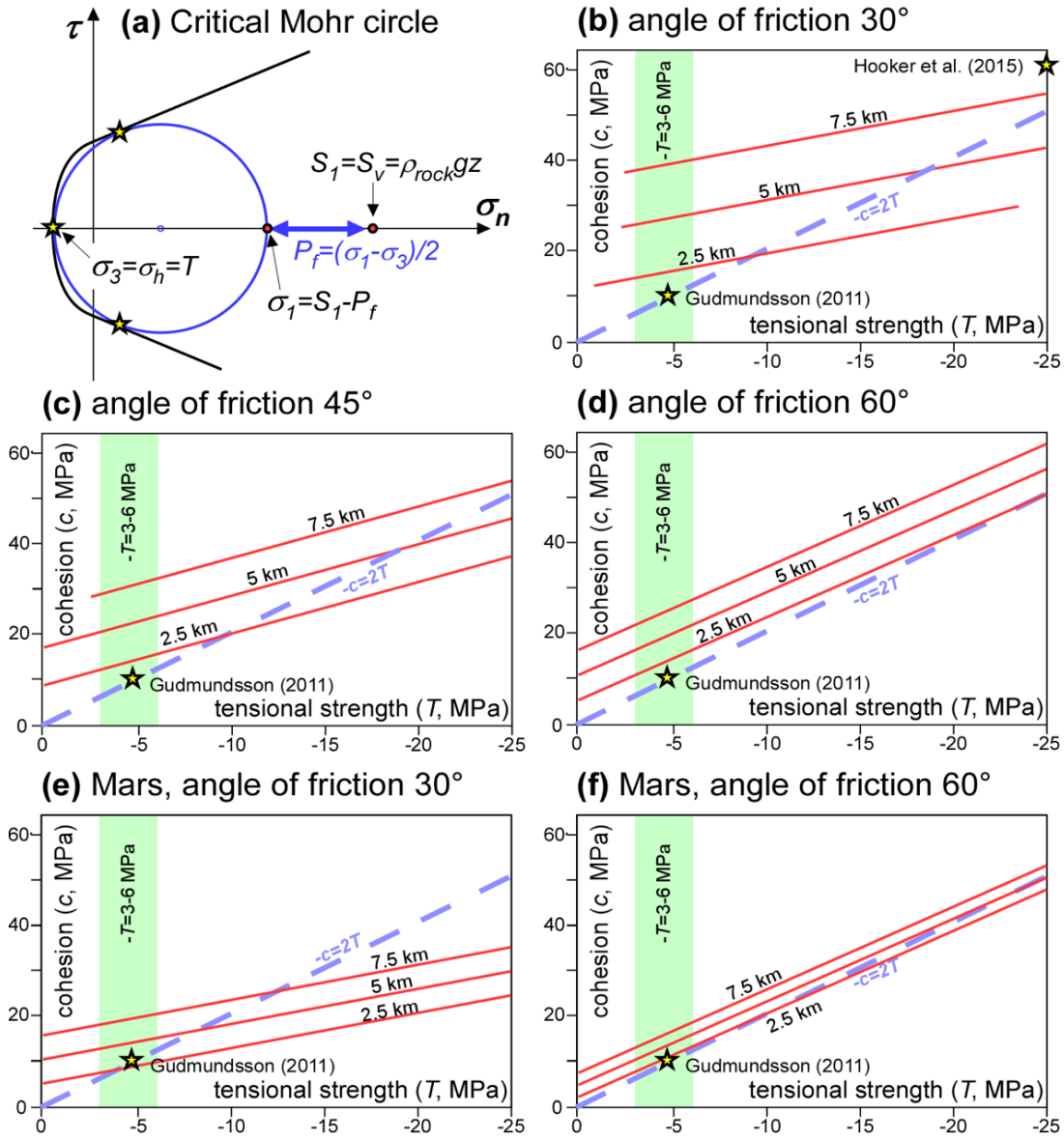

Fig. 11. Maximum depth of tectonic extensional fractures. (a) Mohr-Coulomb diagram with Mohr circle that touches (stars) the failure envelope at both the criterion for tensional failure and for shear failure. When P_f is more than the radius of the Mohr circle, we regard failure as dominantly caused by the elevated fluid pressure, i.e. a hydrofracture. The depth at which this occurs is z_{crit}. (b-d) Graphs of different values of z_{crit} as a function of cohesion (c) and absolute tensional strength (T), and for different angles of internal friction for the Earth's gravitational acceleration of g=9.81 m/s^2 and an assumed rock density of ρ_{rock}=2500 kg/m^3. (e-f) Same graphs for Mars with g=3.721 m/s^2 and ρ_{rock}=3000 kg/m^3.

Mineral veins in sediments on Mars have been interpreted as hydrofractures (Kronyak et al., 2019). However, gravitational acceleration on Mars is only 3.721 m/s^2. Although the olivine-rich clastic sediments may have a higher density, the product of rock density by *g* on Mars is less than half that on Earth, when using rock densities of 3,000 kg/m^3 and 2,500 kg/m^3,

respectively. This means (Eq. 20) that z_{crit} on Mars is more than double that on Earth for the same failure criteria. Unless the depth of formation of the Mars veins can be constrained, care must be taken in using the presence of veins as evidence for hydrofracturing.

The above certainly does not imply that all fractures that formed at a shallower depth than z_{crit} are not hydrofractures. It only means that the mere presence of fractures is not enough to state that fluid pressure was the dominant cause for the fracturing. Additional information can of course further constrain the fluid pressure state. In a basin at rest, for example, one knows that tectonic stresses cannot have caused the fracturing, as otherwise it would not be at rest. Horizontal extensional fractures in such a basin must have formed from fluid overpressure (Eq. 11). However, on Mars, for example, palaeo-stress conditions are poorly constrained and meteorite impacts may have also contributed significantly to fracturing.

4.b. Veins as potential fossil hydrofractures

Formerly open fractures in the geological record are typically identified as veins that are originally open fractures in which the fluid-filled space is now filled by minerals that precipitated from a fluid (Bons et al., 2012). There is no reason to assume that open fractures are always filled with minerals. Instead, they can also remain open, or completely or partially close again. Becker et al. (2010), for example, show that quartz veins in the East Texas Basin (USA) remained (partially) open for 48 Myr. The opposite would be the case in mobile hydrofractures (Bons, 2001), where the fracture propagates and opens at its upper end while closing at its lower one. This process is assumed to be rapid enough to not allow for any significant mineral precipitation to occur in the time that at any one location the fracture is open. Especially for quartz these assumptions seems warranted considering the slow growth rates of <1 mm/Myr up to 250 °C reported by Lander & Laubach (2015). These authors, but also for example Laubach et al. (2004), describe how cracks can be partially filled with bridging crystals that leave fracture porosity in between, as revealed by cathodoluminescence. In some cases it

may be possible to recognise a formerly open fracture that subsequently closed again, maybe only partially filled with minerals, by the distortion of the rock around the former fracture (Fisher & Brantley, 1992; Bons et al., 2008) (Fig. 12).

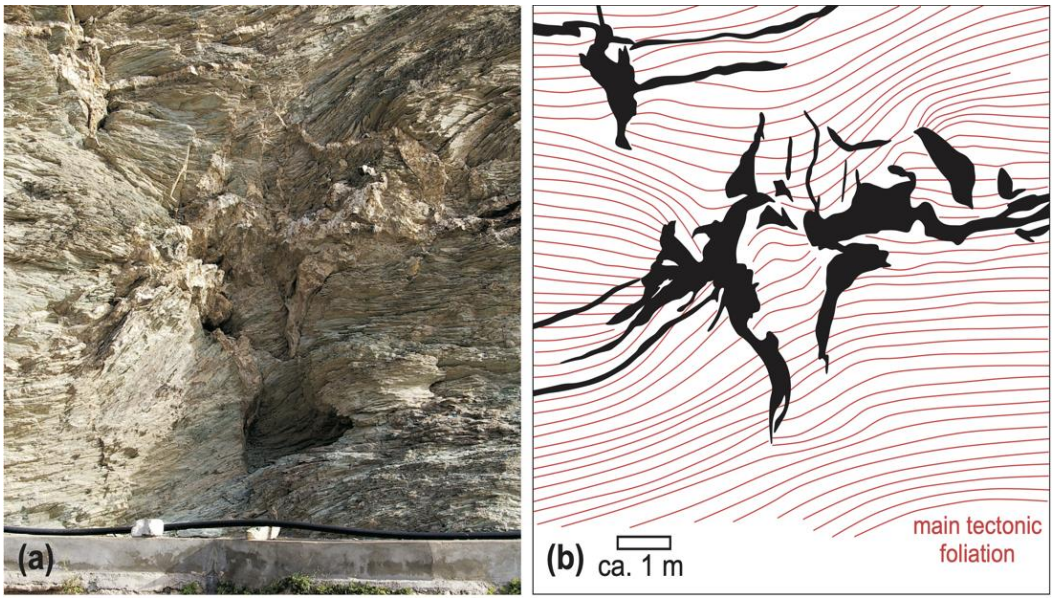

Fig. 12. (a) Network of quartz veins in basement rocks of the Jabal Akhdar dome in Oman (Gomez-Rivas et al., 2014; Ghani et al., 2015). (b) Drawing of the veins and traces of the main tectonic foliation. Inward bending of the foliation indicates that the original fractures, now filled with quartz, partly collapsed.

Veins can provide indications of the stress and fluid pressure conditions at the time of their formation, firstly, by their shape or orientation, and secondly by their internal structure. Moreover, fluid inclusions within vein cement can be used to systematically unravel palaeo fluid pressures (Becker et al., 2010). Durney & Ramsay (1973) introduced the basic terminology and classification of internal vein structures that is still widely used today. It consists of (i) the growth direction of vein crystals relative to the wall rock, and (ii) the morphology of these crystals. This results in three main vein categories (Bons et al., 2012). First, syntaxial veins with blocky or elongate blocky crystals that consistently grow from the wall-rock substrate towards the middle of the vein (Fig. 13a). Second, stretching, or ataxial veins with stretched crystals that grew by repeated fracturing and sealing (Ramsay, 1980) and

that may not show any preferred growth direction (Fig. 13b-c). Finally, antitaxial veins with fibrous crystals that grow against the wall rock as the vein widens (Fig. 13d-e).

The crack-seal theory of Ramsay (1980) is fundamental to the understanding of the formation of veins from fractures. He showed that veins can form by repeated failure that results in opening of a fracture (the 'crack' stage), and subsequent filling of the fluid-filled space with minerals (the 'seal' stage). Mineral precipitation is usually by epitaxial overgrowth of mineral grains at the fracture surfaces, as is visible by the optical continuity between old and new growth stages (Urai et al., 1991; Laubach et al., 2004; Späth et al., 2021). A crack-sealing cycle can occur once for a vein, but also many times, each time adding a slice of mineral precipitate to the widening vein. If the width of the open fracture is large relative to the width of the seed crystals for the mineral veins, we usually observe competitive growth of vein crystals from the fracture surfaces into the fracture space. As a result, some crystals outgrow their neighbours, and the mean crystal width increases towards the middle of the vein (Fig. 13a). This is the classical syntaxial vein geometry in which the crystals typically have blade-like or elongate-blocky shapes (Durney & Ramsay, 1973; Fisher & Brantley, 1992; Hilgers et al., 2001; Okamoto & Sekine, 2011; Späth et al., 2021). Although the original work of Ramsay (1980) and many other subsequent papers assume that the whole crack fills with minerals before the next crack event, this is not always the case, especially under diagenetic conditions. Isolated crystals my already span the crack, while leaving open pore space in between (Laubach et al., 2004; Kling et al., 2017; Späth et al., 2022), or cracks may only fill completely near their tips, but not in their wider central parts (Bons et al., 2012).

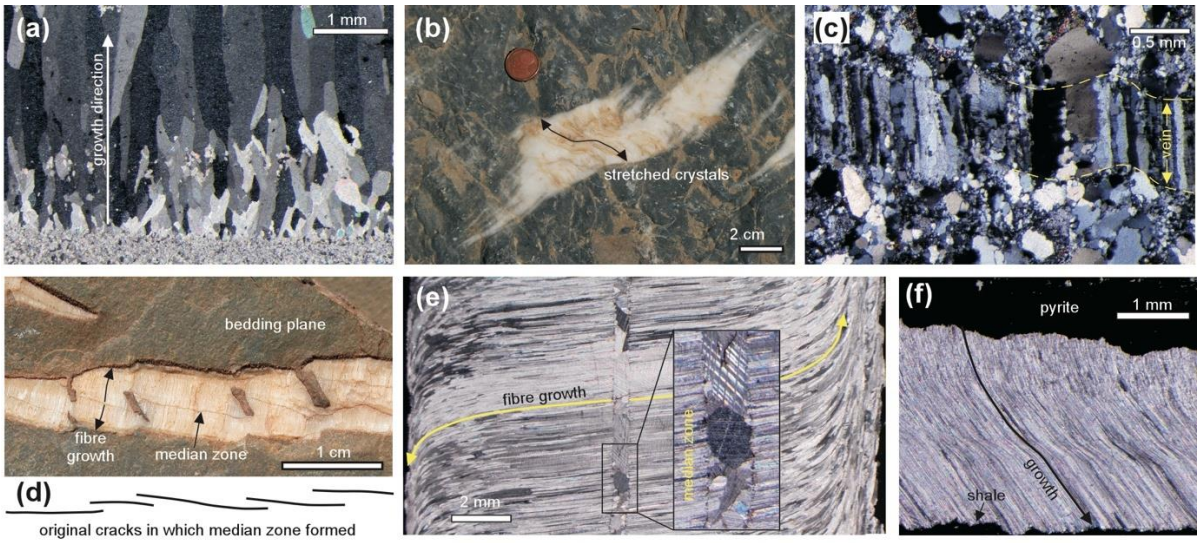

Fig. 13. Representative images of (a) syntaxial, (b-c) stretching, and (d-f) antitiaxial or beef vein types. (a) Syntaxial calcite vein from Biure (NE Spain) showing clear growth competition in the upward growth direction. (b) Stretching vein from the Jabal Akhdar dome, Oman, with long stretched calcite and quartz crystals. The tips of the vein show that the vein formed by many individual crack-seal events. (c) Quartz vein with stretched crystals with parallel serrate boundaries, indicating multiple crack seal events. Yudnamutana, Mt Painter Inlier, South Australia. (d) Antitaxial, fibrous (beef) vein from Oppaminda Ck, Mt Painter Inlier, South Australia. The vein formed by outward growth from originally narrow en-échelon crack-fills shown below. (e) Antitxial fibrous vein from same locality, showing symmetry of curvature of the smooth fibres (compare with (c)) on both side of the median zone, which itself has a very different internal structure. (f) Fibrous vein where the fibres are not seeded on a median zone, but on a layer of pyrite. Minor coarsening of the smooth fibres show the growth direction, with the fibre tips growing against the host-rock shale. Drill core sample of the Lower Silurian Longmaxi Formation shale, Luzhou Block, Southern Sichuan Basin, China.

The crack-seal cycle can also occur many times during the growth of a single vein. The narrow width of the open fracture in each individual crack-seal event inhibits growth competition (Hilgers et al., 2001). Furthermore, the location of each new open fracture may differ from that of the previous one. As a result, individual vein crystals are stretched by inserting slice after slice of epitaxially grown mineral in the gap formed in the crystal each crack-seal cycle. These vein crystals do, therefore, usually not show a consistent widening in one direction, but can become long and narrow (Fig. 13b), often called ‘fibres’, although we prefer the term ‘stretched crystals’ (Bons et al., 2012). The veins are termed ‘stretching veins’ or ‘ataxial veins’ (Passchier & Trouw, 2005), as their crystals show no consistent growth direction. Repeated crack-sealing

can be recognised by the stretched-crystal morphology, where the boundaries between individual crystals are often serrate on the length scale of the individual fracture widths ('radiator structure'; Fig. 13c) and the presence of fracture-parallel bands of fluid inclusions, wall-rock particles, or secondary minerals (Ramsay, 1980; Renard et al., 2005). It should also be noted that an open crack need not fill evenly, but some individual crystal may outgrow others to form bridges across the crack and incrementally restore cohesion until a new failure event occurs (Laubach et al., 2019; Späth et al. 2022). Crystal morphology in crack-seal veins can therefore be variable and repeated crack-sealing may sometimes only be revealed with cathodoluminescence (Laubach et al., 2004; Gale et al., 2010). Syntaxial and ataxial vein growth are endmembers of a continuum and both growth modes may operate in one single vein (Bons et al., 2012).

Recognising crack-sealing in veins is of importance as each crack-seal cycle represents a point in time where the stress and fluid-pressure conditions were such that a dilatant fracture could form to provide the space for subsequent sealing by mineral growth. It is therefore also of equal importance to recognise those veins whose internal structure does not indicate crack-sealing.

Some veins consist of distinctly fibrous crystals that are aligned parallel to each other and that have smooth boundaries. They are often referred to as 'beef veins', as the fibrous texture is reminiscent of beef (Buckland & De La Beche, 1835). Gypsum, calcite and quartz are the most common minerals to form beef veins (Cobbold et al., 2013). Durney & Ramsay (1973) introduced the term 'antitaxial' for veins in which the vein-filling crystals grow outwards towards the vein-wall rock interfaces (Fig. 13d). Crystal growth in antitaxial veins is seeded on what they termed a 'median line', but which Oliver & Bons (2001) termed a 'median zone', as it usually has a finite width (Fig. 13e). Antitaxial veins can be also called beef veins, as their vein crystals are smooth and fibrous. In the literature, the term 'beef' is often used for bedding-parallel fibrous veins, while 'antitaxial' is more often used for fibrous veins in general orientations. Beef veins may lack a median zone, that forms part of the definition of antitxial

veins (Durney & Ramsay, 1973; Passchier & Trouw, 2005; Bons et al., 2012). It should also be noted that the term 'fibrous' is sometimes used for any elongate veins crystals (e.g., Cox, 1987; Zhang et al., 2015) and then erroneously compared to antitaxial or beef veins, because these are fibrous. The term 'fibrous' should therefore only apply to very to extremely elongate crystals with parallel smooth boundaries (Oliver & Bons, 2001).

Many authors recognised the association of fibrous calcite (±quartz) veins with hydrocarbon generation during thermal maturation of organic matter (Bredehoeft et al., 1976; Osborne & Swarbrick, 1997; Cobbold & Rodrigues, 2007; Cobbold et al., 2013; Zanella, Cobbold & Boassen, 2015; Wang et al., 2018; Hooker et al., 2020). Fibrous calcite veins are most common in organic carbon-rich shales (Fig. 13f) and often contain solid bitumen inclusions or hydrocarbon inclusions, which are further indications that the vein formation was synchronous with hydrocarbon generation (Zanella et al., 2015a; Wang et al., 2018; Su et al., 2021). The assumption that fibrous veins are formed by extensional fracturing has led the aforementioned authors and others (e.g. Cosgrove, 2001) to infer that these veins indicate hydrofracturing due to fluid overpressure, possibly caused by hydrocarbon generation during thermal maturation of organic matter. In case that the veins are parallel to horizontal bedding, this would imply that the fluid pressure must have exceeded the vertical overburden load (Section 3.a.2). However, as discussed by Cobbold et al., (2013), it is far from certain that fibrous crystal growth is the result of crack-sealing.

It was already suggested by Taber (1918) that growth must have been continuous, with the crystal-growth front at all times keeping track with the diverging wall rock (Durney & Ramsay, 1973; Urai et al., 1991). This is consistent with the smooth fibre boundaries and lack or suppression of growth competition (Mügge, 1928; Hilgers et al., 2001; Bons & Montenari, 2005). A further argument against growth of the fibres in an open fracture is that fibrous veins can grow simultaneously on both sides of a vein and it seems mechanically improbable that two parallel fractures exist on both sides of a growing vein (Bons & Montenari, 2005). The

simultaneous growth on the outer surfaces of antitaxial veins is particularly conspicuous at intersections of antitaxial veins of different orientations. Here we can observe that both the old and new generation keep widening at their outer surface (Fig. 7 in Oliver & Bons, 2001).

This aggregate of arguments suggests that fibrous growth occurs in the absence of open fractures (Taber, 1918; Mügge, 1928; Bons & Jessell, 1997; Means & Li, 2001; Wiltschko & Morse, 2001; Oliver & Bons, 2001; Meng, Hooker & Cartwright, 2019; Luan et al., 2019; Su et al., 2021). It should be noted that median zones tend to have a different microstructure, typically one that does indicate crack-sealing (Fig. 13e), which led Bons & Montenari (2005) to propose that fibrous veins can be seeded on (narrow) crack-seal veins, but that a switch in the growth mechanism subsequently occurs to fibrous growth without crack-sealing (Su et al., 2021). However, some fibrous veins lack a median zone (Fig. 13f) and they may thus never have experienced any crack-sealing. Instead, the fibrous crystals appear to be seeded on a bed interface or lamination. A number of driving forces for fibrous growth in the absence of an open fracture has been suggested, such as the force of crystallisation (Means & Li, 2001), concentration gradients due to stress or pressure gradients that drive dissolution-precipitation reactions (Fletcher & Merino, 2001; Bons & Montenari, 2005), or even microbial activity (Bons et al., 2007).

As the mechanism of fibrous or beef growth remains enigmatic, care should be taken to infer fluid pressure from such veins and they should not be automatically equated with hydrofractures. We favour distinguishing between the conditions of (i) vein initiation where the median zone (even when completely on one side) is formed from (ii) the subsequent fibrous grows by which the vein widens. Geometry, orientation and internal microstructure of the median zone may indicate a significantly elevated fluid pressure at time of formation. Especially the median zones of horizontal fibrous or beef veins in organic matter-rich shales are probably the result of elevated fluid pressure (Eq. 11, Fig. 2b) that result from hydrocarbon release (see references above). However, the 'Taber school' (based on Taber, 1918) argues that

the outer vein surface is not a crack, but a cohesive interface, where the fibres grow against the wall rock. Whether they do, will depend on the ambient tectonic stress (Fletcher & Merino, 2001) and probably fluid pressure as well, and of course the rock type, minerals involved, etc. Still if the fibres grow in the absence of a fracture, the resulting fibrous vein cannot be called a hydrofracture.

4.c. Breccias

Breccias are rock masses that are composed of broken rock fragments. Breccias can be of a variety of origins. Aside from impact and sedimentary breccias, or those formed by tectonic diminution in faults due to tectonic stresses (e.g., Sibson, 1986; Keulen et al., 2007; Mort & Woodcock, 2008), they can also develop by intensive hydrofracturing due to fluid overpressure as of interest here (Jébrak, 1997; Laznicka, 1989; Lorilleux et al., 2002; Weisheit et al., 2013a). Long distance transport of clasts, and structures that indicate fluidisation, suggest that fluid flow velocities may be as high as m/s (Oliver et al., 2006b). Eichhubl (2000) and Okamoto & Tsuchiya (2009) estimated fluid velocities of 0-01 – 0.1 m/s, while Oliver et al. (2006b) estimated velocities of 5 m/s in the case of a fluidised breccia with m-sized clasts.

To give an example, the Hidden Valley breccia in the Northern Flinders Ranges of South Australia is a massive hydrothermal breccia with a size of about 10 km^2 in outcrop (Weisheit et al., 2013a). The breccia features a continuous power-law distribution of clast sizes that span over six orders of magnitude. Mixed clasts that were originally several km vertically apart are observed. Using thermogeochronology Weisheit et al. (2013b) inferred that the breccia formation extended over a period of more than 150 Myrs during the exhumation of basement gneisses by over 12 km. The estimated total fluid budget responsible for the development of this breccia is about 20 km^3 (Weisheit et al., 2013a). Biotite dehydration seems to be the main fluid source in this case.

To distinguish hydraulic breccias from other types of breccias, the clast size morphology and distribution can be used, in particular their fractal dimension, which is related to the rock fragmentation process (Blenkinsop, 1991; Jébrak, 1997; Lorilleux et al., 2002; Barnett, 2004; Keulen et al., 2007; Weisheit et al., 2013a). The fractal dimension for the size distribution is defined as the absolute power-law exponent (m) that is obtained when the number of breccia clasts that is larger than a certain size is plotted against that size (see e.g. Blenkinsop (1991) for the calculation). Weisheit et al. (2013a) found a constant exponent m_{2D} of about one (using the two-dimensional clast area as the measure of size) for clast areas from about 1 mm^2 to almost 1 km^2. The power-law distribution evidences that the fragmentation process is scale-invariant (Turcotte, 1986), and also emphasises the dynamical behaviour of the fluid flow that produced the breccia. Jébrak (1997) and Barnett (2004) found that hydraulic brecciation results in a small exponent (m≈1), whereas wear abrasion and shear results in larger exponents (m≈2-3), meaning there are relatively many small clasts compared to large ones. The small exponent of about one obtained for the Hidden Valley breccia by Weisheit et al. (2013a) thus indicates it formed by hydraulic brecciation. Round clast shapes and the absence of tectonic structures further confirm a hydraulic origin (Weisheit et al., 2013a). Another indicator is the strong alteration of this breccia which indicates the passage of large fluid volumes.

Weisheit et al. (2013a) argued that, assuming a porosity of 10% and a flow rate of 1 m/s, the estimated cumulative duration of flow through each part of the breccia would be about $2 \cdot 10^4$ s, which is less than a day. Even if the flow rate would be much smaller, the total flow duration would still be a minute fraction of the tens of million years it took to form the breccia. The required fast fluid flow must therefore be highly intermittent with short bursts of flow and very long periods of fluid pressure build-up. The Hidden Valley brecciation could be equivalent to the extremely large fluid escape events in the numerical simulations of de Riese et al. (2020) and shown in figures 9 and 10 with a high proportion of fluid pressure diffusion to accumulate the large fluid volume to create the 10 km^2 breccia.

4.d Recognising hydrofractures in the geological record

This section provides some examples of hydrofracturing in different tectonic settings. Examples of different vein sets from the Ligurian Units near Sestri Levante, Italy, are given in figure 14. The units represent the marine Palombini shales that are thrusted first southwards and later eastwards towards the Apennine mountain chain. Veins in the units show a variety of geometries that point towards different importance of fluid overpressure during the initial fracturing, assuming the veins represent at least partly the original fracture pattern. Examples for high fluid overpressure and thus real hydrofractures include very intense veining in soft layers and within small sheared units (Fig. 14a-b), geometries where bedding parallel and perpendicular veins switch even though the veins are of the same age (Fig. 14a), and early bedding-parallel veins (Fig. 14d). Examples where differential stresses dominated the pattern include conjugate vein sets on bedding surfaces (Fig. 14c), fracture boudinage type veins that fractured layers (Fig. 14d), and extensional fold axis parallel veins that may have developed during folding (Fig. 14c). All the latter examples may have needed local or larger scale fluid overpressure to overcome tensile or shear stresses but fluid overpressure does not seem to have dominated the pattern. Therefore, we would not term them 'hydrofractures'. Real hydrofractures that develop due to a dominance of fluid overpressure are shown in the simulations in figure 4. Figures 4a-b show the development of horizontal fractures in layers or in a sedimentary basin when the fluid overpressure increases at the same rate in all nodes. This pattern represents the developing bedding-parallel veins in figure 14d, which were produced by fluid overpressure. The more complicated branching pattern with horizontal and vertical fractures as well as potentially many small and very closely aligned fractures develops in the simulations when a local region in the rock is over-pressured (Fig. 4c). If the pressurizing fluid is locally produced in layers within laterally confined cells, then a combination of the patterns shown in figures 4c and 4e may develop, which also fits the pattern in figure 14a. The pattern shown in figure 14b that develops in a small fault zone is extreme and potentially would be a further development

of the simulation shown in figure 4c in combination with shearing. It could also be compared with the numerical hydraulic breccia pattern shown in figure 5.

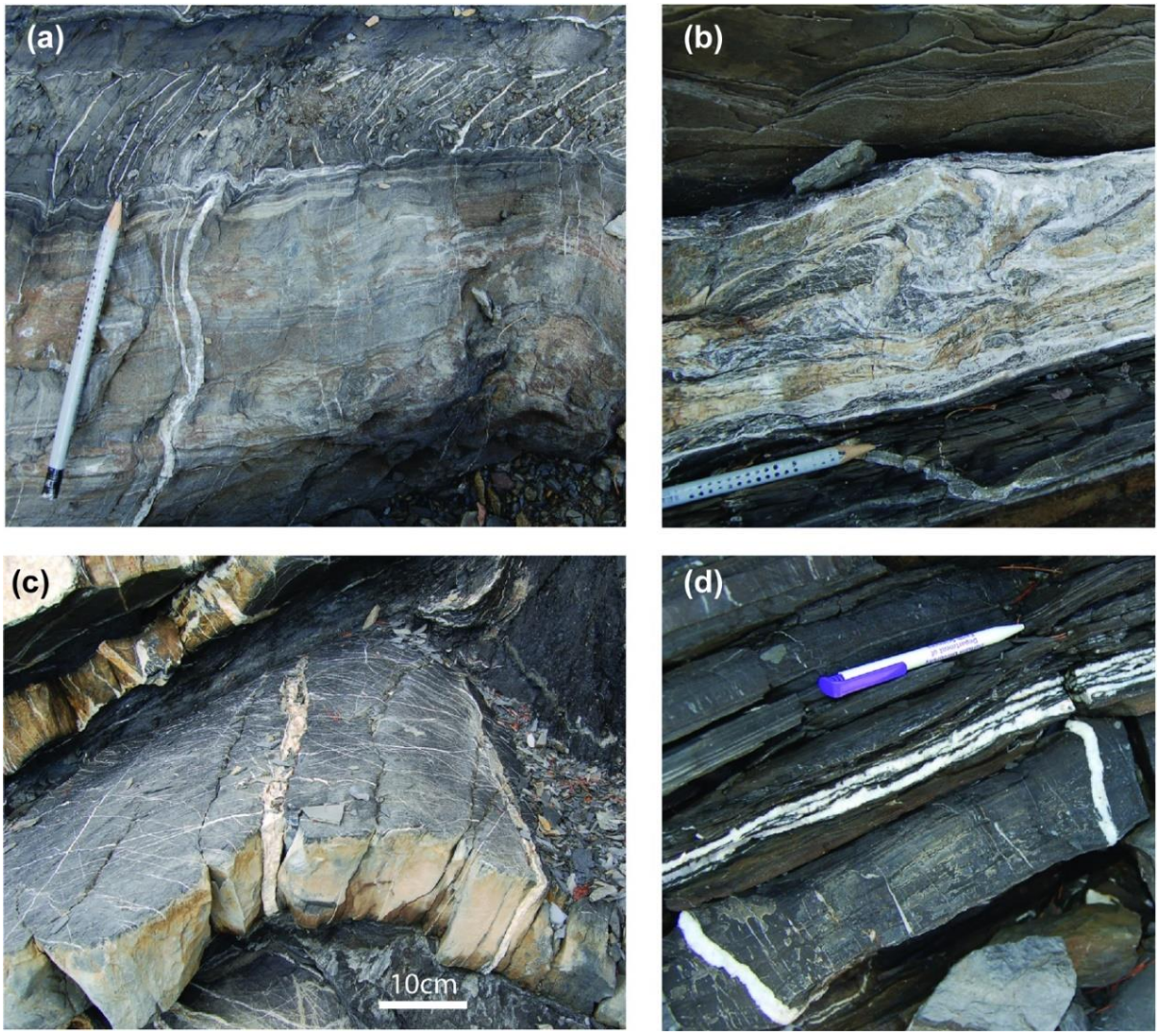

Figure 14. Veins from the Ligurian Units at Sestri Levante, Italy, representing different effects of the fluid pressure assuming they represent the initial fracture geometries. (a) Complex inter-fingering between bedding perpendicular and bedding parallel veins. (b) Intense veining in a small thrust fault zone. (c) Veins in folded layers with early conjugate and later fold axis parallel veins. (d) Early bedding-parallel veins and fracture boudinage type veins in a layer.

Another well-studied area with examples of the effect of fluid pressure on fracture and vein formation is the Jabal Akhdar Dome in the Oman Mountains (Oman) (Fig. 15). The complex tectonic evolution of this area can be traced from the cross-cutting relationships of different faults and sets of calcite veins (Gomez-Rivas et al., 2014). The area was first buried >8 km

under the Semail ophiolite and Hawasina nappes. It subsequently underwent strike-slip deformation from the Late Cretaceous to the Eocene due to the northwards movement of the neighbouring Indian plate. Although exhumation by erosion may have started during this time, the main exhumation happened after the main veining events discussed below. Strike-slip deformation led to the formation of intense calcite vein networks in conjugate sets. Such veins are hosted in limestones of the Cretaceous Shams, Nahr Umr and Natih Fm., just below the Muti Fm., which likely acted as a regional seal for interstitial fluids and fluids derived from the basement (Fig. 12). Extensional and hybrid veins that formed at depths around 8 km would require a significant fluid overpressure and may be assumed to have formed as hydrofractures (Section 4a). A hydrofracture origin is consistent with zones of intensive fracturing that resulted in the formation of veins with chaotic orientations (Fig. 15a-c). In this area there are also pavements (Fig. 14d-e) that contain networks of calcite veins typically arranged in en-échelon conjugate sets (and with crack-seal microstructures; Fig. 13b) (Bons et al., 2012; Gomez-Rivas et al., 2014) that formed under a rotating strike-slip stress field. Individual vein segments are oriented at a very low angle with respect to the principal compressive stress, while the acute angle between conjugate sets is also low (typically 15º-30º). These orientations reveal that such vein systems formed as hybrid fractures, with some individual segments also formed as extensional fractures, again indicating a system characterised by high fluid pressure. However, with these more regular vein sets that indicate a tectonic contribution to fracture orientations, it becomes difficult to ascertain the actual role of fluid overpressure, especially where the depth of fracturing is not well constrained.

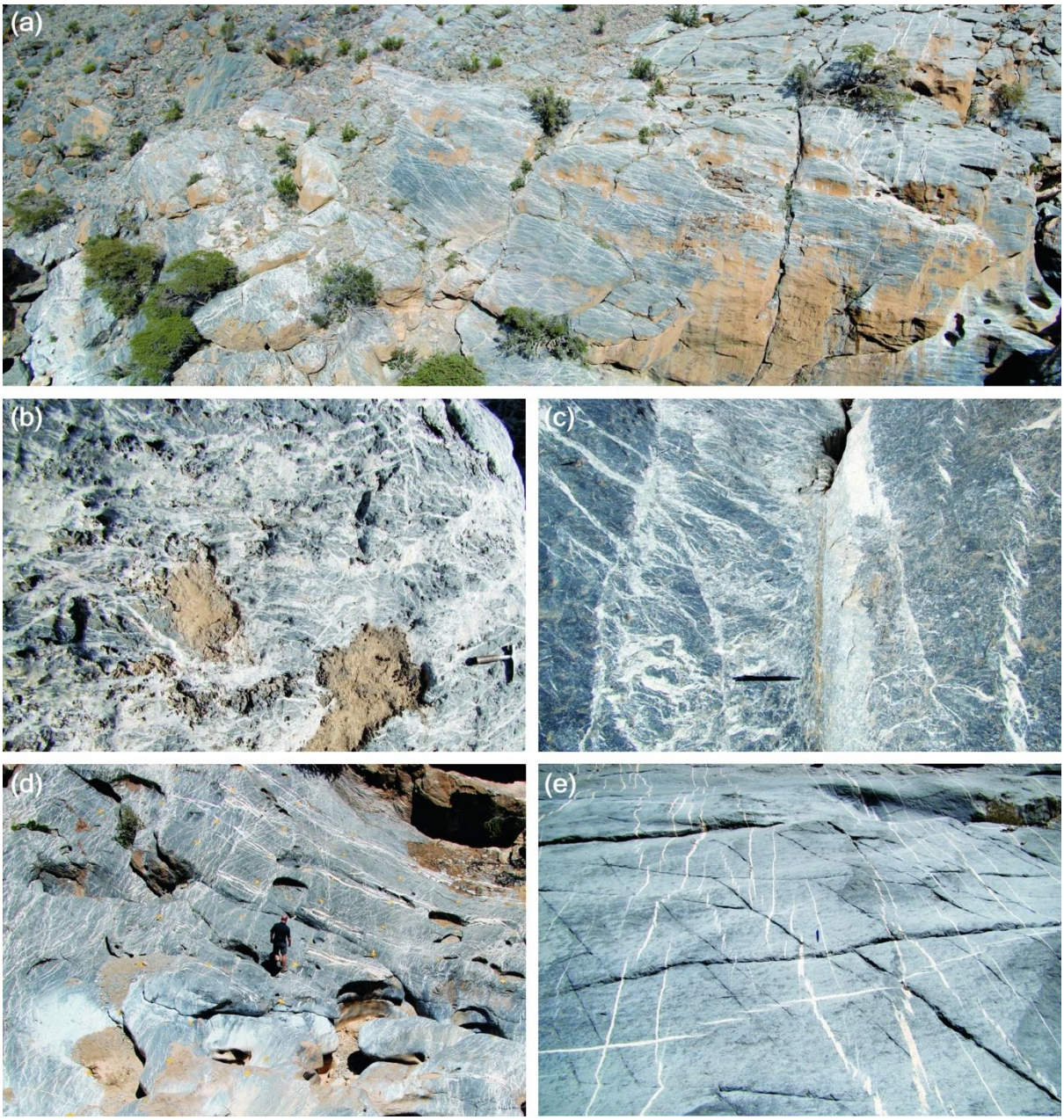

Fig. 15. Examples of calcite veins hosted in limestones of the Natih Formation from the Jabal Akhdar dome (Oman Mountains, Oman), which are interpreted to have formed in a system with relatively high fluid pressure. (a) Dense calcite vein networks with some veins showing systematic orientations while others form a chaotic mesh (Gorge pavement). (b) Detail of a zone with intense and chaotic calcite veining in (a). (c) Damage zone of an outcrop-scale strike-slip fault showing a dense mesh of calcite veins with variable orientations (Wadi Dam). (d) Pavement with different sets of systematically oriented conjugate crack-seal veins formed under different strike-slip stress fields (Wadi Guhl). (e) Detail of conjugate sets of en-échelon strike-slip veins (Gorge pavement). The acute angle between both sets is typically in the range 15º-30º, while individual segments form a very low angle with respect to the principal compressive stress. The dense vein meshes of (a), (b) and (c) clearly formed in a setting dominated by high fluid pressure at a certain depth, and thus formed by hydrofracturing. Systematically oriented strike-slip vein sets can be considered as formed from hybrid fractures in a system with relative high fluid pressure, owing to their orientation with respect to σ_1. For a detailed description of these veins see Gomez-Rivas et al. (2014).

Palaeostress inversion techniques aim to unravel the stress fields under which fractures, faults and other geological structures (e.g., veins, stylolites) formed. Some studies consider fluid pressure as a key parameter for palaeostress determination. Jolly and Sanderson (1997) propose and demonstrate a Mohr circle construction for the analysis of veins or dykes that allows to graphically estimate stress magnitudes and the relative fluid pressure, providing the range of fracture orientations that can open, together with their opening directions. This method is based on the approach by Delaney et al. (1986) that assumes that fractures are opened by fluid pressure when it exceeds the normal stress on the fracture planes. Yamaji et al. (2010) apply the same principle to propose a method for the estimation of the stress of state from clusters of veins formed from multiple events of ascending warm fluids with variable fluid pressures, assuming that most batches arrive at a lower fluid pressure than the maximum one. For that, they evaluate the stress of state of each vein cluster from an orientation distribution that best fits the vein orientation. Other authors carried out palaeostress determinations from veins and palaeo fluid pressure determinations from fluid inclusion microthermometry data (André et al., 2001) or in combination with geothermometers (Jaques & Pascal, 2017). The latter authors applied this method to a case study from the Panasqueira Mine (Portugal), to conclude that horizontal mode I veins formed as hydrofractures at a lithostatic fluid pressure at depths of around 10 km in a compressive stress regime. The reader is referred to Pascal (2021) for a thoughtful review of palaeostress inversion techniques.

5. Effects of hydrofractures in hydrocarbon and ore deposit systems and their relationship with geochemistry

Both natural and human-induced hydrofractures can either favour or constrain the origin, evolution, and exploitation of hydrocarbons. Moreover, understanding the formation mechanisms of hydrofractures and being able to predict their zones of formation is also key for the exploration and production of ore deposits (*e.g.*, vein stockworks and vein-type deposits,

Liu, et al., 2017 Sun et al., 2021), to enhance the production of geothermal energy (*e.g.*, Moska et al., 2021) and to ensure the safe geological storage of geo-energy products, such as captured CO_2, hydrogen, compressed air and natural gas (*e.g.*, U.S. Nuclear Regulatory Commission, 2009; Stork et al., 2015).

Human-induced hydrofracturing in hydrocarbon reservoirs has enabled two major innovations in the energy sector: (i) the enhanced recovery of reserves from producing fields, and (ii) the exploitation of unconventional reservoirs, *i.e.*, those low permeability, 'tight' reservoirs that cannot be exploited by using traditional extraction methods (including shale gas, tight sands gas and coal bed methane gas) (Bennion et al., 1996; Stanchits et al., 2011; Wang et al., 2014). Hydraulic fracturing is nowadays the principal technique for increasing and maintaining well productivity (Montgomery & Smith, 2010).

In the mining sector, hydrofracturing is also employed as a pre-conditioning and pre-weakening technique to induce caving and fragmentation of the orebodies in preparation of extraction (Katsaga et al., 2015; He et al., 2016). The occurrence of hydraulic fracturing is, however, also seen as a hazard during some types of mining operations. For example, during in-situ leach uranium recovery, lixiviant *excursions* can take place through the formation and propagation of hydrofractures in the ore zone and surrounding rocks, giving rise to an unintended spread that may affect the groundwater quality near the well fields (U.S. Nuclear Regulatory Commission, 2009). Natural hydrofracturing processes are also a key phenomenon for the formation and evolution of ore deposits. It is well known that ore deposits are often related to zones of localised deformation, such as fault zones, shear zones, fracture networks and other rock discontinuities (e.g., Groves et al., 2018; Chauvet, 2019). Hydrofracturing is an important mechanism for the generation of some of such zones, and the resulting hydrofractures can act either as conduits or barriers to fluids that transfer heat and chemical components at different levels of the Earth's crust. In particular those ore deposits genetically related to extensional fractures and that formed at a depth below 2-3 km from the Earth's surface are, according to

what has been suggested above, the result of hydrofracturing processes. The role of hydrofractures as fluid baffles or conduits mainly depends on whether they are sealed by mineral precipitation or, alternatively, remain open. In the first scenario, fluid pressure drops linked to failure events can trigger mineral precipitation, and if this process is repeated over a geological time, it can give rise to multi-stage mineralisations of different types (*e.g.*, Xiong et al., 2020; Sun et al., 2021). Otherwise, in the second scenario, the permeability enhancement produced by hydrofracturing can favour subsequent fluid circulation through fracture networks. However, not all fracture-related ore deposits are the result of hydrofracturing, and neither are all hydrofractures ore deposits. For example, Groves et al. (2018) suggested that the occurrence of hydrofractures in Neoarchean terranes could have caused high pressure variations leading to gold deposition through related chemical responses and fluid un-mixing episodes. However, in the same tectonic settings, the existence of "late fractures" (possibly hydrofractures) is also reported and linked to orogenic collapse, in all cases postdating the gold deposition (Vielreicher et al., 2016; Groves et al., 2018). Furthermore, when ore deposits are related to hydrofracturing, the cyclical evolution of fluid pressure and resulting failure events generally give rise to complex geochemical patterns that evolve from repeated depletion to enrichment patterns and from randomly-distributed to spatially-clustered structures, as demonstrated by Xiong et al., (2020) through numerical modelling. Recent advances in the understanding of the relationships between fluid composition, chemical reactions, fracture formation and fracture propagation demonstrate that, in the diagenetic regime (~50-200 °C), there are more profound interactions between these factors than assumed so far (see a review in Laubach et al., 2019).

6. Conclusions

Hydrofracturing, the process of rock failure that is primarily induced by an elevated fluid pressure, is an omnipresent tool in hydrocarbon and ore production, but also geothermal energy generation and underground storage of CO_2, natural gas or nuclear waste. Here we also show

that most natural extensional fractures (pure mode I or hybrid) that formed below about 2-3 km depth on Earth can, for typical rock mechanical properties, probably only have formed as hydrofractures.

We discuss the two main approaches to assess the effect on failure of an elevated fluid pressure: the effective stress according to Terzaghi's and Biot's theory. The two theories are not contradictory but apply depending on the stress and or elastic strain boundary conditions.

Initial failure can be predicted with the Mohr-Coulomb-Griffith theory and appropriate effective stresses. Systems with fractures, however, evolve after fractures first form. Depending on the rate of overpressure generation a system may reach an equilibrium in which fractures form and provide sufficient additional permeability to drain the fluid influx that caused the overpressure. Such systems can also become highly dynamic and self-organise. This leads to fluctuations in fluid pressure and fracture activity. We discuss how the interplay between porous flow and dynamic fracture flow can result in cyclical behaviour and major fluid drainage events.

Finally, we discuss, with examples, veins and breccias that are the products of hydrofracturing. Numerical models show that patterns of veins can be indications of hydrofracturing, especially chaotic, or breccia-like vein patterns. However, we also emphasise that not all veins are former fractures, for example fibrous or 'beef' veins.

Acknowledgements

This study was supported by research projects PID2020-118999GB-I00 and PGC2018-093903-B-C22 (Spanish Ministry of Science and Innovation (MCIN) / State Research Agency of Spain (AEI)). HT and DC acknowledge funding by the Chinese Scholarship Council (CSC) with grant numbers 202006440101 and 202006440128, respectively. EGE acknowledges the PhD grant 2021 FI_B 00165 funded by the Generalitat de Catalunya and the European Social Fund. EGE and EGR acknowledge funding provided by the Grup Consolidat de Recerca 'Geologia Sedimentària' (2017SGR-824). IN wishes to acknowledge funding provided by the DAAD:

German Academic Exchange Service (DAAD), Section ST32, grant nr. 91731924. DK acknowledges funding by the Bavarian Ministry of Science and Art (StMWK) funded projects 'langfristig' and 'regional' of the Geothermal Alliance Bavaria (GAB). EGR acknowledges the Ramón y Cajal Fellowship RYC2018-026335-I, funded by the Spanish Ministry of Science and Innovation (MCIN) / State Research Agency of Spain (AEI) / European Regional Development Fund (ERDF) /10.13039/501100011033. We thank our four reviewers for their abundant and constructive comments.

Declaration of Interest

The authors declare none.

References

ALEKSANS, J., KOEHN, D., TOUSSAINT, R. & DANIEL, G. 2020. Simulating Hydraulic Fracturing: Failure in Soft Versus Hard Rocks. *Pure and Applied Geophysics* **177**(6), 2771–2789.

ANDERSON, E.M. 1905. The dynamics of faulting. *Transactions of the Edinburgh Geological Society* **8**, 387-402.

ANDERSON, E.M. 1939.The dynamics of sheet intrusion. *Proceedings of the Royal Society of Edinburgh* **58**, 242-251.

ANDRÉ, A.-S., SAUSSE, J., & LESPINASSE, M. 2001. New approach for the quantification of paleostress magnitudes: application to the Soultz vein system (Rhine Graben, France). *Tectonophysics* **336**, 215-231.

ATKINSON, B.K. 1984. Subcritical crack growth in geological materials. *Journal of Geophysical Research*, **89**(B6), 4077–4114.

BAK, P., TANG, C. & WIESENFELD, K. 1988. Self-organized criticality. *Physical Review A* **38**(1), 364–374.

BARNETT, W. 2004. Subsidence breccias in kimberlite pipes—an application of fractal analysis. *Lithos* **76**(1–4), 299–316.

BEAR, J. 1988. *Dynamics of fluids in porous media*, New York: Dover, 764p.

BECKER, S.P., EICHHUBL, P., LAUBACH, S.E., REED, R.M., LANDER, R.H. & BODNAR, R.J. 2010. A 48 m.y. history of fracture opening, temperature, and fluid pressure: Cretaceous Travis Peak Formation, East Texas basin. GSA Bulletin 122(7-8), 1081–1093.

BEHRMANN, J.H. 1991. Conditions for hydrofracture and the fluid permeability of accretionary wedges. *Earth and Planetary Science Letters* **107**, 550-558.

BENNION, D.B., THOMAS, F.B. & BIETZ, R.F. 1996. Low Permeability Gas Reservoirs: Problems, Opportunities and Solutions for Drilling, Completion, Stimulation and Production. In *All Days*, pp. SPE-35577-MS. SPE Gas Technology Symposium, Calgary, Alberta, Canada: SPE.

BIOT, M.A. 1941. General Theory of Three-Dimensional Consolidation. *Journal of Applied Physics* **12**(2), 155–164.

BIOT, M.A. 1956. General Solutions of the Equations of Elasticity and Consolidation for a Porous Material. *Journal of Applied Mechanics* **23**(1), 91–96.

BLENKINSOP, T.G. 1991. Cataclasis and processes of particle size reduction. *Pure and Applied Geophysics PAGEOPH* **136**(1), 59–86.

BONS, P.D. 2001. The formation of large quartz veins by rapid ascent of fluids in mobile hydrofractures. , 17.

BONS, P.D. & JESSELL, M.W. 1997. Experimental simulation of the formation of fibrous veins by localised dissolution-precipitation creep. *Mineralogical Magazine* **61**(404), 53–63.

BONS, P.D. & VAN MILLIGEN, B.P. 2001. New experiment to model self-organized critical transport and accumulation of melt and hydrocarbons from their source rocks. *Geology* **29**(10), 919.

BONS, P.D. & MONTENARI, M. 2005. The formation of antitaxial calcite veins with well-developed fibres, Oppaminda Creek, South Australia. *Journal of Structural Geology* **27**(2), 231–248.

BONS, P.D., DOUGHERTY-PAGE, J. & ELBURG, M.A. 2001. Stepwise accumulation and ascent of magmas. *Journal of Metamorphic Geology* 19, 627-633

BONS, P.D., MONTENARI, M., BAKKER, R.J. & ELBURG, M.A. 2007. Potential evidence of Neoproterozoic deep life: SEM observations on calcite veins from Oppaminda Creek, Arkaroola, South Australia. *International Journal of Earth Sciences* **98**, 327-343

BONS, P.D., DRUGUET, E., CASTAÑO, L.M. & ELBURG, M.A. 2008. Finding what is not there anymore: recognizing missing fluid and magma volumes. *Geology* **36**, 851-854

BONS, P.D., BECKER, J.K., ELBURG, M.A. & URTSON, K. 2009. Granite formation: Stepwise accumulation of melt or connected networks? *Earth and Environmental Science Transactions of the Royal Society of Edinburgh* **100**(1–2), 105–115.

BONS, P.D., ELBURG, M.A. & GOMEZ-RIVAS, E. 2012. A review of the formation of tectonic veins and their microstructures. *Journal of Structural Geology* **43**, 33–62.

BONS, P.D., FUSSWINKEL, T., GOMEZ-RIVAS, E., MARKL, G., WAGNER, T. & WALTER, B. 2014. Fluid mixing from below in unconformity-related hydrothermal ore deposits. *Geology*, **42 (12)**, 1035-1038.

BOURNE, S.J. 2003. Contrast of elastic properties between rock layers as a mechanism for the initiation and orientation of tensile failure under uniform remote compression. *Journal of Geophysical Research Solid Earth* **108**(B8), 2395, doi:10.1029/2001JB001725,2003

BREDEHOEFT, J.D., WOLFF, R.G., KEYS, W.S. & SHUTER, E. 1976. Hydraulic fracturing to determine the regional in situ stress field, Piceance Basin, Colorado. *Geological Society of America Bulletin* **87**(2), 250.

BUCKLAND, W. & DE LA BECHE, H.T. 1835. I.-- On the Geology of the Neighbourhood of Weymouth and the adjacent Parts of the Coast of Dorset. *Transactions of the Geological Society of London* **s2-4**(1), 1–46.

CARTWRIGHT, J.A. 1994. Episodic basin-wide fluid expulsion from geopressured shale sequences in the North Sea basin. *Geology* **22**(5), 447.

CASWELL, T.E. & MILLIKEN, R.E. 2017. Evidence for hydraulic fracturing at Gale crater, Mars: Implications for burial depth of the Yellowknife Bay formation. *Earth and Planetary Science Letters* **468**, 72–84.

CHAUVET, A. 2019. Structural Control of Ore Deposits: The Role of Pre-Existing Structures on the Formation of Mineralised Vein Systems. *Minerals* **9**(1), 56.

CLARK, J.B. 1949. A Hydraulic Process for Increasing the Productivity of Wells. *Journal of Petroleum Technology* **1**(1), 1-8.

CLEARY, M.P. & WONG, S.K. 1985. Numerical simulation of unsteady fluid flow and propagation of a circular hydraulic fracture. *International Journal for Numerical and Analytical Methods in Geomechanics* **9**(1), 1–14.

CLEMENS, J.D. & MAWER, C.K. 1992. Granitic magma transport by fracture propagation. *Tectonophysics* 204, 339-360.

COBBOLD, P.R. & RODRIGUES, N. 2007. Seepage forces, important factors in the formation of horizontal hydraulic fractures and bedding-parallel fibrous veins (?beef? and ?cone-in-cone?). *Geofluids* **7**(3), 313–322.

COBBOLD, P.R., ZANELLA, A., RODRIGUES, N. & LØSETH, H. 2013. Bedding-parallel fibrous veins (beef and cone-in-cone): Worldwide occurrence and possible significance in terms of fluid overpressure, hydrocarbon generation and mineralization. *Marine and Petroleum Geology* **43**, 1–20.

CONNOLLY, J.A.D. 1997. Devolatilization-generated fluid pressure and deformation-propagated fluid flow during prograde regional metamorphism. *Journal of Geophysical Research: Solid Earth* **102**(B8), 18149–18173.

COSGROVE, J.W. 2001. Hydraulic fracturing during the formation and deformation of a basin: A factor in the dewatering of low-permeability sediments. *AAPG Bulletin* **85**(4), 7327-748.

COX, S.F. 1987. Antitaxial crack-seal vein microstructures and their relationship to displacement paths. *Journal of Structural Geology* **9**(7), 779–787.

COX, S.F. 1995. Faulting processes at high fluid pressures: An example of fault valve behavior from the Wattle Gully Fault, Victoria, Australia. *Journal of Geophysical Research: Solid Earth* **100**(B7), 12841–12859.

COX, S.F. 2005. Coupling between Deformation, Fluid Pressures, and Fluid Flow in Ore-Producing Hydrothermal Systems at Depth in the Crust. In *One Hundredth Anniversary Volume*, pp., Society of Economic Geologists.

COX, S.F. 2010. The application of failure mode diagrams for exploring the roles of fluid pressure and stress states in controlling styles of fracture-controlled permeability enhancement in faults and shear zones. *Geofluids*.

COX, S.F., ETHERIDGE, M.A. & WALL, V.J. 1986. The role of fluids in syntectonic mass transport, and the localization of metamorphic vein-type ore deposists. *Ore Geology Reviews* **2**(1–3), 65–86.

DAHM, T. 2000. On the shape and velocity of fluid-filled fractures in the Earth. *Geophysical Journal International* **142**(1), 181–192.

DAHM, T., HAINZL, S. & FISCHER, T. 2010. Bidirectional and unidirectional fracture growth during hydrofracturing: Role of driving stress gradients. *Journal of Geophysical Research* **115**(B12), B12322.

DE BOER, R. & EHLERS. W. 1988. A historical review of the formulation of porous media theories. *Acta Mechanica* **74**, 1-8.

DE BOER, R. & EHLERS. W. 1990. The development of the concept of effective stress. *Acta Mechanica* **83**, 77-92.

DELANEY, P.T., POLLARD, D.D., ZIONEY, J.I., & MCKEE, E.H. 1986. Field relations between dikes and joints: emplacement processes and paleostress analysis. *Journal of Geophysical Research* **91**, 4920e4983. doi:10.1029/JB091iB05p04920.

DE RIESE, T., BONS, P.D., GOMEZ-RIVAS, E. & SACHAU, T. 2020. Interaction between Crustal-Scale Darcy and Hydrofracture Fluid Transport: A Numerical Study (ed. A. H. Manning). *Geofluids* **2020**, 1–14.

DURNEY, D.W. & RAMSAY, J.G. 1973. Incremental strains measured by syntectonic crystal growths. In *Gravity and tectonics*, pp., Wiley NY.

EICHHUBL, P. 2000. Rates of fluid flow in fault systems; evidence for episodic rapid fluid flow in the Miocene Monterey Formation, coastal California. *American Journal of Science* **300**(7), 571–600.

ENGELDER, T. 1999. Transitional–tensile fracture propagation: a status report. *Journal of Structural Geology* **21**(8–9), 1049–1055.

ENGELDER, T. & LACAZETTE, A. 1990. Natural hydraulic fracturing. In Barton, N. & Stephansson, O. Eds. Rock joints. A.A. Balkema, Rotterdam, pp. 35-44.

ETHERIDGE, M.A., 1983. Differential stress magnitudes during regional deformation and metamorphism: upper bound imposed by tensile fracturing. *Geology* **11**, 231-234.

FALL, A., EICHHUBL, P., BODNAR, R.J., LAUBACH, S.E. & DAVIS, J.S. 2015. Natural hydraulic fracturing of tight-gas sandstone reservoirs, Piceance Basin, Colorado. *GSA Bulletin*, **127 (1-2)**, 61–75.

FILLUNGER, P. 1936. Erdbaumechanik? Selbstverlag des Verfassers, Wien, 31 pp.

FISHER, D.M. & BRANTLEY, S.L. 1992. Models of quartz overgrowth and vein formation: Deformation and episodic fluid flow in an ancient subduction zone. *Journal of Geophysical Research* **97**(B13), 20043.

FLEKKØY, E.G. 2002. Modeling hydrofracture. *Journal of Geophysical Research* **107**(B8), 2151.

FLETCHER, R.C. & MERINO, E. 2001. Mineral growth in rocks: kinetic-rheological models of replacement, vein formation, and syntectonic crystallization. *Geochimica et Cosmochimica Acta* **65**, 3733-3748.

GALE, J.F.W., LANDER, R.H., REED, R.M. & LAUBACH, S.E. 2010. Modeling fracture porosity evolution in dolostone. *Journal of Structural Geology* **32**(9), 1201–1211.

GEHNE, S. & BENSON, P.M. 2019. Permeability enhancement through hydraulic fracturing: laboratory measurements combining a 3D printed jacket and pore fluid over-pressure. *Scientific Reports* **9**(1), 12573.

GHANI, I., KOEHN, D., TOUSSAINT, R. & PASSCHIER, C.W. 2013. Dynamic Development of Hydrofracture. *Pure and Applied Geophysics* **170**(11), 1685–1703.

GHANI, I., KOEHN, D., TOUSSAINT, R. & PASSCHIER, C.W. 2015. Dynamics of hydrofracturing and permeability evolution in layered reservoirs. *Frontiers in Physics* **3**.

GIBIANSKY, L. & TORQUATO, S. 1998. Rigorous connection between physical properties of porous rocks. *Journal of Geophysical Research* **103**(B10), 23,911-23,9

GOLDFARB, R.J., SNEE, L.W. & PICKTHORN, W.J. 1993. Orogenesis, high- *T* thermal events, and gold vein formation within metamorphic rocks of the Alaskan Cordillera. *Mineralogical Magazine* **57**(388), 375–394.

GOMEZ-RIVAS, E. & GRIERA, A. 2012. Shear fractures in anisotropic ductile materials: an experimental approach. *Journal of Structural Geology* **34**, 61-76.

GOMEZ-RIVAS, E., BONS, P.D., KOEHN, D., URAI, J.L., ARNDT, M., VIRGO, S., LAURICH, B., ZEEB, C., STARK, L. & BLUM, P. 2014. The Jabal Akhdar dome in the Oman Mountains: Evolution of a dynamic fracture system. *American Journal of Science* **314**(7), 1104–1139.

GONZÁLEZ-ESVERTIT, E., CANALS, A., BONS, P.D., CASAS, J.M., GOMEZ-RIVAS, E. 2002. Compiling regional structures in geological databases: the Giant Quartz Veins of the Pyrenees as a case study. *Journal of Structural Geology*, in press, 104705. DOI: 10.1016/j.jsg.2022.104705.

GORDEYEV, YU.N. & ZAZOVSKY, A.F. 1992. Self-similar solution for deep-penetrating hydraulic fracture propagation. *Transport in Porous Media* **7**(3), 283–304.

GOREN, L., AHARONOV, E., SPARKS, D. & TOUSSAINT, R. 2010. Pore pressure evolution in deforming granular material: A general formulation and the infinitely stiff approximation. *Journal of Geophysical Research* **115**(B9), B09216.

GOREN, L., AHARONOV, E., SPARKS, D. & TOUSSAINT, R. 2011. The Mechanical Coupling of Fluid-Filled Granular Material Under Shear. *Pure and Applied Geophysics* **168**(12), 2289–2323.

GRIFFITH, A.A., 1920. The Phenomena of Rupture and Flow in Solids. *Philosophical Transactions: Royal Society, London, Series A* **221**, 163-198.

GRIFFITH, A. 1924. The theory of rupture. *Proc., Ist., Int., Congr., Appl., Mech. Biereno, C.B. Burgers, J.M(eds). Delft: Tech. Boekhandel en Drukkerij. J. Waltman Jr., pp. 54-63.*

GROVES, D.I., SANTOSH, M., GOLDFARB, R.J. & ZHANG, L. 2018. Structural geometry of orogenic gold deposits: Implications for exploration of world-class and giant deposits. *Geoscience Frontiers* **9**(4), 1163–1177.

GUDMUNDSSON, A., 2011. Rock Fractures in Geological Processes. *Cambridge University Press, Cambridge*. 592 pp.

GUERRIERO, V. & MAZZOLI, S. 2021. Theory of Effective Stress in Soil and Rock and Implications for Fracturing Processes: A Review. *Geosciences* **11**(3), 119.

HE, Q., SUORINENI, F.T. & OH, J. 2016. Review of Hydraulic Fracturing for Preconditioning in Cave Mining. *Rock Mechanics and Rock Engineering* **49**(12), 4893–4910.

HILGERS, C., KOEHN, D., BONS, P.D. & URAI, J. 2001. Development of crystal morphology during unitaxial growth in a progressively widening vein: II. Numerical simulations of the evolution of antitaxial fibrous veins. Journal of Structural Geology 23, 873-885.

HILLIS, R.R. 2003. Pore pressure/stress coupling and its implications for rock failure. *Geological Society, London, Special Publications* **216**(1), 359–368.

HOOKER, & FISHER, D.M. 2021. How cementation and fluid flow influence slip behaviour at the subduction interface. *Geology* **49**, 1074-1078.

HOOKER, J.N, LARSON, T.E., EAKIN, A., LAUBACH, S.E., EICHHUBL, P., FALL, A. & MARRETT, R. 2015. Fracturing and fluid flow in a sub-décollement sandstone; or, leak in the basement. *Journal of the Geological Society* **172**, 428-442.

HOOKER, J.N., RUHL, M., DICKSON, A.J., HANSEN, L.N., IDIZ, E., HESSELBO, S.P. & CARTWRIGHT, J. 2020. Shale anisotropy and natural hydraulic fracture propagation: Anexample from the Jurassic (Toarcian) Posidonienschiefer, Germany. *Journal of Geophysical Research: Solid Earth*, **125**, e2019JB018442. Doi:10.1029/2019JB018442

HUBBERT, M.K. 1951. Mechanical basis for certain familiar geologic structures. *Geological Society of America Bulletin* **62**(4), 355.

HUBBERT, M.K. & RUBEY, W.W. 1959. Role of fluid pressure in mechanics of overthrust faulting: I. Mechanics of fluid-filled porous solids and its application to overthrust faulting. *Geological Society of America Bulletin* **70**(2), 115.

HUNT 1990. Generation and Migration of Petroleum from Abnormally Pressured Fluid Compartments. *AAPG Bulletin* **74**.

INGEBRITSEN, S.E. & MANNING, C.E. 1999. Geological implications of a permeability-depth curve for the continental crust. *Geology* **27**(12), 1107.

INGLIS, C.E. 1913. Stresses in Plates Due to the Presence of Cracks and Sharp Corners. *Transactions of the Institute of Naval Architects* **55**, 219-241.

JAEGER, J.C., COOK, N.G.W., ZIMMERMAN, R., 2007. Fundamentals of Rock Mechanics. Wiley.

JAQUES, L., & PASCAL, C. 2017. Full paleostress tensor reconstruction using quartz veins of Panasqueira Mine, central Portugal; part I: paleopressure determination. *Journal of Structural Geology* **102**, 58-74.

JÉBRAK, M. 1997. Hydrothermal breccias in vein-type ore deposits: A review of mechanisms, morphology and size distribution. *Ore Geology Reviews* **12**(3), 111–134.

JOHNSEN, Ø., TOUSSAINT, R., MÅLØY, K.J. & FLEKKØY, E.G. 2006. Pattern formation during air injection into granular materials confined in a circular Hele-Shaw cell. *Physical Review E* **74**(1), 011301.

JOHNSEN, Ø., TOUSSAINT, R., MÅLØY, K.J., FLEKKØY, E.G. & SCHMITTBUHL, J. 2008a. Coupled air/granular flow in a linear Hele-Shaw cell. *Physical Review E* **77**(1), 011301.

JOHNSEN, Ø., CHEVALIER, C., LINDNER, A., TOUSSAINT, R., CLÉMENT, E., MÅLØY, K.J., FLEKKØY, E.G. & SCHMITTBUHL, J. 2008b. Decompaction and fluidization of a saturated and

confined granular medium by injection of a viscous liquid or gas. *Physical Review E* **78**(5), 051302.

JOLLY, R.J.H., & SANDERSON, D.J. 1997. A Mohr circle construction for the opening of a pre-existing fracture. *Journal of Structural Geology* **19**, 887-892.

KATSAGA, T., RIAHI, A., DEGAGNE, D.O., VALLEY, B. & DAMJANAC, B. 2015. Hydraulic fracturing operations in mining: conceptual approach and DFN modeling example. *Mining Technology* **124**(4), 255–266.

KEULEN, N., HEILBRONNER, R., STÜNITZ, H., BOULLIER, A.-M. & ITO, H. 2007. Grain size distributions of fault rocks: A comparison between experimentally and naturally deformed granitoids. *Journal of Structural Geology* **29**(8), 1282–1300.

KLING, T., SCHWARZ, J.-O., WENDLER, F., ENZMANN, F. & BLUM, P. 2017. Fracture flow due to hydrothermally induced quartz growth. *Advances in Water Resources*, **107**, 93-107.

KOEHN, D., ARNOLD, J. & PASSCHIER, C.W. 2005. Fracture and vein patterns as indicators of deformation history: a numerical study. *Geological Society, London, Special Publications* **243**(1), 11–24.

KOEHN, D., PIAZOLO, S., SACHAU, T. & TOUSSAINT, R. 2020. Fracturing and Porosity Channeling in Fluid Overpressure Zones in the Shallow Earth's Crust. *Geofluids* **2020**, 1–17.

KRONYAK, R.E., KAH, L.C., EDGETT, K.S.,VAN BOMMEL, S.J., THOMPSON, L.M., WIENS, R.C., et al. 2019. Mineral-filled fractures as indicators of multigenerational fluid flow in the Pahrump Hills member of the Murray formation, Gale crater, Mars. *Earth and Space Science* **6**,238–265.

KRUEGER, R.F. 1973. Advances in Well Completion And Stimulation During JPT's First Quarter Century. *Journal of Petroleum Technology* **25**(12), 1447–1462.

LANDER, R.H. & LAUBACH, S.E. 2015. Insight into rates of fracture growth and sealing for a model for quartz cementation in fractures sandstones. *GSA Bulletin* **127**, 516-538.

LAUBACH, S.E., REED, R.M., OLSON, J.E., LANDER, R.H. & BONNELL, L.M. 2004. Coevolution of crack-seal texture and fracture porosity in sedimentary rocks: cathodoluminescence observations of regional fractures. *Journal of Structural Geology* **26**(5), 967–982.

LAUBACH, S.E., LANDER, R.H., CRISCENTI, L.J., ANOVITZ, L.M., URAI, J.L., POLLYEA, R.M., HOOKER, J.N., NARR, W., EVANS, M.A., KERISIT, S.N., OLSON, J.E., DEWERS, T., FISHER, D., BODNAR, R., EVANS, B., DOVE, P., BONNELL, L.M., MARDER, M.P. & PYRAK-NOLTE, L. 2019. The Role of Chemistry in Fracture Pattern Development and Opportunities to Advance Interpretations of Geological Materials. *Reviews of Geophysics* **57**(3), 1065–1111.

LAZNICKA, P. 1989. Breccias and ores. Part 1: History, organization and petrography of breccias. *Ore Geology Reviews* **4**(4), 315–344.

LISTER, J.R. & KERR, R.C. 1990. Fluid-mechanical models of dyke propagation and magma transport. In: Mafic Dykes and Emplacement Mechanisms (eds Parker, A. J., Rickwood, P. C. & Tucker, D. H.), pp. 69-80. Balkema, Rotterdam.

LISTER, J.R. & KERR, R.C. 1991. Fluid-mechanical models of crack propagation and their application to magma transport in dykes. *Journal of Geophysical Research* **96**, 10 049-10 077.

LIU, X., XING, H. & ZHANG, D. 2017. Influences of Hydraulic Fracturing on Fluid Flow and Mineralization at the Vein-Type Tungsten Deposits in Southern China. *Geofluids* **2017**, 1–11.

LORILLEUX, G., JÉBRAK, M., CUNEY, M. & BAUDEMONT, D. 2002. Polyphase hydrothermal breccias associated with unconformity-related uranium mineralization (Canada): from fractal analysis to structural significance. *Journal of Structural Geology* **24**(2), 323–338.

LUAN, G., DONG, C., AZMY, K., LIN, C., MA, C., REN, L. & ZHU, Z. 2019. Origin of bedding-parallel fibrous calcite veins in lacustrine black shale: A case study from Dongying Depression, Bohai Bay Basin. *Marine and Petroleum Geology* **102**, 873–885.

Maaløe, S. 1987. The generation and shape of feeder dykes from mantle sources. *Contributions to Mineralogy and Petrology* **96**, 47-55.

MACDONALD, I.R., BUTHMAN, D.B., SAGER, W.W., PECCINI, M.B., & GUINASSO, N.L. 2000, Pulsed oil discharge from a mud volcano. *Geology* 28, p. 907–910.

MANNING, C.E. & INGEBRITSEN, S.E. 1999. Permeability of the continental crust: Implications of geothermal data and metamorphic systems. *Reviews of Geophysics* **37**(1), 127–150.

MARCHILDON, N. & BROWN, M. 2003. Spatial distribution of meltbearing structures in anatectic rocks from Southern Brittany, France: implications for melt transfer at grain- to orogen-scale. *Tectonophysics* **364**, 215–35.

MATTHÄI, S.K., HEINRICH, C.A. & DRIESNER, T. 2004. Is the Mount Isa copper deposit the product of forced brine convection in the footwall of a major reverse fault? *Geology* **32**(4), 357.

MEANS, W.D. & LI, T. 2001. A laboratory simulation of fibrous veins: some first observations. *Journal of Structural Geology* **23**(6–7), 857–863.

MENG, Q., HOOKER, J. & CARTWRIGHT, J. 2019. Role of pressure solution in the formation of bedding-parallel calcite veins in an immature shale (Cretaceous, southern UK). *Geological Magazine* **156**(5), 918–934.

MEYER, B.R. 1986. Design Formulae for 2-D and 3-D Vertical Hydraulic Fractures: Model Comparison and Parametric Studies. In *SPE Unconventional Gas Technology Symposium*, pp.SPE Unconventional Gas Technology Symposium, Louisville, Kentucky: Society of Petroleum Engineers.

MILLER, S.A. & NUR, A. 2000. Permeability as a toggle switch in fluid-controlled crustal processes. *Earth and Planetary Science Letters* **183**(1–2), 133–146.

MOHR, O. 1882. Über die Darstellung des Spannungzustandes eines Korpelementes. *Zivil Ingenieur* **e**, 113.

MONTGOMERY, C.T. & SMITH, M.B. 2010. Hydraulic Fracturing: History of an Enduring Technology. *Journal of Petroleum Technology* **62**(12), 26–40.

MORT, K. & WOODCOCK, N.H. 2008. Quantifying fault breccia geometry: Dent Fault, NW England. *Journal of Structural Geology* **30**(6), 701–709.

MOSKA, R., LABUS, K. & KASZA, P. 2021. Hydraulic Fracturing in Enhanced Geothermal Systems—Field, Tectonic and Rock Mechanics Conditions—A Review. *Energies* **14**(18), 5725.

MÜGGE, O. 1928. Über die Entstehung faseriger Minerale und ihrer Aggregationsformen. *eues Jahrbuch für Mineralogie, Geologie und Paläontologie* **58A**, 303–348.

NAKASHIMA, Y. 1993. Buoyancy-driven propagation of an isolated fluid-filled crack in rock: implication for fluid transport in metamorphism. *Contributions to Mineralogy and Petrology* **114**(3), 289–295.

NIEBLING, M.J., FLEKKØY, E.G., MÅLØY, K.J. & TOUSSAINT, R. 2010a. Mixing of a granular layer falling through a fluid. *Physical Review E* **82**(1), 011301.

NIEBLING, M.J., FLEKKØY, E.G., MÅLØY, K.J. & TOUSSAINT, R. 2010b. Sedimentation instabilities: Impact of the fluid compressibility and viscosity. *Physical Review E* **82**(5), 051302.

NOR, A. & WALDER, J. 1992. Chapter 19 Hydraulic Pulses in the Earth's Crust. In *International Geophysics*, pp. 461–473. , Elsevier.

NUNN, J.A. 1996. Buoyancy-driven propagation of isolated fluid-filled fractures: Implications for fluid transport in Gulf of Mexico geopressured sediments. *Journal of Geophysical Research: Solid Earth* **101**(B2), 2963–2970.

NUR. A. & BYERLEE, J.D. 1971. An exact effective stress law for elastic deformation of rock with fluids. *Journal of Geophysical Research* **76**(26), 6414-6419.

OKAMOTO, A. & TSUCHIYA, N. 2009. Velocity of vertical fluid ascent within vein-forming fractures. *Geology* **37**(6), 563–566.

OKAMOTO, A. & SEKINE, K. 2011. Textures of syntaxial quartz veins synthesized by hydrothermal experiments. *Journal of Structural Geology* **33**(12), 1764–1775.

OLIVER, J. 1986. Fluids expelled tectonically from orogenic belts: Their role in hydrocarbon migration and other geologic phenomena. *Geology* **14**(2), 99.

OLIVER, N.H.S. & BONS, P.D. 2001. Mechanisms of fluid flow and fluid-rock interaction in fossil metamorphic hydrothermal systems inferred from vein-wallrock patterns, geometry and microstructure. *Geofluids* **1**(2), 137–162.

OLIVER, N.H.S., MCLELLAN, J.G., HOBBS, B.E., CLEVERLEY, J.S., ORD, A. & FELTRIN, L. 2006a. 100th Anniversary Special Paper: Numerical Models of Extensional Deformation, Heat Transfer, and Fluid Flow across Basement-Cover Interfaces during Basin-Related Mineralization. *Economic Geology* **101**(1), 1–31.

OLIVER, N.H.S., RUBENACH, M.J., FU, B., BAKER, T., BLENKINSOP, T.G., CLEVERLEY, J.S., MARSHALL, L.J. & RIDD, P.J. 2006b. Granite-related overpressure and volatile release in the mid crust: fluidized breccias from the Cloncurry District, Australia. *Geofluids* **6**(4), 346–358.

OLSON, J.E., LAUBACH, S.E. & LANDER, R.H. 2009. Natural fracture characterization in tight gas sandstones: Integrating mechanics and diagenesis. AAPG Bulletin 93, 1535-1549.

OSBORNE, M.J. & SWARBRICK, R.E. 1997. Mechanisms for Generating Overpressure in Sedimentary Basins: A Reevaluation. *AAPG Bulletin* **81 (1997)**.

PASCAL,C. 2021. *Paleostress Inversion Techniques: Methods and Applications for Tectonics*, Elsevier 274 pp.

PASSCHIER, C.W. & TROUW, R.A.J. 2005. *Microtectonics* 2nd, rev.enl. ed ed., Berlin ; New York: Springer, 366p.

PATI, J.K., PATEL, S.C., PRUSETH, K.L., MALVIYA, V.P., ARIMA, M., RAJU, S., PATI, P. & PRAKASH, K. 2007. Geology and geochemistry of giant quartz veins from the Bundelkhand Craton, central India and their implications. *J. Earth Syst. Sci.* **116**, 497–510.

PERSON, M., MULCH, A., TEYSSIER, C. & GAO, Y. 2007. Isotope transport and exchange within metamorphic core complexes. *American Journal of Science* **307**(3), 555–589.

PETFORD, N., KERR, R.C. & LISTER, J.R. 1993. Dike transport of granitoid magmas. *Geology* **21**, 845-848.

PETTKE, T. & DIAMOND, L.W. 1996. Oligocene Gold Quartz Veins at Brusson, NW Alps: Sr Isotopes Trace the Source of Ore-Bearing Fluid to Over a 10-Km Depth. *Economic Geology* **92**, 389–406.

PHILLIP, S. 2012. Fluid overpressure estimates from the aspect ratios of mineral veins. *Tectonophysics* **581**, 35-47.

PHILLIPS, W.J. 1972. Hydraulic fracturing and mineralization. *Journal of the Geological Society* **128**(4), 337–359.

PIRAJNO, F. 2009. Hydrothermal Processes and Wall Rock Alteration. In *Hydrothermal Processes and Mineral Systems*, pp. 73–164. , Dordrecht: Springer Netherlands.

POLLARD, D.D. 1976. On the form and stability of open hydraulic fractures in the Earth's crust. *Geophysical Research Letters* **3**(9), 513–516.

POLARD, D.D. & AYDIN, A. 1988. Progress in understanding jointing over the past century. *Geological Society of America Bulletin* **100**, 1181-1204.

POLLARD, P.D., FLETCHER, R.C., 2005. Fundamentals of Structural Geology. Cambridge University Press.

PREISIG, G., EBERHARDT, E., GISCHIG, V., ROCHE, V., VAN DER BAAN, M., VALLEY, B., KAISER, P.K., DUFF, D. & LOWTHER, R. 2016. Development of connected permeability in massive crystalline rocks through hydraulic fracture propagation and shearing accompanying fluid injection. In *Crustal Permeability* (eds. T. Gleeson & S. E. Ingebritse), pp. 335–352. , Chichester, UK: John Wiley & Sons, Ltd.

RAMSAY, J.G. 1980. The crack–seal mechanism of rock deformation. *Nature* **284**(5752), 135–139.

RAMSEY, J.M. & CHESTER, F.M. 2004. Hybrid fracture and the transition from extension fracture to shear fracture. *Nature* **428**(6978), 63–66.

Regenauer-Lieb, K., 1999. Dilatant plasticity applied to Alpine collision: Ductile void growth in the intraplate area beneath the Eifel volcanic field. *Journal of Geodynamics* **27**, 1-21.

RENARD, F., ANDRÉANI, M., BOULLIER, A.-M. & LABAUME, P. 2005. Crack-seal patterns: records of uncorrelated stress release variations in crustal rocks. *Geological Society, London, Special Publications* **243**(1), 67–79.

RICE, C.M., MARK, D.F., SELBY, D., NEILSON, J.E. & DAVIDHEISER-KROLL, B. 2016. Age and Geologic Setting of Quartz Vein-Hosted Gold Mineralization at Curraghinalt, Northern Ireland: Implications for Genesis and Classification. *Economic Geology* **111**(1), 127–150.

RICHARD, H.A. & SANDERS, M. 2016. *Fatigue Crack Growth*, Springer Vieweg, Switzerland, 292pp.

RIVALTA, E., BÖTTINGER, M. & DAHM, T. 2005. Buoyancy-driven fracture ascent: Experiments in layered gelatine. *Journal of Volcanology and Geothermal Research* **144**, 273-285

RIVALTA, E., TAISNE, B., BUNGER, A.P. & KATZ, R.F. 2015. A review of mechanical models of dike propagation: Schools of thought, results and future directions. *Tectonophysics* **638**, 1-42.

ROGATZ, H. 1961. Shallow oil & gas fields of the Texas Panhandle and Hugoton. In: Oil and Gas Fields of the Texas and Oklahoma Panhandles, AAPG, p. 8-37.

ROJSTACZER, S.A., INGEBRITSEN, S.E. & HAYBA, D.O. 2008. Permeability of continental crust influenced by internal and external forcing. *Geofluids* **8**(2), 128–139.

ROOKE, D.P. & CARTWRIGHT, D.J. 1976. *Compendium of stress intensity factors*. Her Majesty's Stationary Office, London, 330 pp.

RUBIN, A.M. 1995. Propagation of Magma-Filled Cracks. *Annual Review of Earth and Planetary Sciences* **23**(1), 287–336.

SCHAARSCHMIDT, A., HAASE, K.M., DE WALL, H., BESTMANN, M., KRUMM, S. & REGELOUS, M. 2019. Upper crustal fluids in a large fault system: microstructural, trace element and oxygen isotope study on multi-phase vein quartz at the Bavarian Pfahl, SE Germany. *International Journal of Earth Sciences* **108**(2), 521–543.

SECOR, D.T. 1965. Role of fluid pressure in jointing. *American Journal of Science* **263**(8), 633–646.

SECOR, D.T. & POLLARD, D.D. 1975. On the stability of open hydraulic fractures in the Earth's crust. *Geophysical Research Letters* **2**(11), 510–513.

SHAPIRO, S.A. & DINSKE, C. 2009. Fluid-induced seismicity: Pressure diffusion and hydraulic fracturing. *Geophysical Prospecting* **57**(2), 301–310.

SHARP, Z.D., MASSON, H. & LUCCHINI, R. 2005. Stable isotope geochemistry and formation mechanisms of quartz veins; extreme paleoaltitudes of the Central Alps in the Neogene. *American Journal of Science* **305**(3), 187–219.

SIBSON, R.H. 1986. Brecciation processes in fault zones: Inferences from earthquake rupturing. *Pure and Applied Geophysics PAGEOPH* **124**(1–2), 159–175.

SIBSON, R.H. 2000a. Fluid involvement in normal faulting. *Journal of Geodynamics* **29**(3–5), 469–499.

SIBSON, R.H. 2000b. Tectonic controls on maximum sustainable overpressure: fluid redistribution from stress transitions. *Journal of Geochemical Exploration* **69–70**, 471–475.

SIBSON, R.H. 2003. Brittle-failure controls on maximum sustainable overpressure in different tectonic regimes. *AAPG Bulletin* **87**, 901-908.

SIBSON, R.H., MOORE, J.MC.M. & RANKIN, A.H. 1975. Seismic pumping—a hydrothermal fluid transport mechanism. *Journal of the Geological Society* **131**(6), 653–659.

SIBSON, R.H., ROBERT, F. & POULSEN, K.H. 1988. High-angle reverse faults, fluid-pressure cycling, and mesothermal gold-quartz deposits. *Geology* **16**(6), 551.

Sih, G.C. 1973 *Stress-Intensity Factors for Researchers and Engineers*, Institute of Fracture and Solid Mechanics, Lehigh University, Bethlehem, PA.

SKEMPTON, A.W. 1960. Significance of Terzaghi's concept of effective stress (Terzaghi's discovery of effective stress). In: From theory to practice in soil mechanics (Bjerrum, L., Casagrande, A., Peek, R. B., Skempton, A. W., eds.). John Wiley & Sons, New York - London.

SLEEP, N.H. 1988. Tapping of melt by veins and dikes. *Journal of Geophysical Research* **93**, 10 255-10 272.

SOLOYEV, T.M. & KOBELEVA, V.A. 1960. Ways to intensify oil production. *Petroleum Geology: A digest of Russian literature on Petroleum Geology* **4**(11B), 661-665.

SORNETTE, D. 2009. Dragon-Kings, Black Swans and the Prediction of Crises. *SSRN Electronic Journal*.

SPÄTH, M., SPRUŽENIECE, L., URAI, J.L., SELZER, M., ARNDT, M. & NESTLER, B. 2021. Kinematics of Crystal Growth in Single-Seal Syntaxial Veins in Limestone - A Phase-Field Study. *Journal of Geophysical Research: Solid Earth* **126**(10).

SPÄTH, M., URAI, J.L.. & NESTLER, B. 2022. Incomplete crack sealing causes localization of fracturing in hydrothermal quartz veins. *Geophysical Research Letters* 2022GL098643. Doi: https://doi.org/10.1029/2022GL098643.

SPENCE, D.A. & TURCOTTE, D.L. 1985. Magma-driven propagation of cracks. *Journal of Geophysical Research: Solid Earth* **90**(B1), 575–580.

STANCHITS, S., MAYR, S., SHAPIRO, S. & DRESEN, G. 2011. Fracturing of porous rock induced by fluid injection. *Tectonophysics* **503**(1–2), 129–145.

STAUDE, S., BONS, P.D. & MARKL, G. 2009. Hydrothermal vein formation by extension-driven dewatering of the middle crust: An example from SW Germany. *Earth and Planetary Science Letters* **286**(3–4), 387–395.

STORK, A.L., VERDON, J.P. & KENDALL, J.-M. 2015. The microseismic response at the In Salah Carbon Capture and Storage (CCS) site. *International Journal of Greenhouse Gas Control* **32**, 159–171.

SU, A., BONS, P.D., CHEN, H., FENG, Y., ZHAO, J. & SONG, J. 2021. Age, material source, and formation mechanism of bedding-parallel calcite beef veins: Case from the mature Eocene lacustrine shales in the Biyang Sag, Nanxiang Basin, China. *GSA Bulletin*.

SUN, Z., WANG, J., WANG, Y., ZHANG, Y. & ZHAO, L. 2021. Multistage hydrothermal quartz veins record the ore-forming fluid evolution in the Meiling Cu–Zn (Au) deposit, NW China. *Ore Geology Reviews* **131**, 104002.

TABER, S. 1918. The Origin of Veinlets in the Silurian and Devonian Strata of Central New York. *The Journal of Geology* **26**(1), 56–73.

TAKADA, A. 1990. Experimental study on propagation of liquid-filled crack in gelatin: Shape and velocity in hydrostatic stress condition. *Journal of Geophysical Research* **95**(B6), 8471.

TERZAGHI, K. 1923. Die Berechnug der Durchlassigkeit des Tones aus dem Verlauf der hydromechanischen Spannungserscheinungen. *Sitzungsber. Akad. Wiss.(Wien). Math.-Naturwiss. Kl., Abt. Iia* **132**, 125–138.

TERZAGHI, K. 1943. *Theoretical soil mechanics*, New York, London: John Wiley and Sons,p.

TOWNEND, J. & ZOBACK, M.D. 2000. How faulting keeps the crust strong. *Geology* **28**(5), 399.

TURCOTTE, D.L. 1986. Fractals and fragmentation. *Journal of Geophysical Research* **91**(B2), 1921.

TURCOTTE, D.L. 1999. Self-organized criticality. *Reports on Progress in Physics* **62**(10), 1377–1429.

TZSCHICHHOLZ, F., HERRMANN, H.J., ROMAN, H.E. & PFUFF, M. 1994. Beam model for hydraulic fracturing. *Physical Review B* **49**(10), 7056–7059.

URAI, J.L., WILLIAMS, P.F. & VAN ROERMUND, H.L.M. 1991. Kinematics of crystal growth in syntectonic fibrous veins. *Journal of Structural Geology* **13**(7), 823–836.

U.S. NUCLEAR REGULATORY COMMISSION, U.S. OF A. 2009. Generic environmental impact statement for in-situ leach uranium milling facilities.

VASS, A., KOEHN, D., TOUSSAINT, R., GHANI, I. & PIAZOLO, S. 2014. The importance of fracture-healing on the deformation of fluid-filled layered systems. *Journal of Structural Geology* **67**, 94–106.

VIELREICHER, N.M., GROVES, D.I. & MCNAUGHTON, N.J. 2016. The giant Kalgoorlie Gold Field revisited. *Geoscience Frontiers* **7**(3), 359–374.

VINNINGLAND, J.L., JOHNSEN, Ø., FLEKKØY, E.G., TOUSSAINT, R. & MÅLØY, K.J. 2007a. Experiments and simulations of a gravitational granular flow instability. *Physical Review E* **76**(5), 051306.

VINNINGLAND, J.L., JOHNSEN, Ø., FLEKKØY, E.G., TOUSSAINT, R. & MÅLØY, K.J. 2007b. Granular Rayleigh-Taylor Instability: Experiments and Simulations. *Physical Review Letters* **99**(4), 048001.

VINNINGLAND, J.L., JOHNSEN, Ø., FLEKKØY, E.G., TOUSSAINT, R. & MÅLØY, K.J. 2010. Size invariance of the granular Rayleigh-Taylor instability. *Physical Review E* **81**(4), 041308.

VINNINGLAND, J.L., TOUSSAINT, R., NIEBLING, M., FLEKKØY, E.G. & MÅLØY, K.J. 2012. Family-Vicsek scaling of detachment fronts in granular Rayleigh-Taylor instabilities during sedimentating granular/fluid flows. *The European Physical Journal Special Topics* **204**(1), 27–40.

VIRGO, S., ABE, S. & URAI, J.L. 2014. The evolution of crack seal vein and fracture networks in an evolving stress field: Insights from Discrete Element Models of fracture sealing: DEM crack-seal evolution. *Journal of Geophysical Research: Solid Earth* **119**(12), 8708–8727.

WALDER, J. & NUR, A. 1984. Porosity reduction and crustal pore pressure development. *Journal of Geophysical Research: Solid Earth* **89**(B13), 11539–11548.

WANG, M., CHEN, Y., SONG, G., STEELE-MACINNIS, M., LIU, Q., WANG, X., ZHANG, X., ZHAO, Z., LIU, W., ZHANG, H. & ZHOU, Z. 2018. Formation of bedding-parallel, fibrous calcite veins in laminated source rocks of the Eocene Dongying Depression: A growth model based on petrographic observations. *International Journal of Coal Geology* **200**, 18–35.

WANG, Q., CHEN, X., JHA, A.N. & ROGERS, H. 2014. Natural gas from shale formation – The evolution, evidences and challenges of shale gas revolution in United States. *Renewable and Sustainable Energy Reviews* **30**, 1–28.

WANGEN, M. 2022. A model of fluid expulsion from compacting tight sedimentary rocks based on the Toggle-Switch algorithm. *Applied Computing and Geosciences* **13**, 100079.

WEERTMAN, J. 1971. Theory of water-filled crevasses in glaciers applied to vertical magma transport beneath oceanic ridges. *Journal of Geophysical Research* **76**(5), 1171–1183.

Weinberg. R.F & Regenauer-Lieb, K. 2010. Ductile fractures and magma migration from source. *Geology* **38**, 363-366.

WEIS, P. 2015. The dynamic interplay between saline fluid flow and rock permeability in magmatic-hydrothermal systems. *Geofluids* **15**(1–2), 350–371.

WEISHEIT, A., BONS, P.D. & ELBURG, M.A. 2013a. Long-lived crustal-scale fluid flow: the hydrothermal mega-breccia of Hidden Valley, Mt. Painter Inlier, South Australia. *International Journal of Earth Sciences* **102**(5), 1219–1236.

WEISHEIT, A., BONS, P.D., DANIŠÍK, M. & ELBURG, M.A. 2013b. Crustal-scale folding: Palaeozoic deformation of the Mt Painter Inlier, South Australia. *Geological Society, London, Special Publications* **394**(1), 53–77.

WESTERGAARD, H.M. 1939. Bearing Pressures and Cracks. *Journal of Applied Mechanics* **6**, A49-53.

WILTSCHKO, D.V. & MORSE, J.W. 2001. Crystallization pressure versus "crack seal" as the mechanism for banded veins. *Geology* **29**(1), 79.

XIONG, Y., ZUO, R., CLARKE, K.C., MILLER, S.A. & WANG, J. 2020. Modeling singular mineralization processes due to fluid pressure fluctuations. *Chemical Geology* **535**, 119458.

YAMAJI, A., SATO, K. & TONAI, S. 2010. Stochastic modeling for the stress inversion of vein orientations: paleostress analysis of Pliocene epithermal veins in southwestern Kyushu, Japan. *Journal of Structural Geology* **32**, 1137-1146.

YARDLEY, B.W.D. 1986. Fluid Migration and Veining in the Connemara Schists, Ireland. In *Fluid—Rock Interactions during Metamorphism* (eds. J. V. Walther & B. J. Wood), pp. 109–131. Advances in Physical Geochemistry, New York, NY: Springer New York.

ZANELLA, A., COBBOLD, P.R. & BOASSEN, T. 2015. Natural hydraulic fractures in the Wessex Basin, SW England: Widespread distribution, composition and history. *Marine and Petroleum Geology* **68**, 438–448.

ZHANG, B., YIN, C., GU, Z., ZHANG, J., YAN, S. & WANG, Y. 2015. New indicators from bedding-parallel beef veins for the fault valve mechanism. *Science China Earth Sciences* **58**(8), 1320–1336.

ZHAO, C., HOBBS, B.E. & ORD, A. 2008. *Convective and advective heat transfer in geological systems*, Berlin ; London: Springer, 229p.

ZHU, Q.-Z. 2017. A New Rock Strength Criterion from Microcracking Mechanisms Which Provides Theoretical Evidence of Hybrid Failure. *Rock Mechanics and Rock Engineering* **50**(2), 341–352.

Appendix

1. The raw data for the individual clasts from sample *A* to *E* are presented here: https://osf.io/8aqjb/files/osfstorage/68875a79982ea39c67256cde?view_only=f19e0cf78fb747b5a61f862a111bed07

Numerical model setup

2A. Simulation output data

The code (in C programming lang.) and the output data for the simulations. The code for the main reference run is presented here. However, the different parameters are clearly stated in the paper. The modified inputs for the different simulations are circled in red.

Code: The main section of the code is presented below leaving out the loop (clearly explained in the methodology) sections

```c
/*
 ============================================================================
 Name        : bimodal_transport.c
 Author      :
 Version     :
 Copyright   : Your copyright notice
 Description : Hello World in C, Ansi-style
 ============================================================================
 */

#include <stdio.h>
#include <math.h>
#include <stdlib.h>
#include <stddef.h>
#include <string.h>

#define NR_END 1
#define X 0 // positions of info in elementslist
#define Y 1
#define LANDTYPE 2 // can be land or edge
#define ISBROKEN 3 // can be broken or not
#define NBtop 4
#define NBright 5
#define NBbelow 6
#define NBleft 7
#define NNeighb 8 // how many neighbours 0 to 4
#define NO_NEIGHBOUR -99 // there is no neighbour (edge etc.)

#define EDGE 0 // boundary
#define LAND 1 // normal
#define SURFACE 2 // here water always escapes


#define NOT_BROKEN 0
#define BROKEN 1

double  **dmatrix(long nrl, long nrh, long ncl, long nch);
long int    **limatrix(long nrl, long nrh, long ncl, long nch);
int     **imatrix(long nrl, long nrh, long ncl, long nch);
double  *dvector(long nl, long nh);
int     *ivector(long nl, long nh);
long int *livector(long nl, long nh);
void nrerror(char error_text[]);

void Initialise();
int GetXfromlistindex(long int n);
int GetYfromlistindex(long int n);
long int GetNfromXY(int x, int y);
void FlowLoop();
double  GetRandomDoubleInRange(double min, double max);
double  GetTotalHeight();
double  GetAbsLfValue(double x);
void WriteMapToFile();
double  AddMaterialonOneNode(long int n); // add a bit to one element anywhere in model if n==0, or else add it to node n, returns how much is added
double  AddMaterialonOneNodeAtBottom(); // add a bit to one element in the bottom row, returns how much is added
void    Do_Avalanche(long int n); // carry out an avalanche once failure is reached in one node
void    Do_Diffusion(); // carry out the diffusion bit
void    CheckForAvalanches();

long int **node_state; // x&y coordinates of each element in list, state and neighbours
double  *DiffCoeff;
double  *node_height,*node_change_h; // drive of each element
double *failurelevel,*maxfailurelevel; // value of gradient at which ballistic flow is activated
long int    *randomnodelist;
long int    *clusterlist; // list with all nodes that are part of a cluster
int     *BrokenNodesList;
long int Nelements;
double  t=0.0; // the main time variable
FILE *outputmapfile,*clusterfile,*outputlist,*clustermapfile;

```

```
70
71 // variables that need to be set for the model
72 double  failurethreshold=1.0,incrementfailure=1.0,minfailure=0.0;
73 int     Nbreaks=1; // number of neighbours to consider in fracture propagation
74
75 /*
76  * Here you set the main model parameters
77  */
78 // first the size (dim), duration (endtime) and time step (dt)
79 long int    dim=200; // hor & ver dimensions of the model
80 double  dt=1.0,endtime=500000.0; // time increment and total duration of run
81
82 // next the location and amount of fluid input
83 long int baseinputrow=199,topinputrow=100; // This is where fluid is inserted note that row numbers increase downwards
84 double  snowfallmin=0.0,snowfallmax=0.002; // This is the range of values for the fluid input for one node
85 double  startslope=0.9; // initial slope in fluid pressure
86
87 // now the diffusion settings, which simulates Darcyan fluid flow through the matrix
88 int     ConstantDiffusion=0; // if set at 1, D is D0 for all nodes. If 0, the diffusion rate is set for each node in routine Initialise()
89 double  D0=0.002,Dmax=0.002; // diffusion coefficients for normal diffusion.
90
91 // Also set the intervals and beginning time of recording data in tables and movies. Note that this uses the "counter", so every time you go through the loop once
92 long int startrecordingmovies=0; //begin saving the movies from this time
93 long int savemovieinterval=50; // save a movie slice every given number of time steps
94 long int startrecordingtables=0; //begin saving the data to the tables from this time
95 long int savetableinterval=25; // save the data to the tables every given number of time steps
96
97 /*
98  * Most fractures are only one or two nodes in size. Recording all would result in a very or too large list of fractures
99  * Also, it may take some time to achieve a steady state
100 * To circumvent such problems, you can set the minimum size (number of broken nodes) of a cluster to record, and limit the recording time by stting a beginning and end
101 */
102 long int minsizesavecluster=1; // the minimum nodes in a fracture cluster to be saved to be saved to the cluster file. Many clusters are very small!
103 double startrecordingclusters=0.0; // start recording the clusters to table
104 double endrecordingclusters=500000.0; // start recording the clusters to table
105
106 /*
107  * variables related to recording the average pressure with depth
108  */
109 long int startrecordingpressure=25000,endrecordingpressure=250000;
110 double  *Pprofile;
111 double  Npressuremeasurements=0.0;
112
113 int main(void) {
114     Initialise();
115     printf("finished initialisation\n");
116     FlowLoop();
117     puts("\nFinished!!!\n"); /* prints !!!Hello World!!! */
118     return EXIT_SUCCESS;
119 }
120
121 /*
122  * Main programm loop that carries out the simulation
123  */
124 void FlowLoop()
125 {
126     long int    counter=0,mapslices=0,i,j,lowestaddindex,highestaddindex;
127     double      totaladded=0.0,relheight; // amount of material added in the whole run
128
```

2B. Output data (movies, clusterlist and the heightlist data files) from the simulations: https://osf.io/8aqjb/files/osfstorage/68875bb7a5141887faa23ff6?view_only=f19e0cf78fb747b5a61f862a111bed07

References

Rasband, W. S. (1997-2021). ImageJ. U.S. National Institutes of Health, Bethesda, Maryland, USA. https://imagej.nih.gov/ij/.

de Riese, T., Bons P. D., Gomez-Rivas E., & Sachau, T. (2020). Interaction between crustal-scale Darcy and hydrofracture fluid transport: a numerical study. Geofluids 2020, 1–14.